UNIVERSITY OF SOUTHAMPTON

Faculty of Natural and Environmental Sciences

School of Chemistry

A High-Throughput Thermographic Screen for Model Heterogeneous Catalysts

by

Jovine Kamuhabwa Emmanuel

Thesis for the degree of Doctor of Philosophy

October 2014

UNIVERSITY OF SOUTHAMPTON

ABSTRACT

FACULTY OF NATURAL AND ENVIRONMENTAL SCIENCES

Doctor of Philosophy

A High-Throughput Thermographic Screen for Model Heterogeneous Catalysts

By Jovine Kamuhabwa Emmanuel

Despite the fact that it is now accepted that the particle size and the support in heterogeneous catalysts strongly influences the activity and selectivity of the catalysts, it has been a challenge to measure such effects systematically, especially on model systems. A high-throughput (parallel) thermographic screening methodology is described here, which allows such measurements to be made. A screening chip was designed and fabricated in order to produce multiple fields of low stress silicon nitride membranes that exhibit low thermal conductivity and heat capacity. The heat generated on model, supported catalysts in an exothermic reaction deposited on the membranes could then be monitored using a thermal (infra-red) imaging camera. The temperature of the catalyst under steady state reaction conditions was used as a measure of mass or specific catalytic activity. The effectiveness of the screening method to determine catalytic activity was demonstrated for titania supported platinum and gold model catalysts by studying the CO oxidation reaction. For both supported metals we observe strong particle size effects in the activity.

Platinum nanoparticles in the size range of ca. 1 to 8 nm and gold nanoparticles between ca. 1 to 6 nm in size were deposited on an amorphous titania support, as determined from transmission electron microscope image analysis. The reaction of CO and O_2 on these model catalysts was measured using the thermographic screening method. The model, supported catalysts were also characterised by TEM and XPS both before and after reaction. The reaction over titania supported platinum was investigated in the temperature range of 80 ^{o}C to 240 ^{o}C and pressure range 0.072 mbar to 2.4 mbar. The turnover frequency (TOF) and specific mass activity of Pt for CO oxidation increased monotonically with decreasing particle size by a factor of 17. XPS showed that there was no change in the particle size distribution during the reactions. While there is no apparent consensus in the literature concerning a particle size effect for this system, this result is in good agreement with recent findings on high area supported catalysts, finding a seven-fold increase in activity between 10 nm and 1nm particle sizes.

The CO oxidation on titania supported gold nanoparticles was investigated at 80 ^{o}C and 170 ^{o}C and pressure ranging between 0.06 mbar and 1.5 mbar. The TOF and specific mass activity increased monotonically with decreasing particle size by a factor of 19. XPS again showed that there was no significant change in the particle size distribution during the reactions. While there is no apparent consensus in the literature concerning the activity trend with particle size for this system, this result is consistent with most data published in the literature.

The absolute activities measured at low temperature (ca. 80 ^{o}C) and pressure (0.11 mbar) in this study for Au/TiO_2 nanoparticle catalyst are higher than Pt/TiO_2 nanoparticles over the ranges of particle sizes investigated.

Contents

List of tables

List of figures

Declaration of authorship

I, Jovine Kamuhabwa Emmanuel

declare that the thesis entitled

A High-Throughput Thermographic Screen for Model Heterogeneous Catalysts

and the work presented in the thesis are both my own, and have been generated by me as the result of my own original research. I confirm that:

- this work was done wholly or mainly while in candidature for a research degree at this University;
- where any part of this thesis has previously been submitted for a degree or any other qualification at this University or any other institution, this has been clearly stated;
- where I have consulted the published work of others, this is always clearly attributed;
- where I have quoted from the work of others, the source is always given. With the exception of such quotations, this thesis is entirely my own work;
- I have acknowledged all main sources of help;
- where the thesis is based on work done by myself jointly with others, I have made clear exactly what was done by others and what I have contributed myself;
- none of this work has been published before submission,

Signed: ……

Date:……

Acknowledgements

I am very grateful to my supervisor Prof. Brian Hayden for his overall support. I thank him for all his assistance throughout my PhD, for his vision, encouragement and invaluable scientific insight. Without him it would have been a different story. I would also like to thank my advisor Dr. Andrew Hector for the advice he offered during this project.

I would also like to thank Mkwawa University College of Education and the World Bank for funding this project.

I would like also to thank our lovely and intelligent former postdoc, Dr. Fiona McBride for her amazing help and patience. More importantly I thank her for proofreading my thesis and proving me with very helpful discussions.

I would like to thank Ilika Technologies for technical support with high throughput informatics. Thank you Chris Newman for constructive discussions during the initial design of the high throughput catalysis screening chip, Dr. Clare Mormiche and Dr. Duncan Smith for the IR-camera technique, and Dr. Chris Vian for the data analysis software write-up.

I would like also to thank Mir Enterprises Ltd, London for helpful discussions on design and fabrication of the high throughput catalysis screening chip.

The three years spent within Brian Hayden's research group and the labs have been fabulous due to the group member's corporation. I thank Dr. Louise Hannah and Dr. John Blake for the HT-PVD concepts and operation. I would like to thank Sandy Kerry for assistance during sample preparation in the PVD laboratory. Thank you to Jaffar Saleh for productive discussions on screening chip design, software handling throughout my project and for proofreading my thesis.

The mechanical workshop within the School of Chemistry has been helpful throughout, particularly during the development of an UHV sample holder and heating system.

I am indebted to my wife Edna Kyaruzi for her love, patience, encouragements and understanding when I left home for a foreign land. Thank you for visiting me while I was in studies in Southampton, United Kingdom. I would also like to appreciate the love that our daughters, Jennifer and Jessica have shown over time, especially when they insisted that they need me back home. It is without doubt that we will be together once again.

I would also like to thank my mother, Adelina, my brothers and sister for encouragement prayers throughout my education. Your prayers have been helpful.

Abbreviations

Abbreviation	Meaning
AFM	Atomic force microscopy
DFT	Density functional theory
DSP	Digital signal processing
ecIRT	Emissivity corrected infrared thermography
E-gun	Electron gun
fcc	Face centred cubic
FPA	Focal plane array
FPA-IR	Focal plane array-infrared
GCA	Growth chamber A
HT-PVD	High through-put physical vapour deposition
IR	Infrared
IRT	Infrared thermography
K-cell	Knudsen cell
LEIS	Low energy ion scattering
LP-CVD	Low pressure chemical vapour deposition
MEMS	Microelectromechanical systems
PEMFC	Polymer electrolyte fuel cell
PM-IRAS	Polarization modulation infrared reflection absorption spectroscopy
PVD	Physical vapour deposition
QMS	Quadrupole mass spectrometer
REMPI	Resonance enhanced multiphoton ionization
RF	Radiofrequency
SMSI	Strong metal support interaction
STM	Scanning tunneling microscopy
TEM	Transmission electron microscopy
TOF	Turnover frequency
UHV	Ultra-high vacuum
XPS	X-ray photoelectron spectroscopy
XRD	X-ray diffraction

1. Introduction

1.1 A Brief History of Catalysis and its Developments

Catalysis is a phenomenon well known from ancient times in human history. Today it plays a crucial role in a wide variety of applications including the chemical industry, pharmaceutical, energy conversion and environmental protection.[1] It is estimated that over 90% of chemical production processes rely on one or more catalytic steps.[2] It is without doubt that catalysis in chemical and pharmaceutical industries minimizes the production costs and waste products and helps to preserve resources at the same time.[1] In a modern world where human activities are increasingly causing negative impacts on the environment, catalysis helps to conserve the environment and will continue to play a key role in environmental protection and sustainable energy strategies. Catalysis has a direct impact on quality of life and economic growth.[1, 3] Its development can be divided into a number of important stages over time.

- Catalysis was first used by mankind to make alcohol from sugar by fermentation, although the ancient societies did not realise its theory and impacts.[2, 4, 5] During this time, there were no theories to explain the phenomenon and only isolated observations were irregularly documented and collaboration amongst scientists of the era was uncommon. The principal features of catalysis were first addressed by Fulhame in 1794, who observed that a small quantity of water was necessary for the oxidation of carbon monoxide and water remained unaltered at the end of a chemical reaction.[4] In 1817, Sir Humphry Davy suggested that combustible gases could burst when mixed together if they were exposed to heated platinum, though he was unsure what caused this phenomenon. In 1822, Dobereiner showed that it was possible to combust hydrogen and oxygen at room temperature over a platinum surface, the discovery immediately led to its application in hydrogen lighter.[2, 4, 5] However, this era of catalysis ended with a significant achievement when in 1835 Jons Jacob Berzelius investigated the documented observations and classified them as catalysts.[2, 4, 5]

- During the second period of catalysis, systematic research and discovery of new catalytic processes were undertaken. It emerged that catalysis was important in chemical processes and its application in industry could result into financial benefits.[4] Wilhelm Ostwald formulated this idea of catalysis and wrote that, "*there is probably no chemical reaction which can not be influenced catalytically*".[4] In 1877, Lemoine demonstrated that the rate at which a chemical reaction attains equilibrium could be increased when a catalyst was involved, though the position of the equilibrium remained unchanged.[4]

- The third period of catalysis was marked by the discovery and application of new catalytic processes.[4] This era experienced the development of the ammonia process originally meant to provide Europe with fertilizer to avoid starvation. Later, most of the ammonia produced ended up in the manufacture of nitrogen based explosives.[4] The idea of using ammonia to make explosives is attributed to Ostwald who in 1902 established a process for the oxidation of ammonia to nitric acid.[4] Haber started a small scale catalytic production of ammonia in 1905 by using an iron-based catalyst and the industrial process was later established by Haber, Bosch and Mittasch.[4] Despite the development of catalysis during this era, it ended in embarrassment because it was dominated by the production of weapons of mass destruction used in the First World War.[4]

- The growth of the petroleum industry marked the start of the fourth period of catalysts development immediately after the First World War. This period experienced the large scale industrial production of isopropanol by oil companies.[4] Franz Fischer and Hans Tropsch were able to make hydrocarbons from carbon dioxide and hydrogen at room temperature in 1922.[4] This is one of the most important chemical achievements during this era. The process became crucial during World War Two when enormous demand of hydrocarbons arose. However, the process is still as relevant today as it was almost a century ago, and is being applied by a number of companies including Shell and SASOL.[4] Methanol is the most significant bulk chemical of this era, used in an enormous amount of applications from being a base chemical in the manufacture of formaldehyde, to be-

ing used as a fuel in fuel cell vehicles.[4] Steam reforming, a significant process in the production of hydrogen in the modern chemical industry, was discovered during this catalysis era and the first commercial steam reforming plant dates back to1930 by the Standard Oil Company, in New Jersey.[4] Ammonia production was re-investigated by Temkin in 1940 by addressing the kinetics of ammonia synthesis and the period ended with World War Two in 1945.[4]

- The fifth era of catalysis development is that after World War Two to the early 1970s. The period was largely dominated by the petrochemical industry and vast catalytic processes for the production of synthetic polymers.[4] This domination by the petrochemical industry was sparked by automotive markets that appeared in Europe and North America after World War Two.[4] During this time, the world realised the effects that industry had on the environment and led to the establishment of environmental catalysis.[4] Today, environmental catalysis is considered the drive towards the modern chemical industry where catalysis is applicable to almost every process from production of fine chemicals for pharmaceutical use to the manufacture of bulk chemicals and automotive catalytic converters.[4]

- The sixth and ongoing stage of catalysis is largely described and driven by environmental considerations and the integration of science with new technologies including the use of super computers.[4] The advancement of economical computational systems led to a new area of catalysis called mathematical modelling, currently applicable in developing new catalytic systems.[4] It is not worthwhile detailing the vast amount of new processes, catalysts and discoveries that has taken place and is ongoing in this period. However, important developments have and are being addressed and their impact on the progress of catalysis and the way they affected the world.

Generally, any methodology that can be used to speed up the development of new catalysts will be highly beneficial; therefore, combinatorial methods are one important approach towards high speed catalysts discovery.

1.2 Catalytic Activity

In practical terms, a catalyst increases the rate of a chemical reaction by providing an alternative pathway with as low an activation energy as possible.[6, 7] A catalyst temporarily binds with the reactant molecules and remains wholly unchanged in the end of a chemical reaction.[7] One way of accelerating a chemical reaction is by raising the reaction temperature.[8] On the other hand, the reaction rate can be accelerated by any means that lowers the activation energy of a particular reaction. In this case, at the same reaction temperature, a large proportion of reacting molecules would be able to go through the activation barrier.[8] Since the activation barrier height for a particular reaction can not be managed as it is only determined by the electronic structures of reactants and rearrangement of atoms in the activated complex, changing the activation barrier involves providing another reaction pathway for the reaction by using a catalyst, this results in a new reaction mechanism.[8] Figure 1.1 presents the reaction profiles for both un-catalysed and catalysed reaction path-ways.

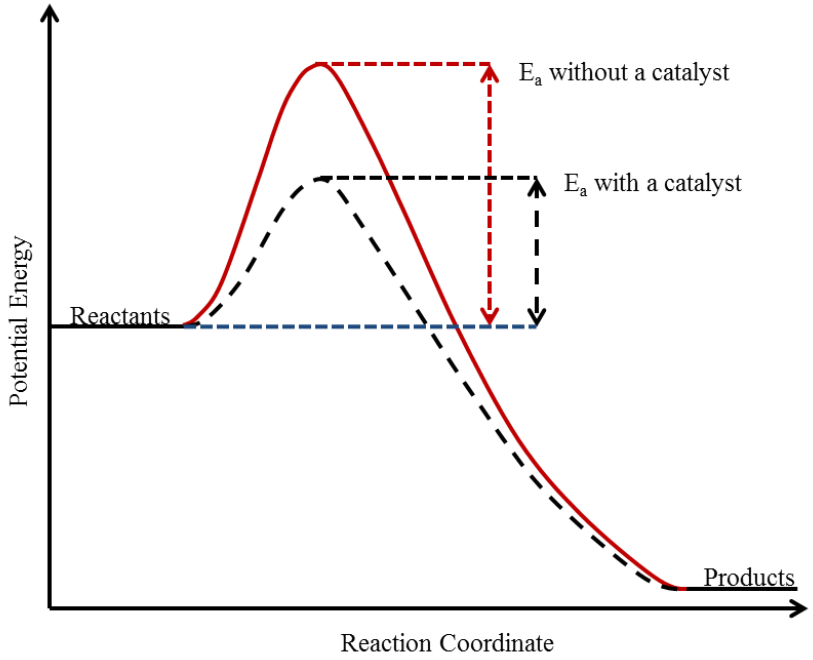

Figure 1.1: A 1 dimensional cut-out of the potential surface of an exothermic reaction without and with a catalyst. The potential energy presents the energy of reactants as results of vibrational of chemical bonds and free electrons. The figure was adapted from reference.[8]

The impact of a catalyst in a reaction is crucial as shown in Figure 1.1, because it not only makes many reactions feasible, it may also improves their selectivity and yield, leading to an incredible impact on manufacturing, production and environmental costs. Catalysts and their biological counterpart called biocatalysts, transform chemical precursors into the exact molecular species that are very important for enormous products. Economically, catalysts are used in the production of over 7,000 compounds amounting to over $3 trillion worldwide. Manufacturing based on catalysts accounts for approximately 60% of chemical production and 90% of processes.[9] These figures are likely to rise due to an increasing demand for the development of environmentally friendly manufacturing processes. However, a good catalyst is expected to show three qualities: activity, selectivity and stability.[10] In heterogeneous catalysis, activity quantification is carried out so that comparison of the activity value obtained on different catalysts is possible.[11] For solid-gas phase reactions, the usual way of quantifying activity is the turnover frequency (TOF) defined as the number of revolutions of the catalytic cycle per unit time (reaction rate) generally in seconds or specific mass activity (per gram of catalyst per second). It is clear that maximising the utilization of a particular catalyst is crucial, especially if the catalyst comprises precious metals such as gold, platinum and platinum group metals. Therefore, maximizing the surface area of a catalytic material by finely dividing the catalyst on a high surface area support is economically important. However, describing a catalyst in terms of mass activity alone neglects the effect of surface structure, an important factor witnessed in a number of reactions whose rates depend on a catalyst's surface structure. Hence the interest in studying supported catalysts in order to explore the particle size, particle morphology and support effects is essential for the development of these catalysts.[12] The observed structure sensitivity of a reaction is a phenomenon first discussed by Boudart.[11, 13] Many catalytic reactions are structure sensitive as their rates rely on the geometrical structure of the surface atoms of the catalyst.[14] Structure sensitivity manifests itself as a dependence of rate per surface atom on the average size of the catalyst particles. The rationale is that for particle size of diameter less than 10 nm, the relative number of kink sites, steps and corners increases exponentially with decreasing diameter. These under-coordinated surface atoms have a significant different capability to interact with molecules from the gas-phase.[14] Therefore, structure sensitivity can reflects a variation in the intrinsic capability of the surface at-

oms to take part in the surface reaction or it can be related to the availability of a certain number of surface atoms in special geometrical arrangements crucial for the interaction with the reacting molecules.[14] A structure insensitive reaction is classified as a reaction where the TOF or specific mass activity does not depend on surface modifications, such as particle size, or crystalline faces in the case of a single crystal, therefore for a structure sensitive reaction, the TOF/specific mass activity depends on these parameters.[13]

The catalyst support induces structural variability of the catalyst and provides the opportunity to explore them. The support controls the shape of supported nanoparticles through the metal-support interaction phenomenon[15] ensuring catalyst stability and determines the particle size by maximising metal dispersion. Enhanced metal dispersion results into a catalyst surface with a vast amount of low coordination reactive sites.[16] TOF/specific mass activity changes with dispersion/particle size (often determined by loading) for a structure sensitive reaction since densities of close packed facets, step, corners or edge sites are typically varying. For a structure insensitive reaction, the TOF (mass activity) would be greater with decreased dispersion of the metal on the support. **Figure 1.2** illustrates how the number of less coordinated atoms varies with the decrease in particle size for Au supported particles.[17]

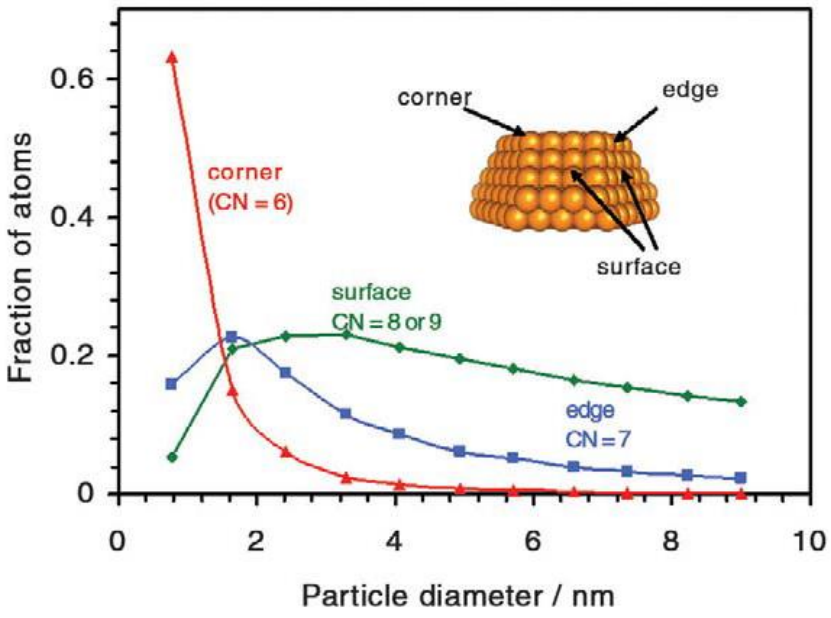

Figure 1.2: Calculated fractions of Au atoms showing the number of atoms present at edges (blue), corners (red), and crystal faces (green) in nanoparticles having the top half of a truncated octahedron. Fractions of atoms are presented as a function of Au particle diameter/ nm. The representative edges, corner and crystal surface atoms positions of a truncated octahedron are shown in the insert. The figure was taken from reference[17]

A common structure sensitive reaction is the solid/gas-phase CO oxidation reaction on a supported gold nanoparticle catalyst, where the particle size effect is commonly observed at a particle diameter below 5 nm.[18] The origin of the particle size effects is often based on the geometric effects, in which different particle geometries have an impact on the catalytic activity. Under-coordinated sites and crystallographic orientations of small particles in addition to the induced strain in supported particles (electronic effect) have been used to explain changes in the binding energies of adsorbates.[19, 20]

The particle size effect also is anticipated to play a significant role in the activity of small particles activity at relatively low temperature, resulting in greater activity with decreasing particle size.[20] The valence band structures of small particles are considerably different from those of bulk metals[21], it is proposed they contain discrete energy levels compared to the continuous band energy structure of bulk metals.[20] Particle size effect has been reported in titania supported gold nanoparticles of less than 5 nm in

size.[20, 22] Particle size effect influences the chemisorption and thermodynamic properties of metallic nanoparticles. However, the particle size effect has been found to be influenced by the physical properties of the support material, which is addressed in terms of a metal-support interaction and support-assisted mechanisms.[19, 23]

Tauster *et al*. used the SMSI phenomenon to address the observed decrease for CO and H_2 chemisorption on titania supported noble metals at high temperature conditions.[23] SMSI was first addressed in 1978 to explain the abrupt changes in the chemisorption properties of group 8-10 noble metals that were anticipated when these substances were supported on titanium dioxide.[23, 24] Over the years the adsorption of hydrogen has been used to show the particle sizes of catalytic metals like platinum.[24] It was addressed that at room temperature, these metals chemisorb one hydrogen atom per surface metal atom when unsupported or supported on a metal oxide support such as alumina.[24] Nevertheless, the capability to chemisorb hydrogen or carbon monoxide was either largely supressed or completely gone when these metals were supported on titanium dioxide and activated in hydrogen at ordinary temperatures.[24] The ascribing this effect to, for example, particle sintering was ruled out, and it was concluded that a SMSI had deprived these metals of one of their crucial properties.[23] Since then, much effort has been dedicated to the understanding of this phenomenon which is limited to titanium dioxide. This has transformed the understanding of supported metal catalysts, especially regarding their morphology due to solid-state transformations that take place in these system.[24] It is now well established that it is not the case that metal nanoparticles remain unaltered on a metal oxide surface as in many systems, metal oxide support can cover the metal surface hence masking a substantial part of it and in such a way it can create special contact zones which enhances the catalytic properties for some reactions.[24] In other instances, the metal disperses to attain its coverage of the metal oxide support, which indicates bonding interactions. There are special features of this bonding that prevent its existence anywhere but at an interface, this renders an understanding of this system very crucial. The chemisorption retardation has been observed with metal nanoparticles as large as 5 nm. It was suggested that titania was in direct contact with at least a portion of metal surface (encapsulation).[24] Madey and co-workers[15] described the interaction of

Au with TiO_2 and that of Pt with TiO_2 at higher temperature. In their study, they found that, after annealing of Au/TiO_2 at about 775 K, the size of Au islands increased with no significant encapsulation by TiO_x. However, at similar conditions, Pt was completely encapsulated by TiO_x.[15] Further evidence of Pt encapsulation was provided by Pesty *et al*..[25] In their study, Pt on TiO_2 surface was investigated by annealing under vacuum with LEIS. The Pt signal decreased and eventually varnished with annealing time while Ti and O signal grew. The rate of Pt signal disappearance was dependent on both coverage and annealing temperature, at a particular temperature, the Pt signal decreased quickly for thinner film layers of Pt suggesting easier encapsulation. The unusually high activity of TiO_2 supported gold particles toward CO oxidation at low temperature exemplifies the support-metal interaction, with charge transfer stabilizing oxygen species on gold with the reactants stabilized by the support (oxygen spillover effect). The reactants go on to react directly with CO adsorbed on the gold-support boundary. Metal support interaction between Pt and TiO_2 and charge transfer has also been widely discussed by Diebold,[26] Madey and co-workers.[15, 25]

This thesis presents the application of a High Throughput method for synthesis and screening of titania supported platinum and gold nanoparticle catalysts of various sizes for the solid/gas-phase oxidation of CO at relatively low reaction temperatures. High through-put techniques have been developed in catalysis and material science and have gained extensive application in both academia and industry to improve known materials and aid the discovery of new materials.[1, 21, 27-30] Physical vapour deposition (mainly sputtering) has been established for the synthesis of compositional gradient thin film materials,[3, 31] and this has recently been extended to MBE based sources by using an arrangement of "shadow" shutters, described in detail in Chapter 3.[32] This method enables the synthesis of a compositional material library of metal alloys and nanoparticles on thin film supports.[33, 34] It has been applied here to synthesise and optimise Au and Pt nanoparticle catalysts supported on titania. The synthesised titania supported Pt/Au nanoparticles have been screened for catalytic activity using a new method of high throughput infrared thermography, developed during this work. The activity of the different catalysts systems for the CO oxidation reaction at relatively low reaction tem-

perature is compared and discussed. These findings are set in the context of the literature, with an overview of the relevant literature given in the proceeding sections.

1.3 Reactions Involving Carbon Monoxide

Carbon monoxide (CO) is a hazardous gas produced as a result of burning any substance that contains carbon such as fossil fuels in insufficient oxygen.[35-37] It is estimated that global emissions of carbon monoxide into the atmosphere reaches 2,600 million tonnes annually with 60 % of total emissions due to human activities while natural processes contribute only 40 %.

The sources of carbon monoxide are diverse. However, they can simply be grouped into two, anthropogenic and natural processes. Anthropogenic activities leading to CO into the environment and indoors include a range of industrial processes, unvented kerosene and gas space heaters and automobile exhaust emissions, while natural sources of CO include volcanic eruptions and natural fires. Of all the anthropogenic sources of carbon monoxide in the UK, exhausts of motor engines are the major contributor responsible for up to 69 % of the UK's CO emissions.[38] Carbon monoxide poisoning is still one of the top causes of unintentional poisoning to humans and animals causing a huge number of deaths worldwide,[39, 40] particularly in Europe and United States each year.[41]

In heterogeneous catalysis, particularly on platinum, carbon monoxide presents a challenge because it poisons the catalyst. Polymer electrolyte membrane fuel cell (PEMFC) technology for instance, is forecasted to play a crucial role in the future of electrical energy production for mobile and stationary applications due to its zero CO_2 emission and high power density.[42, 43] PEMFCs depend on hydrogen fuel which is largely produced from natural gas generating a hydrogen-rich gas mixture that comprises substantial amount of CO.[42] The CO present poisons the platinum catalyst used as the anode of the low temperature PEMFC, where hydrogen oxidation takes place. CO acts as a poison

because it binds irreversibly to the platinum catalyst surface leaving no active sites for further reaction cycles to occur and therefore deactivates the catalyst.[21, 42, 44-46] The deactivation of the platinum catalyst in low temperature PEMFCs by CO present in reformate gas has attracted researchers towards searching for an alternative CO tolerant catalyst system.[43, 46]

The chemistry of CO is of major interest since CO oxidation is among the most crucial transition metal catalysed reactions. The best way to get rid of hazardous carbon monoxide gas in PEMFCs and car exhausts is via catalytic CO oxidation. The carbon monoxide oxidation reaction is therefore crucial in both the exhausts emission control and PEMFC technologies.[47, 48] Technologically, the CO oxidation reaction is crucial for the purification of hydrogen gas to avoid the deactivation of Pt.[49, 50] In such applications, CO oxidation needs to be carried out at relatively low temperatures[51] and therefore the discovery of a catalyst with the capability to convert CO into CO_2 under such conditions and conditions that will not lead to hydrogen oxidation is desirable. More studies have been carried out to investigate the low temperature catalytic oxidation of carbon monoxide due to its enormous range of applications in practical processes and in heterogeneous catalysis research.[49, 52]

1.4 Heterogeneous Catalysis

One of the reasons for looking at chemical reactions on surfaces is to understand the heterogeneous catalytic reaction mechanisms. Heterogeneous catalysis is where the catalyst and the reacting molecules are in different phases, typically a solid catalyst and gaseous reacting molecules. A catalyst acts by forming an intermediate compound with the molecules involved in the reaction, offering an alternative reaction path with low activation energy to the final products. Heterogeneous catalysis is vital to the chemical industry, being key to a number of economically important reactions/processes such as the Haber-Bosch process, where ammonia is synthesized from gaseous N_2 and H_2 using an iron catalyst.[53, 54] The chemical industry would not be as successful as it is today without the implementation of heterogeneous catalysis. Most large-scale industrially catalysed processes depend on heterogeneous catalysis, and the widespread recent ap-

plication of catalysis to car emission control uses such solid catalysts as Pt, Pd and Rh in contact with the gas stream.[6, 54, 55] In these kinds of reactions the nature of the interface is very important for the efficiency of the process. The nature of the catalyst surface dictates how fast a catalytic reaction takes place and additives can retard (poison) or enhance (promote) the reaction.[55]

The application of bulk metal catalysts presents high cost while the catalysts themselves are inefficient. These catalysts become efficient when finely divided, because a large surface area is achieved. However, finely divided metal particle catalysts need to be supported on a cheaper support. Transition metal oxides have been used as a support material. These oxides have extensively been used in electrochemical technology because they offer both potential for stability and conductivity and also are known to influence the activity of supported metal nanoparticles.[34] Titania (TiO_2) is known to be stable in acidic and high temperature conditions and is available in high surface area forms, further; it is sufficiently conducting to serve as a support by its use in substoichiometric or doped states, TiO_2 is also abundant, cheap, hence economical to use. Therefore, the use of TiO_2 as gold/platinum nanoparticle catalyst support for CO oxidation reaction has been of interest and a good number of researchers have reported its effectiveness as compared to other supports.[56, 57] Characterising the nature and behaviour of the supported catalyst surface is crucial to gaining an understanding of the enhanced reactivity.

1.5 Surface Science and Model Catalysts

The catalysts surfaces are of particular interest not only because they are where reactant phases converge but also because they are completely different from the rest of the solid, the bulk. Bonding at the surface is unique as each surface atom has few close neighbours, therefore it is expected that the chemistry at the surface is unique as well. The effect of having unequal forces at the surface subjects the whole surface to a relatively high surface free energy, with a distinct electronic structure compared to the bulk. Since surface atoms cannot satisfy their bonding requirements in the same way as bulk atoms,

they will always want to react in some way, either with each other or with foreign atoms.[53, 54] Catalysis takes advantage of the unbalanced forces on the surface to catalyse different reactions. **Figure 1.3** shows the key steps that take place at the catalyst surface during a catalytic reaction.

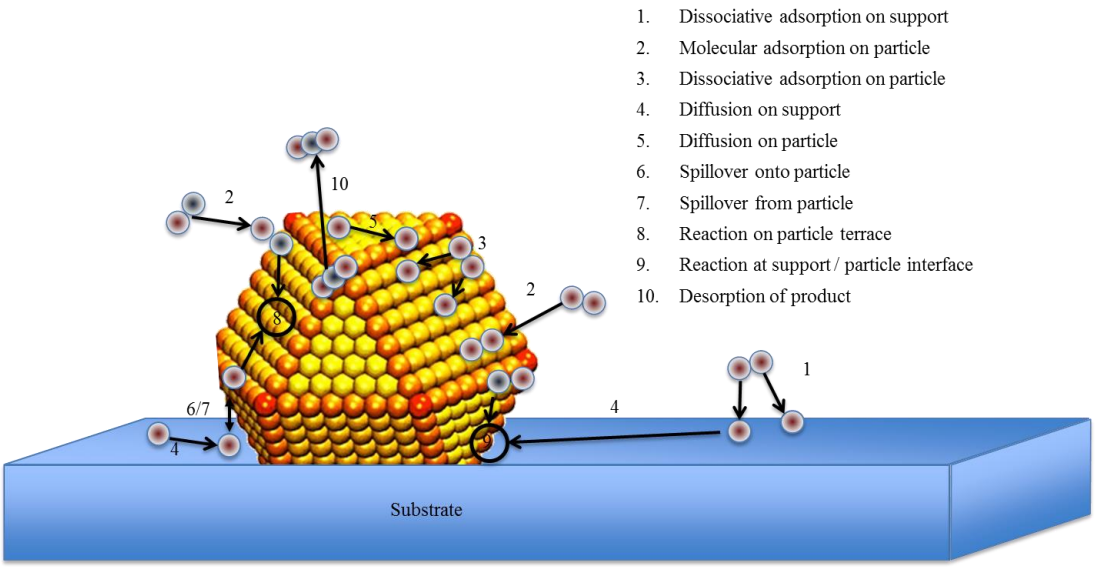

Figure 1.3: Molecular level processes involved in product formation during a catalytic reaction illustrating adsorption of gaseous reactants, dissociation, diffusion, surface reaction and product desorption processes.

Notable improvements have been made over the past few years in the investigation of catalytic properties of industrial heterogeneous catalysts. During the past two decades, a number of groups globally have succeeded in synthesising model metal nanoparticles catalysts supported on planar oxide substrates.[18, 34, 37, 49, 58-70] The synthesised catalysts have been found to be suitable for kinetic and spectroscopic investigations and for study using scanning probe techniques at realistic working temperatures and pressure conditions.[58] Ideally, catalytic scientists would like to relate microscopic properties such as atomic composition, electronic structure and geometric structure to macroscopic properties, such as catalytic activity and selectivity.[58] It is unfortunate that the complexity of real catalysts makes it difficult to explore their microscopic properties. Significant studies using ultra high vacuum (UHV) methodologies provide an atomic view of a catalyst by studying single metal crystals, which differ from real world catalysis, where reac-

tions occur at elevated pressure and high surface area polycrystalline materials.[6, 58] Although the reaction conditions are ideal, some conclusions about bonding and activity can be made. Model catalysts that resemble industrial catalysts in their complexity have been synthesized.[58] Techniques such as polarization modulation infrared reflection absorption spectroscopy (PM-IRAS) have made it possible to study the working catalyst, particularly the in-situ abilities of scanning probe microscopies which allow observation of the morphological modifications that occur on working catalysts.[58]

The nature of the surface participating in heterogeneous catalysis is very important for the catalytic properties.[53, 55] Numerous crystal structures exist, here only face centred cubic (fcc) is considered as an example. This is because most of the technologically important metals such as Au, Pt and Rh exhibit this structure. The fcc structure gives rise to low index faces, the (100), (110) and the (111) planes, **Figure 1.4**.

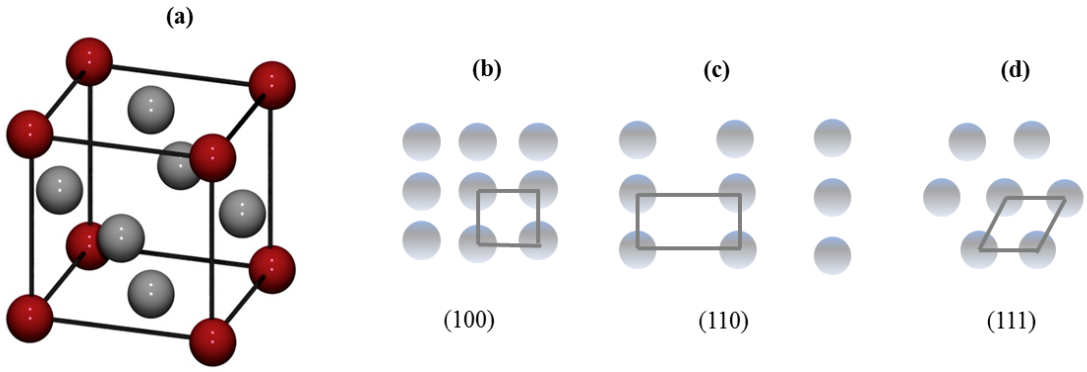

Figure 1.4: Illustration of face centred cubic (fcc) structure and the low index faces, (a) fcc structure and (b) (100), (c) (110) and (d) (111) planes. (a) Was extracted from http://johncarlosbaez.wordpress.com/2012/04/15/ice/.

The coordination number of atoms in each of these surface planes is different. Generally, the surfaces with lower coordinated surface atoms have the highest surface free energy, therefore greater reactivity for adsorption and strongest binding for the adsorbing molecules. From this perspective the (100) has four neighbours in the surface, (110) has only two near neighbours and (111) is in a close packed structure with six neighbours.[55] Since the surface is a region of high surface free energy there is a tendency for surface

atoms to minimize this energy and this takes place in different ways including surface relaxation, reconstruction, sintering and adsorption. It has been reported that some catalytic reactions have less dependence on the nature of surface structure, while others are strongly dependent on surface structure.[55] The phenomenon of catalysis is usually determined by observing how the rate of the reaction on reactive sites varies with changing the active site's properties such as particle size. For reactions where the surface reaction is the rate determining step, it is expected that the structure sensitivity phenomenon will be observed. Considering any particular reaction of interest, it is therefore possible to change the properties of a catalyst for that reaction by any means that changes its surface properties; that is increasing or reducing the surface free energy from a thermodynamic point of view. This can be done by any of the following processes; sintering, dispersion, poisoning, changing support and particle size.

The structure of oxide materials is important both as heterogeneous catalysts themselves, and as supports for metal particles. Titania is a good example of such a support, and there are a wide range of studies on the single crystal surfaces of rutile titania. Single crystal surfaces of metal oxides are widely used in surface studies in order to anticipate how surface structure affects reactivity.[71] The surfaces of real metal nanoparticle catalysts have a more complex structure as they have numerous types of crystallographic planes exposed. Heterogeneous catalysis studies using model systems have discovered that irregularities and additives such as water vapour, are the main features of active surfaces that control catalytic behaviour.[72] Steps and kinks have been identified as the most catalytically influential surface sites on transition metal surfaces due to their low coordination number compared to atoms in the terrace. Reactions on oxides or metal nanoparticles supported on oxides can be studied not only on single crystal oxide surfaces, but also oxides prepared by epitaxial thin film growth on metal substrates. The structure of the substrate is picked specifically to match the particular oxide film to be synthesized because crystal orientation and the nature of the interface are significant parameters in obtaining a high quality film. A thin metal oxide film of several nanometers thick is deposited onto the metal substrate by vapour deposition in an oxygen atmosphere.[58] Thin films of MgO, Ti_xO_y, Al_2O_3, SiO_2, NiO and Fe_xO_y have been prepared

using this methodology.[58] Eventually, metal particles can be grown on the thin film oxide by vapour deposition of the metal of interest, **Figure 1.5**. By careful control of the metal deposition parameters, such as deposition rate and time, metal nanoparticles of various sizes are produced.

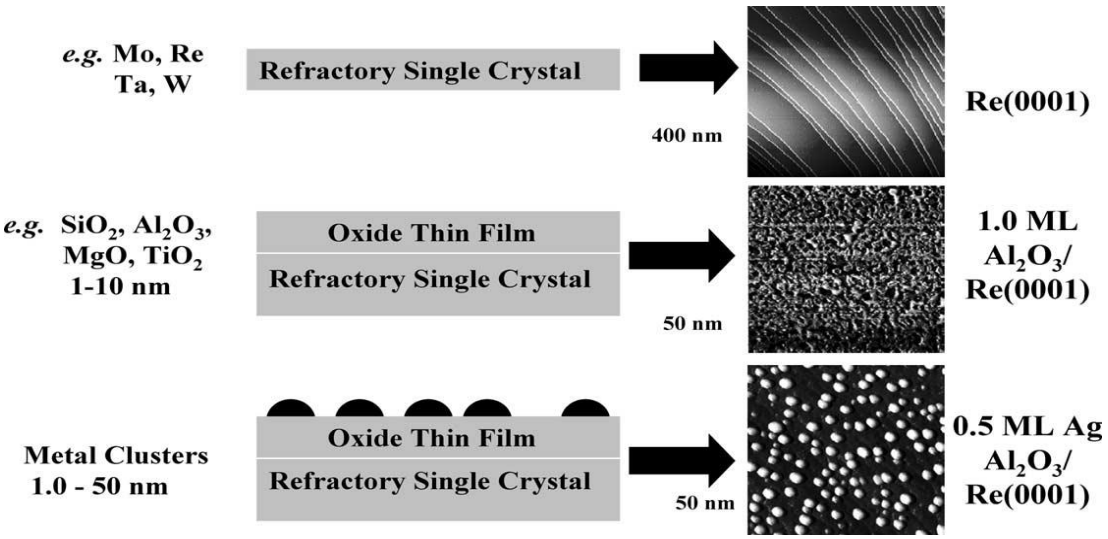

Figure 1.5: Schematic of a planar oxide-supported model catalyst preparation procedure with corresponding STM images of each stage.[58]

Different metal/oxide systems have been reported such as Cu/SiO_2, Pd/SiO_2, Ni/SiO_2, Pd/Al_2O_3, Cu/Al_2O_3, Au/Al_2O_3, Ni/Al_2O_3, Au/TiO_2, Pd/MgO and very recently, organometallic precursors have been used to prepare Ru/TiO_2 and Au/TiO_2.[58]

Catalytic studies on model single crystal surfaces over the decades have provided important information related to chemisorption and the link between surface structure and reactivity, enhancing our knowledge regarding heterogeneous catalytic processes.[12] However, single crystal catalyst systems do not offer the possibility to explore the impact associated with the change of a catalyst surface structure such as particle size, and the presence of an oxide support on the reactivity, therefore the development of a model for supported nanoparticle catalysts is required.

1.6 Supported Nanoparticle Catalysts

Metal oxide supports are important in heterogeneous catalysis as they serve to stabilize the metal nanoparticles and some supports are known to participate directly in the reaction mechanism.[50] These metal oxide supports can be categorised into two groups: non-reducible metal oxides such as Al_2O_3, MgO and SiO_2, and reducible metal oxides such as TiO_2, Fe_2O_3, NiO and CeO_2. These metal oxide supports have been enormously used and continue to be used to support metal nanoparticle catalysts for various applications.[50, 73, 74] It is now well understood that the support material strongly influences the activity of heterogeneous catalysts.[49, 73, 75, 76] More attention is on reducible metal oxides which are largely addressed to participate directly in a reaction mechanism hence enhancing activity of the nanoparticle catalysts as compared to nan-reducible metal oxide supports.[57, 73, 77, 78] Further, it has been addressed that the reducible metal oxide supports such as Fe_2O_3, TiO_2 and NiO provide more stable and more active nanoparticle catalysts as compared to their non-reducible counterparts.[49, 51, 74-76, 79] In the CO oxidation reaction, adsorption capability is quite important. Alexeev *et al.*[80] compared Pt supported on TiO_2 and Al_2O_3 for CO oxidation and found the TiO_2 supported catalysts the most active when reduced in hydrogen at 400 ^oC. In their study, they suggested that perhaps Pt is partially covered by titania (reduced titania) fragments leading to retarded CO adsorption. Additionally, they proposed that, metal support boundary is critical for dissociation of O_2. They assessed the catalysts activity in the presence of hydrogen, an important reaction in purifying H_2 by removal of CO in fuel cells. Herranz *et al.*[57] on the other hand, studied the oxidation of CO on Au nanoparticles supported on TiO_2 and SiO_2 at low temperature and found Au supported on TiO_2 the most active catalyst. Li and co-workers[81] compared CO oxidation on Pt nanoparticles supported on TiO_2 and SiO_2 and they concluded that titania supported catalyst is the most active. Further evidence of support contribution towards CO oxidation was given by Rousset *et al.*[82] in their study, CO oxidation was investigated on Au nanoparticles of approximately 3 nm supported on Al_2O_3, ZrO_2 and TiO_2 supports. Of all these catalysts investigated, Au supported on TiO_2 was found to be the best catalyst. They concluded that titania participates in the reaction process.[82] Schuth *et al.*[77] studied CO oxidation on Au supported on TiO_2, Al_2O_3, ZrO_2 and ZnO and found Au supported on TiO_2 the most active catalyst. These experimental reports indicate that the nature of catalyst support (metal oxide) in-

fluences the activity of heterogeneous catalysts among other factors. Therefore, the appropriate choices of metal nanoparticle support are crucial to ensure the right catalytic activity of the metal.

However, metal nanoparticles supported on metal oxides surfaces such as Fe_2O_3 and TiO_2 have been of much interest to researchers because of their technological applications including: photocatalysts, heterogeneous catalysis and gas sensors.[83, 84] The growth of various metal nanoparticles on TiO_2 has been widely studied.[15, 85-87] Metal nanoparticle nucleation and growth processes that occur on an oxide surface when metal atoms are vapour deposited,[87] are shown in **Figure 1.6**. Metal atoms deposited onto the oxide surface need to undergo adsorption first, if the surface temperature is high, these atoms may desorb. Once adsorbed the atoms diffuse across the surface and become trapped on surface defects, if present, resulting in nuclei formation and this is referred to as heterogeneous nucleation. In the case where atoms do not find defects on the surface to nucleate on, stable nuclei may be formed by the aggregation of at least two metal atoms, this is called homogeneous nucleation. A certain number of metal atoms termed the critical cluster size must be achieved for the formation of a stable cluster and further addition of atoms leads to nuclei growth. Freund *et al*. reported that a homogeneously formed cluster which has not achieved critical size will consequently separate.[83, 87] Particle density on the surface in the case of homogeneous nucleation is a function of the diffusion coefficient on the support and the rate of deposition. On the contrary, for heterogeneous nucleation, the saturation density does not depend on either the diffusion coefficient or rate of deposition, in this case attraction between atoms and defects is robust and defect concentration is relatively high. After nuclei saturation has been achieved, no further nuclei formation occurs and all incoming atoms land on the preformed islands and particle growth proceeds.[83, 87]

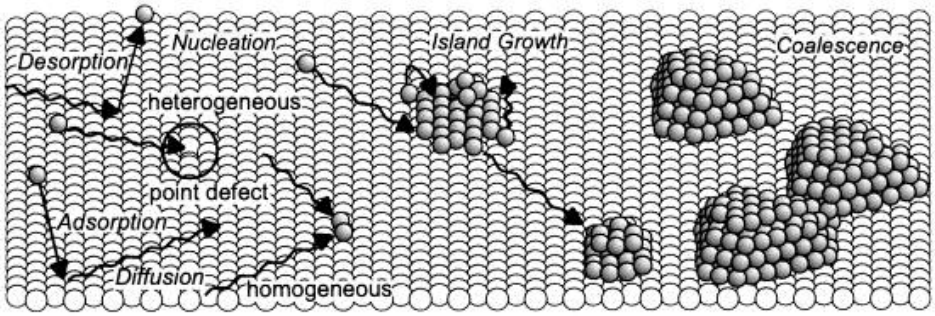

Figure 1.6: Metal deposition on a substrate and particle growth mechanisms, figure reproduced.[87]

The morphology of supported nanoparticles has been addressed as the key aspect that controls their chemical properties.[86] The growth morphology of various metals on TiO_2 has been extensively investigated[15, 26] and was found to depend on surface and interfacial energies (γ_{metal}, $\gamma_{substrate}$ and $\gamma_{interfacial}$). Madey *et al.* discussed the three film growth modes as studied using low energy ion scattering (LEIS), when $\Delta\gamma = \gamma_{metal} + \gamma_{interfacial} - \gamma_{substrate} \leq 0$, film growth goes via layer-by-layer growth (Frank-van der Merwe mode), a $\Delta\gamma$ greater than zero ($\Delta\gamma > 0$) leads to a three dimensional film growth mode called Volmer-Weber growth. In many situations, interfacial energy increases ($\Delta\gamma \leq 0 \rightarrow \Delta\gamma > 0$) after formation of the first or several layers and results into successive islands formation, termed the Stranski-Krastanov growth mode,[15] **Figure 17**.

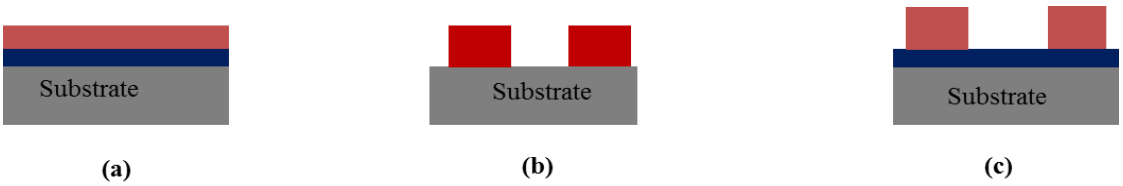

Figure 1.7: Schematic presentation of the three crystal growth modes: (a) Frank-van der Merwe, layer by layer growth (b) Volmer-Weber, 3D island growth and (c) Stranski-Krastanov, layer then 3D island growth.[54]

Since surface free energies of transition metals are always larger as compared to those of metal oxides, a layer-by-layer particle growth mode should be an exception and that the particle growth of 3D particles is very likely, which has been observed in many deposition studies of metals on metal oxides.[87]

Although many different metal nanoparticles have been studied on TiO_2, we shall focus on Au and Pt nanoparticles for the low temperatures CO oxidation.

Theoretical calculations have shown that gold nanoparticles interact weakly with stoichiometric TiO_2 supports as compared to non-stoichiometric titania.[20, 79] The higher adsorption energy of gold nanoparticles on a defected titanium dioxide surface has been reported and defects on TiO_2 are anticipated as the main nucleation and growth sites for gold nanoparticles[20, 79, 88, 89] as shown by STM and theoretical studies. Experimental studies of UHV nucleation and growth of gold nanoparticles on titania are in good agreement with theoretical studies, that nucleation of Au during initial particle growth occurs on titania defects.[79] Two dimensional islands of gold have been primarily observed up to an average critical coverage, and three-dimensional islands are formed at coverages above critical coverage, where the added gold mostly adsorbs on top of the two-dimensional islands, referred as Stranski-Krastonov growth.[15, 83] Experiments have revealed the truncation of Au particles on titania at the initial growth stage (low coverage) with a layer thickness of 1-2 atomic layers and a particle diameter of 0.6-2 nm, which grows into a spherical shape between 2.5 – 5.0 nm particle diameter with increasing loading.[90, 91] Similar growth behaviour has been reported for platinum nanoparticles on titania.[15, 26] However, Madey *et al*. reported that at a later stage of both Au and Pt nanoparticle growth (overlayer thickness > 1 ML), at equivalent temperatures, TiO_2 is more covered by Pt islands than by Au.[15] Studies have shown that nucleation and growth of Au and Pt particles on the titania support is influenced by temperature, and that at 200 ^{o}C, particle nucleation and growth shows 3D growth from the beginning.[15]

The properties of metal nanoparticles interacting with a support have been widely discussed in literature and it is proposed that the support plays a key role in determining the particle shape and enhance particle stability.[16, 86, 87, 91] The equilibrium shape of a particle on the surface of a support has been found to depend on the surface and interfacial energies. For a particle with isotropic surface energy, the particle adopts a truncated

spherical shape with a contact angle given by the Young-Dupre formulation,[91] equation 1.1 and **Figure 1.8** (a).

$$\cos\theta = \frac{\gamma_{sub} - \gamma_{\text{int}}}{\gamma_{met}} \qquad \text{Equation 1.1}$$

where θ is the contact angle, γ_{sub} and γ_{met} are oxide and metal surface energies respectively and γ_{int} is the interfacial energy. However, although this formulation holds true for isotropic liquids, for supported metal particles, faceting is evident due to low index planes and this results into surface energy anisotropy. Therefore, the contact angle is no longer representing the relative interfacial energies, instead it represents relative faceted plane with regards to the substrate, and the equilibrium shape of a particle is therefore predicted by the Wuff formulation, **Figure 1.8 (b)**.

Madey *et al*. have shown that in a Wuff formulation, the ratio of the length of the vector (h) to the surface free energy of a particle is a constant and the particle on the surface of a support is truncated, the particles "sink" into the substrate by Δh, which is a function of the particle surface free energy and adhesion energy, E_{ad}, given by:[86, 87, 91]

$$E_{ad} = \gamma_{sub} + \gamma_{met} - \gamma_{int} \qquad \text{Equation 1.2}$$

and

$$\frac{\Delta h}{h} = \frac{E_{ad}}{\gamma_{met}} \qquad \text{Equation 1.3}$$

Adhesion energy is therefore crucial to particle shape as when it is zero, Δh→0, the particle at equilibrium assumes a free particle shape with no truncation. When adhesion energy is at least twice the particle surface energy, complete wetting is attained with a 2D shape.

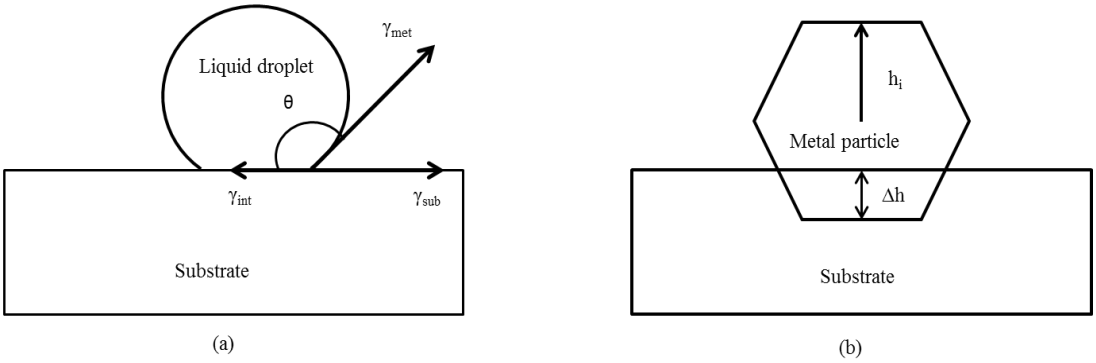

Figure 1.8: Truncation of supported particles at the support-particle interface. **(a)** Represents isotropic surface energy as in liquids, where θ is the contact angle, γ_{sub} and γ_{met} are oxide and metal surface energies respectively and γ_{int} is the interfacial energy. In **(b)** is the Wuff formulation, particle-surface property (anisotropic surface energy), where Δh is the amount of truncation and h_i is the particle height.[92]

However, a more interesting scenario to consider is that of highly dispersed metal systems on metal oxides supports such as those used in the automotive catalytic converters and petrochemical industries. In such a catalyst system, the metal particle size may be as small as 1 nm.[93] It is anticipated that the shape of these small particles is determined by the surface free energy contribution to the total energy. The surface free energy of a crystal of fixed mass to volume ratio can be minimized by either reducing the surface area of the crystalline or exposing only the surfaces of low surface free energy such as (111) planes.[86, 93] Nevertheless, the resolution between exposing only the surface with low surface free energy planes and reducing the surface area is attained by truncating the vertices of the octahedron to produce a cubo-octahedral particle which has (111) and (100) surfaces exposed, which in turn creates many atoms at the corners and intersection of surface planes on the particle and these atoms are under-coordinated.[93] However, this model for the structure of catalytic metal nanoparticles is not correct; it is perhaps reasonable when there is the weak interaction between the metal and the oxide support such as silica. On the other hand, a SMSI is more likely to result to increased wetting of the support by the metal which provides a greater metal-support contact area and a significant different particle morphology.[93] Therefore, for the case of SMSI, the metal-oxide interfacial free energy is less and the surface free energy of the metal particle can not be considered in isolation from that of the support.[23] Figure 1.9 illustrates the metal support interaction and the equilibrium shape of the supported metal particle.

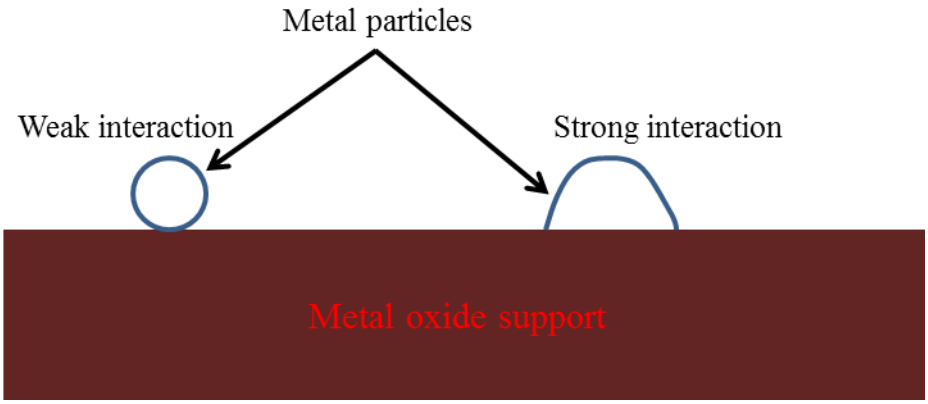

Figure 1.9: Illustration of the metal support interaction showing weak and strong metal support interaction and the equilibrium metal particle shape. The figure was adapted from reference.[93]

To summarize, from the mode of nanoparticle nucleation and growth on a support, it is without doubt that the physical properties of a support surface and the metal-support interaction play a key role in determining the final particle size and shape.

Selecting a support material is clearly a key consideration when investigating catalysts systems. Titania is a popular choice due to its relative abundance and favourable chemical and mechanical properties. This study focuses on the low temperature CO oxidation on titania supported Pt and Au nanoparticles catalysts.

1.7 Carbon Monoxide Chemisorption on Transition Metal Surfaces

The chemisorption of CO on metal surfaces is well studied in cluster chemistry and surface science due to a number of reasons including being a simple adsorbate hence relatively easy to model theoretically in terms of electronic structure, and it has several orbitals that can participate in the bonding to the metal surface.[54, 94-97] Depending on the nature of the metal surface, CO can chemisorb both non-dessociatively and dissociatevely.[98] For instance, CO tends to adsorb dissociatively on W surface and non-dissociatevely on Au.[54] Additionally, CO has the ability to adsorb on various sites on different metal surfaces including: on-top, twofold-bridge and threefold-hollow, respectively depending on the surface coverage.[54, 94, 97] Nevertheless, CO is important in nu-

merous catalytic processes such as automotive emission control, methanol synthesis and in fuel cells technology where these transition metal catalysts are used.[52, 94, 98] Therefore, the chemisorption mechanisms of CO on metal surfaces is well understood and is addressed in terms of σ-donation of electron density from CO to the metal and π-back donation of electron from the metal to CO.[54, 94, 99-102] This adsorption mechanism of CO on metal surfaces was first described Blyholder.[100] The back donation of electrons into 2π* orbital weakens the CO bond and allows the bond to stretch as a result of decreased bond order, because the bond strength is related to the vibrational frequency, decrease in the vibrational frequency is observed.[54, 99] The stretching of CO bond is critical in catalysis, because this leads to increased activity of CO. Figure 1.10 presents a schematic diagram illustrating the synergistic bonding of CO to a metal.

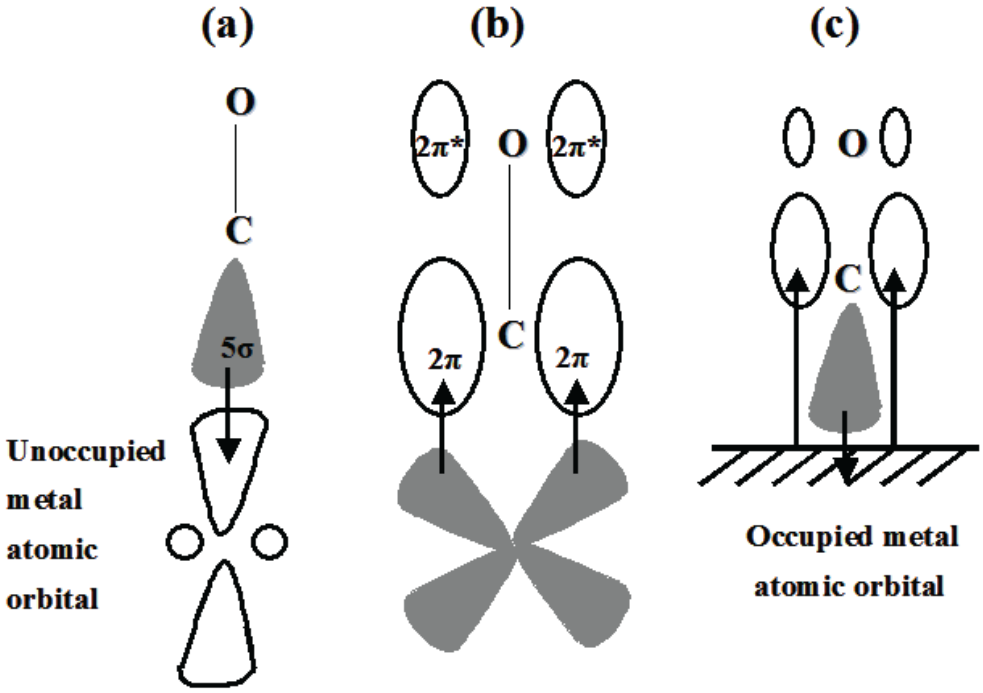

Figure 1.10: Illustration of synergistic bonding of CO to a metal. (a) Shows the interaction of 5σ orbital and (b) the 2π* orbital with a metal in a carbonyl compound. (c) Shows the interaction of adsorbed CO with a surface. The figure was taken from reference.[54]

Infrared spectroscopy has been used recently to study the interaction of CO with metal nanoparticles which have been size-selectively deposited or characterized after deposition.[94, 96, 103] The adsorption of CO can be traced by using the infrared spectra of carbon monoxide. The carbon-oxygen stretching frequency for chemisorbed CO has been antic-

ipated from above 2100 cm^{-1} down to 1800 cm^{-1}.[100] When the adsorption parameters are altered such as surface coverage, the position of infrared bands shifts, and it has been observed that the carbon-oxygen stretching frequency monotonically shifts to higher wave number with increasing surface coverage.[100] It is reported that the carbon-oxygen stretching frequency is very sensitive to the nature of adsorption site and its local electron density.[94] However, the relative intensities of CO on evaporated and supported thin films differ.[100] It has been suggested that the interaction of CO with transition metal nanoparticles such as Pt and Au (which are more relevant to this thesis) strongly depends on the particle size and coordination number of the metal atom adsorption sites. The bonding interaction of the adsorbate is known to be significantly stronger on the low-coordinated adsorption sites, and there are many such sites on metal nanoparticles.[13, 94, 103, 104]

1.8 Titanium Dioxide Properties and Applications

Titanium dioxide displays outstanding resistance to corrosion in aqueous environments, further it is chemically, mechanically and thermally stable, available with a high surface area and electrically conducting.[34, 105] These interesting properties have led to titanium dioxide being used in a wide spectrum of applications from heterogeneous catalyst supports, photocatalysts to cosmetic products.[26, 84, 87] It is clear that the functional properties of TiO_2 are being influenced, or even significantly determined by its surface defects. Crucial properties related to heterogeneous catalysis are: surface properties, charge transport, electronic structure and reactivity.[106] In its reduced form, titanium dioxide contains various defects. However, oxygen vacancies, doubly ionized vacancies, where one oxygen atom leaves behind two electrons and titanium interstitials are the widely known predominant defects.[20, 106] It has been revealed that for a particular defect type to be dominant depends significantly on the preparation method and the density of oxygen defects.[26] Surface defects on titanium dioxide have been found to play a crucial role in the nucleation and growth of metal nanoparticle catalyst.[20] For TiO_2 supported gold nanoparticles catalyst, these defects affect particle shape, stability and electronic properties which influence their catalytic properties.[20, 107] Calculations have shown that the

binding of Au nanoparticles is stronger to a more defective surface compared to a defect free surface and charge transfer is anticipated from the titania support to Au particles.[20]

1.9 Carbon Monoxide Oxidation on Nanoparticle Catalysts

Catalytic oxidation of CO has been extensively investigated over a range of supported metal nanoparticles such as platinum group metals (Pt, Ir, Rh and Pd), Cu, Ni and Au due to its wide range of practical applications such as indoor air cleaning, CO gas sensors, CO_2 lasers, automotive exhaust emission control, in fuel cells and gas masks.[13, 49, 97, 98, 108] There is a general agreement in the literature that the activity of these catalysts toward CO oxidation is strongly influenced by the particles size and support on which they are supported.[51, 68, 81] Typically, particles with diameter less than 10 nm are reported to be the most active ones.[18, 61, 62, 81] Studies have shown that platinum group metals, which are commonly used in such applications, are most active at higher reaction temperature, this is associated with strong interaction with CO which prevents oxygen adsorption and dissociation.[52, 109, 110] CO oxidation on titania supported Au nanoparticles has attracted researchers due to its ability to oxide CO at low temperatures, even below ambient temperature.[57, 68, 74, 97] Despite the fact that supported Au catalysts have received much attention due to their surprising activities at considerably low reaction temperatures, Pt catalysts are also promising for this reaction particularly when Pt is supported on reducible metal oxides such as Fe_2O_3 and TiO_2.[49, 81, 108, 109] Although there are many reports on CO oxidation on a number transition metal nanoparticle catalysts supported on various metal oxide supports, this thesis concentrates on the CO oxidation reaction on Pt and Au nanoparticle catalysts supported on titania at relatively low reaction temperatures and pressure.

1.10 Gold Catalysis

For many years gold has been regarded as catalytically inert compared to platinum group metals[50, 76, 111] because of its high ionization potential leading to low affinity towards adsorbing molecules such as oxygen and hydrogen.[74] The adsorption energy of

gases on bulk gold is very low resulting in high dissociation barriers, an important factor in catalytic processes.[112] The knowledge that small particles of gold might be a potential catalyst was revealed early 1970s.[112] The study by Bond *et al.*[113] in 1973 disclosed the fact that supported gold has some catalytic activity for olefin hydrogenation reactions. However, it was not until the work by Haruta *et al.*[51] in 1987 which revealed that gold nanoparticles highly dispersed on high surface area metal oxides are an effective catalyst for low temperature CO oxidation. This discovery made gold nanoparticles receive attention in catalysis,[62, 73, 114] in contrast to bulk gold, considered to be of low importance in catalysis before this breakthrough. Recently, gold nanoparticles supported on metal oxides have been found to catalyse a number of reactions including; water gas shift, selective hydrogenation of hydrocarbons, hydrochlorination, selective epoxidation[45] just to mention a few. There has been a common interest among researchers toward gold nanoparticle catalyst since its discovery and a vast body of work has been carried out to illuminate the unusual catalytic behaviour of gold.[20, 76, 107, 115, 116]

Experimental studies by Haruta[74] show that small particles of gold, typically less than 5 nm, are active toward CO oxidation even at temperatures far below 300 K, contrary to platinum group metals which are only more active than gold at temperatures higher than 500 K. Generally, gold has been found to be more than four orders of magnitude more active at room temperature compared to platinum group metals commonly used for the CO oxidation reaction. A correlation of supported gold activity with particle size has been described by Haruta,[64] Goodman and co-workers,[20] Goodman[58] and Hayden and co-workers[78] they all pointed out that for CO oxidation on supported gold nanoparticles catalyst, the TOF depends on gold particles size and the most active particles are in the size range of 1 to 5 nm. Of all the reactions studied we will focus on the low temperature oxidation of CO on supported Au and Pt nanoparticle catalysts. The typical experimental results for activity dependence on particle size of titania supported Au nanoparticles of various sizes for CO oxidation are briefly reviewed below. **Figure 1.11** presents the specific mass activity of titania supported Au particles at 70 ^{o}C.[57]

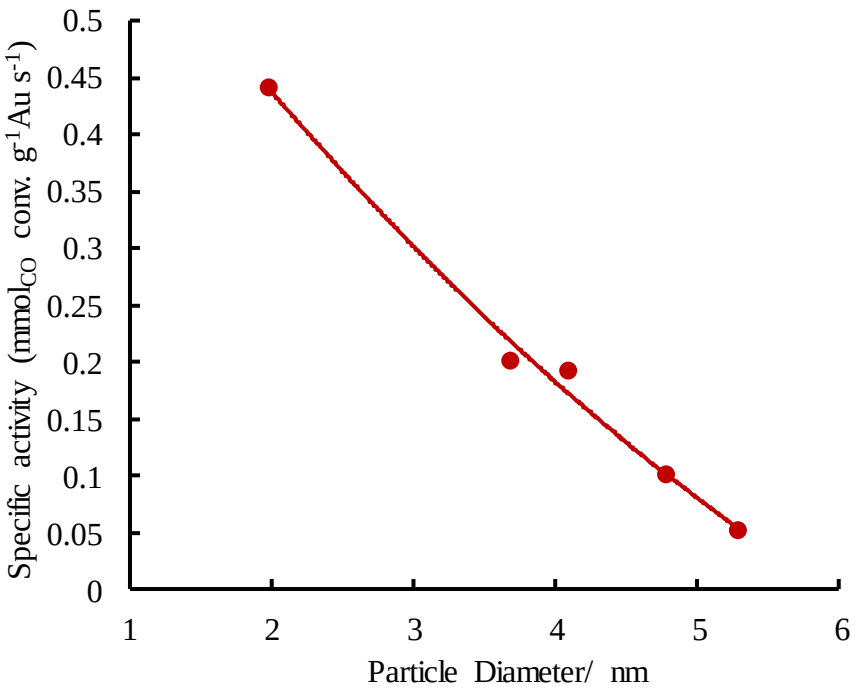

Figure 1.11: Specific mass activity of titania supported Au nanoparticles for the CO oxidation reaction at O_2:CO, 1:1 ratio illustrating the effect of particle size for Au nanoparticles supported on titania at a reaction temperature of 70 ^{o}C.[57]

Herranz *et al*.[57] observed the increase in specific mass activity of Au nanoparticles supported on titania with decreasing particle size, **Figure 1.11**. The maximum specific mass activity achieved was 4.4 x 10^{-4} mmol$_{CO}$ conv. g^{-1}Au s^{-1} for a 2 nm Au particle size, which decreased to 5 x 10^{-5} mmol$_{CO}$ conv. g^{-1}Au s^{-1} for a 5.3 nm particle size.

Reports are also available in the literature addressing the activity of Au nanoparticles supported on titania towards CO oxidation at room temperature. **Figure 1.12** presents the TOF and specific mass activity of Au nanoparticles obtained at room temperature.[22, 62]

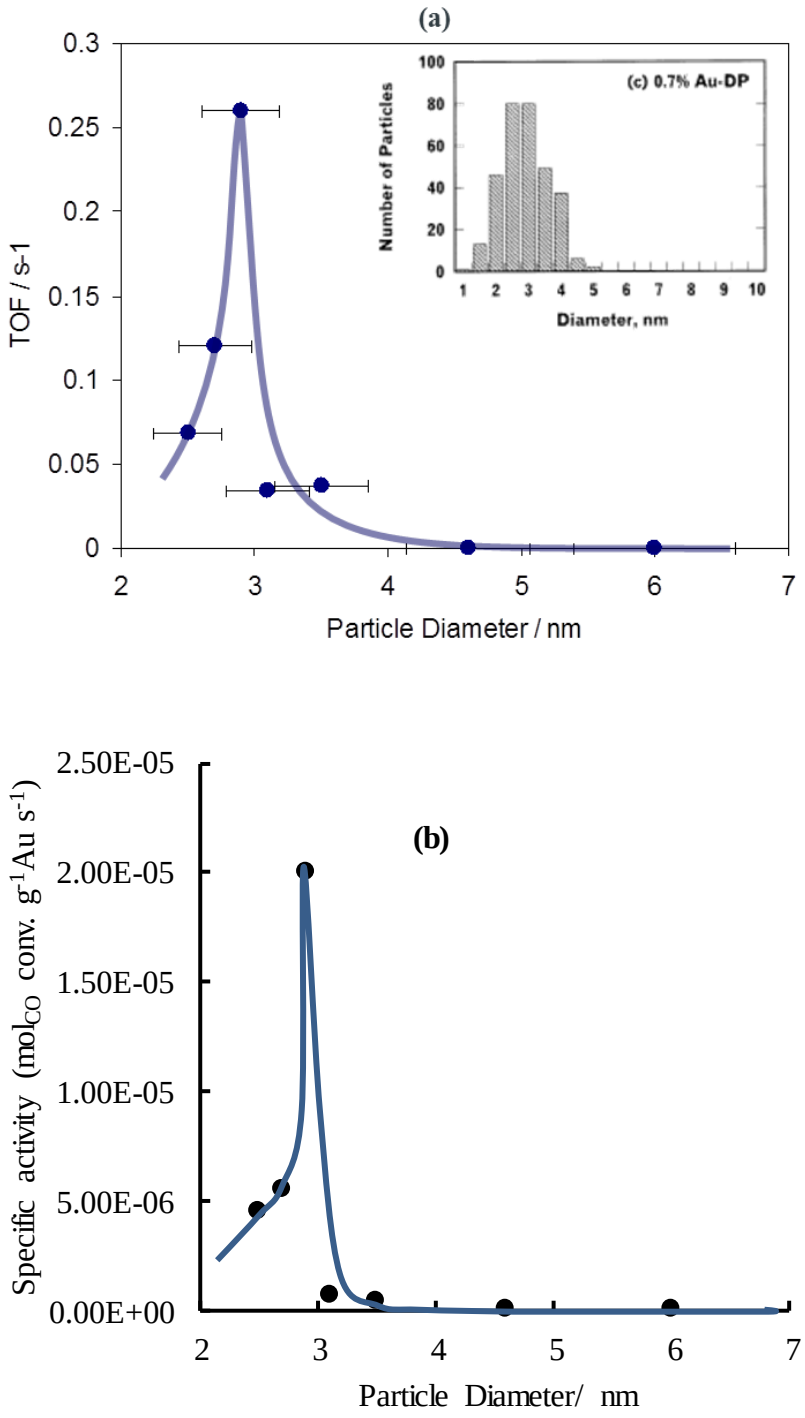

Figure 1.12: (a) TOF, **(b)** specific mass activity of titania supported Au particles for CO oxidation reaction at 300 K.[62]

In the study of CO oxidation reaction on Au particles supported on titania, Goodman and co-workers[22] also reported the particle size dependence for CO oxidation, **Figure 1.13.**

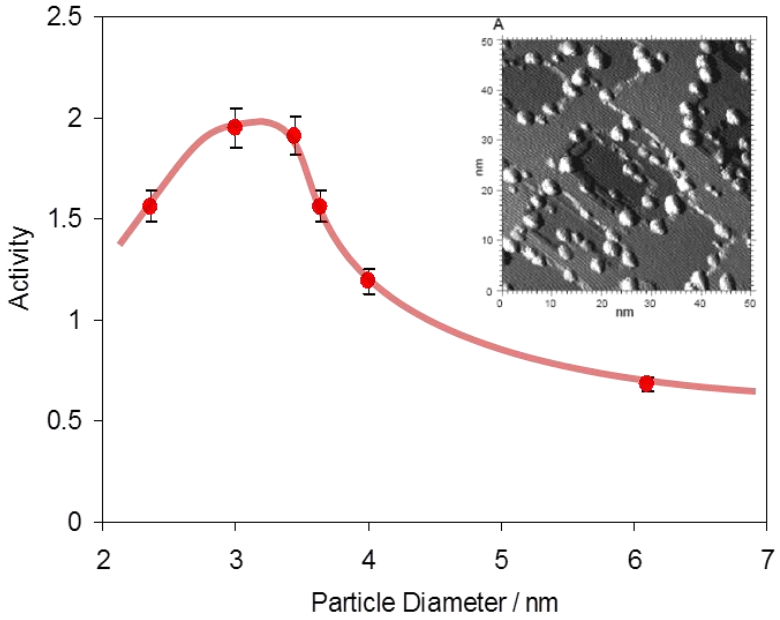

Figure 1.13: The activity of titania supported Au particles for CO oxidation reaction at 350 K and an $CO:O_2$ ratio of 1:5, with a total pressure of 40 Torr.[22]

Experimental results given above illustrate that the CO oxidation reaction on the titania supported Au particles is particle size dependence.

1.10.1 Heterogeneous Catalysed CO Oxidation on Titania Supported Gold Nanoparticles Catalyst

Low temperature oxidation of carbon monoxide by oxygen on supported nanoparticles of gold is well investigated. Researchers have explained that low temperature CO oxidation on supported gold nanoparticles takes place on the Au active sites,[19, 20, 57, 76, 115] termed as a "gold only mechanism". Under-coordinated gold sites on the surface of the nanoparticles are deemed responsible for this surprising activity of gold. It is suggested

that these less-coordinated sites act as adsorption sites for reactants, such as CO and O_2, and stabilize the reaction intermediates, making the reaction feasible.[20, 115] Metallic gold has been found to be very important for CO and O_2 adsorption.[74] The presence of a gold only mechanism common on all supports explains why a range of supports can be successfully applied. The proposed origins for atypical catalytic behaviour of supported gold nanoparticles for the low temperature CO oxidation have been widely discussed by Norskov *et al*.[19, 115] The conclusion is that a high concentration of under-coordinated gold sites is the main source of the unusual catalytic activity of supported gold nanoparticles catalyst.[19] The presence of a second mechanism involving the metal-support interface enhances the catalytic activity; this explains the different activities of gold based catalysts reported on different supports.[19]

An alternative pathway has been proposed to explain supported gold nanoparticles reactivity which is associated to support influence,[19, 20] termed support induced mechanisms. It is suggested that the support charges the gold particles or imparts strain in the gold and this could influence the reactivity of supported nanoparticles for low temperature CO oxidation.

Another metal oxide support induced effect has been put forward, related to the gold activity for the CO oxidation reaction which is "oxygen spill-over" at the metal-support interface.[19, 76] This pathway is believed to occur on reducible metal oxide supports such as TiO_2, Fe_2O_3 and NiO. The support supplies activated oxygen or stabilises reactants and intermediates. The influence of the support as an oxygen supplier is suggested to play a key role in gold nanoparticle based catalysts.[19] It is explained that reducible supports have the capability to trap incoming oxygen and enhance the efficiency of some catalysts through mass transport of reactants to the reaction site. Further, it has been observed that for gold based catalysts, the support helps and stabilizes metal nanoparticle dispersion as well as a given shape.[19] Higher dispersion maximizes the number of under-coordinated sites and hence the number of active sites present which are responsible for gold only mechanisms.

Goodman and Chen on the other hand, associated the unusual activity of gold nanoparticles to quantum size effects. They pointed out that the decreased size of gold nanoparticles affects its valence band structure, which results in a transition from metallic to non-metallic behaviour for nanoparticles.[20]

However, the reaction pathway for CO oxidation on supported Au suggested by different authors is difficult to identify because for a particular reaction system more than one of the above pathways may be in operation, depending on the catalyst system and the type of support. This is why it is experimentally difficult to identify the dominant process among suggested reaction pathways. The generalized mechanisms for CO oxidation on TiO_2 supported gold nanoparticles catalyst as proposed by different authors is presented in **Section 1.5**, **Figure 1.3**.

Turning our attention from unusual/surprising catalytic activity of supported Au nanoparticles to consider a widely used catalyst, here platinum is referred.

1.11 Platinum Catalysis

Platinum is one of the most useful and versatile, heterogeneous metal catalysts which has enjoyed use over many years. Its catalytic activity was identified back in the early 1800s when Dobereiner used it to catalyse the reaction of H_2 and O_2 in his portable lamp.[117] Platinum based catalysts are used in a number of reactions including the conversion of aliphatic straight-chain hydrocarbons to aromatic molecules (dehydrocyclization) and branched molecules (isomerization).[117] It is also applied to large scale hydrogenation in the chemical and petroleum-refining industries and ammonia oxidation, which is a crucial reaction step in the fertilizer production process.[117]

More importantly, platinum is used for the oxidation of carbon monoxide and unburned hydrocarbons in car emissions control.[65] Platinum catalyst is possibly the most commonly used and active electrode in fuel cell technology. Its stability both in oxidizing

and reducing conditions has made it the best catalyst for many applications. Despite its enormous range of applications, platinum is a precious metal of high cost and low abundance making its use in different technologies more difficult.[45] To overcome the cost of using platinum catalysts, its use at the atomic scale has been the focus in heterogeneous catalysis which involves the dispersion of platinum nanoparticles on stable high surface area metal oxide supports, such as Al_2O_3, TiO_2 and Fe_2O_3 hence reducing the amount of platinum incorporated in the catalyst.[117] Supporting platinum catalysts, however, does not only lower the catalyst cost but also maximizes the active surface area of the catalyst and stabilizes the catalyst nanoparticles. On the other hand, some supports, such as TiO_2, participate directly in the reaction mechanisms by activating the reactants and intermediates which in turn enhances the activity, **Figure 1.3.**

Carbon supported platinum nanoparticles catalysts (Pt/C) have been the most used catalyst in PEMFCs technology in particular. The application of this catalyst system is hampered due to the loss of catalytic efficiency as a result of nanoparticle degradation, corrosion of cathode support, and CO poisoning.[44] The loss of efficiency occurs due to the strong interaction of Pt with CO preventing oxygen from adsorbing onto the catalyst surface. [49,76, 116] Supported Pt catalysts are therefore known to be catalytically poor for CO oxidation at low temperature.[109] In order to overcome these shortcomings of carbon supported Pt, researchers have dedicated their efforts towards looking for more efficient Pt nanoparticle supports to combat the effect of catalyst degradation, corrosion and high temperature reaction catalysis.

Very recently, a Fe_2O_3 supported Pt nanoparticle catalyst has been revealed to show unusually high catalytic behaviour for CO oxidation at low temperature.[49] The activity has been attributed to the capability of Fe_2O_3 to supply active oxygen during the reaction. Studies have also shown that the CO oxidation reaction on titania supported Pt particles below 5 nm either display low activity or show no strong size dependence.[118] Theoretical calculations suggest that Pt particle of 1 or 2 nm sizes are more active for CO oxidation.[119] Kageyama *et al*. reported that Pt particles of 2 nm size are the most active for CO oxidation compared to 3 nm and 5 nm sizes.[108] **Figure 1.14** presents typical exper-

imental results showing the TOF and specific mass activity trend of titania supported Pt nanoparticles for CO oxidation as a function of particle size.[62]

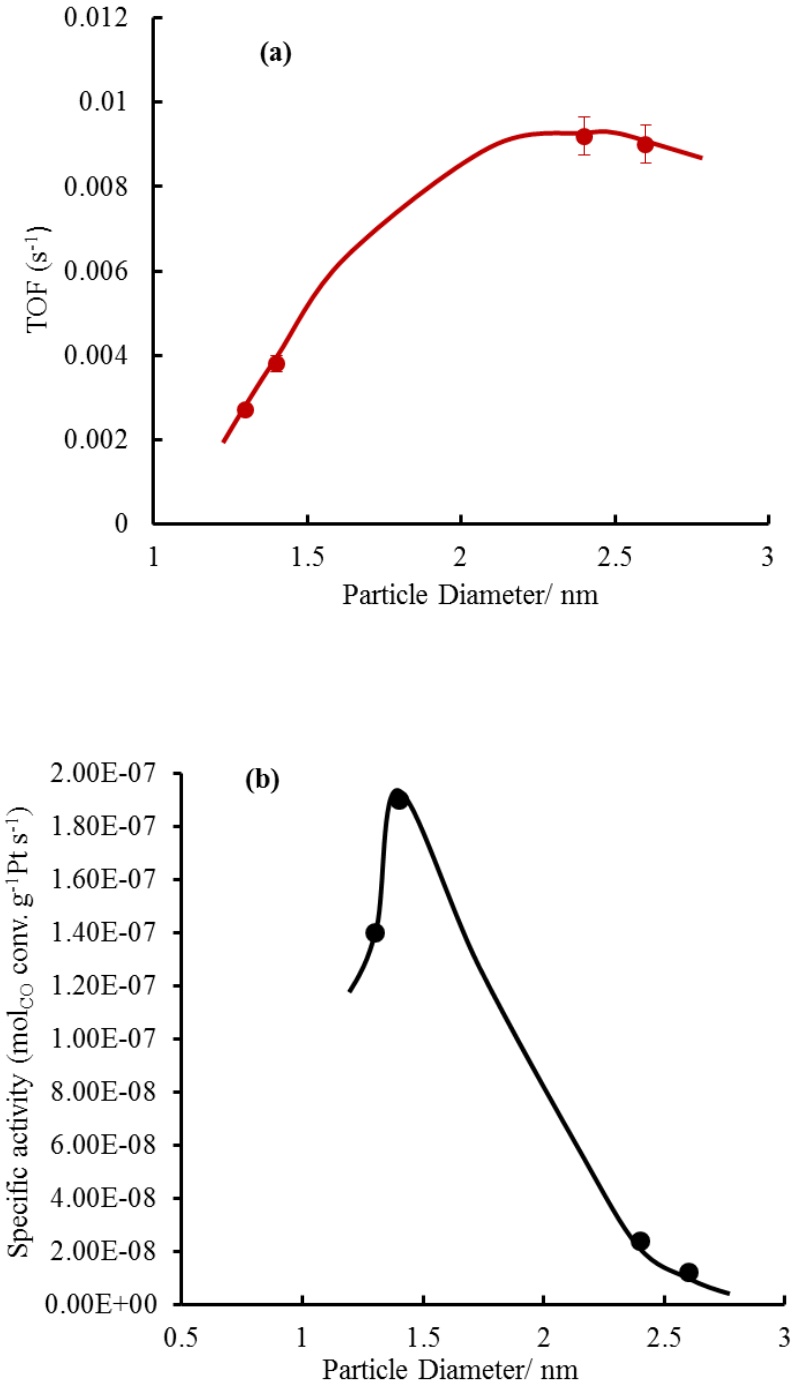

Figure 1.14: (a) TOF, **(b)** specific mass activity of titania supported Pt nanoparticles for the CO oxidation reaction illustrating the effect of particle size for Pt nanoparticles supported on titania at a reaction temperature of 300 K.[62]

For the sake of this study, the focus will be on using TiO_2 supported platinum and gold nanoparticles for CO oxidation reaction at moderately low reaction temperature and the catalytic effects of both systems for CO oxidation will be investigated. It is worthwhile comparing the catalytic activity of both Au and Pt supported on the titania support for low temperature CO oxidation.

1.11.1 Heterogeneous Catalysed CO Oxidation on Titania Supported Platinum Nanoparticle Catalyst

Heterogeneous catalysed CO oxidation reaction has been widely investigated both on Pt single crystals[52, 95, 97, 110] and supported Pt nanoparticle catalysts.[49, 69, 97, 119, 120] It is now well established that due to the strong interaction between oxygen and the platinum surface, oxygen adsorbs dissociatively to form active surface adsorbed atomic oxygen, which reacts with adsorbed CO to form CO_2.[62, 74, 110] For CO adsorption on metal surface catalysts three different adsorption sites have been identified,[54, 94, 97] on-top, twofold-bridge and threefold-hollow, **Figure 1.15**. However, on most of the transitional metal nanoparticles CO binds in an on-top geometry, though it depends on the surface coverage, as at low coverages on-top adsorption is favoured.[94]

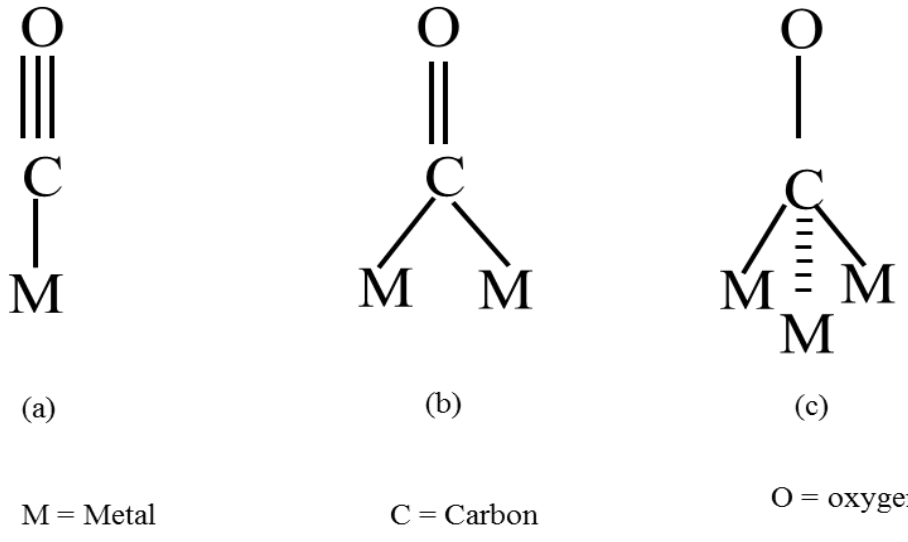

Figure 1.15: Schematic diagram illustrating the CO adsorption sites on a metal surface. **(a)** On-top, **(b)** twofold-bridge and **(c)** threefold hollow.[54]

A simple donor-acceptor model first described by Blyholder is used to study the adsorption of CO on metal surfaces.[94, 97, 100] CO adsorbs on the metal surface through a lone pair of electrons in the 5σ orbital, which is donated to the metal and donated back from the metal d-band to the CO 2 π* antibonding orbital.[94] The CO adsorption strength onto a metal surface is said to be enhanced by the back donation of electrons; this kind of interaction is referred to as synergistic bonding, **Figure 1.10**. For metal oxide supported platinum therefore, the CO oxidation reaction follows the mechanisms[52, 95, 121] shown below:

$CO_{(g)} \leftrightarrow CO_{(ads)}$ Equation 1.4

$O_{2(g)} \rightarrow 2O_{(ads)}$ Equation 1.5

$CO_{(ads)} + O_{(ads)} \rightarrow CO_{2\,(g)}$ Equation 1.6

The CO oxidation reaction proceeds very efficiently on platinum surfaces, with a conversion rate proportional to the carbon dioxide and oxygen partial pressures at a given temperature. Earlier studies have shown that the reaction requires both chemisorbed oxygen and carbon dioxide on the platinum surface,[49, 52, 54, 99, 121] a reaction pathway termed as Langmuir-Hinshelwood mechanism.

Other researchers have reported that this reaction depends on the pressure of reactants in the gaseous phase, coverage and surface temperature.[99] A competitive adsorption between CO and O_2 has been observed, while CO can adsorb on an O_2 covered surface, O_2 is unable to adsorb on a CO covered surface. At high CO surface coverage therefore, the reaction is limited by O_2 and increasing the CO pressure hinders the reaction as there are no more adsorption sites for oxygen to adsorb. On the other hand, at low CO coverage oxygen adsorption occurs more readily and the reaction depends on the surface coverage of both CO and O_2.[99] Despite the catalytic efficiency of supported platinum nanoparticles catalyst, its activity is affected by CO poisoning both in the gas-phase CO oxidation reaction and PEMFCs operation. Generally, maximum CO conversion to CO_2 is achieved at conditions that favour minimal CO surface coverage.[52] For this reason, an improvement of Pt catalyst system has been the focus of researchers in the area of heterogeneous catalysis. In order to experimentally produce and screen supported Au/Pt nanoparticle catalysts as efficiently as possible, a new methodology must be employed.

1.12 Combinatorial High Throughput Methods in Heterogeneous Catalysis

1.12.1 A Brief History of Combinatorial Chemistry

Combinatorial high throughput chemistry is a rapidly growing area, which encompasses the design and rapid synthesis of a multiplicity of material libraries and testing them in a parallel manner for their specific chemical or physical properties of interest in a timely and economically efficient manner.[3, 9, 28] The fast and cost effective discovery of new catalysts and optimization of existing ones is of utmost significance from an industrial point of view. Combination of fast and effective industrial technologies is predicted to play a key role in cost-effective creation of material libraries that are catalytically important for different applications.[7] A number of catalysts-in commercial use, either heterogeneous or homogeneous were developed through some form of combinatorial approach, although the term has been coined very recently.[122] Over one and a half centuries ago, Thomas Edson used a combinatorial method to identify a suitable material for a durable filament in his light bulb invention.[7] He synthesized and tested thousands of various filaments until a filament was discovered which could last for more than 1,500 hours, which transformed the use of electric light. Few decades later, the father of combinatorial catalysis, Mittasch synthesized and screened 6,500 catalysts in distinct experiments over three years evaluating different combinations of supports, catalysts, processing and conditions and created an improved version of the Haber-Bosch ammonia synthesis process.[7, 122] In the Haber process explored by Mittasch, the catalyst runs at a temperature between 450 ^{o}C and 650 ^{o}C and pressure of about 100 Mpa, the oxidation of CO to CO_2 on automotive catalysts, hydrocarbons to CO_2 and water, and reduction of nitrogen oxides operates at a temperature between 300 ^{o}C and 650 ^{o}C.[122] The methodological points reproduced from Mittasch's logbook are:

- Research in catalysis necessitates carrying out experiments with a certain number of elements with numerous additives.
- Testing at high pressure and temperature (in situ) as in Haber ammonia synthesis experiments.

- A very large number of test-series will be required.

Despite the advantages of the discovery of combinatorial techniques a century ago, Mittasch's experiments were very slow and the development of new ammonia synthesis catalyst took several years. However, in the sense applied in drug discovery, combinatorial chemistry can contribute to the synthesis of catalysts either by pooled or parallel approach.[122] Nevertheless, catalyst synthesis is one step in a chain that involves processing, characterization and catalytic testing, therefore the term "High-Throughput Experimentation" can be appropriately used.[7, 122] Combinatorial high throughput approach in catalysis describes to some degree, a logical continuation of an ongoing industrial trend toward reduced reactor sizes, parallel testing, and computerized experimental control and data handling. The technology today promises greater efficiency through miniaturization, automation, integration and the effective usage of computation.[122] Figure 1.16 presents the infrastructure and methods that facilitate high throughput catalytic material library discovery.[28]

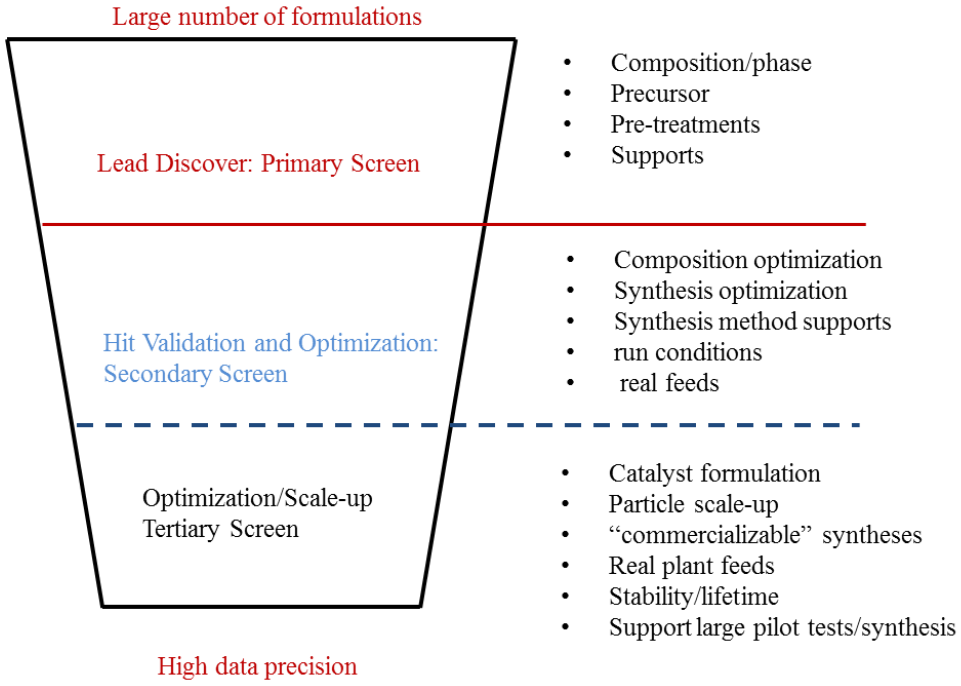

Figure 1.16: Stages of catalyst material library discovery and optimization showing parameters generally screened in each step. The scheme was adapted from[28]

In the steps identified in **Figure 1.16**, the first stage, called "primary screening" is meant to screen multiple families of materials that logically could perform the catalytic transformation of interest. This step of research is purposely designed for the discovery of "hits" which present new material that are promising for a specific usage.[28] While looking to optimize the quality of data and to mimic the real process conditions during primary screening, the volume of experiments makes it difficult to obtain conventional laboratory quality data. However, in a primary screening, one looks for qualitative trends in the data in order to omit family of materials from a diversified library hence identifying the hits that have promise to become leads for testing in the secondary screening stage.[28] The potential hits identified in the primary screening are further scrutinized in the secondary screening stage, at this stage screening technologies that are at least precise as conventional laboratory techniques are required. Secondary screening technologies in heterogeneous catalysis are capable of producing the optimized leads appropriate for the tertiary screening stage: scale-up and commercial testing in pilot or semi-works plants.[28]

Combinatorial chemistry has become popular in a variety of fields in recent years. Merrifield[123] reported the use of combinatorial chemistry for the first time in 1963, based on peptide synthesis by using solid resins. Combinatorial methodologies have advanced rapidly since then because of fast advancing technology and computing. This advancement in technology has led to the rapid discovery and optimization of drugs and other materials, such as super-conducting, ferroelectric, dielectric and luminescent materials as well as ceramics, zeolites, organic materials and polymers.[3]

Combinatorial techniques to synthesize solid state libraries of superconducting materials were reported by Hanak[31] in 1970. A radio-frequency sputtering method was applied to synthesize binary or tertiary films that have a linear change in composition, as the targets were located at 180^{o} for binary and 120^{o} for tertiary films relative to the sample. Hanak reported a thirty-fold increase in the rate of materials discovery using this technique. Sputtering involving physical masking has been applied in recent years to deposit solid state libraries for the discovery and optimisation of CO oxidation catalysts[9]. Wilson *et al.*[124] in 1996 applied a high throughput infrared thermography technique to

screen combinatorial libraries of heterogeneous catalysts for hydrogen oxidation reaction activity.

Weinberg *et al.*[125] reported in 1999 a combinatorial methodology used to sequentially produce material libraries of Pt, Rh, Pd and Cu, for CO oxidation and NO reduction activity. Radio-frequency sputtering was used to deposit materials through masks onto a quartz substrates with a diameter of 75 mm achieving a triangular library which contained 120 catalysts made in one hour, followed by library annealing at 773 K for 2 hours to obtain alloy catalysts. Scanning mass spectrometry was used to screen each catalyst by direct sampling of products via a capillary transfer line. The disadvantages of such a sequential masking technique is the time consuming process required to change the position of the masks and the subsequent annealing step to ensure precursors mix to achieve the materials required.

1.12.2 Combinatorial Methodologies in Heterogeneous Catalysis

Nearly all High through-put catalyst screening to date has been on high area catalysts which are rather undefined or uncharacterized. There is a need for methods with sufficient sensitivity to be used on planar model catalysts where the substrate and particle size can be better controlled and defined, as has been achieved in electrochemical work.[60] The role of combinatorial chemistry in heterogeneous catalysis is vital in the modern chemical industry, as economic and environmental gains can be attained via catalysts formulation and optimization. High throughput screening techniques are crucial in conjunction with the combinatorial material library synthesis, as the library can be rapidly screened. The activity for exothermic reactions can be screened using an IR thermal camera. An infrared thermography technique for the screening of heterogeneous catalyst libraries was first reported by Wilson *et al.*[124] Saalfrank and Maier applied a high throughput infrared thermography method for the discovery and development of multi-component oxides of Co, Mn and Ni for low temperature CO oxidation reaction.[47]

Hagemeyer and co-workers[48] applied a combinatorial method to synthesize a catalyst library of 256 materials for efficient low temperature CO oxidation. Parallel screening

of the activity of a library of catalysts was achieved by an infrared thermography technique.[48] The optical screening of catalytic libraries using an infrared technique is parallel and fast for obtaining qualitative or semi-quantitative data.

Hahndorf *et al.*[126] reported a sequential impregnation method based on robotic functionality used to prepare multicomponent catalytic materials on an alumina substrate using precursor materials. Parallel screening of heterogeneous catalysts libraries was carried out in a 64 multi-channel ceramic reactor connected to a fast GC/MS analysis. Senkan and Ozturk described the application of an in-situ resonance-enhanced multi-photon ionization (REMPI) system with microelectrode detection coupled with a novel array of micro-reactors used for the discovery of an optimal composition in ternary Pt/Pd/In metal catalysts for the dehydrogenation of cyclohexene into benzene.[127] Array micro-reactors enable parallel screening of large numbers of catalysts at similar experimental conditions. Supported multi-metallic catalyst formulations were automatically prepared using a conventional co-impregnation technique in which pellets of porous alumina were introduced into an aqueous solution of catalysts precursors at varied concentrations.[127] Solutions were evaporated and pellets dried first at 90 ^{o}C for four hours followed by further drying at 120 ^{o}C for four hours. The impregnated pellet catalyst libraries consisting 66 ternary combinations of Pt, Pd and In were eventually calcined at 500 ^{o}C for 2 hours.

It is apparent that some of the high throughput combinatorial techniques for synthesis of heterogeneous catalyst libraries reviewed here involve masking part of a substrate at a time during material synthesis.[125] However, the synthesised library is later subjected to further treatment such as drying and annealing. Such an approach of combinatorial material library synthesis is considerably time consuming. Some of the high throughput screening methodologies addressed on the other hand are also challenging. For instance, REMPI can only be applied to screen specific molecules and many molecules do not have REMPI features. Mass spectrometry, despite its growth and wide applicability in gaseous mixture analysis, requires sample withdrawal and application to combinatorial catalysis requires the development and application of new approaches. The quadruple mass spectrometry (QMS) technique needs to be physically moved from one site to

another during screening of a catalyst material library and therefore the time spent to screen the whole sample is significant. Any combinatorial approach in heterogeneous catalysis requires the implementation of a parallel strategy both in catalyst material library synthesis and screening for desirable properties.

High throughput combinatorial methods established for solid/gas-phase oxidation screening of heterogeneous catalysts by Hayden's research group at the University of Southampton need recognition, as these were applied to produce this work. A high throughput combinatorial approach based on physical vapour deposition (HT-PVD) has a high capability to simultaneously synthesize various material libraries.[32] The technique has been coupled with high throughput material screening techniques to test synthesised materials for their specific properties. Since then, a number of papers have been published by the group based on the application of this combinatorial approach.[21, 34, 128-131] The methodology has the capability to produce combinatorial libraries with high control of material composition ranges across the substrate and can achieve parallel deposition of more than one element. This method has been applied and continues to be applied in the synthesis of catalysts supports and supported metal electrocatalysts,[34, 59, 129, 132] hydrogen storage materials,[128] ternary metal alloy electrocatalysts,[21] supported metal nanoparticles electrocatalysts[129] and corrosion resistant thin film alloys.[131] Importantly, high throughput methodologies have been applied in the synthesis and discovery of new heterogeneous catalysts for solid/gas-phase, solid/liquid-phase reactions[29, 48, 133] and in heterogeneous catalysts research.[28, 29] Andrew and associates[134] have recently reported similar high throughput combinatorial method for material synthesis that incorporates rotatable "shadow" mask to synthesise material libraries with a composition gradient across the substrate, referred as rotatable shadow mask compositional spread alloy films (RSM-CSAF) deposition tool.

This work has extended the application of the high throughput methodology developed by the Southampton group to synthesize TiO_2 supported platinum and gold nanoparticle heterogeneous catalyst for CO oxidation at relatively low reaction temperatures. The HT-PVD technique has been coupled alongside with a newly developed high-throughput method to screen well-controlled supported model heterogeneous catalyst using a high throughput infrared thermography technique. This approach allowed us to

investigate the particle size effect of supported platinum and gold nanoparticle catalysts for the CO oxidation reaction. The approach is advantageous as it is a non-contact technique allowing measurements to be performed in an UHV environment, recording changes across the whole sample at the same time and provides a direct temperature measurement from the exothermic reaction, which is translated into catalyst activity.

1.12.3 Infrared Thermography

The infrared thermography technique is the optical techniques most used in the screening of catalytic activities of materials libraries, due to its ease of applicability.[9] The IR thermal imaging of combinatorial material libraries is a highly parallel approach for the screening of heterogeneous catalysts reactivity.[9, 124] The robustness of the infrared thermography technique in parallel screening of material libraries has been discussed in the literature.[124]

Maier and co-workers later refined the IR thermography technique by taking into account the emissivity differences of catalysts on the library making the technique more quantitative.[135] The technique was used to detect the activity of a combinatorial library of heterogeneous catalysts for the hydrogenation of 1-hexyne and the oxidation of isooctane and toluene. Maier and Holzwarth[133] later applied the emissivity corrected infrared thermography (ecIRT) technique to screen heterogeneous catalyst library for toluene oxidation. Maier *et al*.[42] addressed the application of the ecIR technique in the discovery and optimization of new catalysts for hydrogen-rich gas purification by CO methanation. Subsequently, IR thermography gained momentum in screening for heterogeneous catalysts discovery, catalysis research and to the study of catalysts properties and potentialities.

Maier and Saalfrank applied a high throughput IR thermography method in the discovery and development of multicomponent oxides catalysts for low temperature CO oxidation.[47] Hagemeyer and co-workers[48] applied a parallel IR method in the screening of

heterogeneous catalyst library which led to the discovery of efficient catalysts for low temperature CO oxidation. The application of high throughput IR thermography technique in the study of the dehydrogenation process of cyclohexene over carbon supported Pt catalysts was recently reported by Ichikawa and co-workers[136] and Digilov *et al.*[137] reported the application of the IR technique in the study of oscillatory behaviour during catalytic oxidation of CO over supported Pd.

Very recently, Loskyll and co-workers reported the ecIRT technique as a strong tool in catalysis research.[138] In high-throughput screening, particularly primary screening, the choice of technique is based on targeted properties of interest, needed for qualitative catalyst selection, as well as the reliability and robustness of the technique. For instance, when a catalyst is to be developed or discovered its catalytic activity needs to be accessed simply instead of screening for structure and other behaviours which could result in unnecessary data.[1] Therefore, to minimize analysis time of high-throughput catalyst screening, parallel methods which lead to fast and parallel data acquisition from the catalyst libraries are very important. There is no doubt that the screening time of the IRT method does not scale with sample quantity/library components. IR-thermography is a robust technique due to its non-invasiveness and non-contact mode of sample screening, allowing measurement even in an inaccessible environment. Since most chemical reactions consume or produce heat, catalytic activity can be quantified by measuring the change in sample surface temperature.[1]

IR-video imaging is a very sensitive method for the detection of temperature changes. A major setback of this technique is attached to signal intensity which is always related to the amount of heat released. The signal from side or parallel reactions adds to the intensity, which introduces an error into the measurement; therefore it is necessary to carefully select the reaction under observation.[47] Active catalysts reveal themselves as "hot spots" in IR images of exothermic reactions; this is the basis of IR thermography. Catalysts on the solid state library are tested simultaneously and in-situ using this technique. Infrared thermography has consequently been used recently for screening of hydrogen storage materials,[128, 139] in high throughput experimentation for the discovery of active catalysts for solid/gas-phase, solid/liquid phase reactions[1, 47, 48, 124, 138, 140, 141] and in endothermic dehydrogenation reactions.[140] The use of infrared thermography screening

technique indicates the activity of a sample regardless of the product composition and is the fastest truly parallel analysis technique.[47, 142]

Because of the high throughput property of the physical vapour deposition system[32] and a new high throughput heterogeneous catalysis screening chip developed during the course of this work, a high throughput IR thermography technique was applied in the work presented herein. This approach enabled parallel screening of titania supported Pt and Au particles of various sizes across a screening chip for CO oxidation properties at low temperature.

1.13 Objectives

The main aim of this project was to develop a new heterogeneous catalyst for heterogeneous catalysed CO oxidation at relatively low temperatures. A high throughput approach was implemented in the synthesis and screening of heterogeneous catalysts libraries for CO oxidation activity. The libraries of heterogeneous catalysts were synthesized by using a high throughput physical vapour deposition technique recently developed by Hayden *et al*.[32] Platinum and gold nanoparticles of various sizes supported on titania were synthesized and screened to investigate the effect of particle size for the CO oxidation reaction at low reaction temperatures. For the investigation of catalytic activity as a function of particle size, a new high throughput heterogeneous catalysis screening chip for solid/gas-phase reactions was developed in order to allow catalyst activity quantification, followed by development of an UHV high throughput heterogeneous catalysis screening reactor. A high throughput infrared thermography technique first reported in heterogeneous catalysis by Willson *et al.*[124] and later revised by Maier *et al.*[135] was adapted to enable parallel screening of heterogeneous catalyst libraries synthesized by a PVD method for CO oxidation activity. The results obtained, demonstrate the capability of a HT-PVD method in material synthesis on a newly developed heterogeneous catalysis screening chip. Additionally, the applicability of a high throughput infrared thermography technique in parallel screening of a catalyst library for the CO oxidation reaction has been demonstrated.

1.14 Project plan

The experimental work carried out in this project was divided into the following sub-sections:

1. The need for a high throughput heterogeneous catalysis screening chip was identified as an appropriate approach to allow catalytic activity quantification of supported nanoparticle catalysts. The screening chip was designed to enable the investigation of particle size effect for the CO oxidation reaction using a high-throughput approach.

2. Development of an UHV heterogeneous catalysis screening reactor.

3. Syntheses of heterogeneous catalyst support (TiO_2) and supported catalyst libraries of Pt and Au particles of a range of sizes using HT-PVD technique.

4. Characterization of catalyst support and supported catalysts by XRD, AFM, TEM and XPS.

5. Screening of Pt and Au nanoparticle catalysts deposited on a high throughput screening chip for the CO oxidation reaction using an infrared thermography method for activity quantification.

2. High Throughput Heterogeneous Catalysis Screening Chip Development

2.1 Introduction

This chapter addresses the development of a new high throughput catalysis screening chip for the solid/gas-phase reactions. Only a general description of the main procedures and approaches involved will be considered. The concept of using a microfabricated screening chip was developed during this work. The requirements and specifications were established by considering the need as described in this chapter, **Section 2.5.1**. Thus, this was designed based on some previous experience with the hotplate chip developed by Duncan Smith *et al*.,[143] using silicon nitride back-etched membranes. Temperature and heat characteristics were optimized in collaboration with Chris Newman using finite element methods. Two chip designs were made with two thickness membranes and two field sizes in order to make sure that the membrane supports were sufficiently robust. The final design was given to Mir Enterprises Ltd, London, who made card drawings based on our geometries end design, manufactured the required masks and manufactured the chips. The fabrication of a new high throughput heterogeneous catalysis screening chip in this study was to be undertaken within Hayden's group in collaboration with the Electronics and Computer Science department at the University of Southampton. However, after some difficulties early at the start of the chip fabrication process, including the technical problems and fabricating equipment, it was advised that for the chip to be fully fabricated, it would take up to 8 months. Despite the fact that the chip would have been fabricated within 8 months, there was no technical assurance whether the chip would be fit for the intended use. Following this dilemma, the best option was to hire a fabrication company which fabricated the chips within a reasonable short time and with technical assurance of the final chip, and this was anticipated to serve time and have this project running as early as possible.

2.2 High Throughput Screening in Catalysis

High throughput screening in combinatorial catalysis has become part of almost every experimental process for the screening of combinatorial material libraries since its discovery.[42, 47, 124, 125, 135, 138, 144] Sophisticated screening technologies are being implemented in the discovery of new efficient catalysts and improving existing catalysts. The combination of high throughput combinatorial material synthesis and high throughput screening approaches is promising for rapid commercialization and development costs.[3, 9, 34, 125] Combinatorial catalysis therefore includes micro-fabrication, instrumentation, robotics and informatics as these play a key role in catalytic reaction control.[9] The design and fabrication of a new high throughput catalysis screening chip made of silicon nitride membranes has been undertaken in this work and its development is addressed.

High throughput methods have been applied to study catalytic activity of various materials.[21, 60, 138, 145-147] The activity evaluation of these material libraries has been accomplished using flow/tube reactors packed with catalytic materials, where reactant gases are allowed to flow through, trapping the products on the other side using a quadrupole mass spectrometer in order to establish the product distribution.[9, 126, 127, 148-150] Therefore, the catalytic activity and selectivity of such catalysts would be established. However, for well characterised model catalysts, activity evaluation is experimentally difficult.[144] The ideal would be to measure the product distribution (obtain activity and selectivity) but this is difficult to achieve because of sensitivity. In the setup implemented in this work using a single collision reactor, product distribution and selectivity is difficult to attain. Additionally, the conversion may be very low due to the nature of the reactor system; hence the sensitivity becomes a major problem. Generally, the major interest in this work is to measure the relative activity across a catalyst library for CO oxidation by measuring the temperature change from the heat of reaction.

2.3 Silicon Nitride MEMS Membranes and Applications

Silicon nitride (Si_3N_4) is a promising ceramic material developed in 1960s in the search for high toughness and high strength materials.[151] Thin films of silicon nitride are of interest in making various microelectromechanical devices such as pressure sensors, ink

jets, x-ray masks, etch masks and micro-positioners.[152-154] The increasing use of silicon nitride membranes is due to its high thermomechanical properties including durability, high temperature mechanical strength, high thermal shock resistance and chemical corrosion resistance. Additionally, Si_3N_4 is potentially a high thermal conductivity material, registering an intrinsic conductivity of 200 $Wm^{-1}K^{-1}$.[151, 155] Low stress Si_3N_4 is commonly made by a low pressure chemical vapour deposition (LP-CVD) technique from a gaseous mixture of dichlorosilane (SiH_2Cl_2) or silane (SiH_4) and ammonia (NH_3) at a temperature range of 700 to 900 ^oC, and a pressure below one Torr.[152, 156] The film synthesis can be controlled by providing excess SiH_2Cl_2 or SiH_4, producing a Si-rich uniform film. This film is more stable and stress-free than a film made by plasma enhanced chemical vapour (PE-CVD) technique.[152, 155, 157, 158] A stress-free Si_3N_4 membrane is stable and resistant to cracking during handling and operation. However, depending on the intended application and cost of production, a Si_3N_4 membrane can be produced using different techniques and processes.[153, 156, 159, 160]

2.4 Modelling of the Temperature Change from the CO Oxidation Reaction from Supported Pt and Au Catalysts

Theoretical determination of the expected temperature change on the silicon nitride membrane from the exothermic reaction of CO oxidation on titania supported gold and platinum nanoparticle catalyst has been undertaken. This was done through temperature modelling with the help of Chris Newman at Ilika Technologies by using COMSOL MULTIPHYSICS® simulation software provided by the University of Southampton. The finite element thermal modelling of the temperature change on silicon nitride membrane is given in equation **2.1**. The model estimates the amount of heat in terms of power that is required to produce a given temperature raise in the centre of the membrane, which is related to the membrane area, thickness and thermal conductivity. In the thermal model, the temperature is integrated over the area across the membrane in the same way an IR- thermal camera integrates the temperature across the membrane to give an exact temperature raise on the membrane. The thermal conductivity of silicon nitride[161] membrane used during the modelling was 10 $Wm^{-1}K^{-1}$; however, thermal conductivity of thin membranes can vary significantly from their bulk value depending on the mem-

brane temperature and thickness.[159, 162] Temperature loses via conduction was considered, ignoring radiation loses since the temperature difference is small. Therefore, the temperature difference between the membrane and substrate would be the same at any substrate temperature. **Figure 2.1** shows silicon nitride membrane.

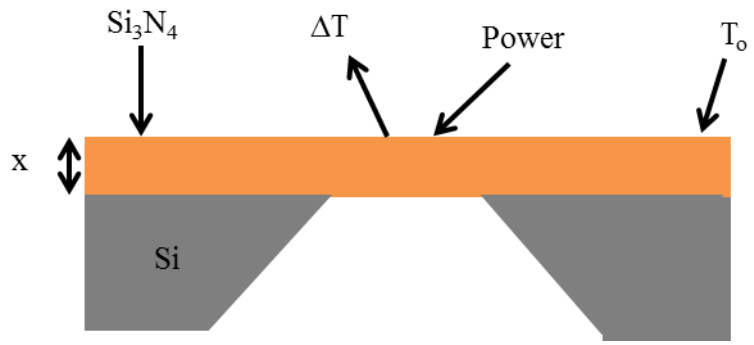

Figure 2.1: Illustration of silicon nitride membrane with the thickness **x** on a backside etched silicon substrate at the initial temperature (T_o). The power P from CO oxidation reaction on the membrane results to the raise in temperature (ΔT). The figure was adapted from reference.[153]

$$P\left[\mu W m m^{-2}\right] = \frac{13.5 \times x(\mu m) \times \Delta T(K) \times k\left(W m^{-1} K^{-1}\right)}{A\left(mm^2\right)} \qquad \text{Equation 2.1}$$

where, P = power ($\mu W mm^{-2}$) in the form of heat required to raise the temperature of the centre of the membrane T (K), x is the membrane thickness in μm, A is the membrane area, square field in mm^2 and *k* is the membrane thermal conductivity in $Wm^{-1}K^{-1}$.

Equation 2.1 can be modified into equation 2.2 below in order to present the power in terms of $J\ s^{-1}\ mm^{-2}$:

$$P\left[J s^{-1} m m^{-2}\right] = \frac{13.5 \times x(\mu m) \times \Delta T(K) \times k\left(W m^{-1} K^{-1}\right) \times 10^{-6}}{A\left(mm^2\right)} \qquad \text{Equation 2.2}$$

The thermal conductivity of silicon nitride membrane was modified to incorporate other films of different materials added onto it during material synthesis and catalyst activity screening. Since titania thin film was deposited onto the membrane as a catalyst support, and carbon sprayed onto the reverse side of the membrane to provide constant emissivity. The thermal conductivity of silicon nitride membrane was modified by

summing the thermal conductivities in proportional to their relative thicknesses as demonstrated through equation 2.3.

$$k = \frac{\left(k_1 t_1 + k_2 t_2 + k_3 t_3\right)}{t_T} \qquad \text{Equation 2.3}$$

where, k = thermal conductivity ($Wm^{-1}K^{-1}$), t is the thickness (μm) and t_T is the total thickness in μm.

Given titania thickness of 200 nm as measured by AFM and thermal conductivity of titania film[163] of 0.87 $Wm^{-1}K^{-1}$ while that of carbon film is 1.8 $Wm^{-1}K^{-1}$[1164] and the thickness of 200 nm, taking the thermal conductivity of silicon nitride membrane to be 10 $Wm^{-1}K^{-1}$, the modified thermal conductivity of the membrane from equation 2.3 is given by:

$$k = \frac{\left(10 \times 0.6 + 1.8 \times 0.2 + 0.87 \times 0.2\right)}{1} = 6.53 Wm^{-1}K^{-1}$$

Therefore, the modified silicon nitride membrane thermal conductivity is 6.63 $Wm^{-1}K^{-1}$.

The model gives the insight of the expected experimentally measured temperature values using an IR-thermal camera in quantifying the catalyst activity, as it is measured in terms of temperature change from the surface reaction. Since the CO oxidation reaction is exothermic, the higher the temperature raise on the catalyst surface the higher the catalyst activity.

However, it is crucial to define the quantities of reactant gases which are dosed onto the surface of a catalyst. Exposing the surface to a gas, the dosage is usually measured in terms of the pressure of adsorbing reactant gas and the length of time it is present in the reaction chamber.[54] These factors determine the number of molecular collisions encountered at the surface. The number of reactant gaseous molecules striking the catalyst surface per second can be calculated using the gas-phase collision theory, a molecular collision rate per unit area is given by:[54]

$$\frac{dN}{dt} = \frac{P}{\sqrt{2\pi mkT}} \qquad \text{Equation 2.4}$$

dN/dt = number of molecules per unit time, P = the gas pressure (Nm^{-2}), *m* = the molecular mass (Kg), *k* = the Boltzmann constant (1.38 x 10^{-23} J/K), T = temperature (K) and $\pi = 3.1416$.

Assumption 1: Every molecule that arrives at the surface reacts, assuming the reactant pressure to be 1 x 10^{-3} mbar (0.1 Nm^{-2}) and the reaction is carried out at 300 K.

The number of molecules, (CO) striking the surface per square millimetre per second is determined to be;

$$\frac{dN}{dt} = \frac{0.1}{\left[2 \times 3.1416 \times 28 \times 1.66 \times 10^{-27} \times 1.36 \times 10^{-23} \times 300\right]^{1/2}} \qquad \text{Equation 2.5}$$

$$= 2.87592 \times 10^{21} \text{ molecules } m^{-2}s^{-1}$$

$$= 2.87592 \times 10^{15} \text{ molecules } mm^{-2}s^{-1}$$

The synthesis of gold nanoparticles of an average diameter of 1.4 nm (radius = 7 x10^{-7} mm) and particle density of 5.5 x 10^{12} cm^{-2} (5.5 x10^{10} mm^{-2}) was previously reported.[129]

Assumption 2: Gold/platinum nanoparticles are hemispherical:

The area, **A** (mm^2) of one hemispherical gold particle is given by the equation below:

$$A = 2\pi r^2 \qquad \text{Equation 2.6}$$

A = 2 x 3.1416 x $(7 \times 10^{-7})^2$

A = 3.08 x 10^{-12} mm^2

The area of all gold nanoparticles therefore is given by area of one particle multiplied by particles density;

3.08 x 10^{-12} mm^2 x 5.5 x 10^{10} mm^{-2} = 0.1694 mm^2 of gold on 1mm^2 of titania.

The total number of molecules striking the surface per second is given by the total gold/platinum particle area multiplied by the number of molecules of reactant gas arriving at the surface per second;

0.1694 mm^2 x 2.87592 x 10^{15} = 4.8718 x 10^{14} molecules per second on 1 mm^2 of titania.

The number of moles of CO molecules arriving at the surface per second is given by;

1 mole x 4.8718 x 10^{14} molecules / 6.022 x 10^{23} molecules = 8.09 x 10^{-10} moles per second.

Since[165], CO (g) + 1/2O (g) → CO_2 (g) $\Delta H = -283000\ Jmol^{-1}$.

If the oxidation of 1 mole of CO gives 283000 $Jmol^{-1}$, oxidation of 8.09 x 10^{-10} moles could give;

8.09 x 10^{-10} mol per second x (-283000 $Jmol^{-1}$) = -2.289 x 10^{-4} J s^{-1} mm^{-2}

The estimation of the amount of heat required to produce a given temperature rise in the centre of the membrane was modelled using equation 2.2, which relates the membrane area, thickness and membrane thermal conductivity. From equation 2.2, for a membrane size of 1.5 mm x 1.5 mm, hence **A** = 2.25 mm^2, **P** = 2.289 x 10^{-4} J s^{-1} mm^{-2}, ***k*** = 7 $Wm^{-1}K^{-1}$ and **t** = 0.6 μm, the temperature change T/ K on silicon nitride membrane can be estimated:

$$\Delta T[K] = \frac{P\left(Js^{-1}mm^{-2}\right)\times A\left(mm^2\right)\times 10^6}{13.5\times x(\mu m)\times k\left(Wm^{-1}K^{-1}\right)} \qquad \text{Equation 2.7}$$

$$\Delta T = \frac{2.289\times 10^{-4}\,Js^{-1}mm^{-2}\times 2.25mm^2\times 10^6}{13.5\times 0.6\ \mu m\times 7Wm^{-1}K^{-1}} = 9K$$

The temperature change in the centre of the membrane is estimated to be 9 K for a reaction probability of unity where every molecule of CO and O_2 on the surface reacts. However, this is the highest temperature raise compared to that observed from experimental measurements. Perhaps due to assumptions made in the model. Nevertheless, the model still holds true as the interest is to obtain the absolute values of reactivity which provide activity trends across the catalyst library. **Figure 2.2** shows simulated surface temperature and cross-section temperature distribution on a square silicon nitride membrane of 1.5 mm x 1.5 mm x 0.6 μm obtained by using the theoretical power of 2.289 x 10^{-4} J $s^{-1}mm^{-2}$ from equation 2.2 at 300 K. This gave the TOF of 205 s^{-1}, (specific mass activity = 1.06 x 10^{-2} mol_{CO} conv. g^{-1}Au mm^{-2} s^{-1}).

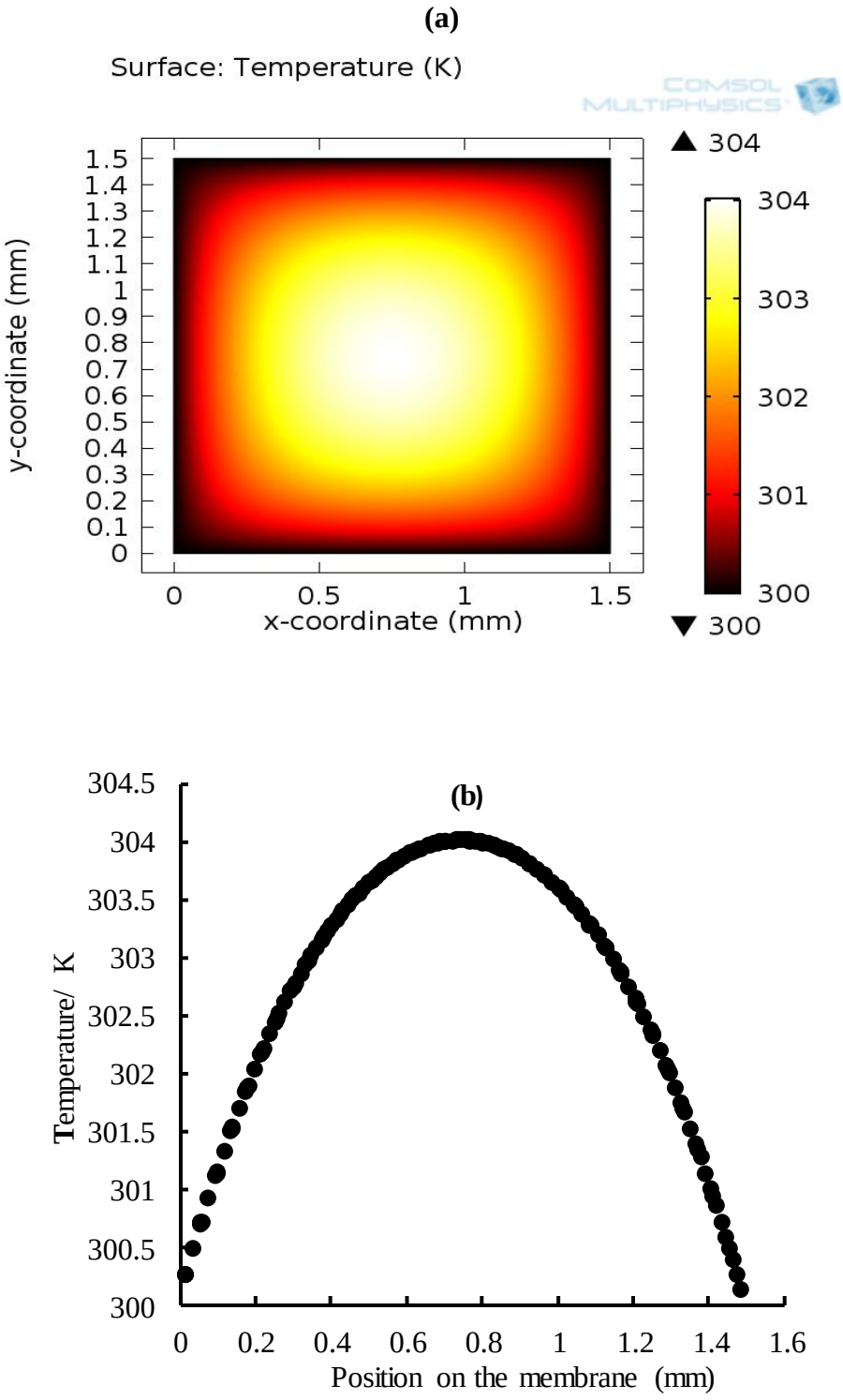

Figure 2.2: (a) Image showing the surface temperature on a 1.5 mm x 1.5 mm x 0.6 µm silicon nitride membrane, **(b)** illustrates the temperature profiles across the membrane. The simulation membrane temperature was 300 K and the theoretical power of 2.289 x 10^{-4} J s^{-1} mm^{-2}.

However, it was necessary to model the temperature change on the whole screening chip in order to get an insight of the temperature profile that represents 144 or 100 square membranes on the screening chip. In turn this would reveal the amount of temperature raise on the substrate when a certain amount of heat is produced in the centre of the membrane as a result of exothermic reaction. The heat losses due to conduction only at the edges of the substrate were considered, this is the likely case producing a higher temperature in the centre of the substrate than the edges. The substrate edge temperature was fixed at 300 K and the thermal conductivity of Si was 130 $Wm^{-1}K^{-1}$. The power was obtained by summing all individual membrane's power for 100 square membranes on the screening chip. **Figure 2.3** shows the simulated surface temperature and cross-section temperature distribution of a substrate under these conditions, assuming a theoretical power of 2.289 x 10^{-2} J s^{-1} mm^{-2}. The temperature raise in the centre of the substrate under these conditions was 0.018 K. Further in **Figure 2.4** is the simulated surface temperature and cross-section temperature distribution for the whole screening chip obtained using experimental power of 1.064 x 10^{-3} J s^{-1} mm^{-2}, which resulted into a maximum temperature raise of 0.0009 K in the centre of the chip. This shows that, for the heat produced from the CO oxidation reaction on titania supported Pt and Au nanoparticle catalysts, heat losses from silicon nitride membrane to the substrate is negligible.

(a)

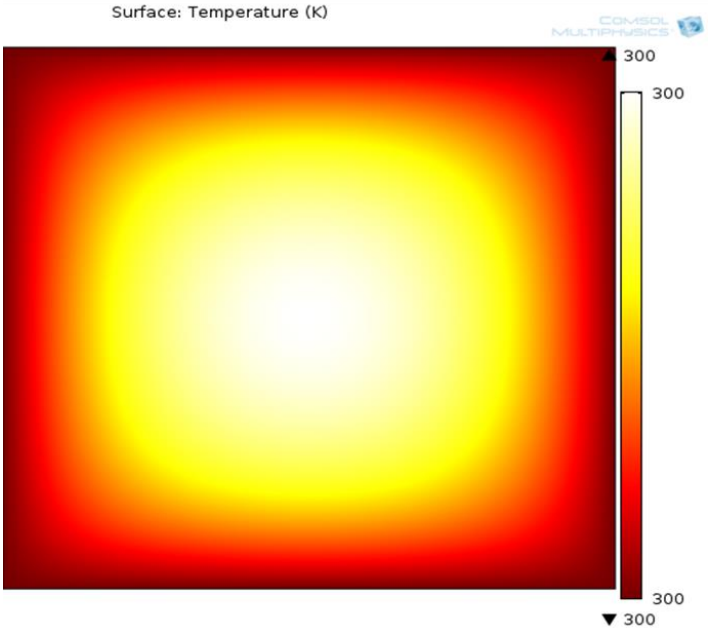

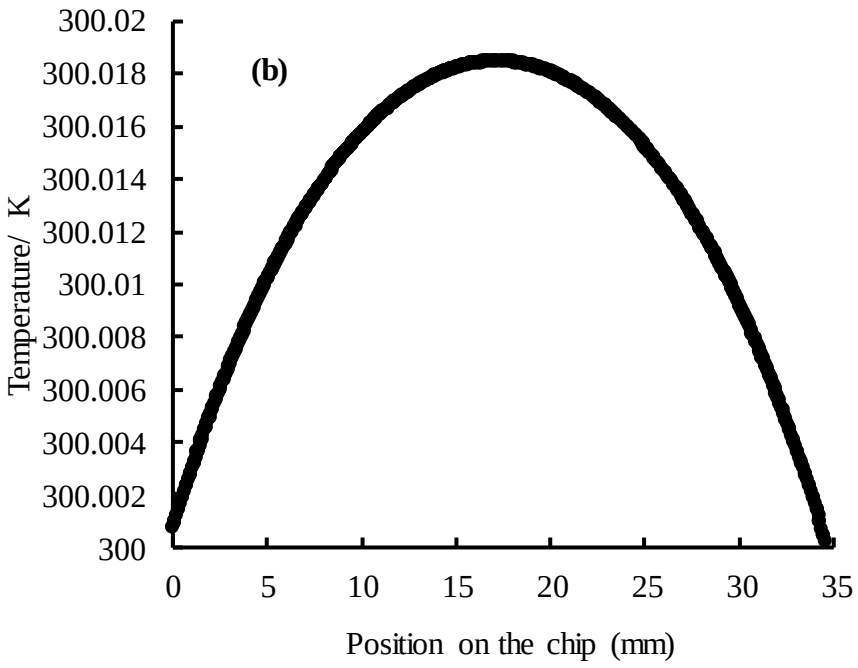

Figure 2.3: (a) Image showing the surface temperature on whole screening chip (35 mm x 35 mm x 0.45 mm), **(b)** illustrates the temperature profiles across the chip. The simulation chip temperature was 300 K and the theoretical power of 2.289 x 10^{-2} J s^{-1} mm^{-2}.

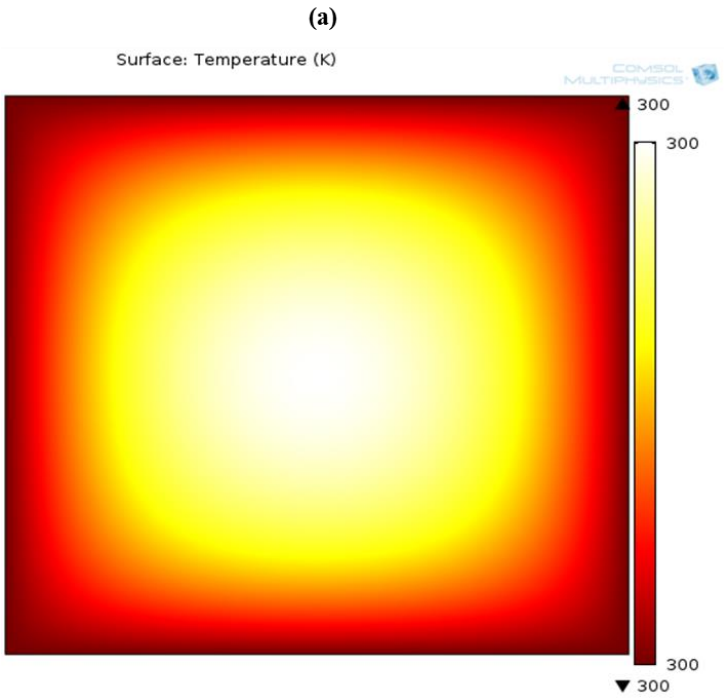

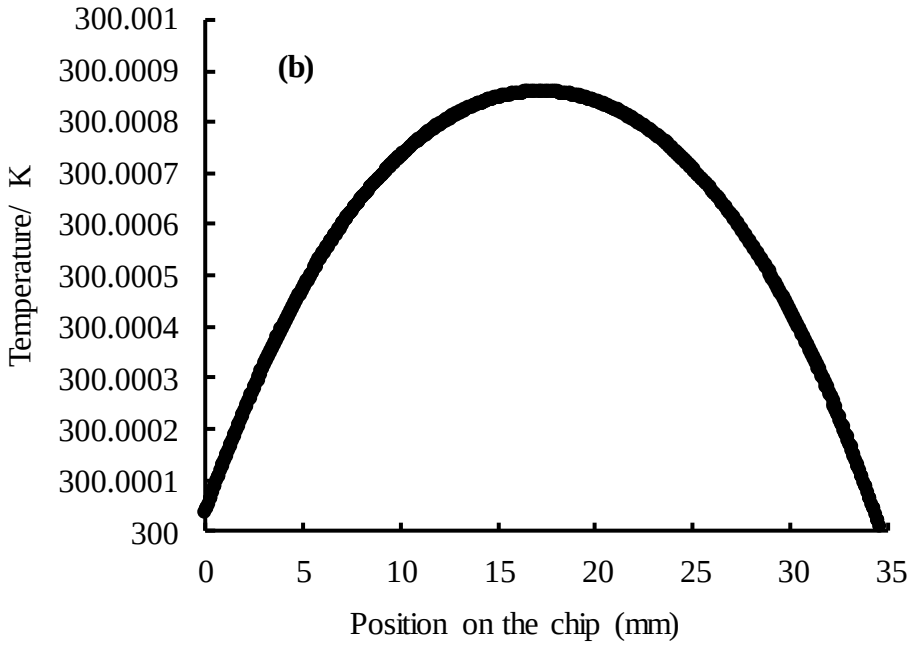

Figure 2.4: (a) Image showing the surface temperature on whole screening chip (35 mm x 35 mm x 0.45 mm), **(b)** illustrates the temperature profiles across the chip. The simulation chip temperature was 300 K and the experimental power of 1.064 x 10^{-3} J s^{-1} mm^{-2}.

F**igure 2.5** shows the simulated surface temperature and cross-section temperature distribution on a square silicon nitride membrane of 1.2 mm x 1.2 mm x 0.6 μm at 300 K from experimentally determined power of 3.15 x 10^{-4} J s^{-1} mm^{-2} which gave the TOF of 4.355 s^{-1}, (specific mass activity = 4.281 x 10^{-4} mol_{CO} conv. g^{-1}Au mm^{-2} s^{-1}).

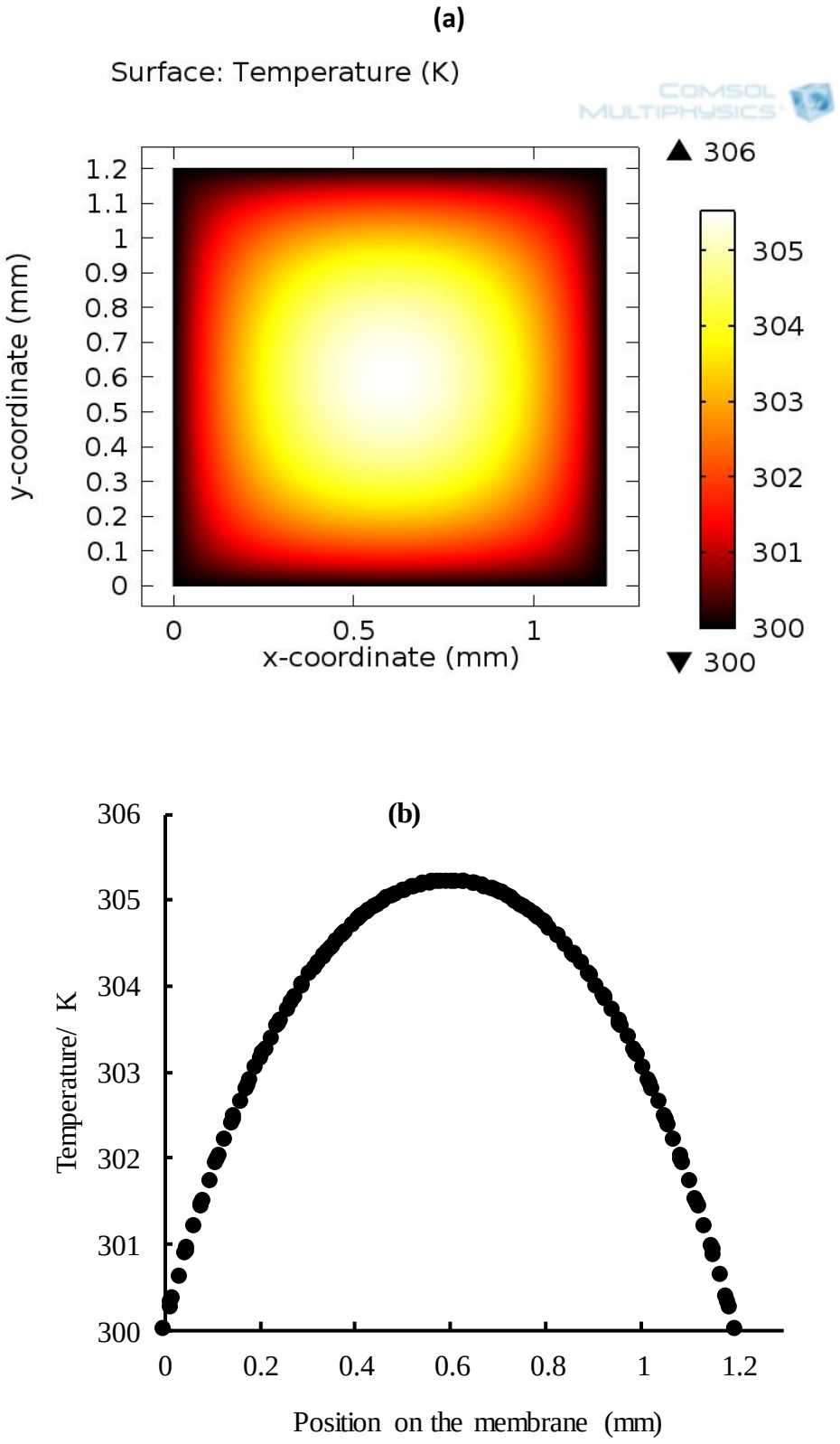

Figure 2.5: (a) Image showing the surface temperature on a 1.2 mm x 1.2 mm x 0.6 µm silicon nitride membrane, **(b)** illustrates the temperature profiles across the membrane. The simulation membrane temperature was 300 K and experimental determined power of 3.15 x 10^{-4} J s^{-1} mm^{-2}.

Figure 2.6 is the surface temperature and cross-section temperature distribution on a square silicon nitride membrane of 1.5 mm x 1.5 mm x 0.6 µm for 1.122 x 10^{-4} J s^{-1} mm^{-2} at 300 K. The TOF was 1.558 s^{-1}, (specific mass activity = 6.61 x 10^{-4} mol_{CO} conv. g^{-1}Au mm^{-2} s^{-1}).

(a)

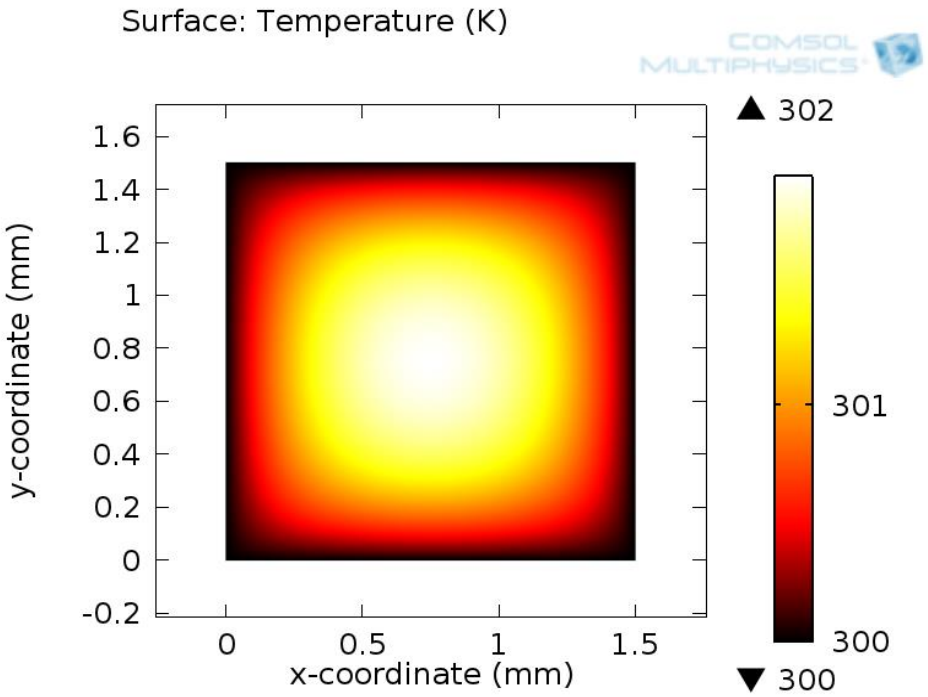

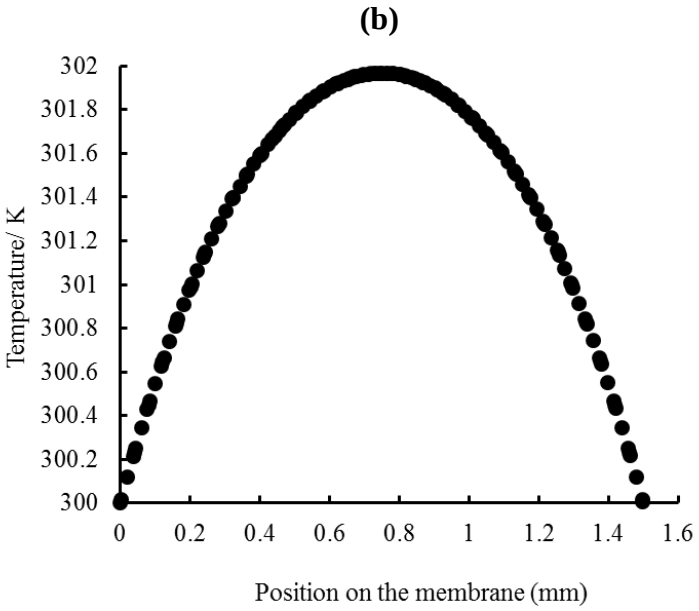

Figure 2.6: (a) Image showing the surface temperature on a1.5 mm x 1.5 mm x 0.6 μm silicon nitride membrane, **(b)** illustrates the temperature profiles across the membrane. The simulation membrane temperature was 300 K and experimentally determined power of 1.22 x 10^4 J s^{-1} mm^{-2}.

2.5 High Throughput Screening Chip Design and Fabrication

The use of combinatorial methods in catalysis research is growing rapidly. The availability of a reliable high throughput method for the fast screening of catalytic activity is crucial.[29] The HT-PVD methodology was applied in the synthesis of supported Pt and Au particle catalysts libraries as described in previous sections. A new catalyst screening methodology for solid/gas-phase reactions was developed and provides a way to study the activity behaviour of supported nanoparticle catalysts when combined with a high throughput infrared thermography technique. A high throughput heterogeneous catalyst screening chip was fabricated by Mir Enterprises Ltd, London. The screening chip is made up of multiple areas of LP-CVD silicon nitride membranes on a silicon substrate which is back-etched to facilitate an infra-red thermal imaging of heterogeneous catalysts activity, **Figure 2.7**.

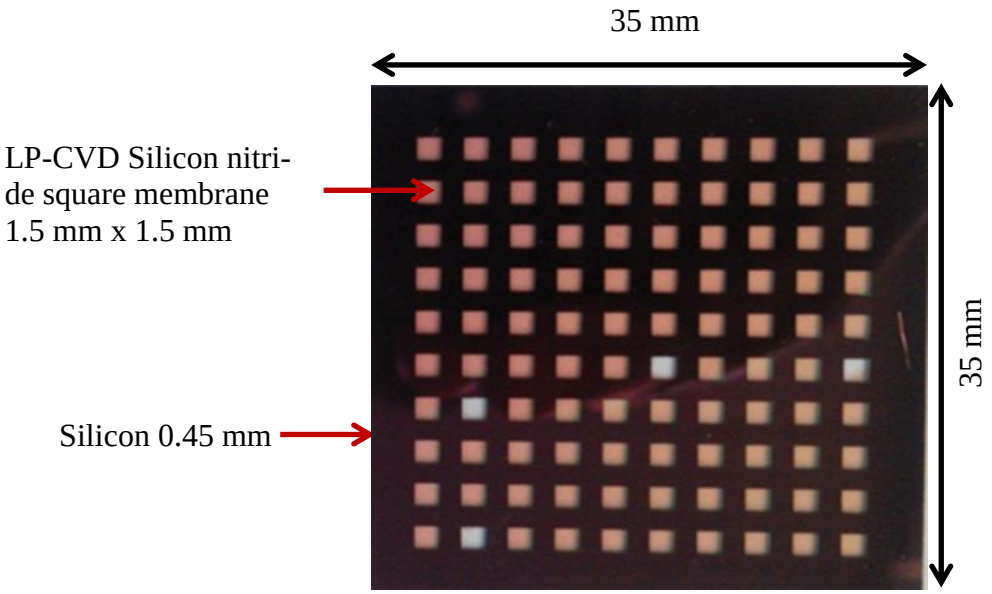

Figure 2.7: A photograph showing the microfabricated high throughput catalysis screening chip for a 10 x 10 array. The small squares indicate transparent silicon nitride membranes after silicon backside wet etching using KOH. The squares appearing grey are where the silicon nitride membrane is broken.

2.5.1 High Throughput Screening Chip Requirements

The footprint of a fabricated silicon chip conforms to the geometry required in relation to the holders and masking system incorporated into the HT-PVD system.[32] The newly fabricated heterogeneous catalysis screening chip has the following qualities:

- Sufficiently thin membranes to reduce heat conduction of the support so that heat generated would result in a sufficient temperature to be observed with existing IR thermal camera (*ca.* > 0.1 K).
- The heat capacity was also required to be as low as possible (the same reason as above).
- The field size had to be sufficiently large to measure the temperature rise with the resolution of the existing thermal imaging camera, while imaging the all of the fields simultaneously.
- Suitably robust to avoid membrane breakage during normal usage. Very thin membranes are susceptible to breakage during processing and even during device

usage, therefore membrane thickness has to be optimized. Therefore a silicon nitride membrane made via LP-CVD is desired.

- Membranes with capability to withstand a base temperature of up to 600 ^{o}C.
- Size compatible with high throughput synthesis system (35 mm x 35 mm).
- Support sufficiently robust for measurements.

2.5.2 High Throughput Screening Chip Masks and Lithography

The requirements of a MEMS device fabrication process sequence involve one or more mechanical processes to micromachine the materials. The selection of a micromachining process begins with a design of the device, detailing the dimensions and tolerances desired which are used to make a photomask. A mask is crucial as it contains the pattern of a device to be fabricated. The mask used to produce a high throughput catalysis screening chip was designed using Tanner EDA L-Edit software provided by the University of Southampton. The mask designed is shown in **Figure 2.8** on a 6″ silicon wafer.

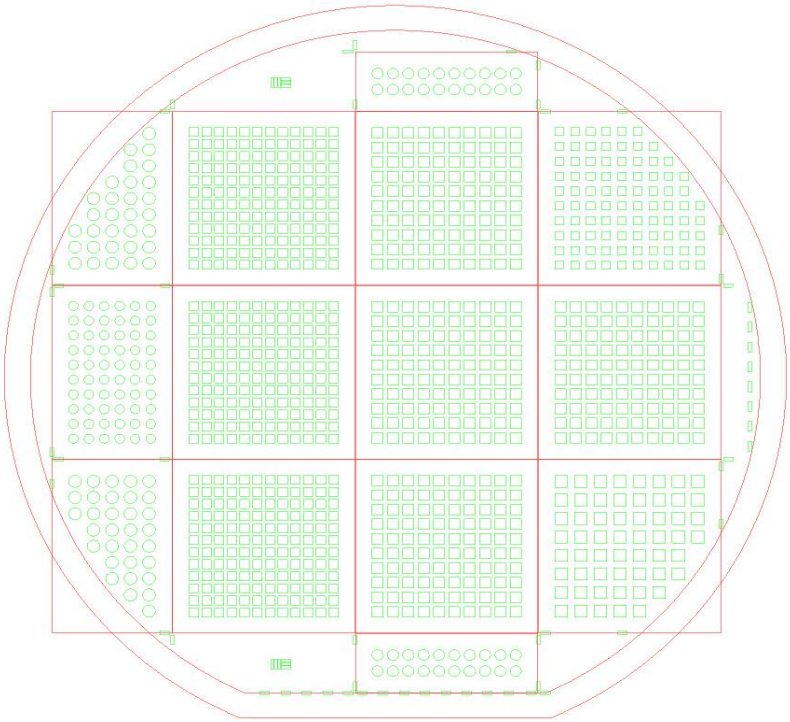

Figure 2.8: Silicon backside etching mask design showing screening chips layout on a 6″ silicon wafer. Green squares and circles represent silicon nitride membranes.

The micromachining process starts with a lithography process, an optical technique used to transfer a pattern from a mask onto a resist coated surface of a solid material such as a silicon wafer.[155] Lithography uses a photoresist material, a light sensitive material commonly applied in industrial processes, for patterning onto a surface of a material. Before resist coating a silicon substrate, a thin layer of oxide is grown on a wafer surface by heating the silicon wafer between 900 and 1150 ^{o}C in a humidified oxygen flow. The oxide formed can act as a mask in a following wet etch process.[155] A photograph of a silicon wafer after the lithographic process is shown in **Figure 2.9**.

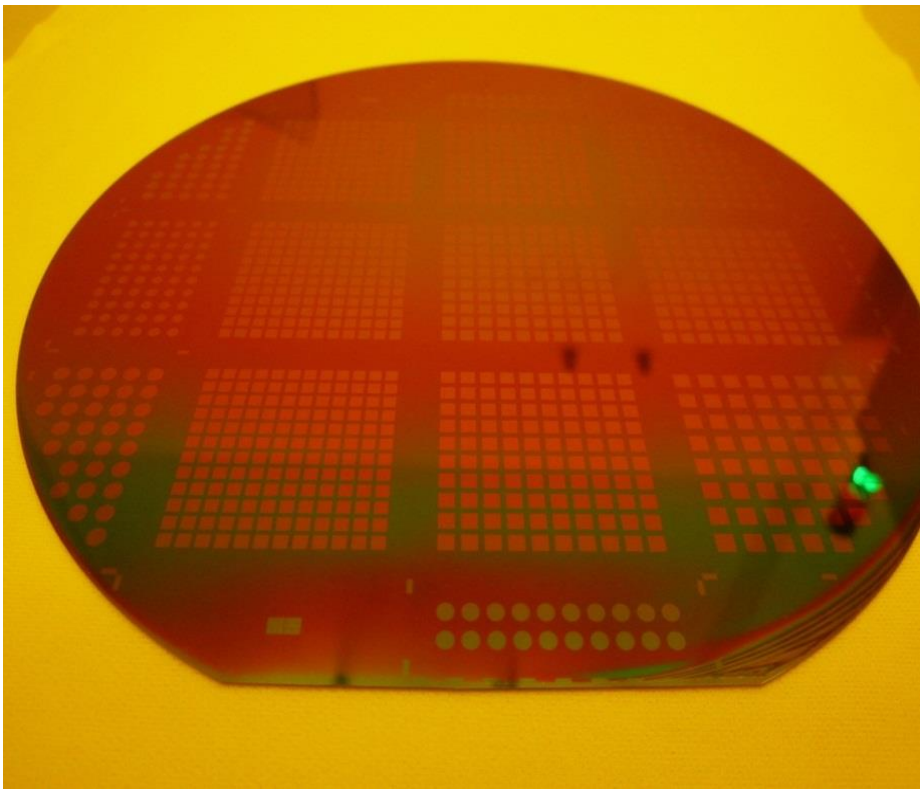

Figure 2.9: Photograph showing the screening chips after the mask was transferred onto a silicon wafer on the backside by a lithography process at a magnification of 250 µm. Squares and circles show the positions of the silicon nitride membranes where etching will be effective.

2.5.3 High Throughput Screening Chip Arrays

The standard screening chip dimensions of the newly designed screening chip are 35.02 mm x 35.02 mm with a tolerance of ± 0.01 mm for the outer chip dimensions and the active fabrication area of 28 mm x 28 mm on the membranes side. Two membrane

thicknesses were fabricated, 300 nm & 600 nm on a silicon substrate of 0.45 mm thick. Two membrane sizes were designed, 1.5 mm x 1.5 mm for a 10 x 10 array and 1.2 mm x 1.2 mm for a 12 x 12 array, **Figure 2.10 (a)** & **(b)**. Dimensions are given in millimetres and square fields represent transparent silicon nitride membranes after back etching of the silicon substrate.

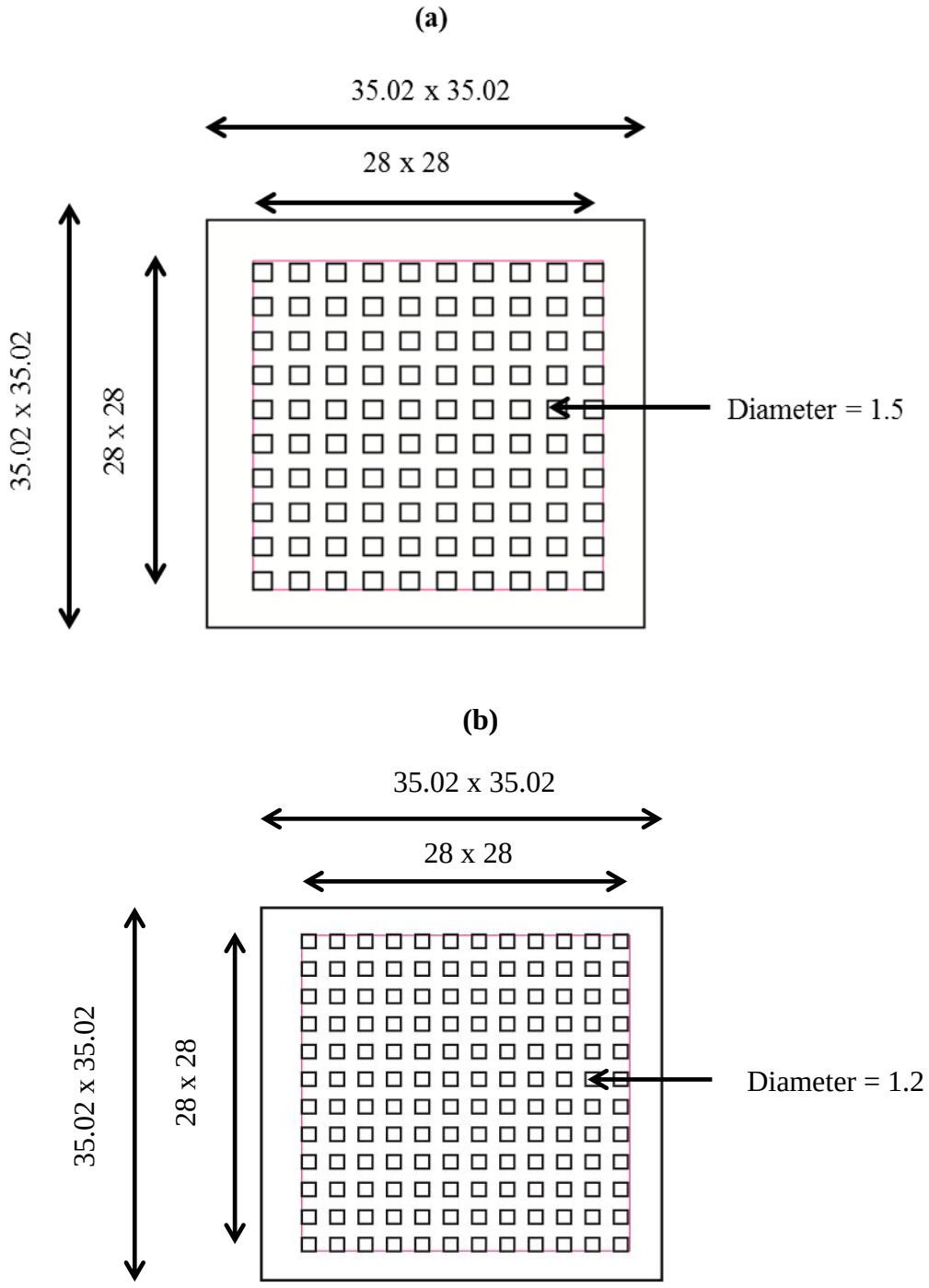

Figure 2.10: Designed catalysis screening chip dimensions for **(a)** 10 x 10 chip array, **(b)** 12 x 12 chip array. Squares represent LP-CVD silicon nitride membranes. All dimensions shown are in millimetres.

Figure 2.11 represents the geometrical considerations involved during the catalysis screening chip mask design. An anisotropic silicon substrate etched by KOH was considered, a 10 x 10 array is demonstrated, and similar considerations apply for a 12 x 12 array. All measurements are given in millimetres. **Table 2.1** presents the membrane parameters on both the membrane side and the reverse side of the silicon nitride membranes.

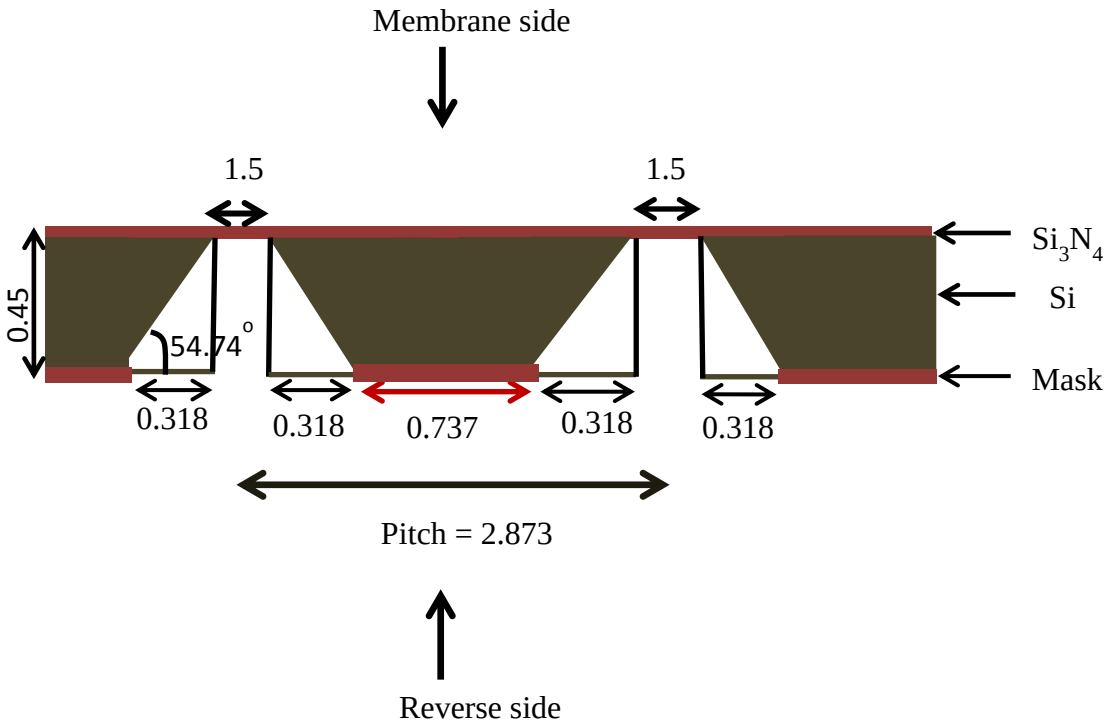

Figure 2.11: A schematic diagram illustrating the mask designing process for the microfabrication of a catalysis screening chip, with transparent silicon nitride membranes via wet anisotropic etching of silicon substrate by KOH. The architecture and dimensions have been given both on the membrane side and reverse side.

Membrane type	Array	Membrane size (mm)	Reverse side (mm)	Array pitch (mm)
Square	12 x 12	1.2 x 1.2	1.836 x 1.836	2.469
Square	10 x 10	1.5 x 1.5	2.136 x 2.136	2.873

Table 2.1: Device description in the mask designing process providing the dimensions of a high throughput catalysis screening chip. Array pitch is the distance from the centre to centre of neighbouring membranes on the reverse side of the chip.

2.5.4 High Throughput Screening Chip Backside Silicon Substrate Wet Etching

Backside wet etching of the silicon substrate with LP-CVD grown silicon nitride membrane on top was undertaken using KOH etchant. Wet etching techniques are widely used in micro-fabrication because of their low cost, high throughput and good selectivity.[160] The capability to micro-machine membranes by wet anisotropic etching of silicon is vital in MEMS system device fabrication.[160] Wet etching of silicon using KOH is favoured in bulk micromachining methods because it is safer to use compared to ethylenediamine-pyrocatechal and water.[160]

The etching mask was designed to incorporate the effect of anisotropic etching of silicon aligned with (111) planes from a (100) surface plane which forms 54.74 degrees from the surface and produces a V-shaped groove resulting in the formation of a square membrane of a pre-determined size, **Figure 2.12**.

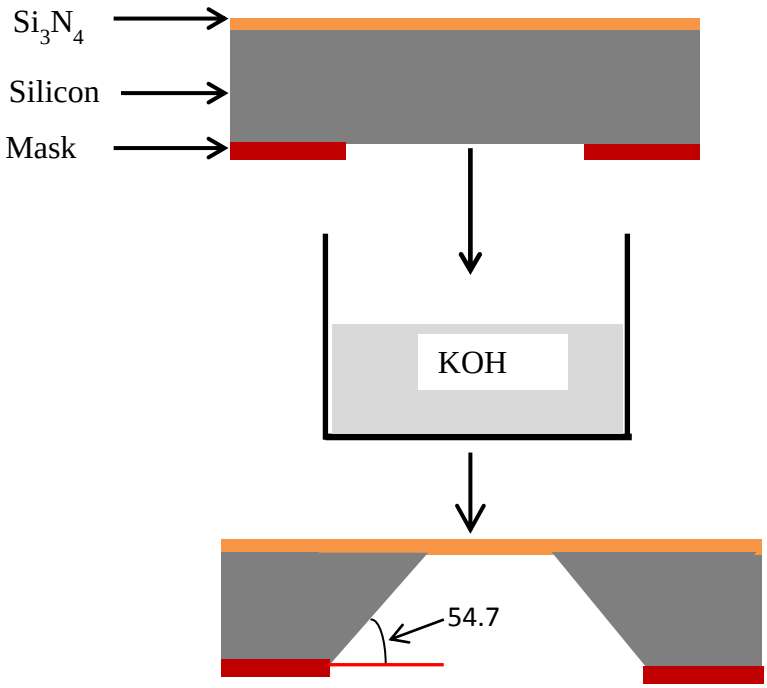

Figure 2.12: Wet anisotropic silicon backside etching by using KOH etchant to form the square membrane. The deviation from the square pattern on the reverse side is shown.[153]

Since the angle formed as a result of wet anisotropic etching of silicon and the silicon substrate thickness are known, the size of the window on the backside of the membrane is determined from equation **2.8**.

Membrane window size = $2tan\theta + L$ Equation 2.8

where ***L***, is the pre-determined membrane size in millimetres and **θ** is an anisotropic etching angle.

Figure 2.13 (a) shows a backside etched silicon wafer and **Figure 2.13 (b)** is a photo-graph of the screening chips on the silicon wafer after the etching process has been completed.

(a)

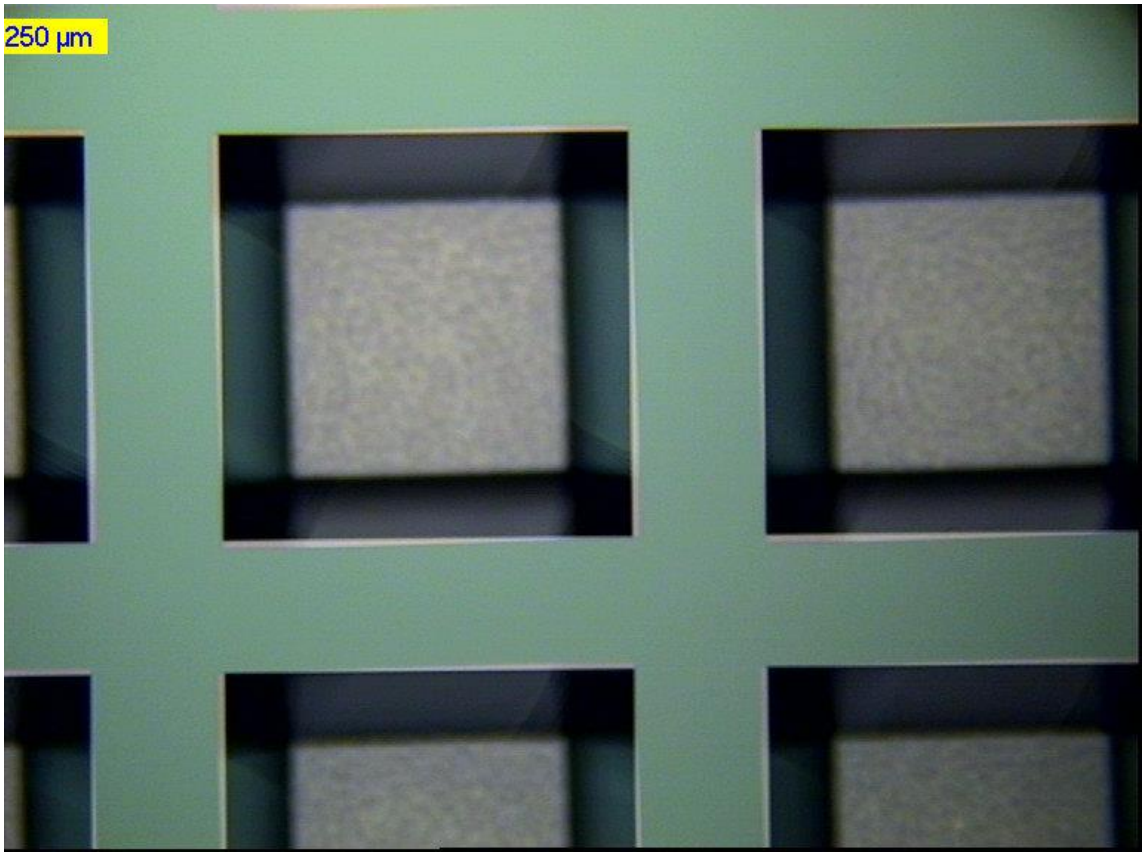

(b)

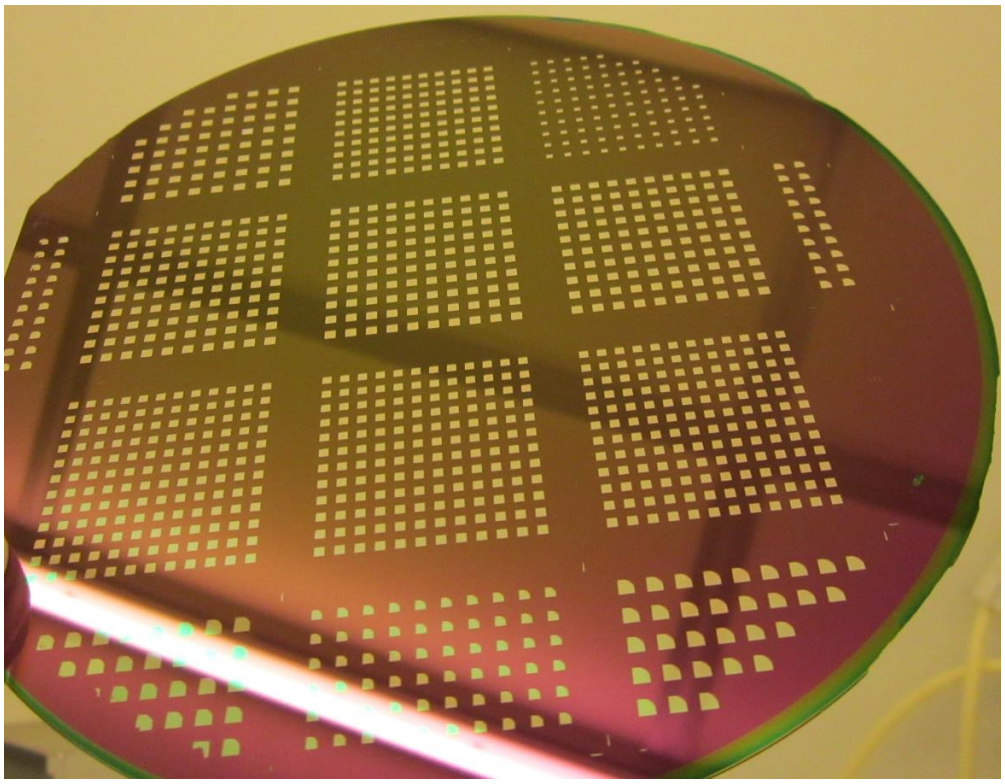

Figure 2.13: (a) A photograph showing backside etched silicon substrate to produce silicon nitride membranes. **(b)** Shows the chips on a silicon wafer after the etching process has been completed. Squares indicate transparent silicon nitride membranes.

Following the completion of the etching process, the silicon wafer is diced into individual high throughput catalysis screening chips 35 x 35 mm in size, ready for catalyst material libraries synthesis using a HT-PVD technique. **Figure 2.14 (a)** & **(b)** present the finished micro-fabricated screening chips for both arrays. Square transparent silicon nitride membranes are evident from anisotropic wet etching of silicon substrate.

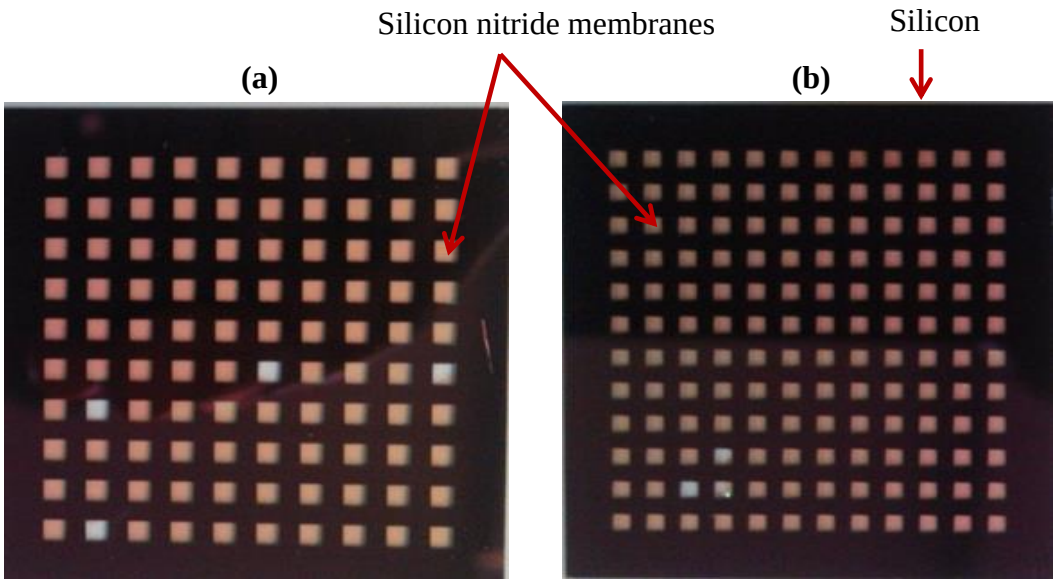

Figure 2.14: A photograph showing the microfabricated high throughput catalysis screening chips. **(a)** Shows a 10 x 10 array and **(b)** is a 12 x 12 array. The small squares indicate transparent silicon nitride membranes after silicon backside wet etching using KOH. The squares appearing grey are where the silicon nitride membrane is broken.

2.6 The MEMS Membranes and IRT Temperature Calibration

Quasi-parallel methods such as spatially resolved mass spectrometry are time consuming in screening, especially with increasing numbers of samples.[133] On the other hand, an IRT technique which measures heat production on the surface of a catalyst is a parallel technique and its screening time is independent of the number of samples on a library. This technique has been applied effectively to the solid/gas-phase reactions as described previously. The emissivity correction improves the reliability for the temperature resolution. However, parallel and sequential reactions for some reactions present a significant challenge to the quantification of catalytic activity on the library using IRT, because the heat increase can not be attributed to a higher catalytic activity, but instead to an increase in the number of side reactions. Selective oxidation is an example of such an issue where combustion is the undesired side reaction which leads to an intensive heat signal.[29] When sequential or side reactions are omitted, for instance in the CO oxidation reaction, signal quantification has a significant beneficial effect on correcting the signal from the CO oxidation reaction. This makes ecIRT a useful technique for activity screening since the heat produced becomes proportional to the enthalpy of the reaction

studied. Since the heat produced is unmeasurable directly, it is calculated from the observed emission variations recorded by ecIRT which is converted into surface temperature.

To measure the heat of reaction, calibration of the IR pixel sensitivity is necessary, due to the inhomogeneity of detector responses, a problem for all high resolution FPA-IR cameras. This is usually carried out by measuring an approximate black body radiator at different temperatures. As the black body has an emissivity of approximately 1 at each point, the differences in the detector pixel sensitivities are electronically corrected by the DSP unit using correction data calculated from calibration images taken prior to experimental measurements.[133] Calibration of the silicon nitride membrane temperature was carried out using an IR thermal camera (Jade III, CEDIP, Paris). The heated membranes on the screening chip were carbon coated (GRAPHIT 33) on both the membrane and reverse side and were heated in a narrow temperature window spanning the experimental temperature range. The temperature of the membranes was recorded by both the IR thermal camera and a K-type thermocouple under vacuum conditions. By this procedure, emissivity correction, individual sensitivities of the detector pixel and temperature homogeneity across the substrate were calibrated. The membrane was heated to 250 ^{o}C and its temperature was measured by IR thermal camera alongside the thermocouple directly mounted on the substrate. A linear plot was obtained between the temperature measured by the IR camera and the thermocouple, **Figure 2.15**. During the course of catalyst activity screening, silicon nitride membrane was coated with carbon at the reverse side in order to ensure similar emissivity from a catalyst library.

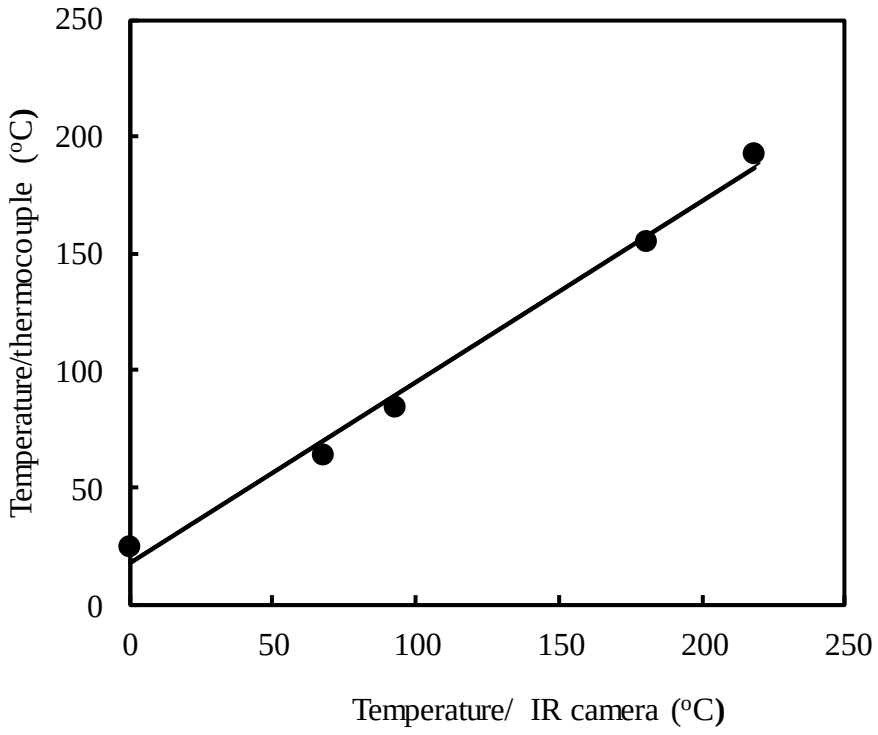

Figure 2.15: Calibration plot for the blank sample, the temperature of the silicon nitride membrane was recorded using an IR camera and the K-type thermocouple directly positioned on the sample. The screening chip was coated with carbon both on the membrane and reverse side.

However, achieving a homogeneous temperature distribution across the catalyst library is very difficult because of the temperature loses at the edges of the chip by conduction. Homogeneous temperature across the library is crucial because of the temperature dependence of chemical reactions,[29] and ensuring that the temperature change measured during the experiment is from the CO oxidation reaction and not an effect of or masked by inhomogeneous heating. Thus, a device capable of efficient library heating is required to achieve a homogeneous temperature across the library. The heating device designed in this work is described in the experimental section. **Figure 2.16** shows the temperature profile for a sample holder heated to approximately 213 °C.

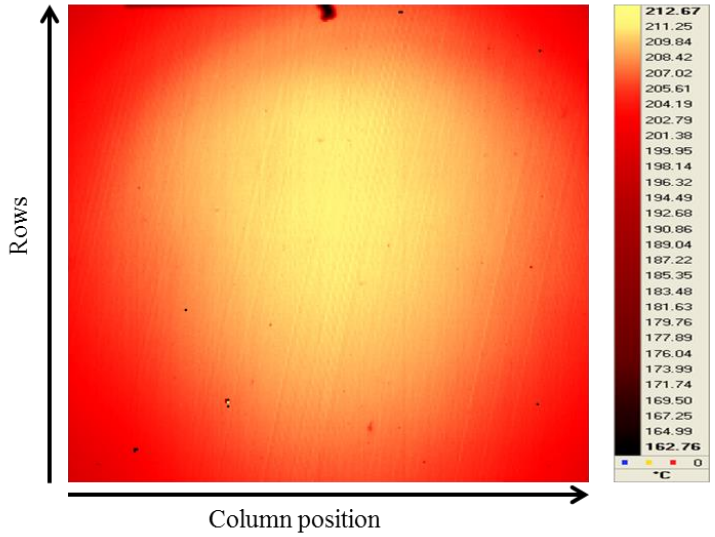

Figure 2.16: IR image showing the sample holder heated to approximately 213 °C. The temperature gradient between the centre and the edges of a sample holder is evident.

Figure 2.17 (a) & **(b)** presents a plot of the temperature gradient across the sample holder. Only a few points on the rows and columns from the edges and centre of the heater were taken as a function of position on the sample holder. The profile indicates the temperature inhomogeneity across the heater with the hottest points in the centre and the coolest fields along the edges of the sample holder.

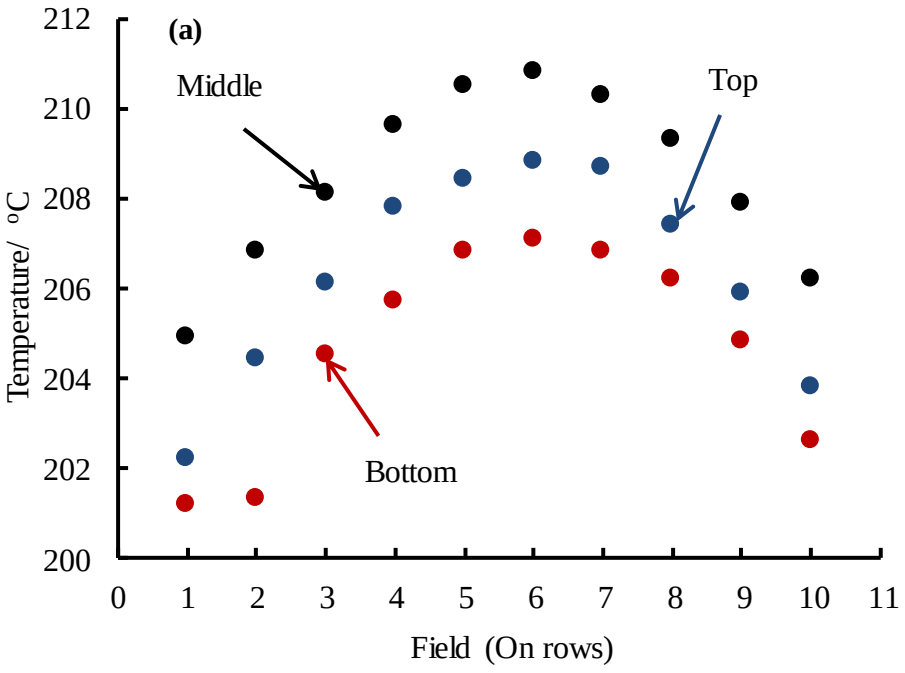

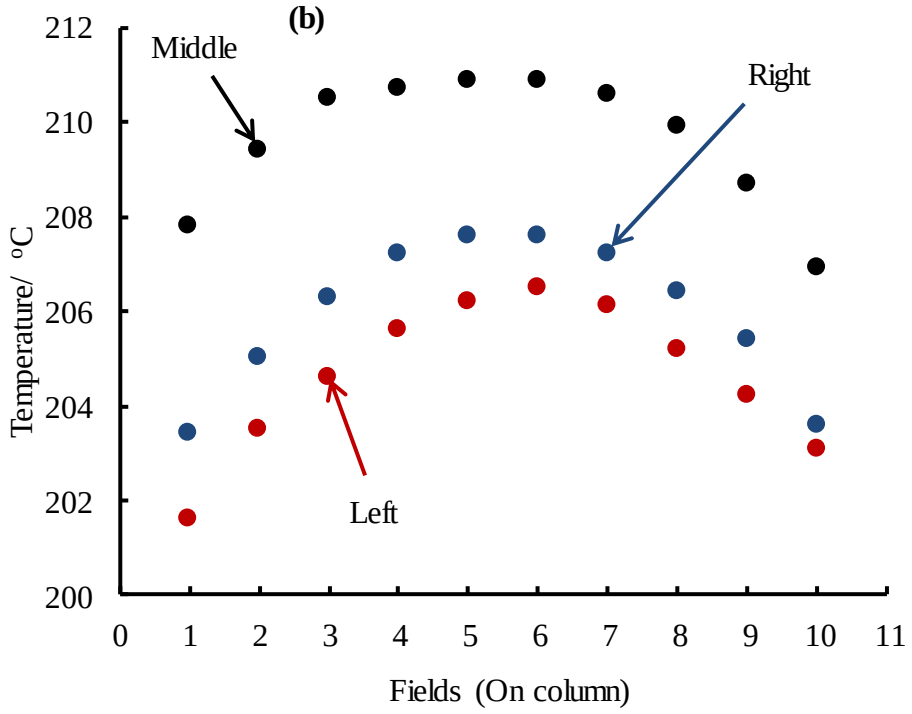

Figure 2.17: A plot of temperature as a function of position on the sample holder. **(a)** Indicates the temperature across the rows and **(b)** is the temperature along the columns. The sample heater was heated to approximately 213 ^{o}C.

Figure 2.18 shows the temperature profile for a screening chip mounted on a holder heated to approximately 190 ^{o}C. **Figure 2.19 (a)** & **(b)** present a plot of the temperature gradient across the screening chip coated with carbon on both the reverse side and membrane side and mounted on the sample heater. Only a few rows and columns from the edges and centre of the chip were selected as a function of position on the screening chip. The profile indicates the temperature inhomogeneity across the screening chip with the hottest fields at the centre and the coolest fields along the edges of the screening chip.

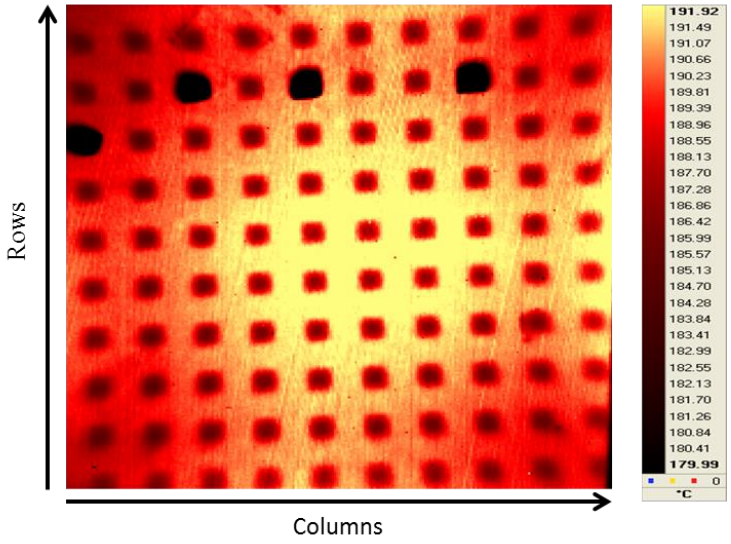

Figure 2.18: IR-thermal image showing a high throughput screening chip mounted on the sample heater and heated to about 190 °C. The chip is made from a silicon nitride membrane which has been coated with carbon on both reverse and membrane side. The temperature gradient between the centre membranes and the edges of a screening chip is evident.

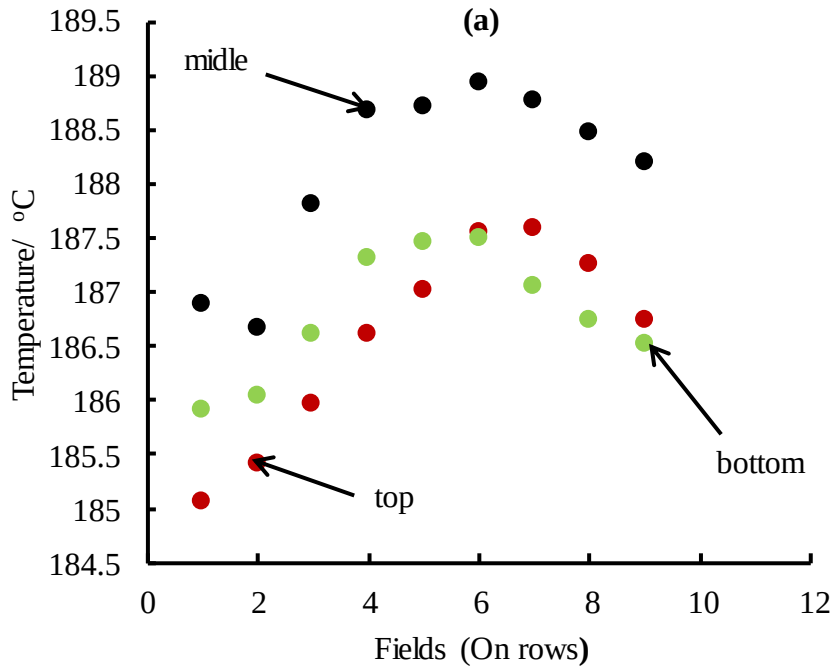

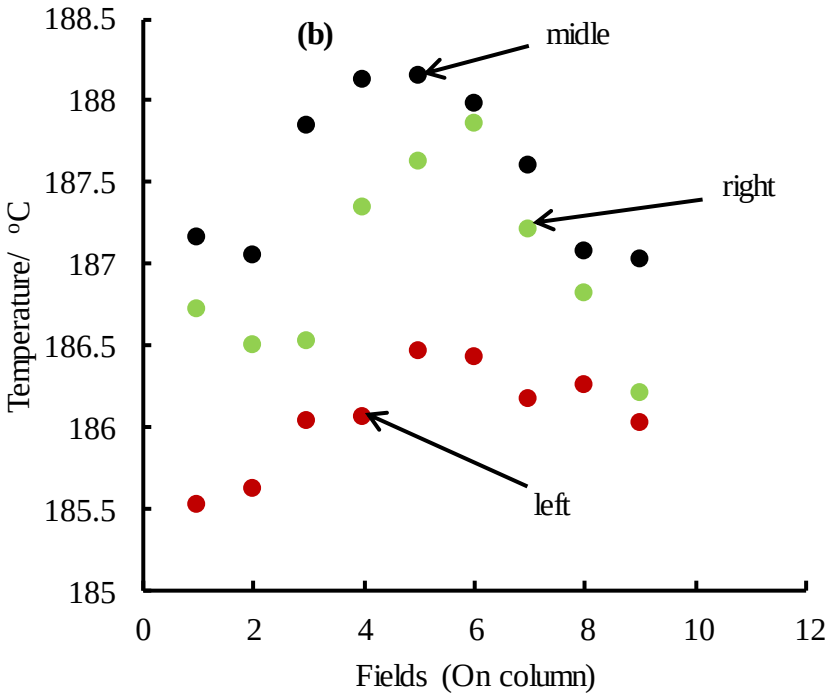

Figure 2.19: A plot of temperature as a function of position on the screening chip. **(a)** Indicates the temperature across the rows and **(b)** is the temperature along the columns. The screening chip was heated to approximately 190 ^{o}C. The temperature gradient across the chip arising from the heating device was about 4 ^{o}C.

The temperature gradient between membranes in the centre compared to the edge was about 4 ^{o}C. This is in agreement with other library heating devices reported elsewhere for primary screening.[29] Therefore, this technique is still reliable for the catalyst activity screening even with a temperature gradient of approximately 4 ^{o}C.

Figure 2.20 shows how the software integrates the IR-thermal images with time on a silicon nitride membrane of a particular area. The pixels are indicated within a square membrane of 1.5 mm x 1.5 mm, and the temperature change on each pixel as recorded by an IR-camera is averaged by the software over time of reactant gases exposure to give an exact average temperature for the whole square membrane. The exact temperature of all square membranes on a screening chip is obtained in the same way.

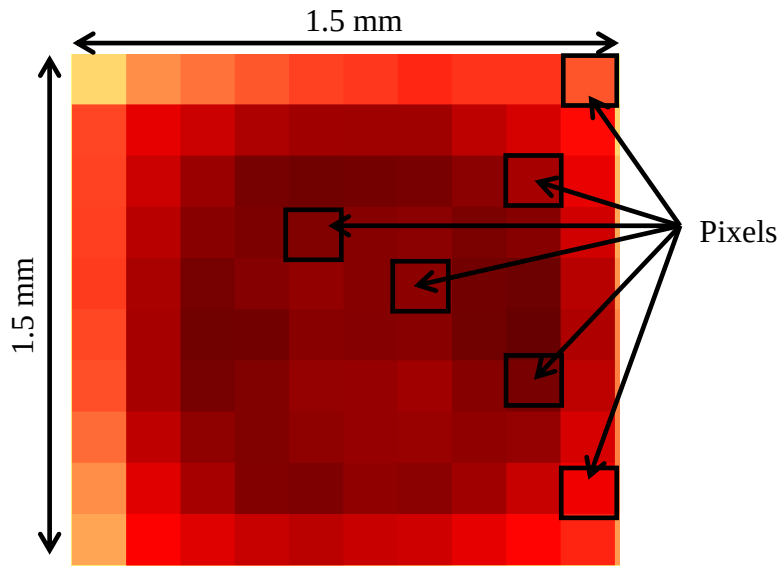

Figure 2.20: IR-thermal image showing the 100 pixels on a silicon nitride membrane of 1.5 mm x 1.5 mm area. All pixels are averaged over time by the IR-thermal camera software to give an exact temperature on a whole membrane.

3. Experimental

This chapter addresses the experimental procedures, techniques and instrumentation that were applied throughout this project for the sample preparation and characterization. General descriptions are given and more specific information is provided in subsequent result chapter.

3.1 High Throughput Physical Vapour Deposition

A high-throughput method based on a high throughput physical vapour deposition (HT-PVD) recently established[32] was used to synthesize thin films of TiO_2 and TiO_2 supported platinum and gold nanoparticle catalysts for the CO oxidation reaction at low reaction temperatures. This method deposits thin films by condensation of a vaporized material onto a substrate. **Figure 3.1** shows a schematic of HT-PVD system. The system has two separate film growth chambers A and B both for thin film material deposition by physical vapour deposition (PVD), sputtering chamber and a surface analysis chamber (DCA Instruments). All chambers are connected by a series of buffer lines separated by the gate valves. Samples are moved to and from the growth chambers via buffer lines under ultra-high vacuum. The PVD system has a base pressure of $1x10^{-10}$ mbar, which is achieved by a combination of pumps including: Rotary (Varian), turbo molecular (Pfeiffer), ion (Varian), titanium sublimation (Varian), and cryogenic (CTI Cryogenics). Samples are introduced to the system via a load lock which is easily vented and rapidly set back to vacuum condition. The samples are moved along the buffer lines by a trolley and sample pick up mechanisms are incorporated to enable sample changeover from the trolley to the transfer arm, which finally transfers the sample (to and) from the growth chambers. A manipulator is also incorporated in the growth chambers which is used to pick-up the sample from the transfer arm and retains it throughout the material deposition time. Where necessary, the sample on the manipulator can be heated in the temperature range 300 K-1100 K during or after deposition and rotated if required.

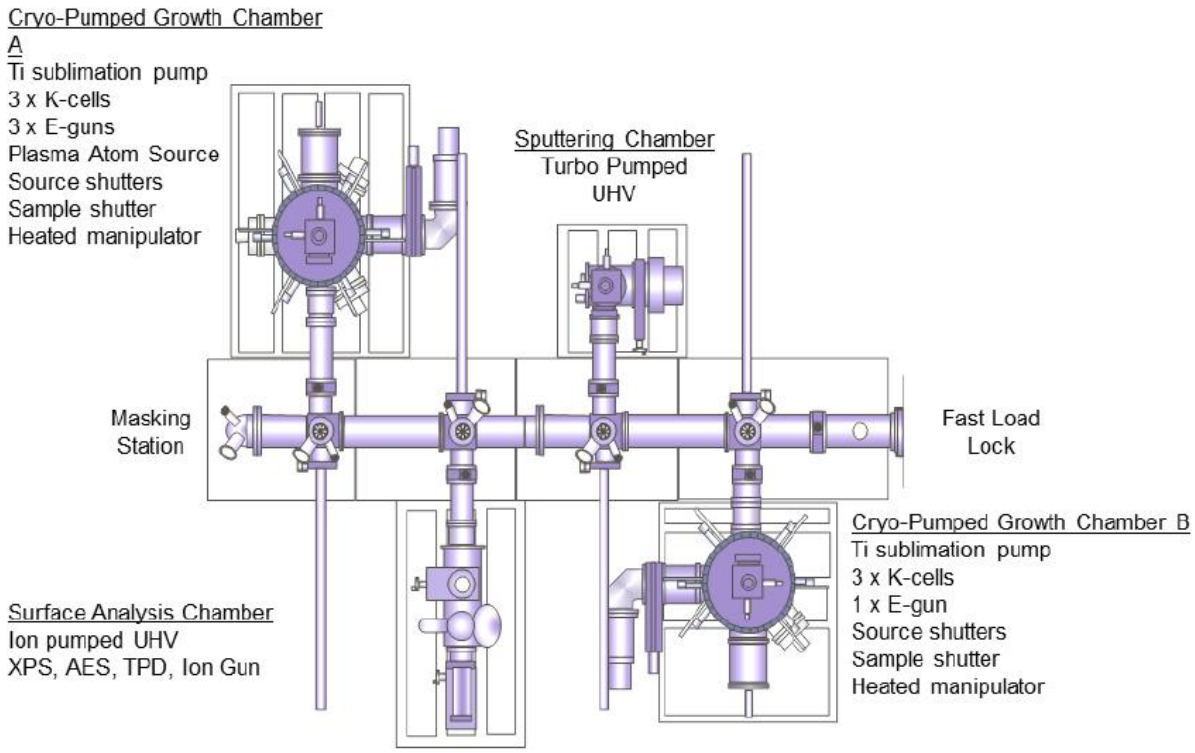

Figure 3.1: Schematic representation of a Physical Vapour Deposition system showing two cryo-pumped thin film growth chambers A and B, sputtering chamber, surface analysis chamber and the load lock.[166]

All samples presented in this work were made using growth chamber A (GCA). This chamber has up to six off-axis sources enabling the simultaneous co-deposition of different materials, **Figure 3.2 (a)** & **(b)**. The sources include three electron beam sources (Temescal) and three Knudsen cells (DCA). The electron beam source uses a beam of electrons to evaporate the source materials, while the Knudsen cell uses a heating filament surrounding a crucible to evaporate the source material. In this work, electron beam sources, E-gun 1 was used to evaporate Ti, and Pt/Au was evaporated from E-gun 3. Growth chamber A has a cryo-pump which maintains ultra-high vacuum. The pump traps gaseous molecules and vapours and condenses them on a surface cooled by compressed helium.

(a)

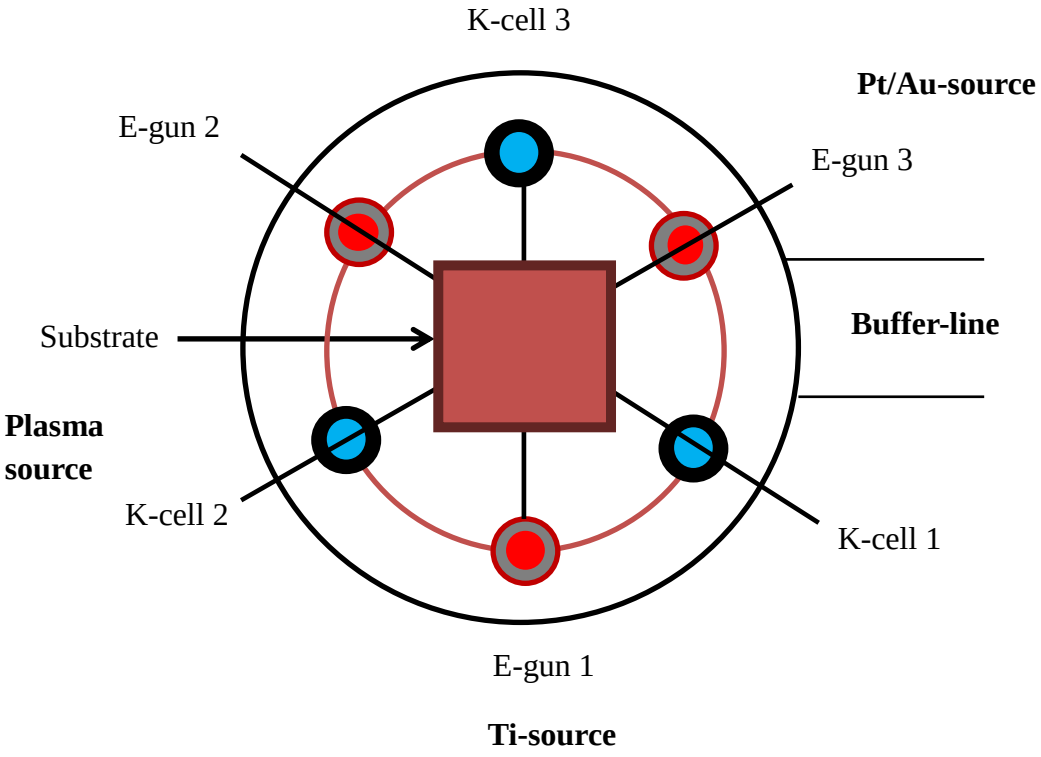

(b)

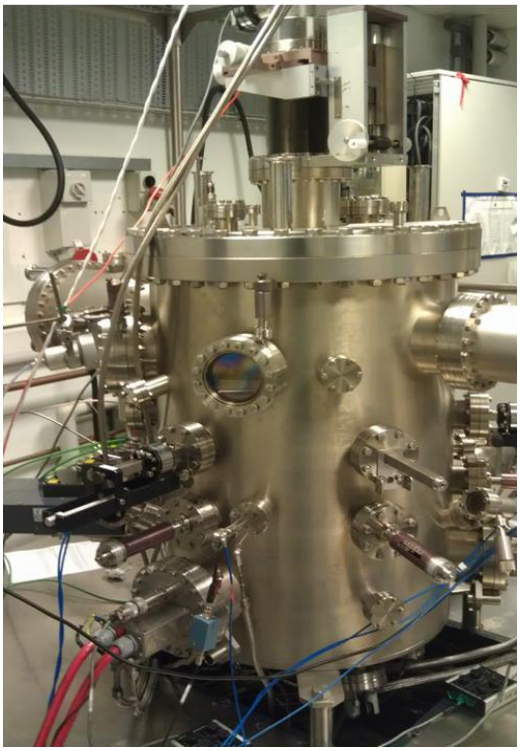

Figure 3.2: (a) Top view of the alignment of the evaporation sources in the HT-PVD chamber A in which all samples in this work were prepared,[92] **(b)** is the HT-PVD growth chamber used.

Each material source operates under both a main shutter and a wedge shutter. The main shutter controls the deposition by moving it out of the material plume permitting the material flux to get onto the substrate. A wedge shutter, on the other hand, is located directly above the source material and can be used to alter the material flux towards the substrate, as it can be moved in or out of the evaporated material plume using a linear drive actuator. In this work, a wedge shutter was not applied during sample preparation (completely out of the material plume) because only the main shutter was required to control the growth of various particle sizes on a substrate.

3.1.1 Deposition Calibration and Sample Deposition

3.1.1.1 Catalyst Material Support: Titanium Dioxide

A titanium dioxide layer was deposited onto a silicon square substrate covered with a 10 x 10 array contact mask in order to establish the titanium dioxide layer thickness as a function of deposition time, at a deposition rate of 4 Å/s. The thickness of titanium dioxide deposited increased with deposition time as established by AFM measurements, **Figure 3.3**. The titanium deposition rate from E-gun 1 was maintained at 4 Å/s during the calibration process with the plasma source, P_{rf} = 300 W, oxygen flow rate of 1 sccm and an oxygen pressure of 9.7 x 10^{-6} Torr during film synthesis. The chamber pressure was maintained at 3.6 x 10^{-6} Torr (ion gauge) by a constant inlet of oxygen into the deposition chamber. Contact masks were used to constrain the material to unmasked areas of the substrate during material synthesis. Contact masks were used to expose 100 or 144 squares on the silicon nitride membrane on a screening chip where the titanium layer was later deposited. Titanium dioxide layers of approximately 200 nm thickness were synthesized, the thickness was determined by AFM. The substrate was kept at room temperature during deposition.

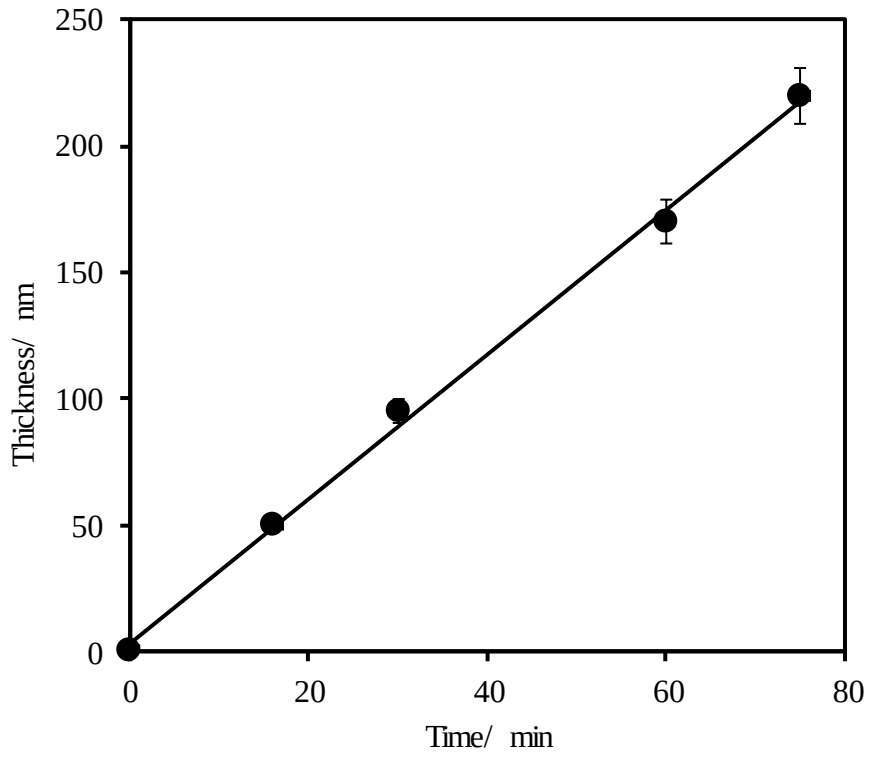

Figure 3.3: Calibration plot used for titanium dioxide layer synthesis showing thickness as a function of time. Deposition rate used was 4 Å/s, with an oxygen flow rate of 1 sccm and a P_{rf} of 300 W.

3.1.1.2 Synthesis of Amorphous Titanium Dioxide Layers

Titanium dioxide layers were first deposited onto silicon and silicon nitride covered silicon substrate for AFM and XRD measurements respectively, using titanium (99.995 %, Alfa Aesar metals) from E-gun 1 and oxygen (Air products, special gases, 99.999 %) at a constant pressure of 9.7 x 10^{-6} Torr at 1 sccm oxygen flow rate and plasma source, P_{rf} = 300 W and deposition rate of 4 Å/s. The substrate was kept at room temperature during film synthesis.

For material screening purposes, titanium dioxide films of approximately 200 nm was deposited on a 10 x 10 and a 12 x 12 array micro-fabricated catalyst screening chip (450 µm silicon wafer thickness) on which a low pressure chemical vapour deposited (LP-CVD) silicon nitride membrane has been deposited. The screening chip has been back etched to produce individual membranes. The deposition of titania layers was carried

out at the same deposition conditions described above. The substrate was rotated during deposition in order to achieve a homogeneous film thickness across the substrate.

3.1.2 TEM Specimen

For particle size characterization and distribution, transmission electron microscopy (TEM) was used. A thin layer of titanium dioxide, 15 nm to 25 nm thick, was deposited onto small carbon coated copper TEM grids (Agar scientific). These grids had TiO_2 deposited under similar deposition conditions as a catalyst screening chip, **Figure 3.4**.

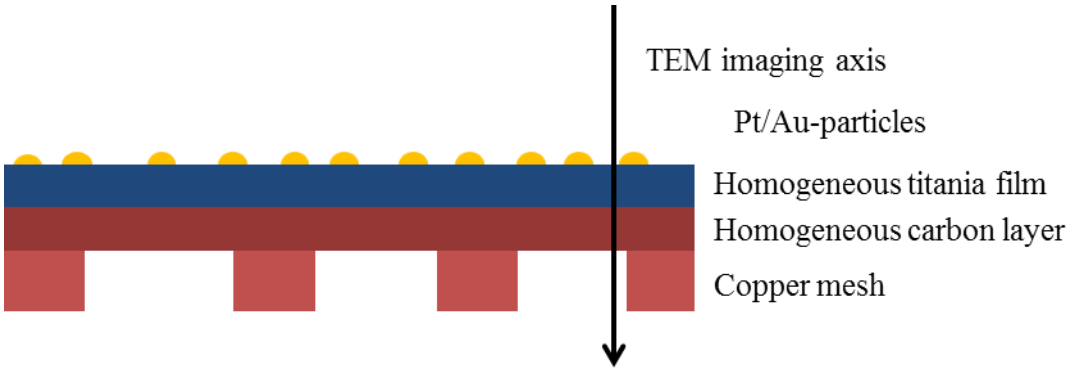

Figure 3.4: Schematic of a transmission electron microscopy specimen. The figure was adapted from reference.[92]

3.1.3 Pt/Au Particles Calibration and Deposition

3.1.3.1 Pt/Au Particles Calibration

To deposit Pt or Au particles onto a screening chip for the purpose of catalyst activity screening, it was necessary to calibrate the materials sources as a function of the main shutter positions for a controlled material synthesis across the substrate. This was done by depositing a thick film of platinum/gold on a glass (SiO_2) substrate using a 10 x10 array contact mask from platinum/gold evaporation source (E-gun 3) while moving the shutter relative to the substrate, to establish the shutter positions for a controlled material deposition. After the shutter positions were established, a thick film of platinum/gold

was deposited onto a silicon square with a 10 x 10 array contact square mask on top, from short to longer deposition times (24 min to 120 min). The main shutter position was used to create five different thicknesses across the array each with two rows having the same thickness in order to establish the particle thicknesses as a function of deposition time at a given deposition rate. The main shutter which is positioned directly below the substrate is used to mask part of the substrate from all material sources and can be moved relative to a substrate as preferred, hence providing a mechanism to control the deposition time of materials across the substrate. Particle thickness was determined by AFM, which established film thickness as a function of deposition time, **Figure 3.5** and **Figure 3.6**, and was then related to platinum/gold monolayers characteristically needed to make Pt/Au particles of 0.4 to 3 monolayers thick. Based on a calibration plot and by computing the estimated thickness of 0.4 to 3 monolayers of platinum/gold, particle deposition times were accurately established for each particle size desired.

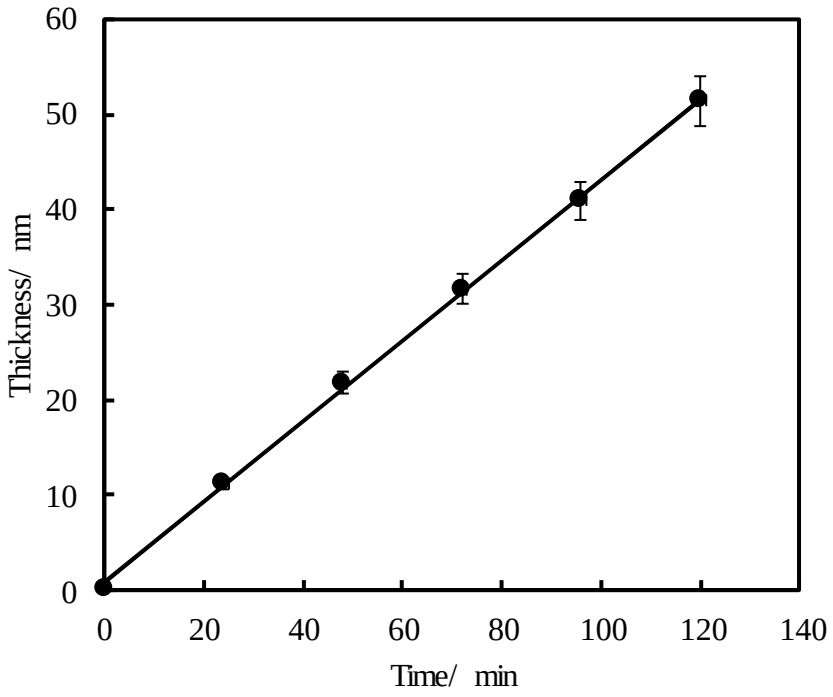

Figure 3.5: Thickness as a function of deposition time plot used for platinum particles calibration. The deposition rate used was 0.4 Å per second.

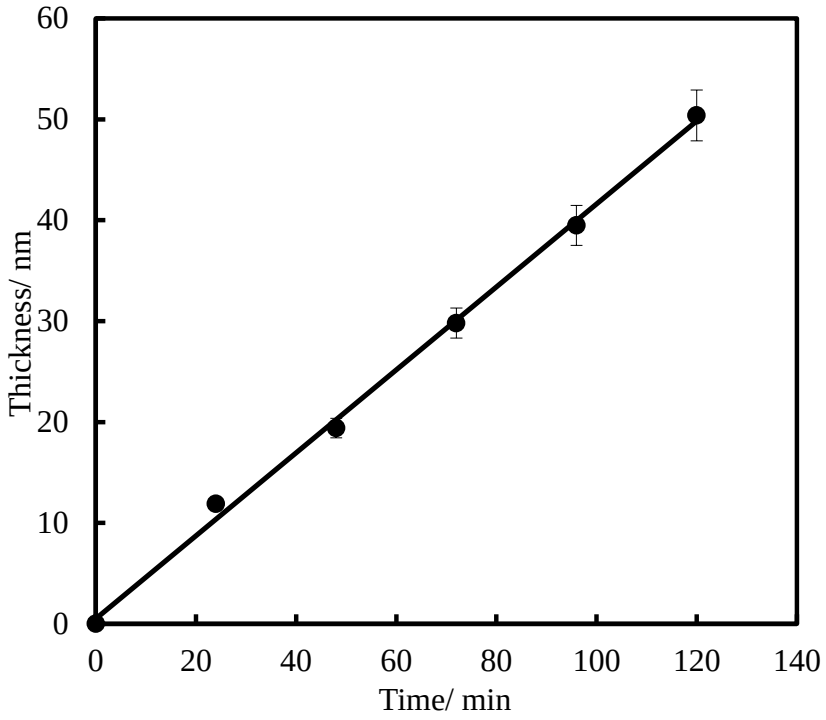

Figure 3.6: A plot of thickness as a function of deposition time used for calibrating the gold particle size. The deposition rate was 0.4 Å per second.

3.1.3.2 Platinum and Gold Particles Deposition

Platinum/gold particles from a platinum/gold source (E-gun 3, **Figure 3.2**) were deposited onto a screening chip on which a titanium dioxide support material has been previously grown using a PVD method. Short deposition times (30 seconds to 6 minutes) were used to achieve small particle sizes across a screening chip, **Figure 3.7**. The chamber pressure of 4.6 x 10^{-8} Torr was maintained during deposition and the deposition rate was 0.15 Å/s as established from particle size calibration.

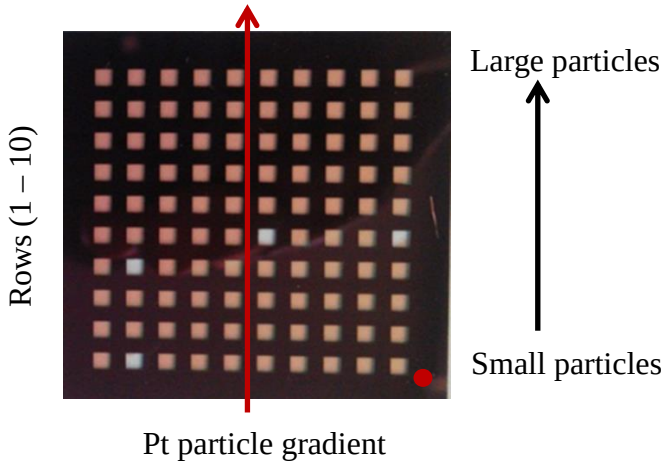

Figure 3.7: Illustration of a 10 x 10 array screening chip showing particle growth direction.

For surface characterization of platinum/gold particles on the titania layer, platinum/gold particles were deposited onto Formvar® carbon coated copper grids (Agar scientific) on which a thin film of titanium dioxide, 15 nm to 25 nm thick has been grown, using the PVD method which was used for TEM analysis. Particle characterization was carried out using TEM before deposition onto the screening chip, to ensure that particles were being synthesized. Particle depositions onto a screening chip were carried out by moving the main shutter to sequentially reveal the screening chip in order to achieve a range of particle sizes across the substrate. The shutter was moved to ten or twelve positions, depending on the screening chip array, so that each row has a different particle size. The relocation of the main shutter relative to the screening chip is shown in **Figure 3.8**.

Particles on TEM samples were made in between the screening chip samples, under similar deposition conditions to ensure accuracy in the determination of particle size distribution on a screening chip. This was necessary as direct analysis of particle sizes on the screening chip was not possible via TEM. The TEM grids were mounted in a holder arranged in a 4 x 4 fashion during deposition, corresponding to row 1, 4, 7 and 10 on the screening chip. This kind of TEM sample deposition enables the mapping of various particle sizes on the screening chip. The screening chips and TEM grids were held at 200 ^{o}C during deposition, this temperature was reported to produce stable particles elsewhere.[15, 166]

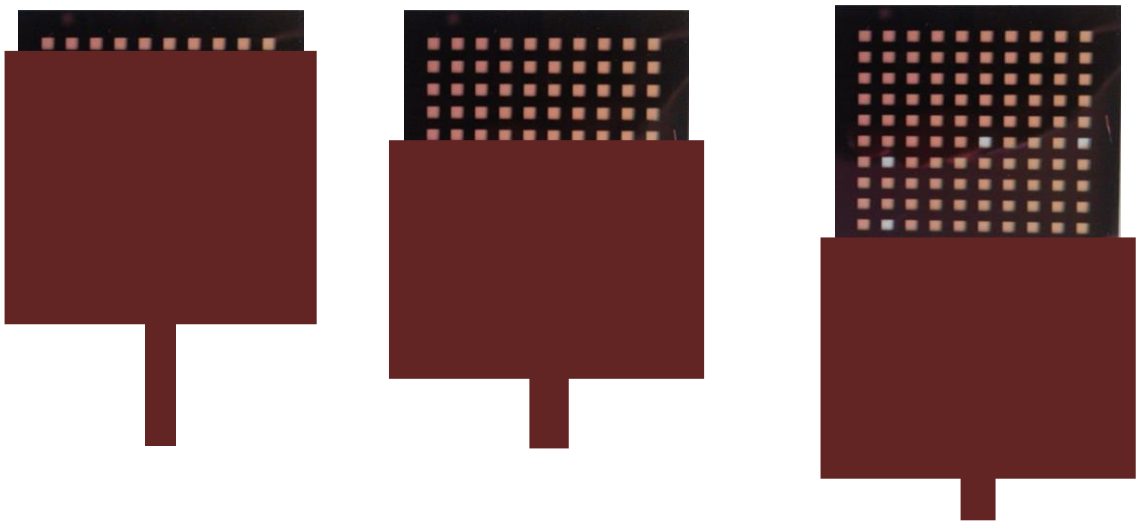

Figure 3.8: Schematic diagram to illustrate the relocation of the main shutter across the screening chip during particle deposition time. The reference dot is on the bottom right.[166]

3.2 Advantages of the Physical Vapour Deposition System

A HT-PVD system used in this work for sample preparations has been addressed in the former sections of this chapter and its suitability towards the synthesis of thin film material libraries has been discussed. The strengths of using this technique include:

- The control of material synthesis by wedge shutters, main shutter and deposition rate.[32, 167, 168]
- Creation of a material library on a small area substrate, ca 28 mm x 28 mm.[92, 166]
- Reproducibility of deposition conditions to reproduce the material in subsequent synthesis.[92, 143]
- The system can be combined with micro-fabricated arrays/chips of different types for the high throughput synthesis and screening of different materials.[167, 169]
- The system enables the synthesis of both nanoparticles and thin films samples. The application of the main shutter permits the synthesis of metal nanoparticles on the same substrate in a controlled fashion.[33, 166]

- No annealing of samples is needed for material mixing; this permits the synthesis of either amorphous or crystalline solid material libraries.[167]
- Material annealing during or after deposition is possible; this provides thermodynamic phases.[166]
- A plasma source is incorporated to enable the synthesis of oxides, mixed oxides, nitrides and hydrides.[34, 92, 143]
- The sample can be rotated during deposition to achieve a homogeneous thin film across the substrate.[34]

This makes the HT-PVD method more suitable for making samples compared to other techniques where further sample treatment like calcination is often required.

3.3 Surface Analytical Tools

3.3.1 Atomic Force Microscope (AFM)

Atomic Force microscopy (AFM) is a very high resolution type of scanning probe microscopy typically used for surface topography imaging.[166] The AFM consists of a cantilever with a sharp tip (probe) on its end that is used to scan the sample surface. As the tip approaches the sample surface, forces between the tip and the sample result in a deflection of the cantilever. It has a deflection sensor which reflects a laser beam from the back of the cantilever onto a position sensitive photodetector (PSPD), **Figure 3.9**. This technique can be used on non-conducting (insulating) and conducting surfaces.

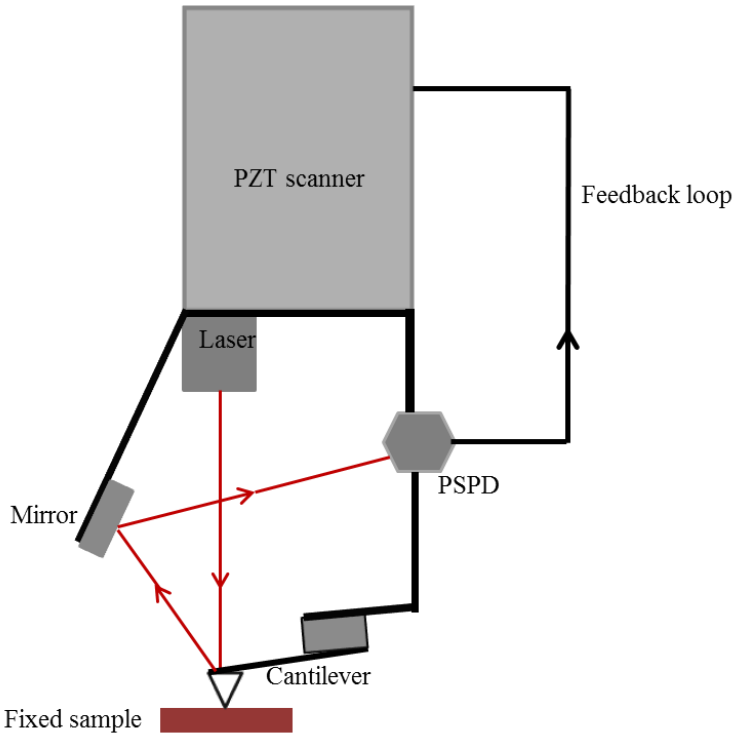

Figure 3.9: Schematic diagram of the AFM showing different parts.[166] A position sensitive photodetector (PSPD) is an optical position sensor that measures the position of a laser beam from the back of the cantilever.

A contact mode was used where the tip is brought onto the sample surface and feels the repulsive forces which deflect the cantilever. The bending of the cantilever shifts the tip from the sample surface causing the laser on PSPD to shift. The cantilever deflection is converted by the software to construct the topographic image of the sample surface. The AFM in this work was used to determine the thickness of titania, Pt and Au films made by the HT-PVD method. The AFM (Vecco Autoprobe M5) instrument was used with a silicon cantilever, resonance frequency of 180 kHz, spring constant of 5Nm^{-1} with an approximate tip (CSC17 probe, MikroMasch) curvature of 10 nm.

3.3.2 X-Ray diffraction (XRD)

X-ray diffraction (XRD) is a technique used to study the structure of a crystalline material, which diffracts a beam of X-rays. The X-ray diffraction results from the constructive interference of a monochromatic X-ray beam with a crystalline material. The scat-

tering of the X-rays is due to the electrons in an atom. Since the crystal structure has atoms positioned in a regular fashion, constructive interference occurs when Bragg's equation is fulfilled,[166] **Figure 3.10**. X-rays from constructive interference are detected together with intensities and the diffraction angle at which they were reflected. A diffractogram unique to the material is produced which leads to the identification of that particular material. In this work, X-ray diffraction was used to characterize a thin film of titania.

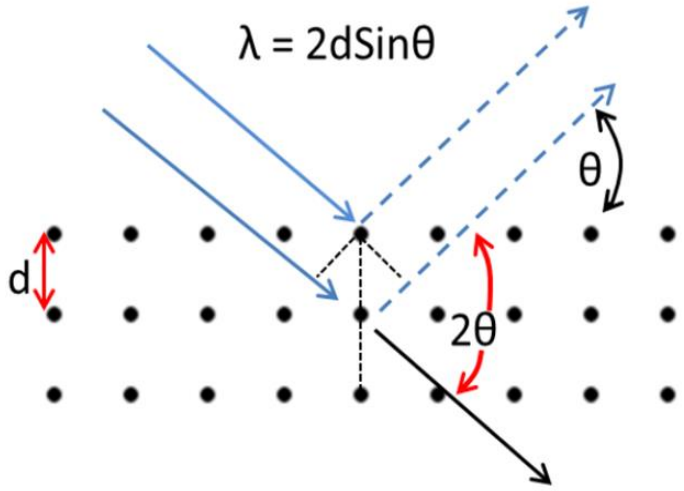

Figure 3.10: Schematic diagram showing X-rays as diffracted by the crystal planes.[166]

A Bruker D8 powder diffractometer with C2 area detector using a Cu $K_{\alpha 1}$ X-ray source was used. The X-ray source was fixed at 11^{o} and the general area detector fixed at 25^{o} allowing the reflections between 15^{o} and 40^{o} (2θ) to be recorded. XRD data presented in this thesis was collected using this set up. The measurements were taken with the help of Louise Hannah.

3.3.3 Transmission Electron Microscope (TEM)

Transmission Electron Microscope (TEM) is a tool with the capability of imaging to the nano-scale, **Figure 3.11**. The TEM uses a tungsten filament to generate a beam of electrons by thermionic emission. An electric potential is used to accelerate the beam of

electrons which is focussed into a coherent beam with the help of the first and second condenser lenses. The beam of electrons is transmitted through an ultra-thin specimen and interacts with the specimen as it travels through and eventually strikes a fluorescent screen or can be detected by a sensor and charge-coupled device (CCD) camera. An image is created from the interaction of the transmitted electrons through the specimen; the image is magnified and focussed onto an imaging device. As a beam of electrons travels through a specimen some of the electrons are scattered and these disappear from the beam. Those electrons which reach the fluorescent screen create a shadow image of the specimen. The apertures are then used to study the specimen, such as selecting a preferred contrast and resolution.

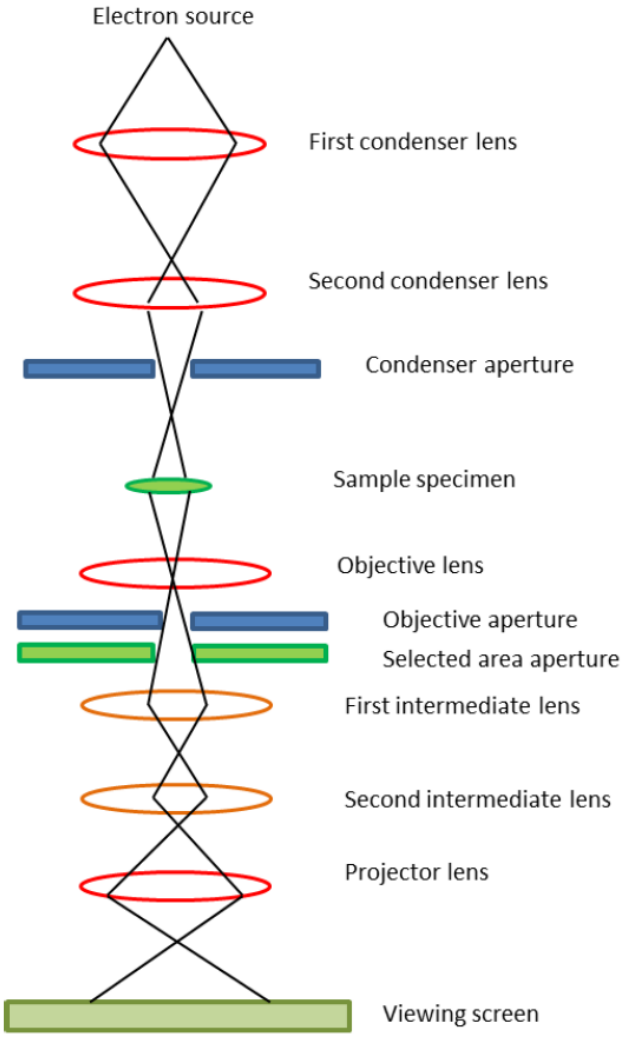

Figure 3.11: Schematic diagram of a transmission electron microscope displaying the main the components.[166]

TEM was used to study the particle morphology and size distribution of the nanoparticles made by a PVD technique. The TEM images were acquired using a Jeol 3010 instrument at an accelerating voltage of 300 kV. A Gatan CCD camera was used to record the images for further processing. Images for Pt nanoparticles were taken with a support of Dr. Jon Davies and Au images were taken with the help of Sandy Kerr. The images were further processed to obtain the particle size and distribution on the titania substrate using Paradise software developed by Ilika Technologies.

3.3.4 X-Ray Photoelectron Spectroscopy (XPS)

X-ray Photoelectron spectroscopy (XPS) is a surface sensitive technique that measures the surface elemental composition.[170] The X-rays are generated by bombarding an anode with high energy electrons. The electrons are obtained from a thermal source, usually in the form of an electrically heated tungsten filament in some focusing X-ray monochromator. The electron energy determines the efficiency of X-ray emission from the anode. Whereas, the XPS anode material determines the energy of X-ray transition generated. The most commonly used anode materials are magnesium and aluminium which are usually supplied in a single X-ray gun with a twin anode configuration providing MgKα or AlKα photons. When an X-ray photon of energy *hv*, hits the surface of the sample material, a photoelectron is ejected from the atom, **Figure 3.12**.

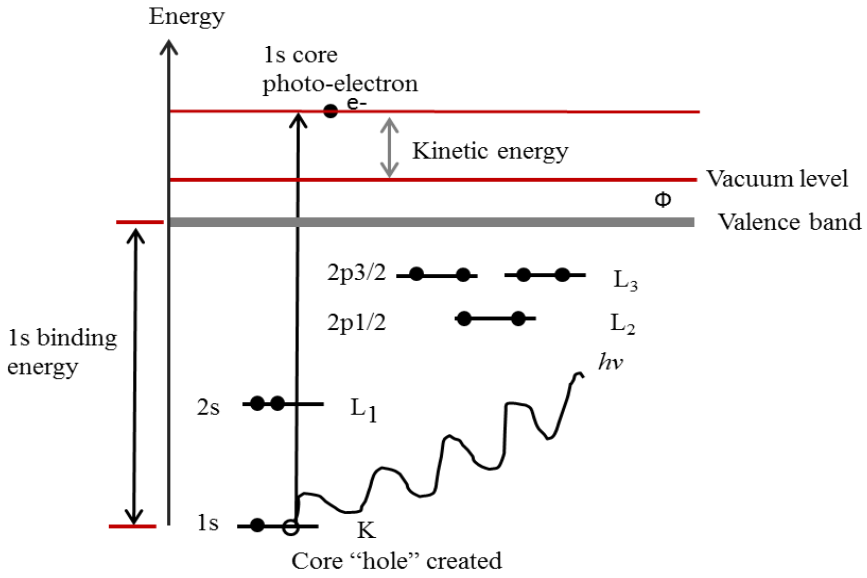

Figure 3.12: Schematic diagram of the XPS process, illustrating photoionization of an atom by the ejection of a 1s electron.[170]

The relationship between the different parameters involved in the XPS experiment is given by the equation below:[170]

$$E_B = h\nu - E_K - \phi \qquad \text{Equation 3.1}$$

Where E_K is the kinetic energy of ejected electron, $h\nu$ is the photon energy; E_B is the binding energy of electron and ϕ is the work function.

The kinetic energy of emitted photoelectrons is analysed by the electron spectrometer and the data is presented as a graph of intensity as a function of electron energy. XPS operation requires an ultra-high vacuum environment in order to avoid sample surface contamination and interference of emitted electrons by gas molecules. The XPS can be used to analyse the surface chemistry (a few nanometres depths) of a sample both qualitatively which elements are present and quantify the relative amounts. XPS measurements were undertaken in a UHV system incorporating a twin anode X-ray source (Mg Kα and Al Kα), and a VG Clam Single Channel XPS system analyser. The Mg Kα X-ray source (1253.6 eV) was used. Measurements were made with the support of Jaffar Saleh. XPS spectra were analysed using CasaXPS software.

3.4 Sample Characterization

3.4.1 Titania Thin Films

Titanium dioxide thin films have been prepared previously using a diverse range of preparation techniques including: R.F and magnetron sputtering,[105, 171] plasma enhanced chemical vapour deposition[172, 173] and PVD.[34, 173] As-deposited titanium dioxide thin film by evaporation techniques onto substrates at room temperature yields predominantly amorphous/polycrystalized materials with a small amount of anatase and rutile.[92, 171, 172, 174] Kunihito *et al*. reported that a titanium oxide thin film prepared at room temperature did not display a significant peak from XRD measurement, an indication that it is amorphous.[174] Further, it was shown that when the as-deposited thin film was heated to 500 ^{o}C for one hour, a diffraction peak due to anatase was observed, which indicates the crystallization of the as-deposited thin film of TiO_2. Transformation to the rutile phase was noticed at about 850 ^{o}C when diffraction peaks due to rutile were detected and 39 % of rutile was formed at about 900 ^{o}C.[174]

In this work, titania thin films were prepared with a substrate at room temperature using the HT-PVD system. Before deposition of a titania thin film on a catalyst screening chip, TiO_2 layers were first deposited on silicon and silicon nitride coated silicon substrates for calibration purpose as described in **Section 3.1.1.1**. The titania support was a continuous thin film of roughness or effective area of *ca*. 1 to 3 times the geometric area. These amorphous thin films are identical to those used elsewhere in high throughput studies of titania supported gold and platinum nanoparticles electrocatalysts.[34, 61, 78, 175] XRD results showed that as-deposited titania layer was amorphous, **Figure 3.13**, which is in agreement with findings reported in literature.[92, 172, 174] As addressed in literature, to achieve crystalline structures, the annealing of as-deposited titania in an oxygen background for several hours at a temperature of about 400 ^{o}C and above is needed. [92, 172, 174]

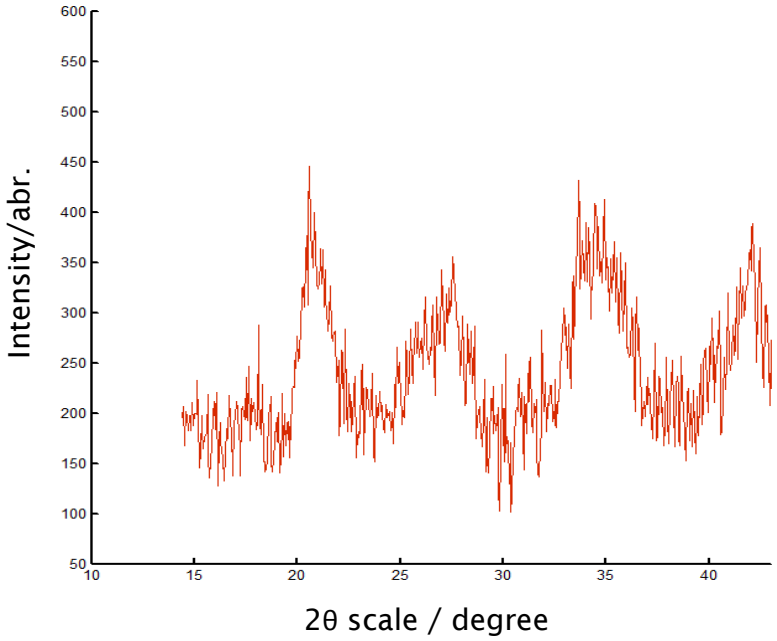

Figure 3.13: XRD measurement on amorphous titanium dioxide film, oxygen pressure = 9.6 x 10^{-6} Torr. The Cu $K_{\alpha 1}$ X-ray source was used.

3.4.2 Platinum and Gold nanoparticles on Titania Layers

The calibration and deposition procedures for Pt and Au nanoparticles on titania are described in **Section 3.1.3**. Pt and Au particles on titania were made using the HT-PVD method and characterization was carried out using TEM (Jeol 3010) instrument and XPS.

3.4.2.1 Platinum Nanoparticles on Titania Layers

Images of platinum particles obtained for TEM samples for various Pt particle sizes on TiO_2 for four different deposition times are presented in **Figure 3.14**. The dark fields are associated with platinum nanoparticles while the lighter fields are attributed to the titania support. It is evident from the TEM images that at longer deposition times, lager Pt particles were deposited corresponding to a mean particle size of 6.7 nm as estimated from TEM image analysis. The particles are eventually seen to aggregate on the surface at the longest deposition times/highest Pt exposures, **Figure 3.14 (d)**. At a reduced deposition time, the particles are well distributed across the support and are small in size,

Figure 3.14 (c). At shorter deposition times, Pt particles are very small and well distributed on the support because limited material is deposited. TEM images in **Figures 3.14 (a)** & **(b)** show clearly how Pt particles are distributed on the support.

TEM image analysis software integrated in the Paradise software package (Ilika Technologies) facilitated the size determination of Pt nanoparticles for each TEM image, corresponding to each deposition time and matched to their corresponding row on the catalyst screening chip. The mean particle sizes acquired from TEM images analysis are presented in red as a function of position (row) on the screening chip, **Figure 3.15**. Regression analysis was performed on the data acquired from the TEM image analysis to obtain an equation used to estimate the mean particle sizes for all of the positions on the catalyst screening chip shown in blue in **Figure 3.15**. **Table 3.1** presents the estimated and experimental mean particle sizes for the four different deposition times. The estimated mean particle size of Pt particles on the titania support ranges between 1.3 nm to 7.8 nm.

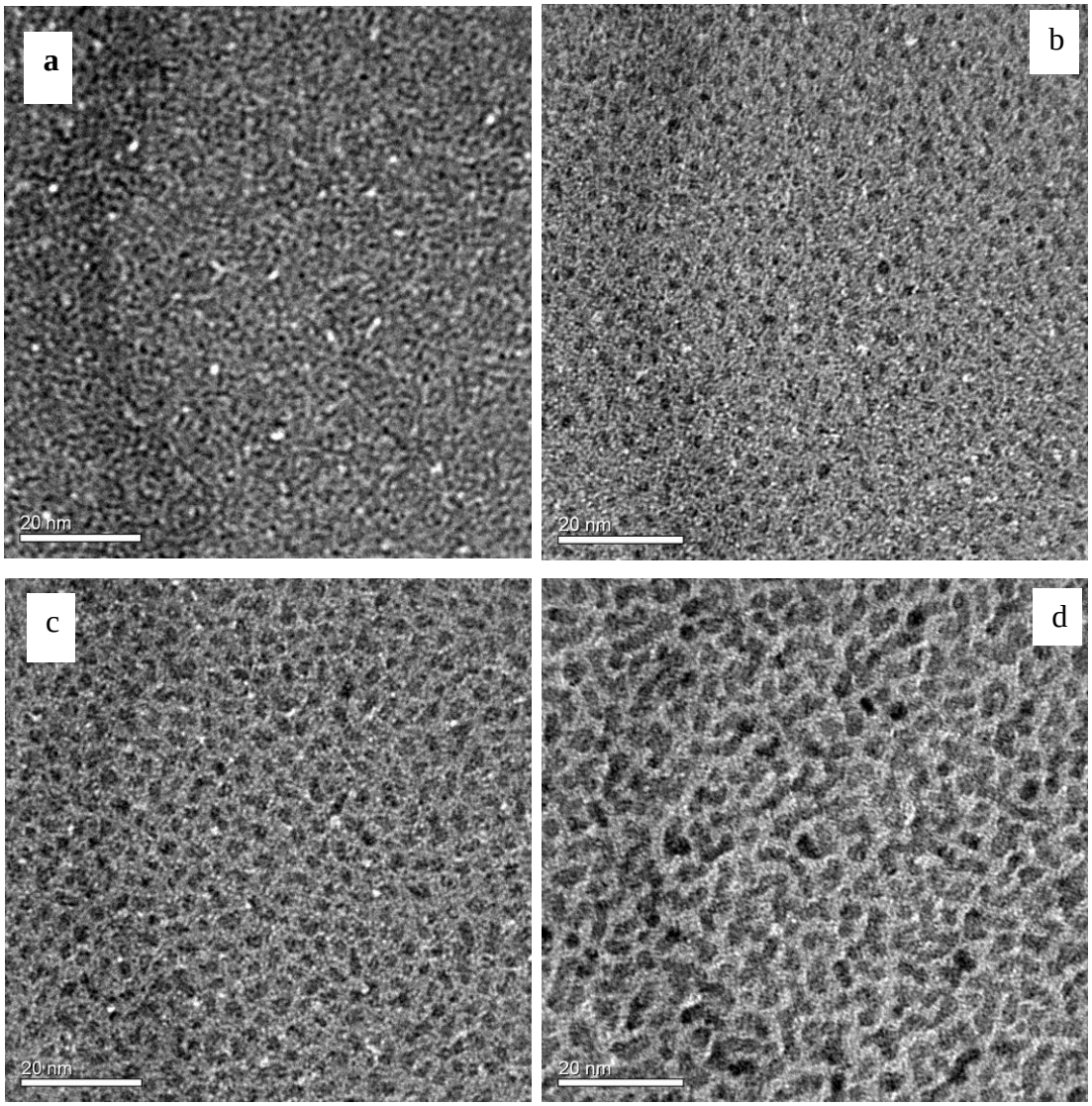

Figure 3.14: TEM images of TiO_2 supported Pt nanoparticles for the four different deposition times, **(a)** 30 sec, **(b)** 2 min, **(c)** 3.5 min and **(d)** 5 min corresponding to mean particle sizes of **(a)** 1.6 nm, **(b)** 2.6 nm, **(c)** 4.9 nm and **(d)** 6.7 nm. Particles were deposited at the rate of 0.15 Å/s and the substrate deposition temperature was 200 ^{o}C.

Row	Estimated mean particle size (nm)	Mean particle sizes from TEM images (nm)
1	1.3 ± 0.3	1.6 ± 0.6
2	1.9 ± 0.5	
3	2.5 ± 0.7	
4	3.1 ± 0.8	2.6 ± 0.9
5	3.7 ± 1.0	
6	4.2 ± 1.1	
7	4.8 ± 1.3	4.9 ± 1.3
8	5.4 ± 1.4	
9	6.0 ±1.6	
10	6.6 ± 1.7	6.7 ± 20
11	7.2 ± 1.9	
12	7.8 ± 2.0	

Table 3.1: Estimated mean particle sizes and mean particle size from TEM images analysis for the four deposition times for Pt particles as a function of position on the screening chip. TEM images analysis data were subjected to regression analysis in order to estimate Pt particle sizes across the chip. Since the errors (standard deviation) in the Pt mean particle sizes from the TEM images analysis are linear, the errors increases as the particle size become larger and broader; the regression analysis was used on the standard deviation in order to estimate the errors for the intermediate particles in the estimated particle sizes.

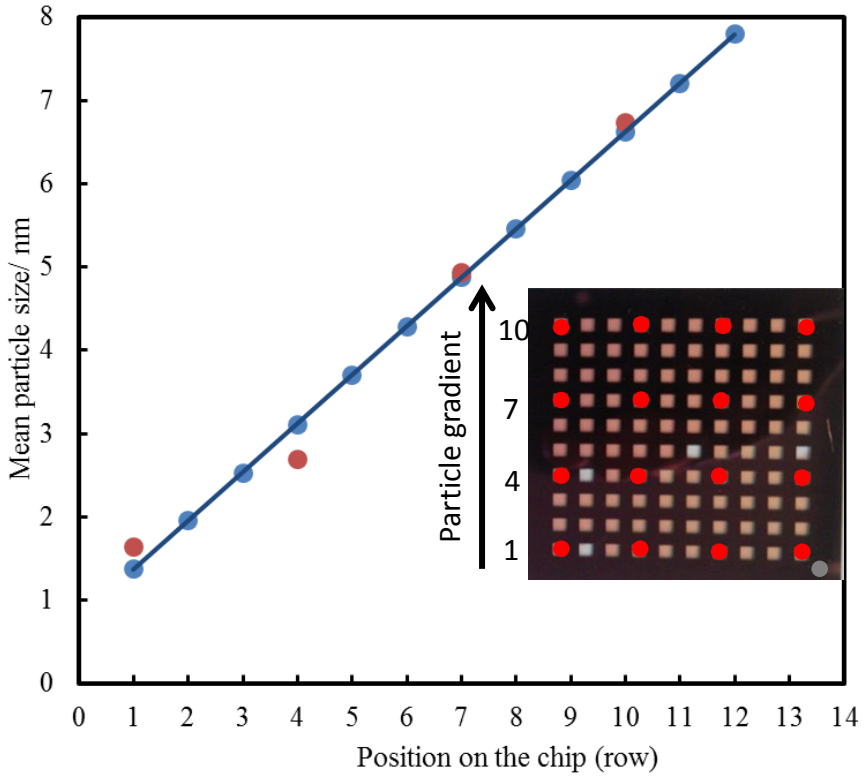

Figure 3.15: Particles size analysis obtained for Pt nanoparticles on titania support. Red dots on the plot show the mean particles size from TEM images analysis as a function of position on the screening chip. The blue dots show the estimated particle sizes across the chip. Regression analysis was done on the TEM data to obtain the estimated Pt particles sizes across the screening chip (10 x 10 or 12 x 12 arrays). The inserted figure indicates the position of TEM images on the screening chip.

Figure 3.16 below shows Pt nanoparticle size distribution attained from two TEM images with a mean particle diameter of 1.6 nm. 280 Pt particles were analysed for the particle size distribution. Pt particle distribution on the titania support is in good agreement with that reported in literature.[68]

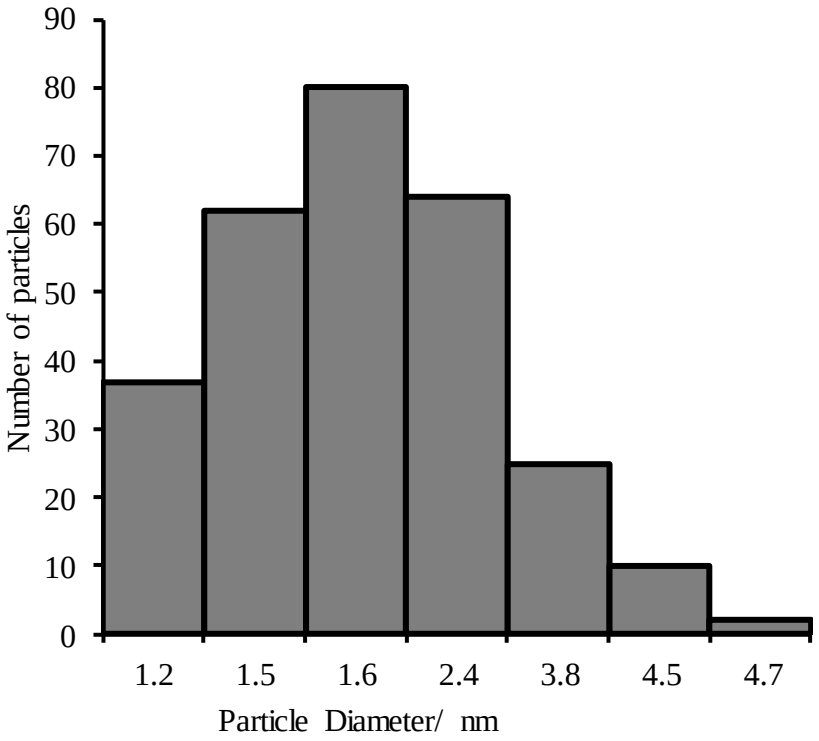

Figure 3.16: Particle size distribution of platinum nanoparticles supported on a titanium dioxide support (mean particle size = 1.6 nm). The number of particles sampled was 280.

A quantitative analysis of Pt nanoparticle sizes as a function of deposition time is presented in **Figure 3.17**. It is shown that at short deposition times (t_{dep} = 30 s), mean particle diameters are approximately 1.6 nm and particle sizes are confined in a contracted range of sizes. When the deposition time is increased, particle size increases resulting into a wider range of particle size distributions and lower particle density (t_{dep} =300 s). The highest particle density recorded for one square centimetre was estimated to be 4.6 x 10^{12} cm^{-2} for Pt particles of a mean particle size of 1.6 nm.

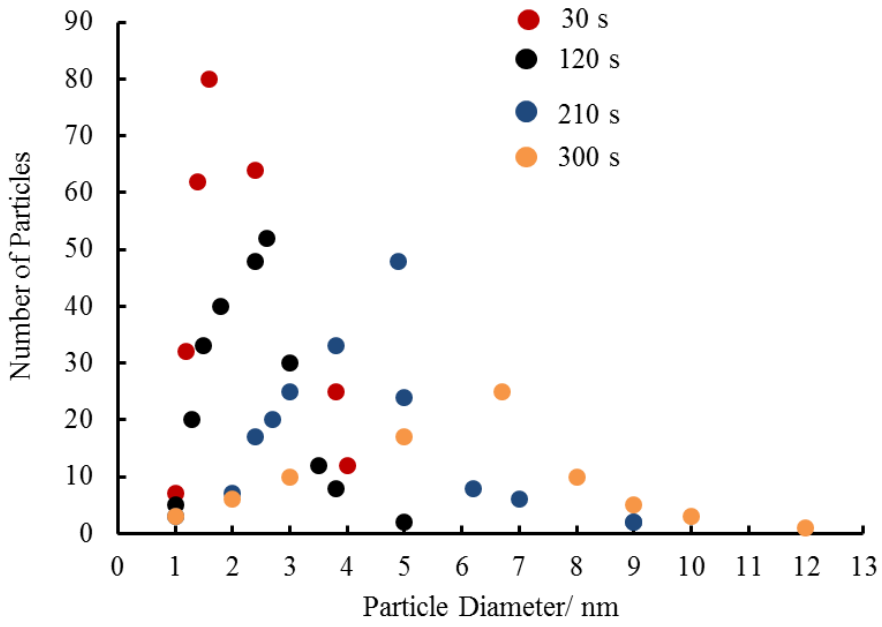

Figure 3.17: Supported Pt nanoparticle size distributions as a function of number of particles obtained from TEM measurements for four different deposition times. The deposition times have been indicated in the figure legend. With increasing deposition time, hence particle size, the number of particles sampled in each case were; 280 particles (at t = 30 s), 250 particles (at t =120 s), 200 particles (at t = 210 s) and 120 particles (at t = 300 s), respectively.

From the mean particle size of Pt obtained from TEM image analysis for four different deposition times, the area of each particle was estimated. This was combined with the particle density in order to estimate the total surface area or total mass of the Pt particles deposited on the screening chip, assuming hemispherical particle morphology. The total Pt surface area/mass is crucial for the determination of catalytic activity of the Pt/TiO_2 nanoparticle catalyst for the CO oxidation reaction under investigation. **Figure 3.18** shows the estimated total surface area of Pt nanoparticles as a function of mean particle size.

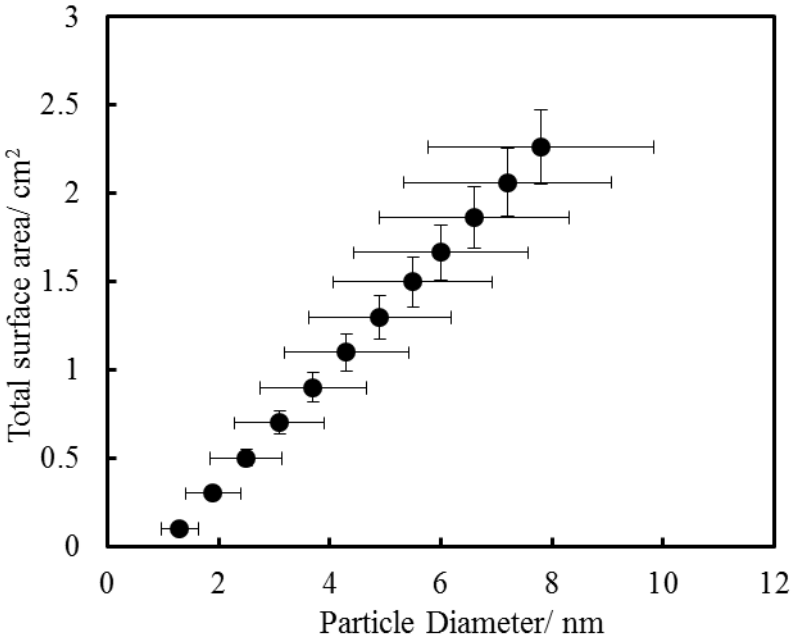

Figure 3.18: Pt surface area as a function of mean particle sizes. Regression analysis was done on the TEM data to obtain the equation used to estimate the total surface area for all Pt particle sizes across the screening chip. Since the area of Pt (hemispherical) particle is a function of particle diameter, the standard deviation in the particle diameter from TEM image analysis were used to estimate the errors in the area by undertaking the regression analysis.

3.4.2.2 Gold Nanoparticles on Titania Layers

Images obtained from the TEM samples of different Au particle sizes supported on titania layers for four different deposition times are presented in **Figure 3.19**. The dark fields are associated with gold nanoparticles and lighter fields are attributed to the titania support. The TEM images show that at longer deposition times, lager Au particles were deposited on the titania, corresponding to a mean particle size of 5.8 nm as anticipated from TEM image analysis. The particles can be observed to aggregate, forming larger particles on the surface at the longest deposition times, **Figure 3.19 (d)**. At a reduced deposition time, the particles are seen to be distributed randomly across the support and are small in size, **Figure 3.19 (c)**. At shorter deposition times, Au particles are well distributed on the support because a limited amount of material is deposited. TEM images in **Figure 3.19 (a)** & **(b)** shows clearly how Au particles are distributed on the titania support.

The TEM image analysis software integrated in the Paradise software package (Ilika Technologies) facilitated the size determination of Au nanoparticles for each TEM image, corresponding to each deposition time and matched to their corresponding row on the screening chip. The mean particle sizes obtained from TEM images analysis are presented in red as a function of position (row) on the screening chip, **Figure 3.20**. Regression analysis was performed to the data acquired from TEM images analysis to obtain an equation which was used to estimate the mean particle sizes for all of the positions on the screening chip shown in blue. **Table 3.2** presents estimated mean particles sizes and mean particle sizes from TEM images analysis for the four different deposition times. The estimated mean particle sizes of Au particles on the titania support ranges between 1.5 nm to 6.8 nm.

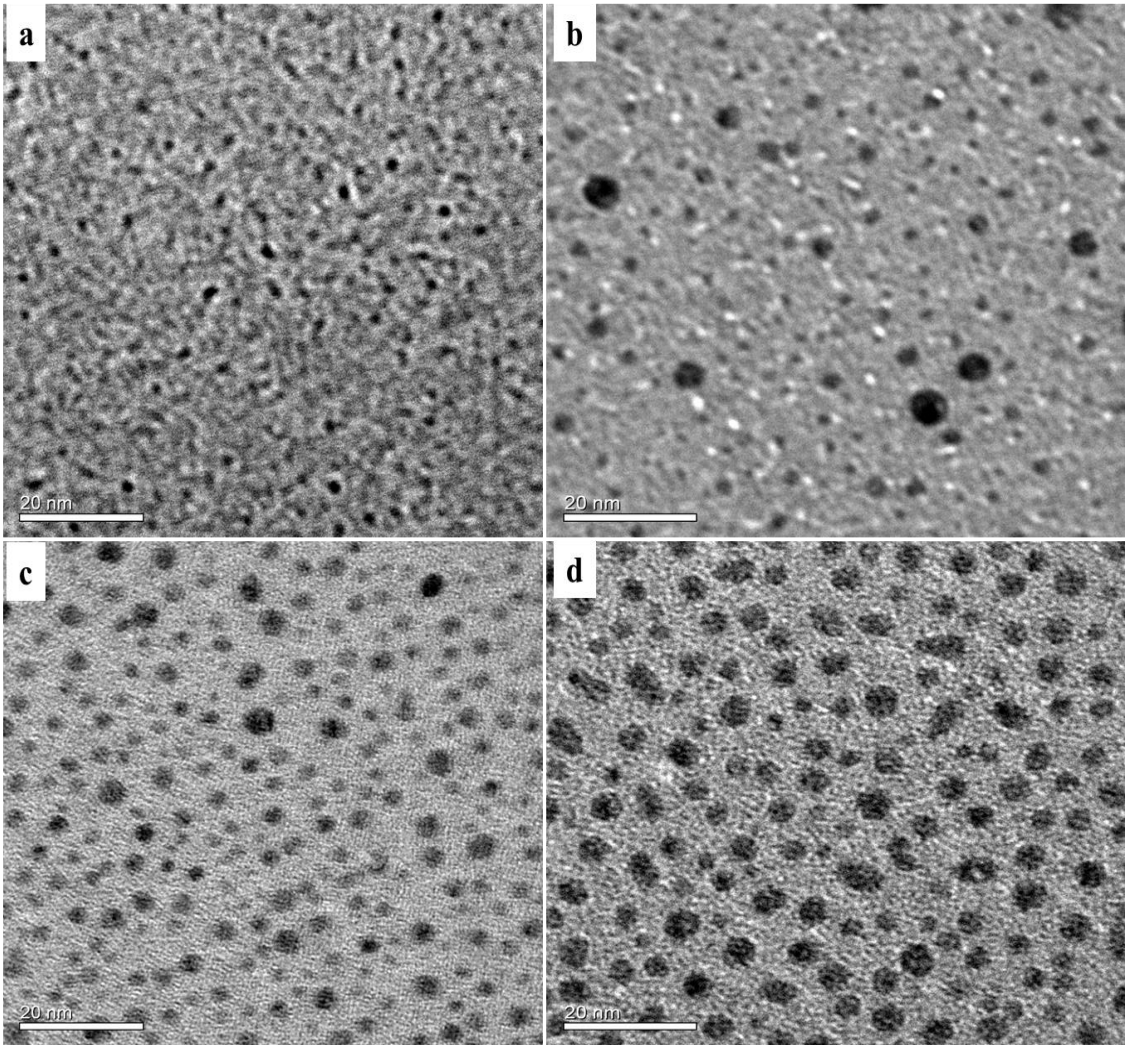

Figure 3.19: TEM images of titania supported Au nanoparticles for the four different deposition times, **(a)** 30 sec, **(b)** 2 min, **(c)** 3.5 min and **(d)** 5 min corresponding to a mean particle size of **(a)** 1.5 nm, **(b)** 2.8 nm, **(c)** 4.5 nm and **(d)** 5.8 nm. Particles were deposited at a Au deposition rate of 0.15 Å/s and a substrate deposition temperature of 200 ^{o}C.

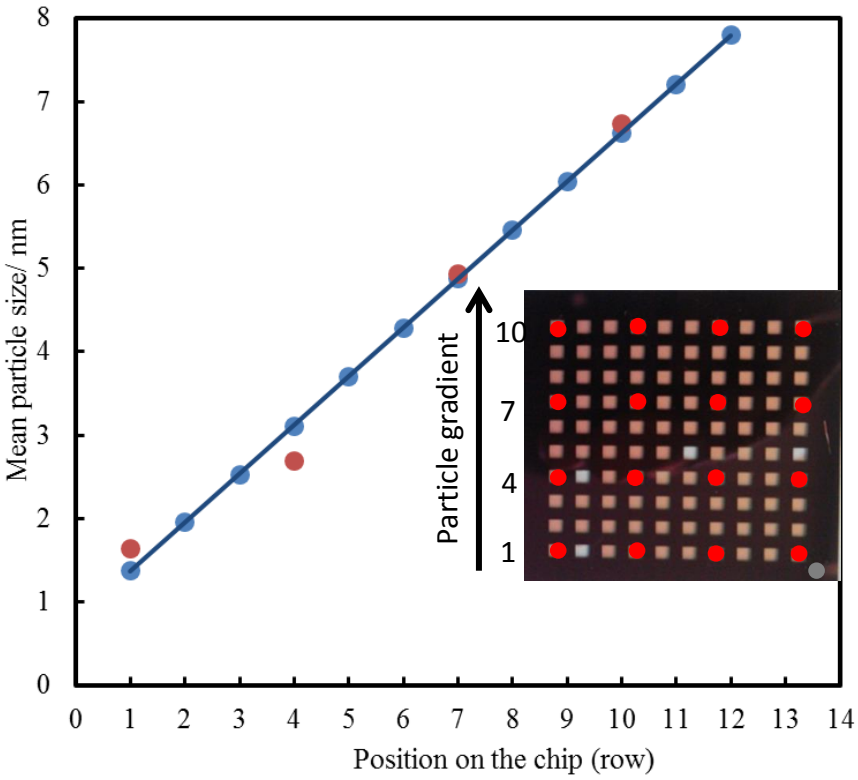

Figure 3.20: Particle size analysis obtained for gold nanoparticles on a titania support. Red dots on the plot show the mean particles size from TEM image analysis as a function of position on the catalyst screening chip. The blue dots show the estimated particle sizes across the chip. Regression analysis was done on the TEM data to obtain the equation which was used to estimate Au particle sizes across the catalyst screening chip. The inserted figure indicates the position of the TEM images on the screening chip.

Row	Estimated mean particle size (nm)	Mean particle sizes from TEM images (nm)
1	1.5 ± 0.5	1.5 ± 10
2	1.9 ± 0.6	
3	2.5 ± 0.8	
4	2.9 ± 1.0	2.8 ± 1.6
5	3.4 ± 1.1	
6	3.9 ± 1.3	
7	4.4 ± 1.5	4.5 ± 1.8
8	4.8 ± 1.6	
9	5.3 ± 1.9	
10	5.8 ± 2.0	5.8 ± 2.6
11	6.3 ± 2.1	
12	6.8 ± 2.3	

Table 3.2: Estimated mean particle sizes and mean particle size from TEM image analysis for the four various deposition times for Au particles as a function of position on the catalyst screening chip. TEM images analysis data were subjected to regression analysis in order to estimate Au particle sizes across the chip. Since the errors (standard deviation) in the Au mean particle sizes from the TEM images analysis are linear, the errors increases as the particle size become larger and broader; the regression analysis was used on the standard deviation in order to estimate the errors for the intermediate particles in the estimated particle sizes.

Figure 3.21 below shows the Au nanoparticle size distribution attained from two TEM images with the mean particle diameter of 1.5 nm. 196 Au particles were analysed for the particle size distribution investigation. The particle distribution data are in good agreement to that reported elsewhere.[68, 92]

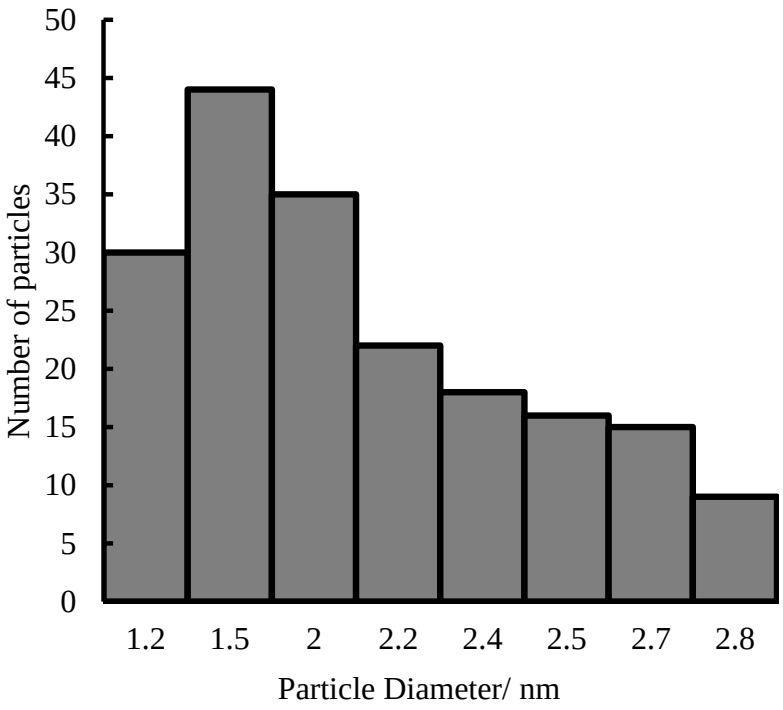

Figure 3.21: Particle size distribution of gold nanoparticles supported on a titanium dioxide support (mean particle size = 1.5 nm). The number of particles sampled was 196.

A quantitative analysis of Au nanoparticle sizes as a function of deposition time was carried out and is presented in **Figure 3.22**. It is shown that at short deposition times (t_{dep} = 30 s), mean particle diameters are about 1.5 nm and particle sizes are in a narrow range of sizes. As the deposition time is increased, particle size increases resulting into a wider range of particle size distributions and a lower particle density (t_{dep} = 300 s). The greatest particle density at one centimetre square was calculated to be 3.89 x 10^{12} cm^{-2} with a mean particle size of 1.5 nm.

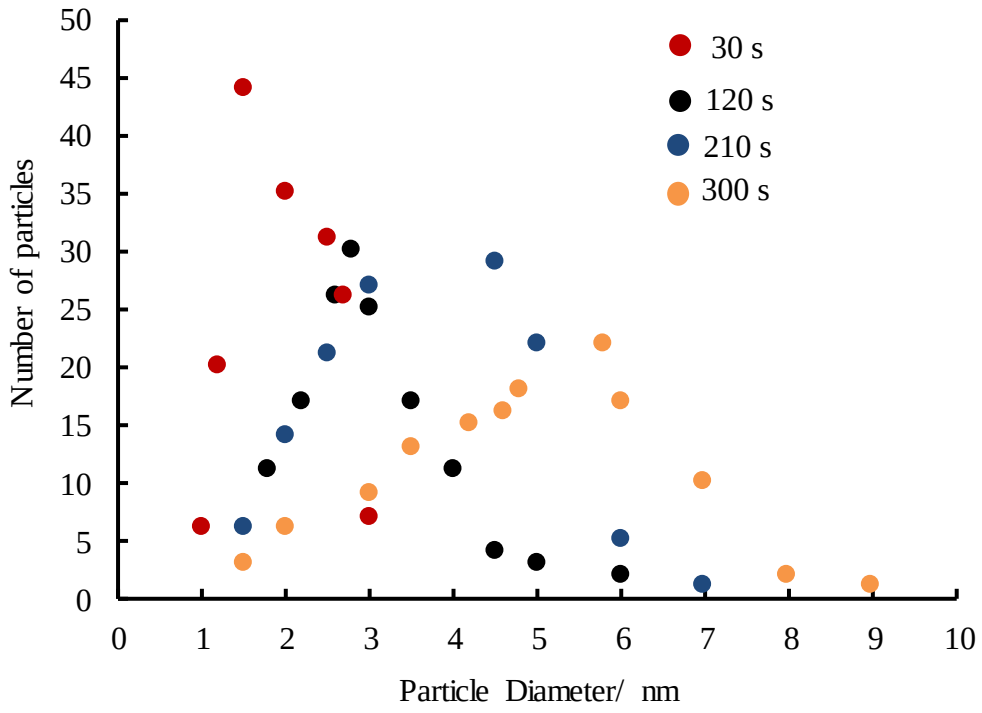

Figure 3.22: Titania supported gold nanoparticle size distributions as a function of number of particles as obtained from TEM images analysis for four different deposition times. The deposition times are indicated in the figure legend. With increasing deposition time, hence particle size, the number of particles sampled in each case were; 196 particles (at t = 30 s), 160 particles (at t =120 s), 132 particles (at t = 210 s) and 127 particles (at t = 300 s), respectively.

From the mean particle sizes of Au obtained from TEM image analysis for four different deposition times, the area of each particle size was estimated. This was combined with particle density in order to estimate the total surface area or total mass of Au particles deposited on the screening chip, hemispherical particles were assumed. The total Au surface area/mass is important for the determination of specific catalytic of Au nanoparticle catalyst for the CO oxidation reaction. **Figure 3.23** shows the estimated total surface area of gold nanoparticles as a function of mean particle size.

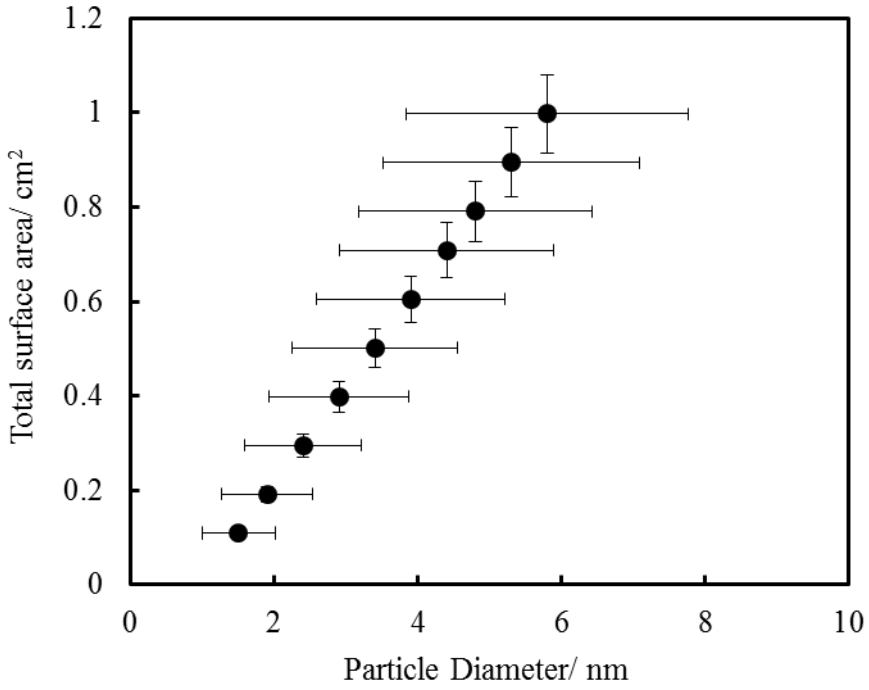

Figure 3.23: Gold surface area as a function of mean particle sizes. Regression analysis was carried out on the TEM analysis for surface area based data to obtain the equation which was used to estimate the total surface area for all gold particles of various sizes across the screening chip. Since the area of Au (hemispherical) particle is a function of particle diameter, the standard deviation in the particle diameter from TEM image analysis were used to estimate the errors in the area after carrying out regression analysis.

3.5 High Through-put Heterogeneous Catalyst Screening

A high-throughput heterogeneous catalyst screening for the CO oxidation reaction was carried out using a new screening methodology developed during this work. The technique using a high through-put screening chip made up of silicon nitride membranes to screen supported metal nanoparticle catalysts was extended from a micro-fabricated electrochemical screening array commonly used to screen high surface area supported electrocatalyst.[145]

3.5.1 Ultra-High Vacuum IR Thermography Reactor System

Catalyst screening was carried out in a separate UHV high through-put heterogeneous catalyst screening chamber, designed to suit the screening needs of the solid/gas-phase

reactions, **Figure 3.24 (a)** and **Figure 3.24 (b)**. The reaction chamber is designed to provide a contamination free environment for catalyst screening purposes.

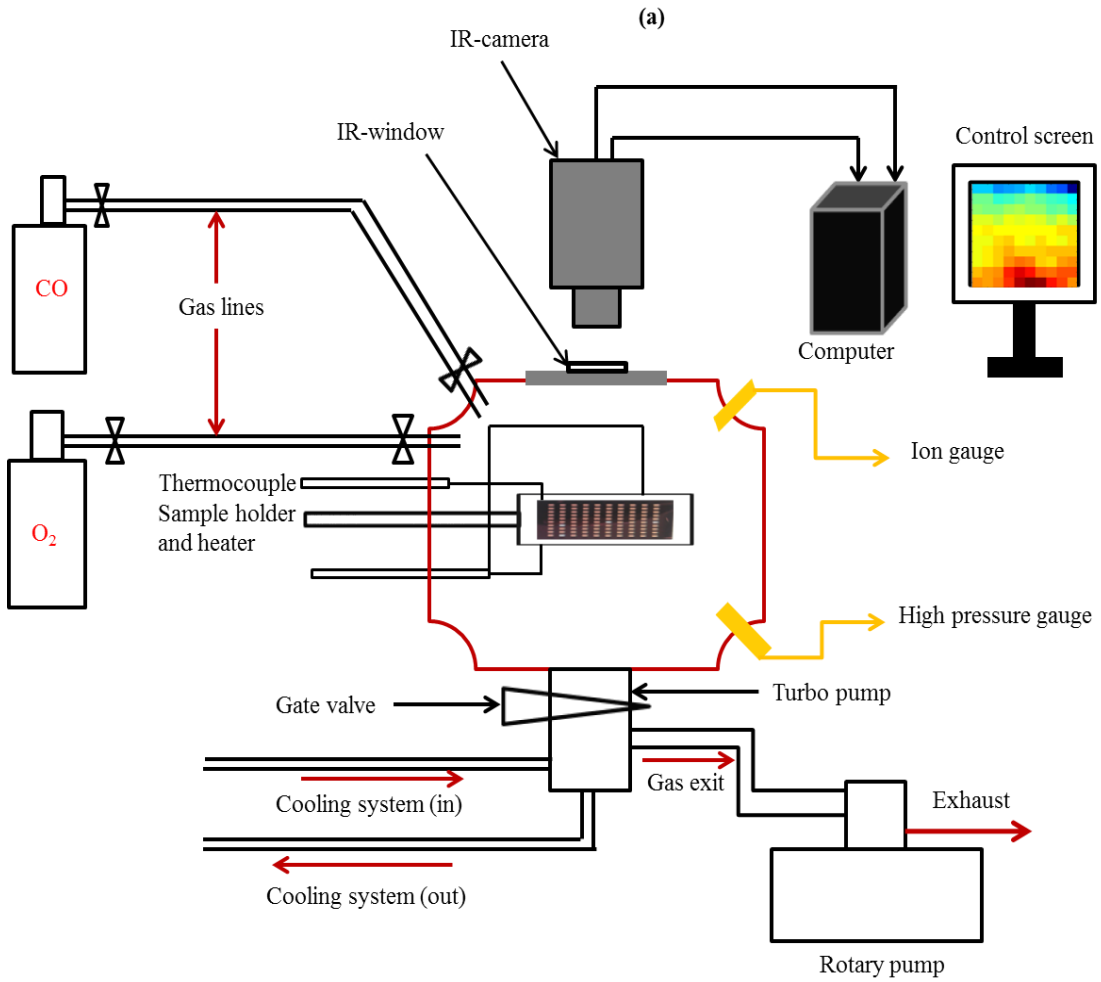

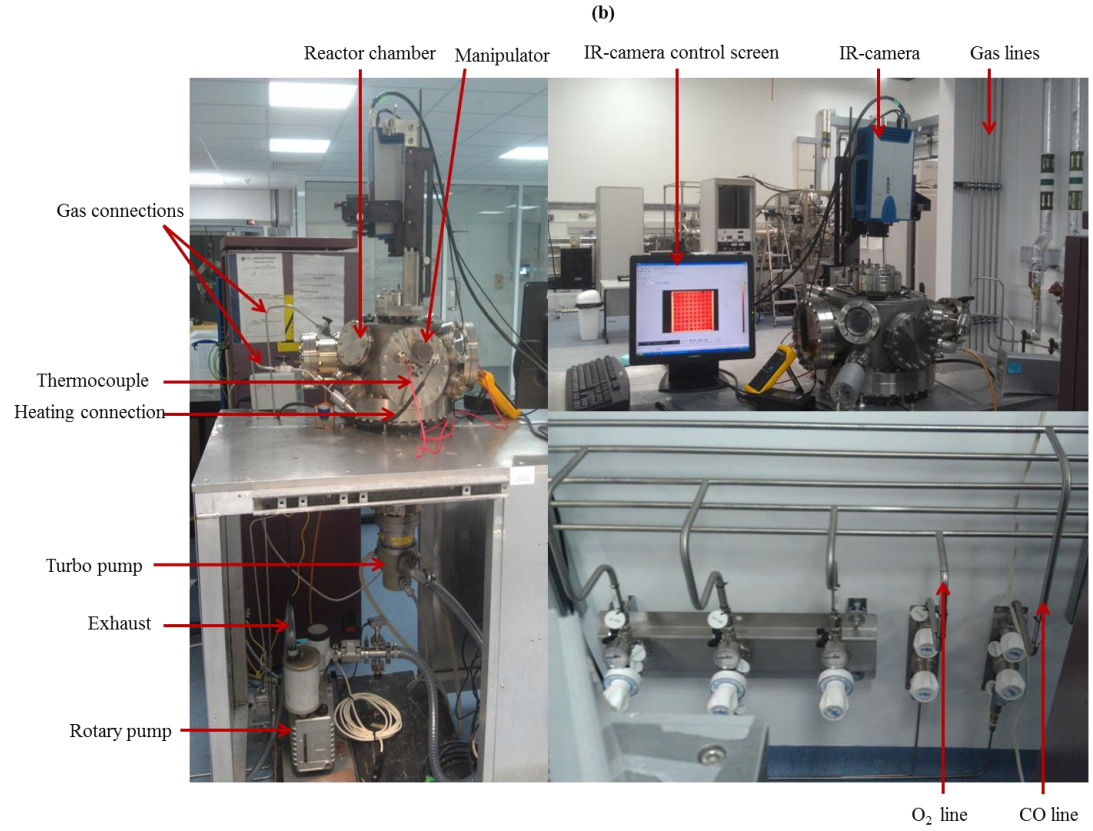

Figure 3.24: (a) Schematic diagram of an UHV high through-put heterogeneous catalyst screening chamber showing the IR-camera arrangement and other important components. **(b)** The photography of a screening chamber indicating various parts and the gas lines connections.

Figure 3.25 presents the first design of the heater (sample holder) used to heat the screening chip on which the catalyst libraries were deposited. The sample holder is made of two copper bars (50 mm x 50 mm x 10 mm) in which ceramic tubes used as wire insulator have been positioned to avoid heating wire contact and tungsten heating wire rapped through which then exits the chamber via electrical feed-through towards external power supply for sample heating. A K-type thermocouple made of Kapton coated thermocouple wire has been mounted on a copper bar sample holder. The thermocouple exits the chamber via the feed-through and is then externally connected to the multimeter for temperature reading during catalyst screening process. The thermocouple is intended to record the temperature at which the sample is being heated while activating the catalyst. The sample holder is connected to the manipulator to allow for easy rotation of the sample to a required position during imaging process.

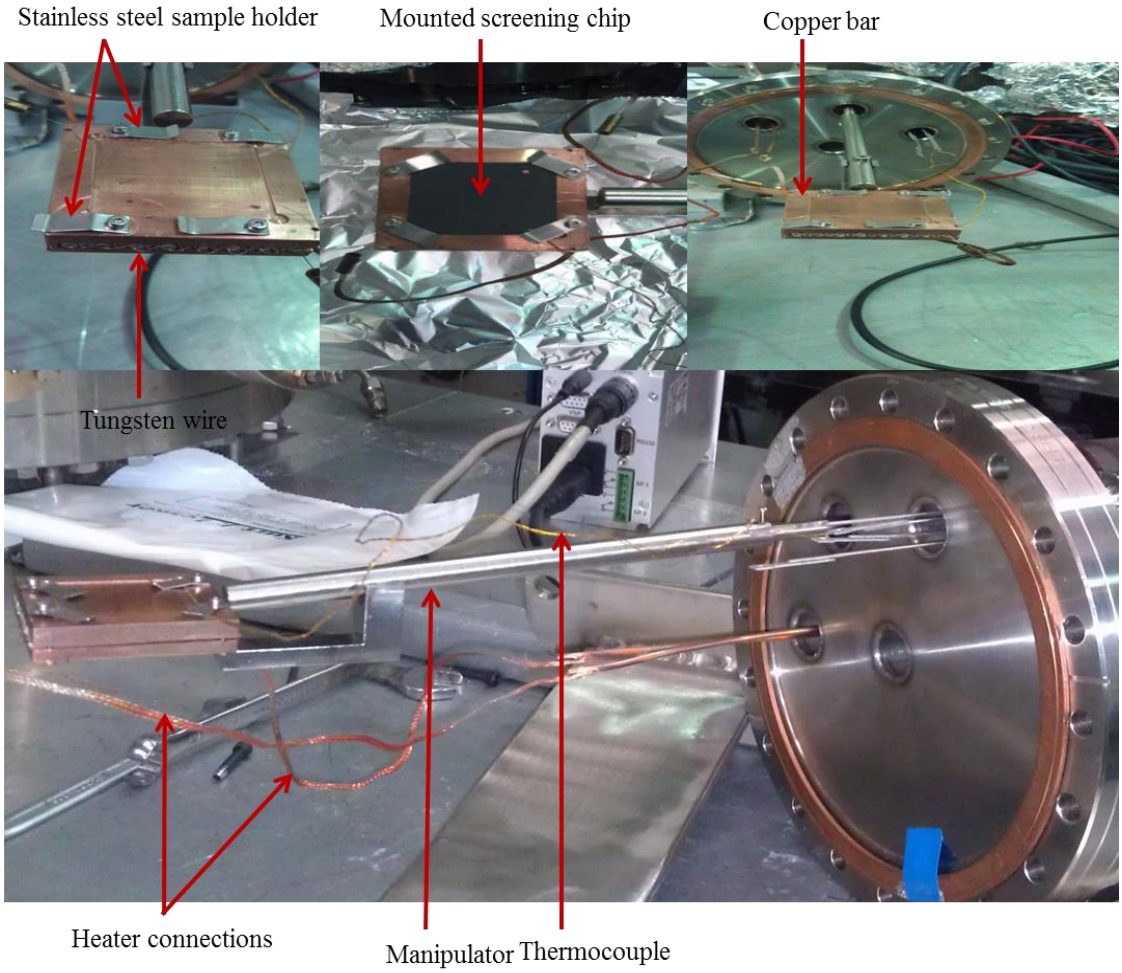

Figure 3.25: The photography of the first sample holder design illustrating the heater configuration and its various components. The way the sample is mounted on the heater is also shown.

However, this design could not work well because of the higher thermal conductivity of copper which resulted to the higher temperature loss across the heated substrate, which in turn led to the higher temperature gradient across the catalyst library. On the other hand, since the silicon nitrides membranes on the screening chip are transparent, it was not possible to image the surface of the membrane using the IR thermal camera, instead the camera could directly image the surface of the heater. To achieve the best temperature gradient across the heated substrate (catalyst library), a new heater design with ceramic material was necessary. Despite the fact that the membranes transparency problem re-occurred in the new heater design, the resolved by the use of carbon spray in the reverse side of the screening chip. The new heater design used during the library screening process that produced the result presented in this thesis is described below.

The chamber is fitted with a sample holder made of two flat square ceramic heating blocks, 11 mm x 85 mm x 100 mm (Macor ceramic, RS Components) between which a Nichrome (Ni80/Cr20) heating wire of 0.5 mm diameter (Goodfellow) is wrapped and exits the chamber via an electrical feed-through to an external power supply for sample heating, **Figure 3.26**.

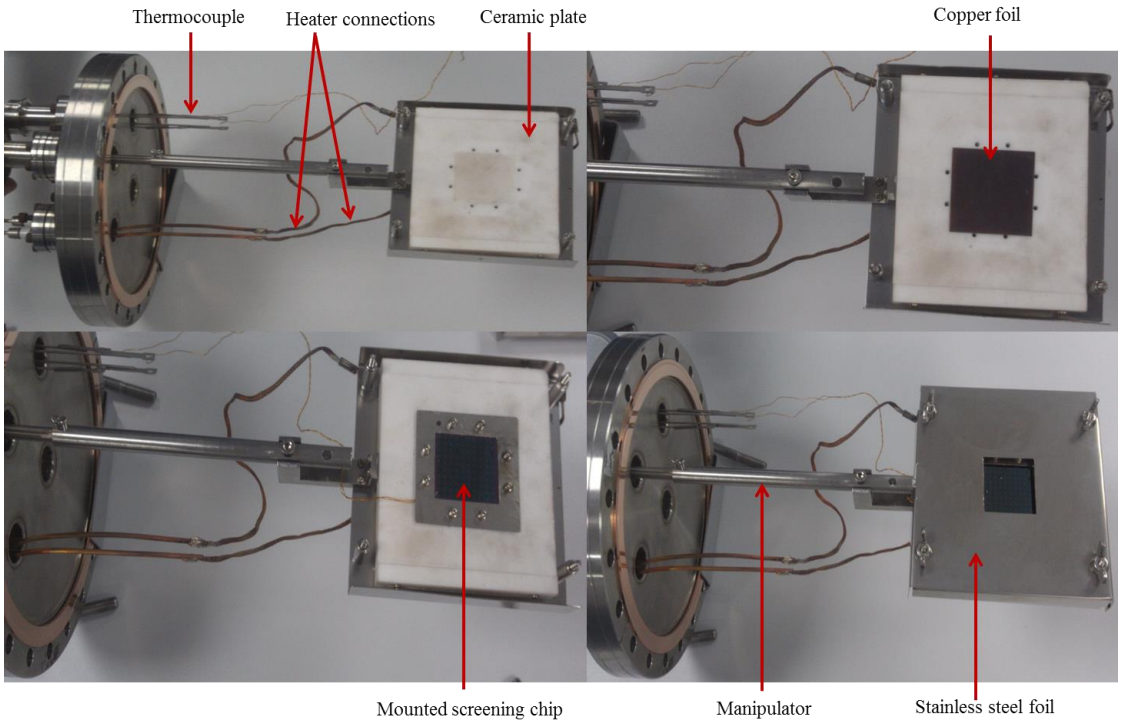

Figure 3.26: The photography of the sample holder illustrating the heater configuration and its various components. The way the sample is mounted on the heater is also shown.

Figure 3.27 presents a cross section of the components arrangement on the sample heater as mounted during the catalyst screening for CO oxidation activity.

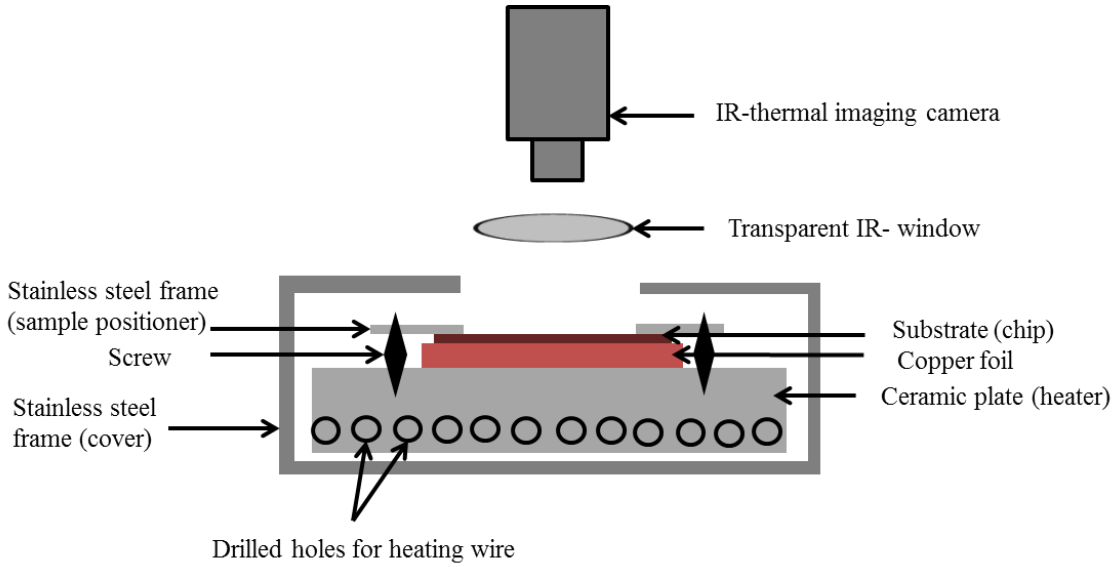

Figure 3.27: A cross section of the components on a sample heater showing the way the sample is kept in place during activity screening. An IR- thermal imaging camera is shown from the top focusing through a transparent window.

The heater is enclosed in a 0.5 mm stainless steel foil, 23 mm x 110 mm x 120 mm (RS Components) to reduce heat loss from the edges of the heater. A K-type thermocouple made of Kapton coated thermocouple wire has been incorporated. The thermocouple exits the chamber via the feed-through and is externally connected to the multimeter which gives a direct temperature reading. The thermocouple records the temperature at which a sample is being heated during the catalyst screening process. The sample holder is connected to the manipulator to allow for easy rotation of the sample to a required position during the imaging process. The catalyst library is heated on a 0.5 mm x 36 mm x 36 mm piece of copper foil (RS Components) placed on top of the heater to provide a homogeneous temperature rise. The sample is kept in place by a stainless steel frame, 0.5 x 50 mm x 50 mm (RS Components). The chamber is equipped with a CaF_2 IR-transparent window to allow the non-contact imaging of the catalyst screening chip in the chamber using an IR thermal imaging camera. The reactant gases have been connected to the reaction chamber via gas lines with valves placed before the chamber for gas inlet control. An ion gauge and high pressure gauge have been fitted on the reaction chamber for pressure monitoring.

3.5.2 Infrared Thermography Technique

A high through-put infrared thermography technique was constructed for direct measurement of the energy released, and consequent temperature rise from a surface exothermic reaction. The principal and experimental configuration used is similar to the thermography techniques developed for the high throughput screening of hydrogen storage materials.[143] The IR camera was mounted on top of the chamber facing an IR-transparent window as illustrated in a general scheme of the set up in **Figure 3.24**. In this work, a Jade III (CEDIP, Paris), InSb based camera (stirling cooled) with a spectral range of 3.6 to 5.1 μm , a resolution of 320 x 240 pixels, temperature range of -40 ^{o}C to 1200 ^{o}C and thermal sensitivity of 20 mK and a 50 mm focal length was used. CIRRUS and ALTAIR software were incorporated for camera control, image acquisition and processing.

3.6 Gases used in Catalysts Activity Screening

For catalysts activity screening of Pt and Au supported nanoparticle catalysts, carbon monoxide oxidation by oxygen was selected as the model exothermic reaction. During CO oxidation, carbon monoxide gas (99.999 %, Air Products) and oxygen (99.999%, BOC Gases) were used.

3.7 Activity Measurement Acquisition Procedures and Data Analysis

Platinum and gold nanoparticle catalyst supported on amorphous titania was pre-heated on a sample holder in an UHV high throughput heterogeneous catalyst screening chamber in a flow of oxygen gas. The catalyst was left for two hours (2hrs) for the temperature to equilibrate to a required reaction temperature before measurements could be taken. Before starting the measurement, an IR video of the material library was taken which was subtracted as the background (T_o) so the display of temperature change due to catalytic reaction of catalyst in the library could be quantified.

The test experiments were first carried out to assess the validity of activity results obtained from CO oxidation reaction on titania supported Pt and Au nanoparticle catalysts.

The catalyst library was heated to a desired experimental temperature as in normal experiments undertaken in this work. Experiments were conducted by adding the same or different pressure of a pre-adsorbed reactant gas into the screening chamber, measurements were taken and data analysed. The negative temperature changes were obtained when the same reactant gas was allowed into the reaction chamber, which indicates that there was no heat released, therefore no reaction took place, instead the catalyst was cooled in contrast to when a different reactant gas is added making a mixture of two reactant gas in the feedstock, **Figure 3.28**.

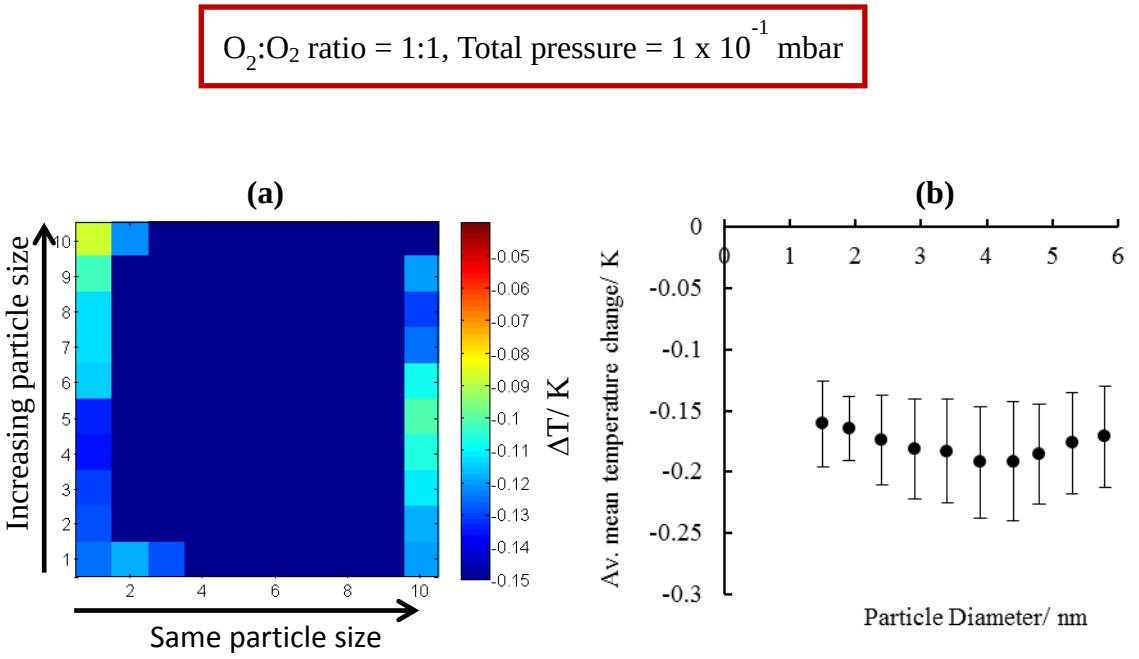

Figure 3.28: The absolute temperature change on Au/Pt/TiO_2 catalyst as a function of particle size at an O_2:O_2 ratio of 1:1, with a total pressure of 1 x 10^{-1} mbar. **(a)** Presents infrared image and **(b)** presents the average mean temperature change as a function of particle sizes. The row and column numbers are shown on the x and y axes on the IR-images. The reaction temperature was 80 ^{o}C at an exposure time of 5 minutes.

In this case, if CO was added as the second reactant gas in the feedstock, it would have resulted into a raise in temperature on the catalyst surface, which signifies heat production from the CO oxidation reaction. Therefore, if O_2 or CO is added alone in the reaction chamber, no raise in temperature is observed, hence in order to observe the raise in temperature both reactant gases have to be present in the reaction feedstock. This exper-

imental result proves that the temperature change obtained is from CO oxidation reaction involving both O_2 and CO reactant gases on the surface of Au/Pt catalysts.

The catalyst was then subjected to both reactant gas, O_2 and CO at the desired pressure ratios and the IR video was recorded. The pressure of reactant gases were altered at each stage when the measurement was sought and measurements were taken after five minutes of exposure. At each measurement, a background measurement was recorded and subsequently used as a baseline for that particular measurement during data analysis. The change in temperature due to catalytic activity was determined with reference to a background measurement when a catalyst was exposed to O_2 or CO gas alone.

Data analysis was carried out using both the Matlab (provided by the University of Southampton) and Paradise (Ilika Technologies) software. The change in temperature from a catalytic surface exothermic reaction was determined from the difference between the background temperature (T_o) and the temperature at which the catalyst was exposed to both the reactant gas (T_r), as shown in equation **3.2**.

$$\Delta T = T_r - T_o \qquad \text{Equation 3.2}$$

In order to obtain the normalized temperature change (i.e. row and column compensated) from the catalytic activity across Pt and Au nanoparticle catalysts with various particle sizes, the measured temperature change (ΔT) for each square membrane on the screening chip was normalized by multiplying with a normalization factor (s) **x**. The normalization factors were calculated from the equation below:

$$\Delta T_1 \times x = \Delta T_2 \qquad \text{Equation 3.3}$$

where $\Delta \boldsymbol{T_1}$ is the temperature change across the row where particle sizes are constant and $\Delta \boldsymbol{T_2}$ is the highest temperature change across the same row. The normalization factors were computed for each individual row on the screening chip. The same normalization factor (s), were then applied to optimize the temperature change along the columns where particle sizes are changing. The optimization was undertaken in order to compensate for the background temperature inhomogeneity across the screening chip and the temperature loses at the edges of the chip.

Therefore, normalization of the temperature change was carried out by multiplying the temperature change with the normalization factor (i.e. $x\Delta T_1$).

Figure 3.29 shows the typical experimental results for the row uncompensated and row compensated infrared images as well as the temperature change for the uncompensated and compensated and how the normalization was undertaken. Only one row is shown for illustration.

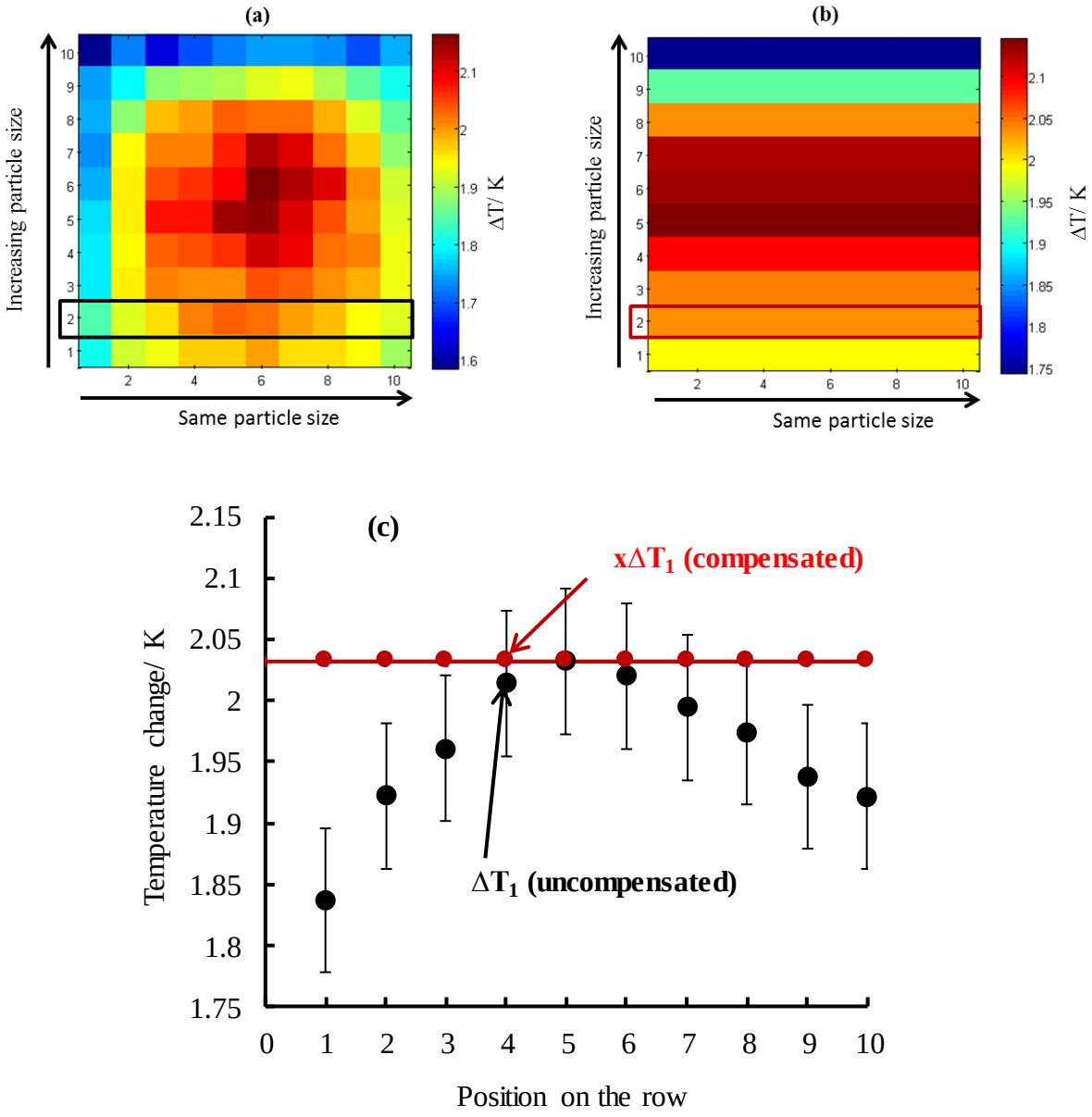

Figure 3.29: Temperature change on the catalyst as a function of membrane position on the row. **(a)** Presents uncompensated infrared image, **(b)** row compensated and **(c)** uncompensated and compensated temperature change on the row. The row and column numbers are shown on the x and y axes on the IR-images. The reaction temperature was 80 ^{o}C at an exposure time of 5 minutes.

Figure 3.30 shows the normalization of temperature change along the column where particles sizes are changing using the same normalization factors used across the row on the screening chip. Only one column is shown to illustrate the data normalization procedures.

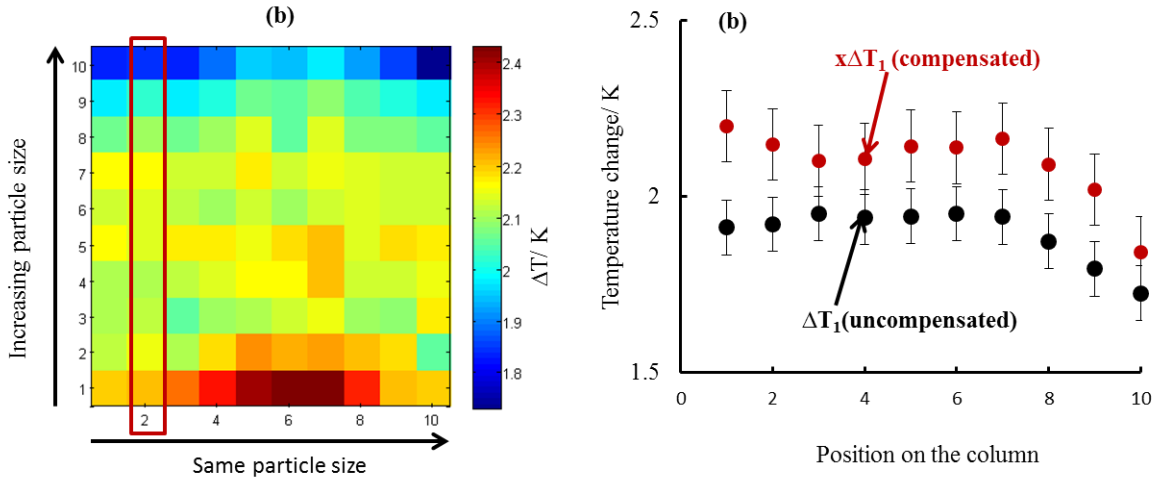

Figure 3.30: Temperature change on the catalyst as a function of membrane position on the rcolumn. **(a)** Presents column compensated infrared image and **(b)** column uncompensated and compensated temperature change. The row and column numbers are shown on the x and y axes on the IR-images. The reaction temperature was 80 ^{o}C at an exposure time of 5 minutes.

Figure 3.31 presents the TOF frequency for the uncompensated and compensated temperature change as a function of particle size calculated from equation 3.5. One column was used to demonstrate the normalization approach.

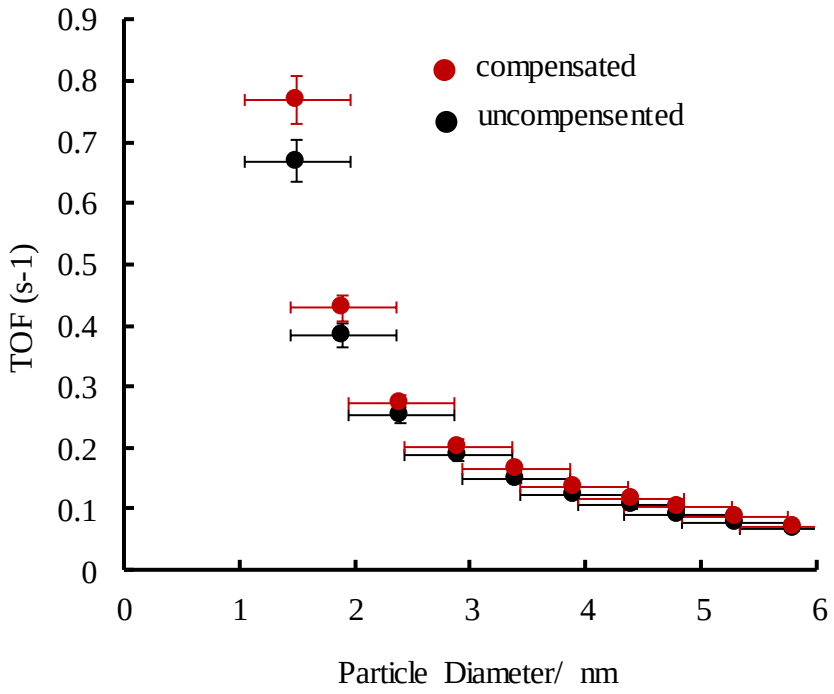

Figure 3.31: The TOF of nanoparticle catalyst supported on titania for the CO oxidation reaction as a function of particle size (diameter/ nm) from uncompensated and compensated temperature change along the column. The reaction temperature was 80 ^{o}C.

By performing this compensation on the temperature change data, the temperature change entirely from the catalysts reactivity were obtained, hence the modulation across the various Pt and Au particle sizes across the screening chip.

The TOF and specific mass activity for the CO oxidation reaction were calculated through equation **2.7** by computing the number of moles of CO converted per mm^{-2} per second obtained from the temperature change from CO oxidation reaction as shown in equation 3.4 below:

$$\Delta T = \frac{n\left(mm^{-2}s^{-1}\right)\times 283\times 10^{3}\left(J\right)\times Area\left(mm^{2}\right)\times 10^{6}}{13.5\times x\left(\mu m\right)\times k\left(Wm^{-1}K^{-1}\right)} \qquad \text{Equation 3.4}$$

where n is the number of moles of CO converted per mm^{2} per second. TOF is calculated from the equation below:

$$TOF\left[s^{-1}\right] = \frac{n_{molCO}\left[mm^{-2}s^{-1}\right]}{s_{mol\,Au/Pt}\,mm^{-2}} \qquad \text{Equation 3.5}$$

where *s* is the number of moles Au/Pt in the catalyst per mm^{-2}.

The number of moles of CO converted is computed using the equation below:

$$n_{CO}conv.\left[mm^{-2}s^{-1}\right]=\frac{P\left[Js^{-1}mm^{-2}\right]}{283\times10^{3}\left[J\right]} \qquad \text{Equation 3.6}$$

Where is the power in $Js^{-1}mm^{-2}$ 283 x 10^3 J is the enthalpy change for the oxidation of one mole of carbon monoxide at 298 K, assuming that the enthalpy change of a reaction is independent of temperature within a small range of temperatures.[8]

The specific mass activity was computed through the equation below:

$$Spec.activity\left[mol_{CO}conv.g^{-1}{}_{Au/Pt}mm^{-2}s^{-1}\right]=\frac{n_{molCO}\left[mm^{-2}s^{-1}\right]}{g_{Au/Pt}} \qquad \text{Equation 3.7}$$

where *g* is the weight in gram of Au/Pt in the catalyst per mm^{-2} which is calculated from the equation below, assuming hemispherical particle:

$$Mass_{Pt/Au}\left[g\right]=Density_{pt/Au}\left[gcm^{-3}\right]\times Volume_{Pt/Au}\left[cm^{3}\right] \qquad \text{Equation 3.8}$$

Since the area of Au/Pt is given by the particle density times the area of one particle, assuming hemispherical particle and the number of atom density in the surface for an Au (111)[176] and Pt (111)[177] face of 1.4 x 10^{15} cm^{-2} and 1.5 x 10^{15} cm^{-2}, respectively.

The moles of Au/Pt in the catalyst are given by:

$$Moles_{Au/Pt}\left[mm^{-2}\right]=\frac{Area_{Pt/Au}\times AD\left(mm^{-2}\right)}{N_A} \qquad \text{Equation 3.9}$$

where AD is the is the atom density per mm^{-2} and N_A is the Avogadro's constant, 6.023 x 10^{23} atoms.

The example on how the catalyst activities are calculated through various equations is shown in appendix 3.

4 Results

4.1 Introduction

This chapter presents the results obtained from the XPS analysis undertaken on real sample and a high throughput activity screening of titania supported Pt and Au nanoparticle catalysts of various particle sizes for CO oxidation at relatively low reaction temperatures. The discussion of results and comparison of activities for both Pt and Au nanoparticle catalysts are addressed. The results presented in this chapter are set within the context of the literature.

4.2 Platinum and Gold Nanoparticle Catalyst

4.2.1 XPS Measurements

Titania and titania supported Pt and Au nanoparticles were further analysed using the XPS. **Figure 4.1 (a)** shows the Pt XPS spectra of Pt 4*f* core level for the 1.3 nm, 4.5 nm and 6.6 nm mean particle diameter and bulk Pt, **Figure 4.1 (b)** presents the binding energy as a function of particle size. A shift in the Pt $4f_{7/2}$ peak for the 1.3 nm particles of 0.7 eV to higher binding energy (72.1 eV) is observed. This shift increases to 0.9 eV at a peak position of 72.3 eV for 4.5 nm particles followed by a dramatic drop to 0.5 eV at a peak position of 71.9 eV for the 6.6 nm particle size relative to bulk Pt $4f_{7/2}$ at 71.4 eV. The shift to higher binding energy for the smallest particles of Pt is consistent to that reported in the literature and was attributed to final state effect.[178] To get an insight of Pt nanoparticles catalyst after reaction, XPS study was carried out after the catalyst was submitted to the reaction conditions. The results did not show any significant change in binding energy shift as shown in **Figure 4.1 (b)**. **Figure (c)** and **Figure 4.1 (d)** present the integrated XPS intensity (Pt 4f/Ti 2p) as a function of Pt particle size (nm) and effective thickness (nm), respectively. The increase in the intensity is observed with increasing particle size, which indicates that Pt particles grow in size as more Pt is deposited.

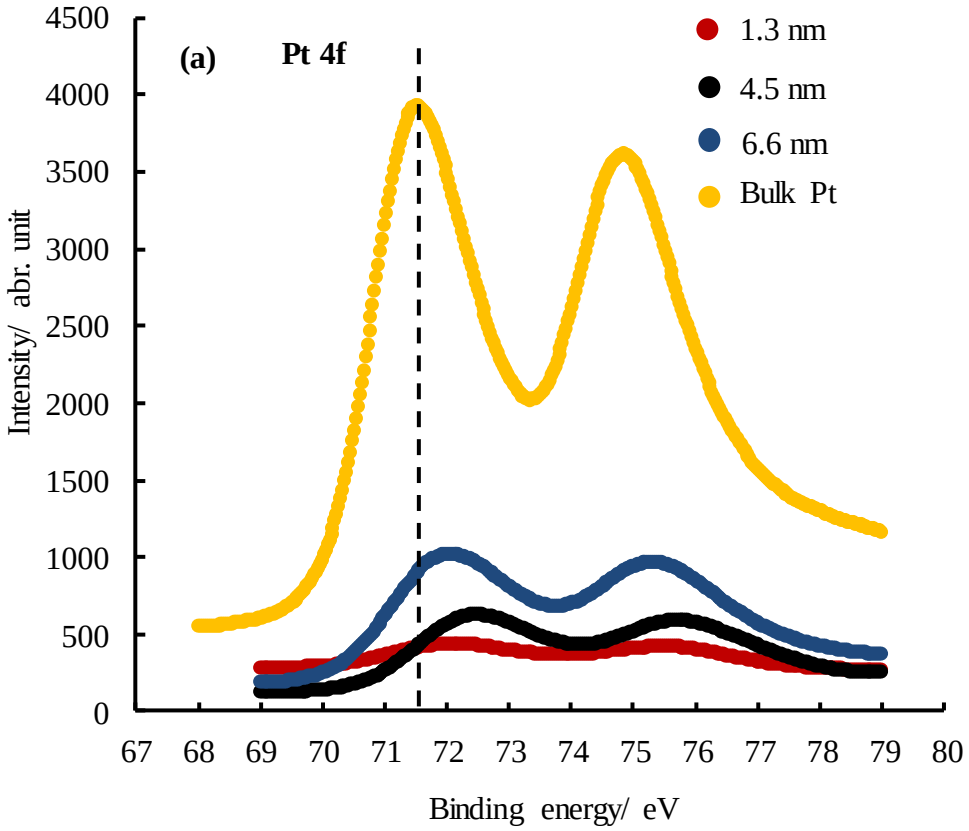
(a)
Pt 4f
1.3 nm
4.5 nm
6.6 nm
Bulk Pt
Intensity/ abr. unit
Binding energy/ eV

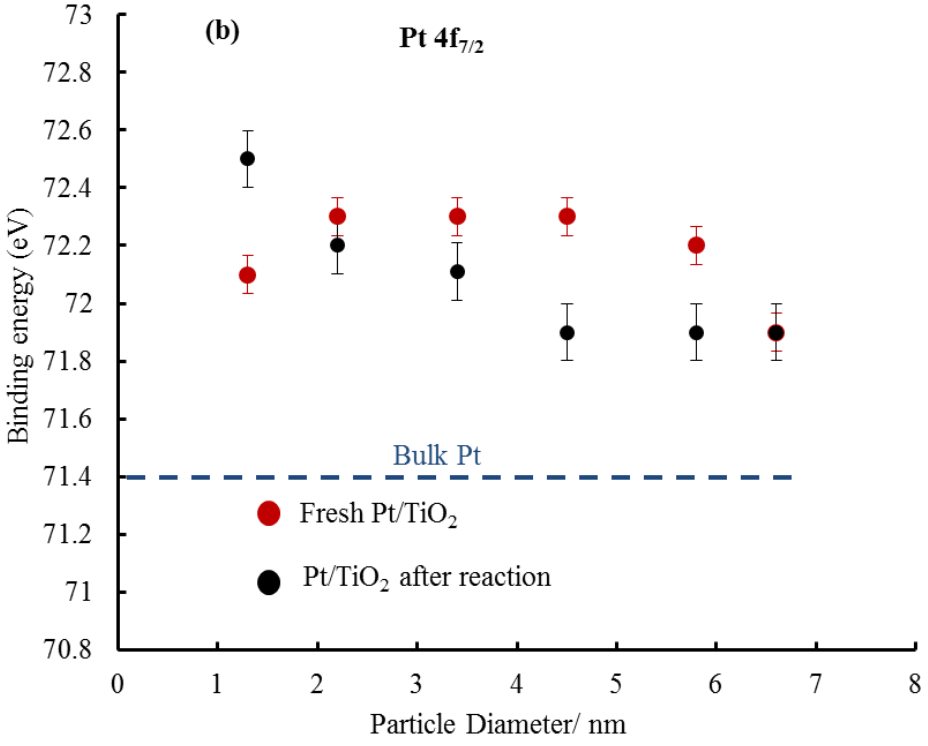
(b)
Pt 4f7/2
Bulk Pt
Fresh Pt/TiO2
Pt/TiO2 after reaction
Binding energy (eV)
Particle Diameter/ nm

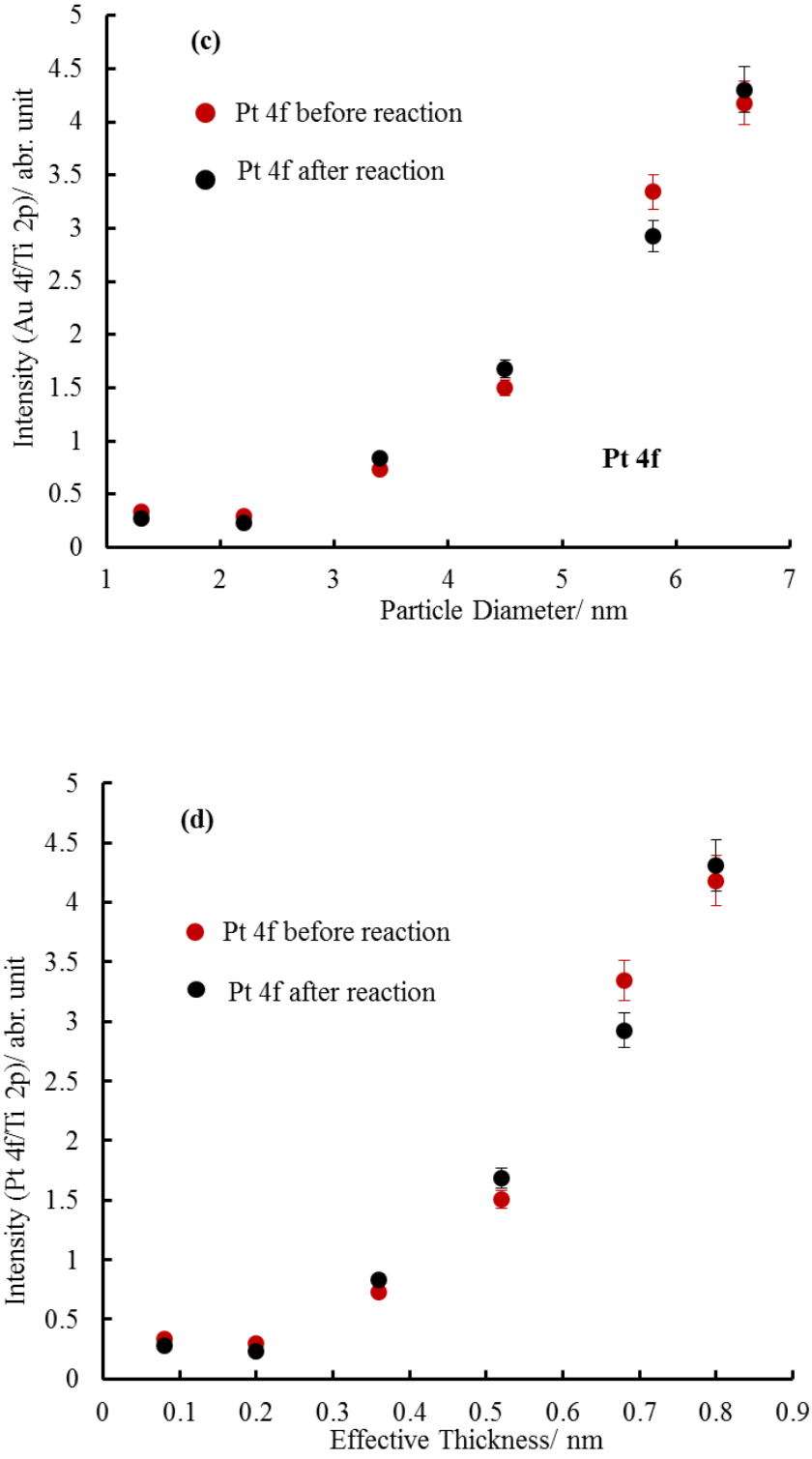

Figure 4.1: (a) XPS spectra of the Pt (4f) core level for titania supported Pt particles with a mean diameter of 1.3 nm, 4.5 nm and 6.6 nm and bulk Pt **(b)** Presents the binding energy as a function of Pt particle size for the Pt $4f_{7/2}$ before and after catalytic reaction, **(c)** and **(d)** present the integrated XPS intensity (Pt 4f/Ti 2p) as a function of particle size (nm) and effective thickness (nm) for the Pt (4f), respectively, before and after reaction. Spectra identification is shown in the figure legend.

Figure 4.2 (a) shows Au XPS spectra of 4*f* core level for 1.5 nm, 4.1 nm and 5.8 nm mean particle diameter sizes and bulk Au. A shift in the peak position is observed for 1.5 nm particles of approximately 0.42 eV to higher binding energy (84.42 eV) relative to bulk Au for the $4f_{7/2}$ core level at 84 eV, **Figure 4.2 (b)**. This shift decreases with increasing particle size to 0.1 eV for the 4.1 nm particles at 84.1 eV and it is 0.2 eV below bulk Au at 83.8 for 5.8 nm particles, consistent with previous findings. Previous XPS results on titania supported Au nanoparticles observed an upward shift to higher binding energy with decreasing particle size for Au $4f_{7/2,}$ this was attributed with final state effect.[15, 34] The XPS study after Au nanoparticles catalyst was subjected to reaction conditions did not show significant change in binding energy shift, **Figure 4.2 (b)**. This suggests that the particles retained their state throughout the experimental condition used in this work. **Figure 4.2 (c)** and **Figure 4.2 (d)** present the integrated XPS intensity (Au 4f/T 2p) as a function of Au particle size (nm) and effective thickness (nm), respectively. The observed increase in the intensity with increasing particle size indicates that much Au was being deposited.

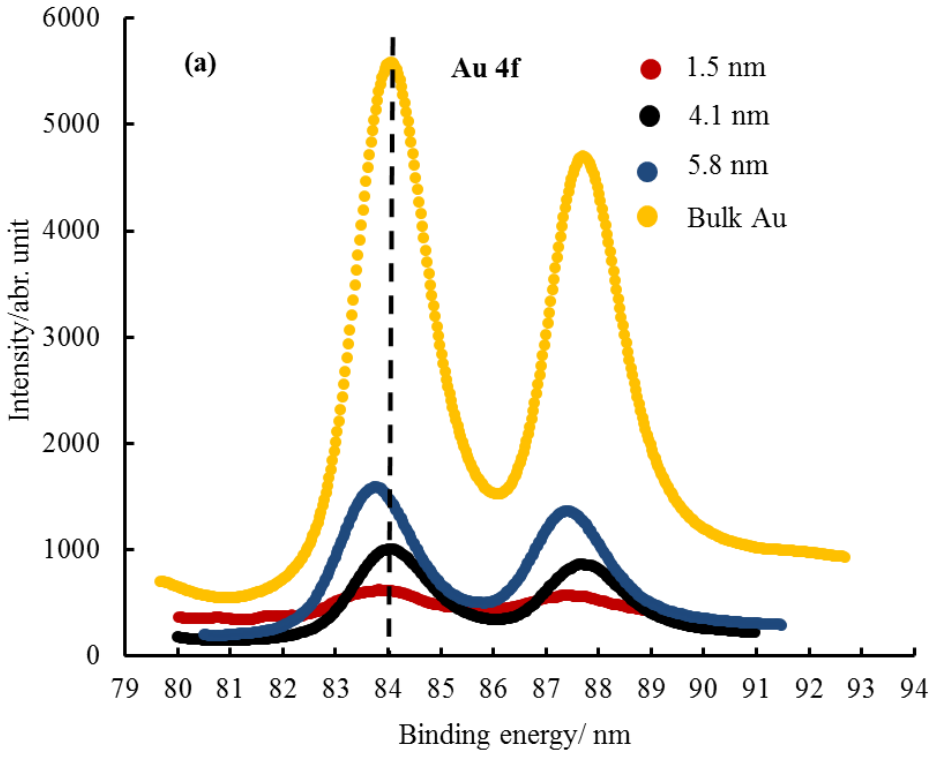

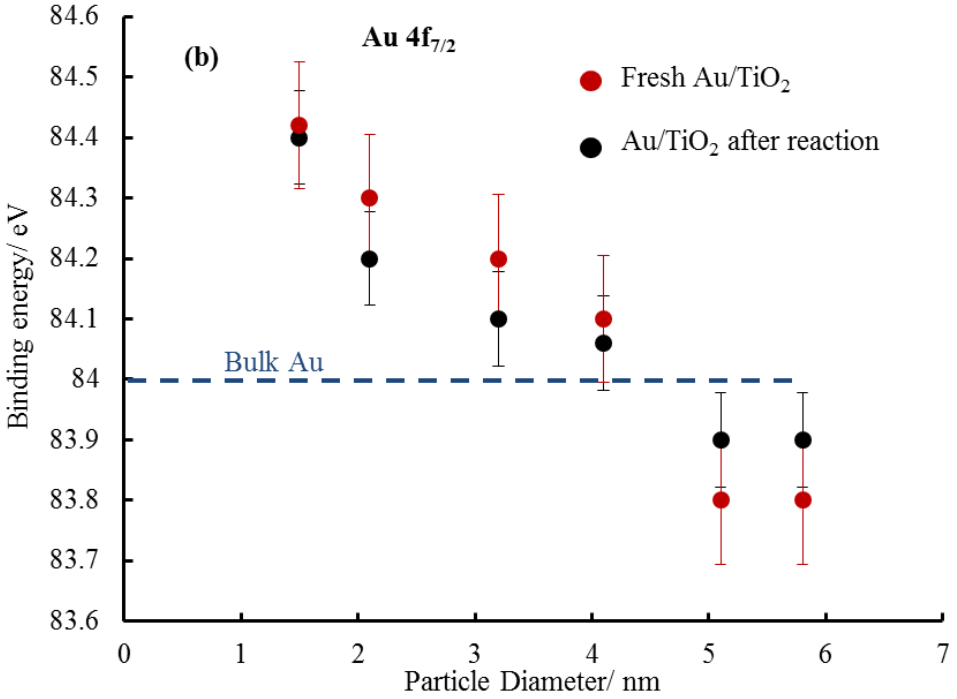
(b)
Au 4f7/2
Fresh Au/TiO2
Au/TiO2 after reaction
Bulk Au
Binding energy/ eV
Particle Diameter/ nm
84.6
84.5
84.4
84.3
84.2
84.1
84
83.9
83.8
83.7
83.6
0
1
2
3
4
5
6
7

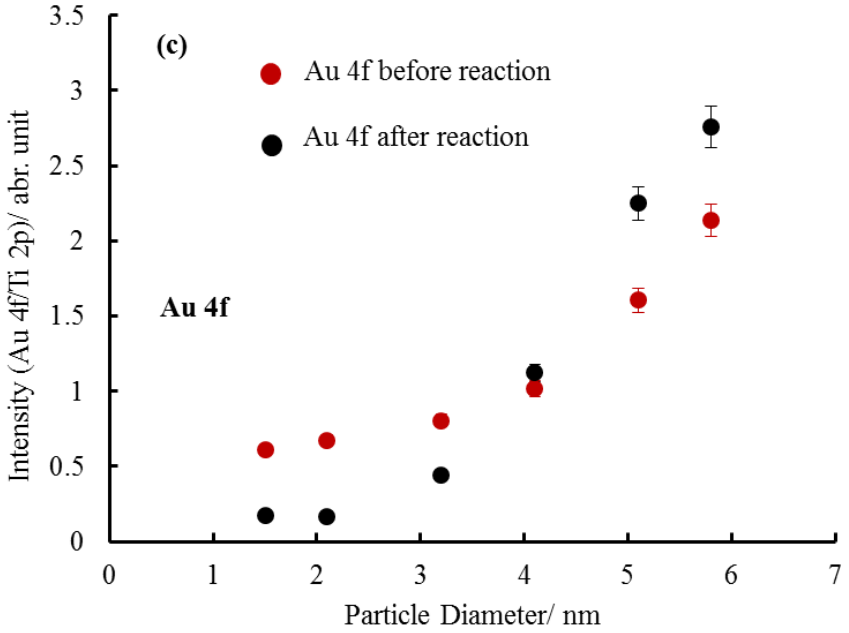
(c)
Au 4f before reaction
Au 4f after reaction
Au 4f
Intensity (Au 4f/Ti 2p)/ abr. unit
Particle Diameter/ nm
3.5
3
2.5
2
1.5
1
0.5
0
0
1
2
3
4
5
6
7

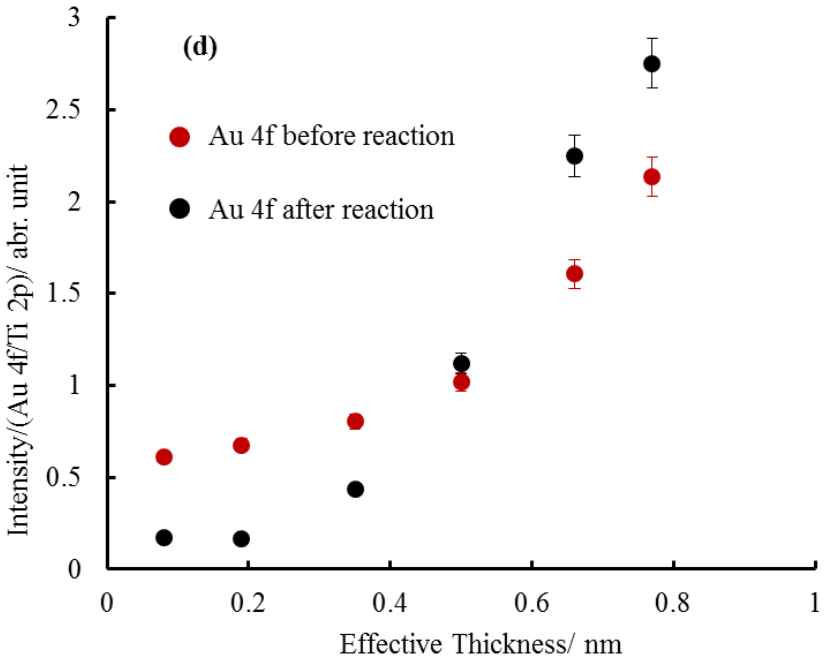

Figure 4.2: (a) XPS spectra of the Au (4f) core level for titania supported Au particles of 1.5 nm 4.1 nm and 5.8 nm mean diameter and bulk Au. **(b)** Presents the binding energy as a function of Au particle size for the Au $4f_{7/2}$ before and after catalytic reaction **(c)** and **(d)** present the integrated XPS intensity (Au 4f/Ti 2p) as a function of particle size (nm) and effective thickness (nm) for the Au 4f, respectively, before and after reaction. Spectra identification is shown in the figure legend.

Investigation of the Pt and Au core level energies shows that there is a small but detectable shift in the binding energy. These binding energy shifts however, depend on the species to which an atom is bonded.[99, 170] The binding energies shifts for the core level electrons can arise from either initial-state or final-state effects.[99] Initial-state effects (chemical shift) are associated with chemical bonding, which significantly influences the electronic configuration of an atom, this can result in a significant shift in binding energy, which in certain cases can be up to 10 eV.[170] Therefore, atoms in a high oxidation state produce XPS peaks at high binding energy as compared to the same atom found in low oxidation state.[170] Depending on the nature of interaction between the atom and its surroundings, the chemical shift could be either to higher or lower binding energy. Generally, as the oxidation state of an atom increases, the binding energy increases and vice versa. This can be rationalized in terms of the magnitude of the first and second ionization energy, equally, the higher the effective positive charge on the atom, the higher the binding energy of the photoelectron. The final-state effects on the other hand are the result of the removal of an electron from an atom which corresponds

to an ionic state, creation of a hole in place of the ejected photoelectron.[99] The effect toward the binding energy shift as a result of final-state is always a slight binding energy shift compared to that of initial-state effect. Since the core level binding energy shift for Pt and Au nanoparticles observed in this study is smaller, less than 1 eV, these shifts are associated with the final state-effect.[15, 34, 178]

Figure 4.3 presents the XPS spectra for the Ti 2p core level from TiO_2 upon which both Pt and Au particles were supported. The Ti $2p_{3/2}$ peak in the titania film appears between 459.9 eV and 461 eV, which is at a higher binding energy than that of Ti metal 454 eV, this is equivalent to the binding energy of Ti in TiO_2 (457.5 to 464.9 eV) which indicates that Ti is bonded to oxygen in the +4 oxidation state.[174] **Figure 3.3 (a)** presents the Ti 2p XPS spectra where Au particles were grown. A small change in Ti 2p intensity as a function of particle size is observed, perhaps Au particles exhibit 3D growth from the beginning, which results to smaller proportion of the substrate being covered. The XPS investigation of the effect of temperature on the growth mode of metal clusters has shown that both Au and Pt particles exhibit 3D growth from the beginning at a deposition temperature of about 475 K.[15] **Figure 3.3 (b)** presents the binding energy of Ti $2p_{3/2}$ as a function of particle size (nm). The Ti $2p_{3/2}$ peak appears at 458.4 eV and exhibits a small shift (0.1eV) to higher binding energy with no further shift with increasing particle size. **Figure 3.3 (c)** presents the Ti 2p spectra from TiO_2 upon which Pt particles were deposited. A constant Ti 2p intensity is observed as a function of particle size, followed by a reduction in the Ti 2p intensity at a Pt particle size of 6.6 nm. The decline in intensity at larger particle sizes of Pt can be explained in terms of larger particles being able to approach each other and form aggregates, hence covering a large area of the substrate as reported elsewhere.[26] However, there is still evidence that Pt particles exhibit a 3D growth mode from the beginning of deposition because of the unchanging intensity. Since both Au and Pt particles in this study were deposited at 200 ^{o}C, 3D particle growth from the beginning of particle growth would be expected. **Figure 3.3 (d)** presents the binding energy of Ti $2p_{3/2}$ as a function of particle size. The Ti $2p_{3/2}$ peak appears at 461 eV and slightly shifts by 0.1 eV to a higher binding energy, no further peak shift with increasing particle size is observed. The peak shift to higher

binding energy exhibited by Ti $2p_{3/2}$ where both Au and Pt particles are supported may indicate that their is an interaction between Pt/Au and the substrate.[89, 179]

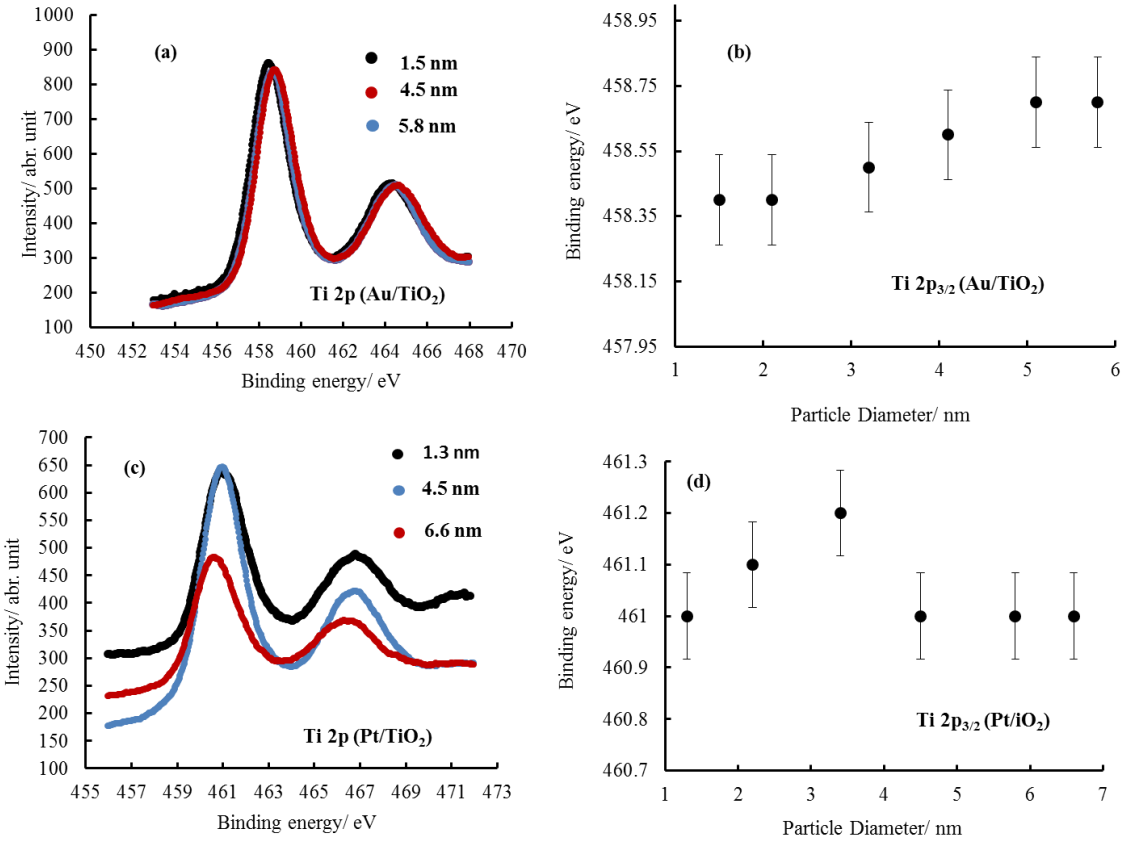

Figure 4.3: **(a)** XPS spectra of the Ti 2p core level for titania where Au particles of various sizes are supported. **(b)** Shows the binding energy of Ti $2p_{3/2}$ core level as a function of Au particle size. **(c)** Presents the binding energy of Ti $2p_{3/2}$ core level as a function Pt particle size. **(c)** Presents the XPS spectra of the Ti 2p core level of titania where Pt particles are supported and **(d)** presents the binding energy of Ti $2p_{3/2}$ core level as a function of Pt particle size. XPS spectra identification and particles sizes presented are shown in the figure legend.

Figure 3.4 presents XPS spectra of O1s core level for titania where both Pt and Au particles of various sizes are supported.

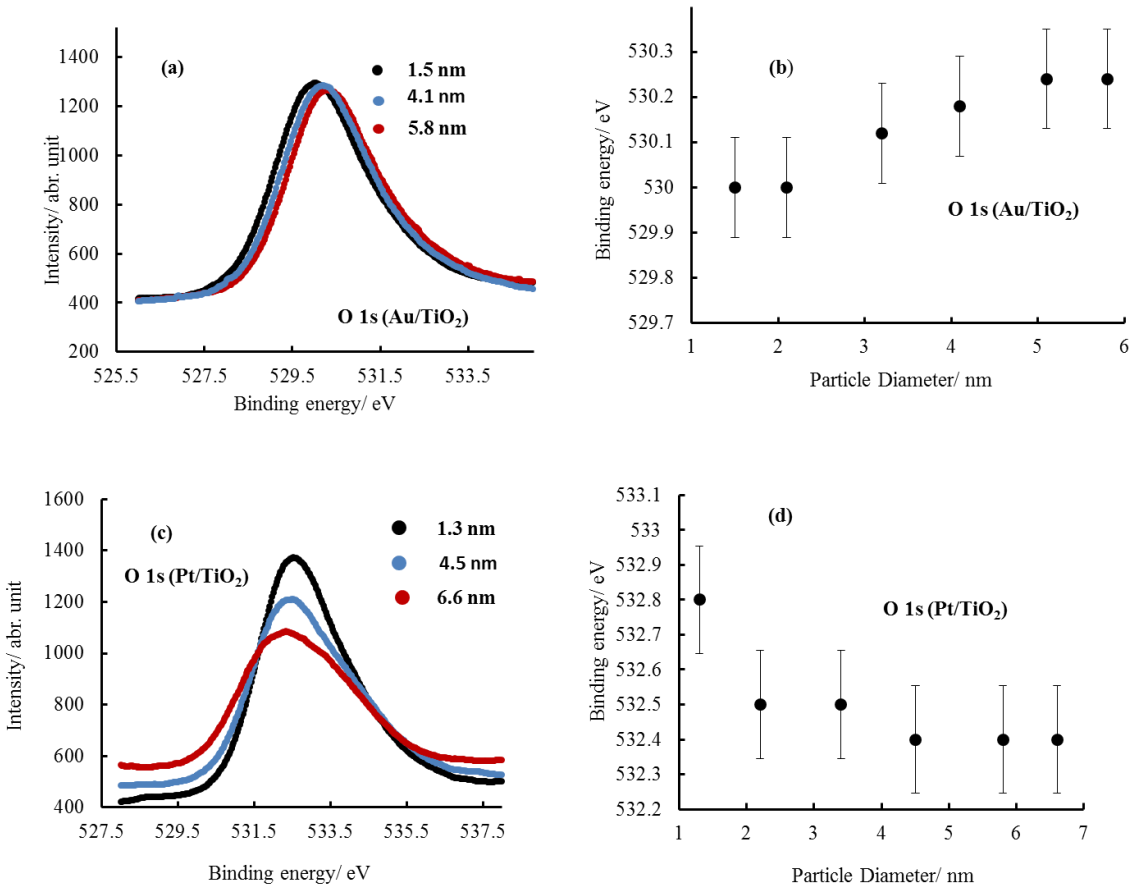

Figure 4.4: **(a)** XPS spectra of the O1s for titania where Au particles were supported. **(b)** Presents the binding energy as a function of Au particle size. **(c)** Present the XPS spectra of O1s core level where Pt particles were supported and **(d)** is the binding energy as function of Pt particle size. XPS spectra identification is also shown in the figure legend.

The O1s peak where Au particles were supported, **Figure 3.4 (a)** appears at about 530 eV with a slight peak shift to higher binding energy at constant intensity, the peak is at a position similar to the binding energy of O1s in TiO_2.[174] The O1s peak where Pt particles are supported, **Figure 3.4 (c)** shifted to higher binding energy at about 532.5 eV compared to that of its Au counterpart with observed decline in peak intensity as Pt particle sizes grow larger, which indicates that larger particles of Pt covered a larger area of the substrate.

4.3 Heterogeneous Catalysed CO Oxidation on Pt/TiO_2 Nanoparticle Catalyst

Figure 4.5 presents the absolute temperature change for CO oxidation activity on Pt nanoparticles at 80 ^{o}C and an approximately O_2:CO ratio of 1:1, with a total pressure of 1.1 x 10^{-1} mbar. The absolute temperature change at a total pressure of 1.1 mbar is presented in appendix **$1A_1$**. **Figure 4.6** presents the activity in TOF (s^{-1}) and specific mass activities (mol_{CO} conv. g^{-1}Pt mm^{-2} s^{-1}) as a function of particle size at an approximately O_2:CO ratio of 1:1, with a total pressure of 1.1 x 10^{-1} mbar and 1.1 mbar, respectively. **Table 4.1** presents the Pt particle sizes with their corresponding specific mass activity and TOF at a total pressure of 1.1 x 10^{-1} mbar. The particle sizes with their corresponding specific mass activity and TOF at 1.1 mbar is presented in appendix **$1A_2$**. **Table 4.2** presents the reactant gas pressure; total reactant gas pressure and the surface average mean temperature change across a catalyst surface.

O_2:CO ratio = 1:1, Total pressure = 1.1 x 10^{-1} mbar

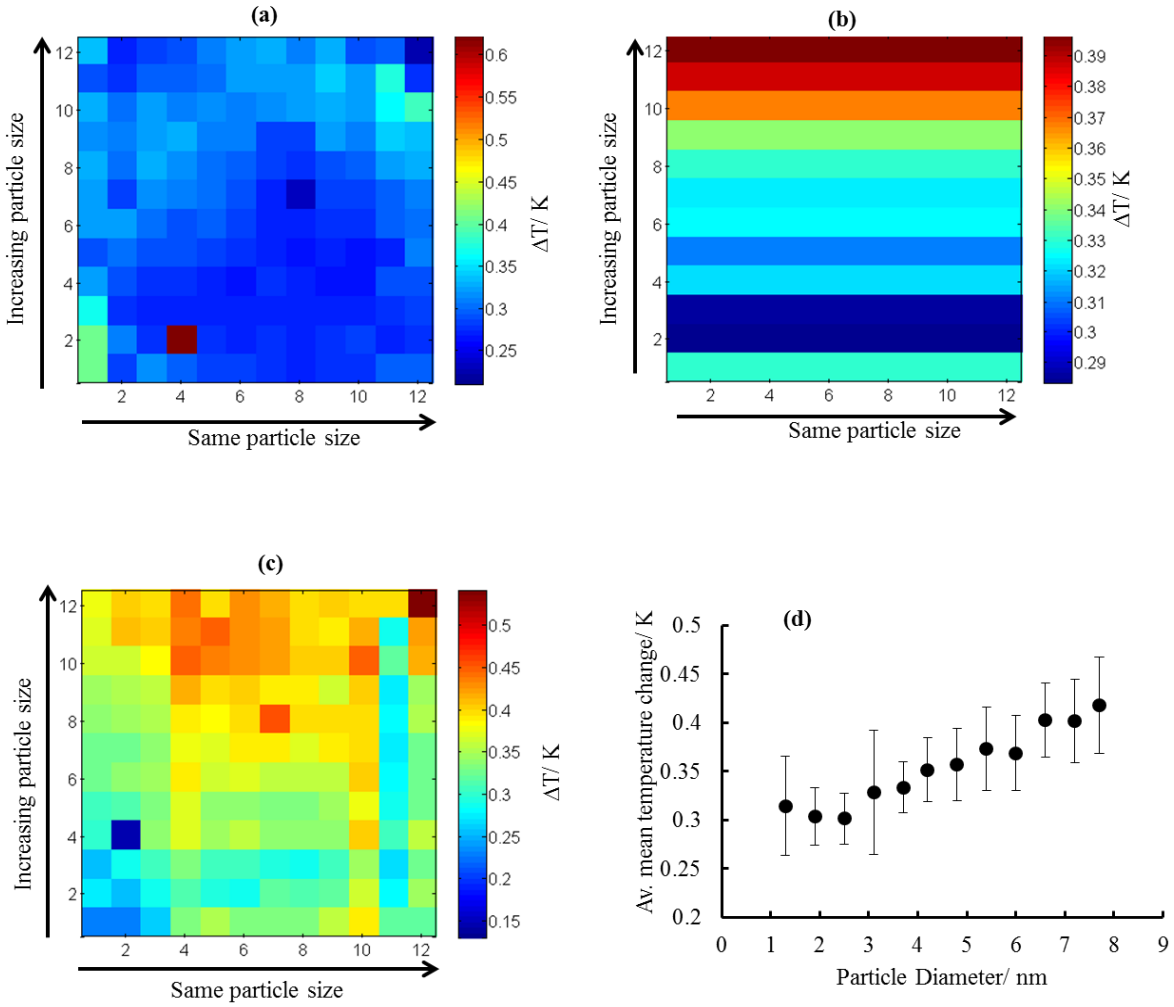

Figure 4.5: The absolute temperature change on Pt/TiO_2 catalyst as a function of particle size at approximately O_2:CO of 1:1, total pressure of 1.1 x 10^{-1} mbar. **(a)** Presents uncompensated infrared image, **(b)** row compensated and **(c)** row and column compensated image. **(d)** Presents the average mean temperature change as a function of particle sizes for the row and column compensated infrared images. The row and column numbers are shown on the x and y axes on the IR-images. The reaction temperature was 80 ^{o}C at an exposure time of 5 minutes.

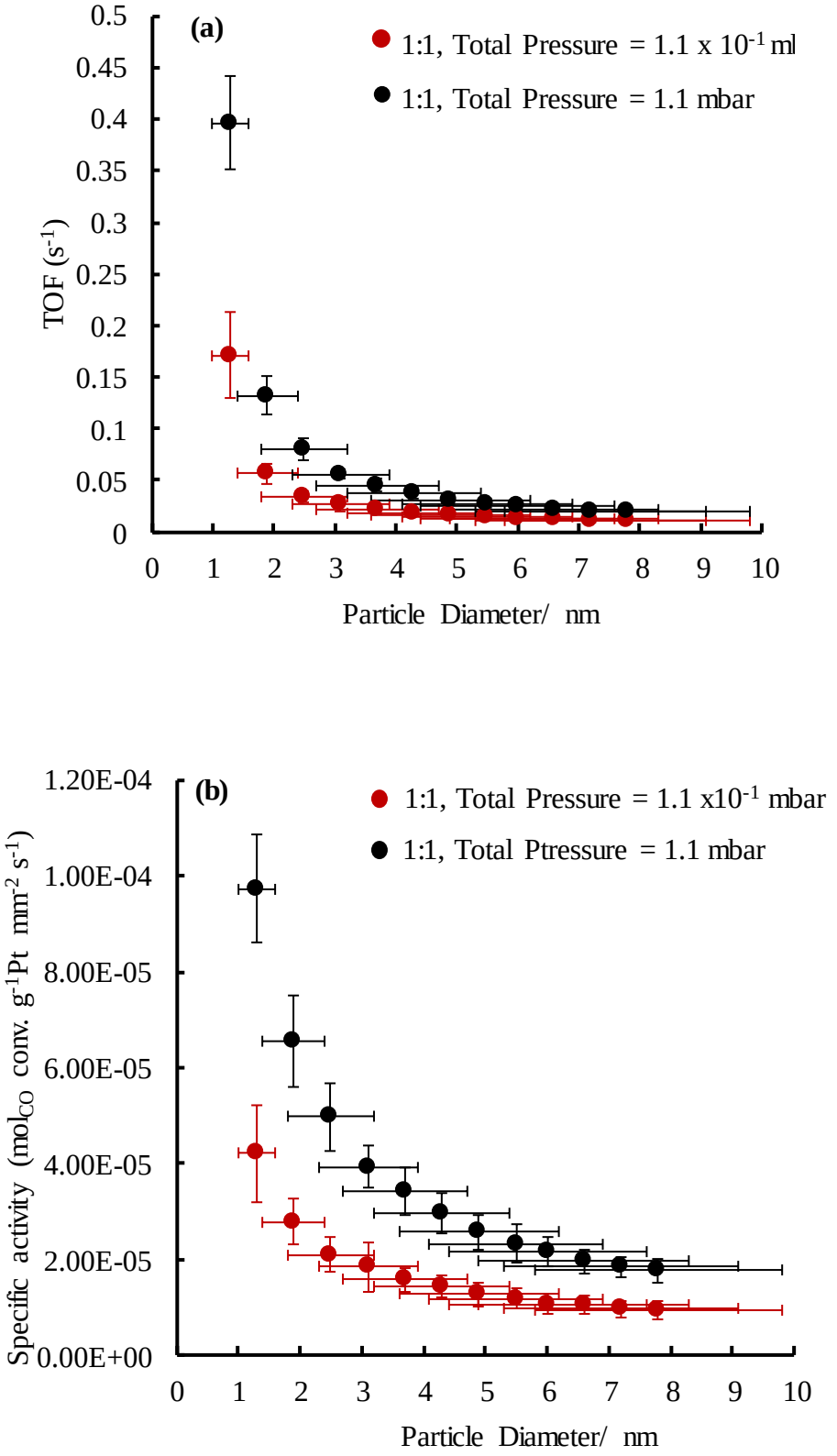

Figure 4.6: (a) TOF, **(b)** specific mass activity of Pt nanoparticle catalyst supported on titania for the CO oxidation reaction as a function of particle size (diameter/ nm) at approximately an O_2:CO ratio of 1:1, with a total pressure of 1.1 x 10^{-1} mbar and 1.1 mbar, the reaction temperature was 80 ^{o}C. The total pressure is also indicated in the figure legend.

P.diameter (nm)	ΔT/K	Power ($Js^{-1}mm^{-2}$)	mol_{CO} conv.($mm^{-2}s^{-1}$)	Total particle mass (g)	Total particle area (mm^2)	mol_{Pt} in the surface (mm^{-2})	Spec. mass activity (mol_{CO} conv.g^{-1}Pt mm^{-2} s^{-1})	TOF (s^{-1})
1.3±0.3	0.314±0.05	1.239E-5±2.94E-6	4.378E-11±1.04E-11	1.04E-6 ±8.3E-14	10.262±0.9	2.556E-10±2.24E-11	4.210E-5±1.00E-5	0.171±0.041
1.9±0.5	0.303±0.03	1.196E-5±2.06E-6	4.227E-11±7.31E-12	1.52E-6 ±1.2E-13	30.206±3.0	7.524E-10±7.47E-11	2.781E-5±4.81E-6	0.056±0.009
2.5±0.7	0.301±0.03	1.187E-5±2.07E-6	4.196E-11±7.32E-12	2.00E-6 ±1.6E-13	50.150±4.6	1.249E-9±1.15E-10	2.098E-5±3.66E-6	0.034±0.005
3.1±0.8	0.328±0.06	1.292E-5±3.43E-6	4.566E-11±1.21E-12	2.46E-6 ±1.9E-13	70.094±7.0	1.746E-9±1.74E-10	1.841E-5±5.07E-6	0.024±0.006
3.7±1.0	0.333±0.03	1.313E-5±2.17E-6	4.638E-11±7.66E-12	2.96E-6 ±2.3E-13	90.038±8.0	2.243E-9±1.99E-10	1.567E-5±2.59E-6	0.021±0.003
4.2±1.1	0.352±0.03	1.384E-5±2.25E-6	4.891E-11±7.97E-12	3.44E-6 ±2.7E-13	109.982±10	2.740E-9±2.49E-10	1.422E-5±2.31E-6	0.018±0.002
4.8±1.3	0.357±0.04	1.406E-5±2.66E-6	4.968E-11±9.43E-12	3.92E-6 ±3.1E-13	129.926±12	3.236E-9±1.99E-10	1.268E-5±2.41E-6	0.015±0.002
5.5±1.4	0.373±0.04	1.468E-5±2.72E-6	5.188E-11±9.61E-12	4.40E-6 ±3.5E-13	149.870±14	3.733E-9±3.49E-10	1.179E-5±2.18E-6	0.014±0.002
6.0±1.6	0.368±0.04	1.452E-5±2.67E-6	5.129E-11±9.45E-12	4.80E-6 ±3.8E-13	166.490±16	4.140E-9±3.99E-10	1.069E-5±1.97E-6	0.012±0.002
6.6±1.7	0.403±0.04	1.585E-5±2.81E-6	5.602E-11±9.94E-12	5.28E-6 ±4.2E-13	186.434±17	4.644E-9±4.23E-10	1.061E-5±1.88E-6	0.012±0.002
7.2±1.9	0.402±0.04	1.581E-5±2.80E-6	5.590E-11±9.91E-12	5.76E-6 ±4.6E-13	206.378±19	5.141E-9±4.73E-10	9.705E-6±1.72E-6	0.011±0.002
7.8±2.0	0.418±0.05	1.644E-5±3.27E-6	5.810E-11±1.16E-12	6.24E-6 ±4.9E-13	226.322±21	5.637E-9±5.23E-10	9.312E-6±1.85E-6	0.010±0.002
		Equation 2.2	**Equation 3.6**	**Equation 3.8**	**Equation 2.6**	**Equation 3.9**	**Equation 3.7**	**Equation 3.5**

Table 4.1: Pt/TiO_2 particle size and their corresponding specific mass activity and TOF at a reaction temperature of 80 ^oC and approximately O_2:CO ratio of 1:1, at a total pressure of 1.1 x 10^{-1} mbar. Parameters used to compute the activity values are also included. The equations used to compute the parameters presented in the table are shown. Silicon nitride membrane area is (1.44 ± 0.01) mm^2, silicon nitride thermal conductivity (7 ± 0.2) $Wm^{-1}K^{-1}$ and silicon nitride membrane thickness is 0.6 ± 0.02 μm. The standard deviation for the temperature change was obtained from twelve points on each low. The estimated errors in other parameters were estimated from the deference between the average value and the maximum possible value calculated using respective errors in each formula used to compute each parameter.

Pressure range	O_2-pressure (mbar)	CO-pressure (mbar)	Total pressure (mbar)	Average mean surface temperature change (K)
1	5.3×10^{-2}	5.7×10^{-2}	1.1×10^{-1}	0.35 ± 0.03
2	5×10^{-1}	6×10^{-1}	1.1	0.73 ± 0.02

Table 4.2: Oxygen and Carbon monoxide gas pressure ratios, total reactant gas pressure and the average mean surface temperature change across the catalyst surface from the catalytic activity of Pt/TiO_2. The reaction temperature was 80 ^oC at an exposure time of 5 minutes.

The CO oxidation by O_2 on Pt supported nanoparticle catalyst of sizes ranging between 1.3 nm and 7.8 nm particle sizes was investigated at 80 ^oC. The TOF and specific mass activity increased with decreasing particle size, **Figure 4.6 (a)** and **Figure 4.6 (b)**. The TOF increased from 0.01 s^{-1}, (specific mass activity = 9.312×10^{-6} mol_{CO} conv. $g^{-1}Pt$ mm^{-2} s^{-1}) for 7.8 nm to 0.171 s^{-1}, (specific mass activity = 4.21×10^{-5} mol_{CO} conv. $g^{-1}Pt$ mm^{-2} s^{-1}) for a Pt particle size of 1.3 nm, **Table 4.1**. The activity increased with increasing reactant gas pressure for both TOF and specific mass activity to 0.396 s^{-1}, (specific mass activity = 9.743×10^{-5} mol_{CO} conv. $g^{-1}Pt$ mm^{-2} s^{-1}) for the smallest Pt particle.

Figure 4.7 presents the temperature change for the CO oxidation reaction on Pt at 170 ^oC and O_2:CO ratio of 1:1 at a total pressure of 7.2×10^{-2} mbar. The temperature change at a total pressure of 8.4×10^{-2} mbar and 1.04×10^{-1} mbar is presented in appendix **$1B_1$** and **$1B_2$**, respectively. **Figure 4.8** presents the TOFs and specific mass activities as a function of particle size at an O_2:CO ratio of 1:1, total pressure of 7.2×10^{-2} mbar, 8.4×10^{-2} mbar and 1.04×10^{-1} mbar, respectively. **Table 4.3** presents Pt particle sizes with their corresponding specific mass activity and TOF at a total pressure of 7.2×10^{-2} mbar. The particle sizes with their corresponding specific mass activity and TOF at a total pressure of 8.4×10^{-2} mbar and 1.1×10^{-1} mbar is presented in appendix **$1B_3$** and **$1B_4$**, respectively. **Table 4.4** presents reactant gases pressure, total pressure and surface average mean temperature change across a catalyst surface.

O_2:CO ratio = 1:1, Total pressure = 7.2 x 10^{-2} mbar

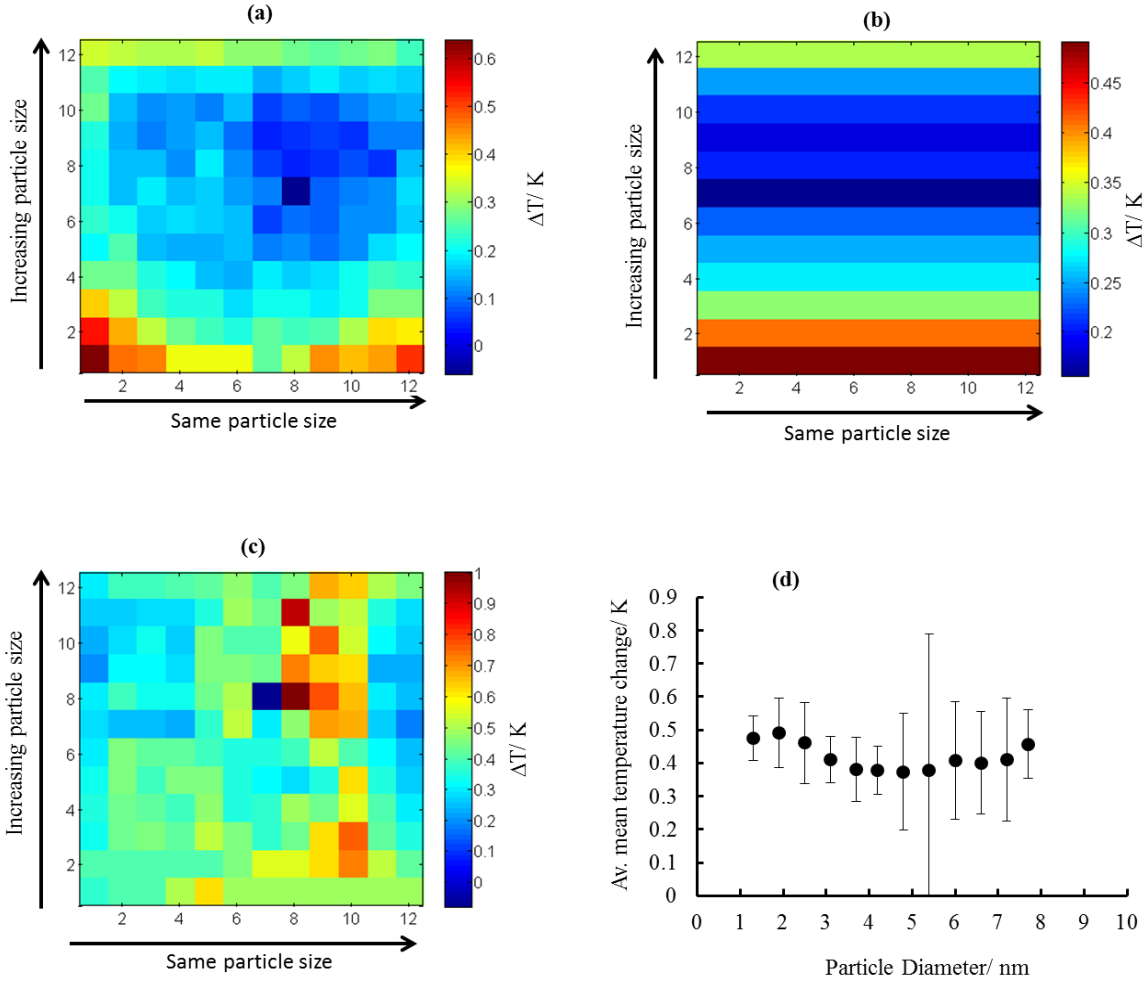

Figure 4.7: The temperature change on Pt/TiO_2 catalyst as a function of particle size at approximately O_2:CO ratio of 1:1, total pressure of 7.2 x 10^{-2} mbar. **(a)** Presents uncompensated infrared image, **(b)** row compensated and **(c)** row and column compensated images. **(d)** Presents the average mean temperature change as a function of particle sizes for the row and column compensated infrared images with column and row numbers indicated on the x and y axes. The reaction temperature was 170 ^{o}C at an exposure time of 5 minutes.

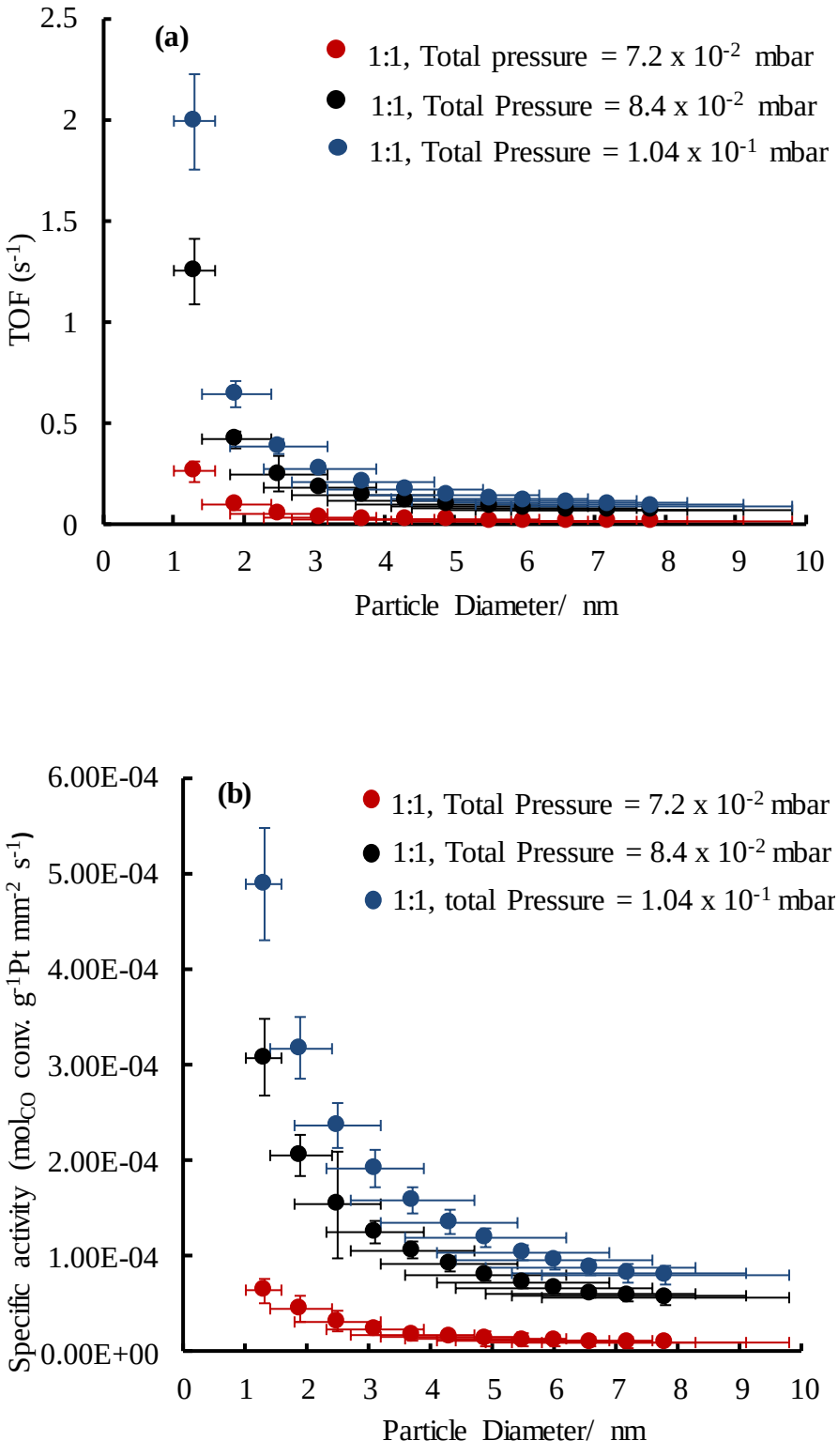

Figure 4.8: (a) TOF, **(b)** specific mass activity of Pt nanoparticle catalyst supported on titania for the CO oxidation reaction as a function of particle size (diameter/ nm) at an O_2:CO ratio of 1:1, with a total pressure of 7.2 x 10^{-2} mbar, 8.4 x 10^{-2} mbar and 1.04 x 10^{-1} mbar. The reaction temperature was 170 ^{o}C. The total pressure is also indicated in the figure legend.

P.diameter (nm)	ΔT/K	Power ($Js^{-1}mm^{-2}$)	mol_{CO} conv.($mm^{-2}s^{-1}$)	Total particle mass (g)	Total particle area (mm^2)	mol_{Pt} in the surface (mm^{-2})	Spec. mass activity (mol_{CO} conv.g^{-1}Pt mm^{-2} s^{-1})	TOF (s^{-1})
1.3±0.3	0.475±0.06	1.873E-5±3.81E-6	6.618E-11±1.34E-11	1.04E-6±8.3E-14	10.262±0.9	2.556E-10±2.24E-11	6.364E-5±1.30E-5	0.259±0.052
1.9±0.5	0.491±0.10	1.932E-5±5.58E-6	6.826E-11±1.97E-11	1.52E-6±1.2E-13	30.206±3.0	7.524E-10±7.47E-11	4.491E-5±1.30E-5	0.091±0.026
2.5±0.7	0.461±0.12	1.815E-5±6.32E-6	6.416E-11±2.23E-11	2.00E-6±1.6E-13	50.150±4.6	1.249E-9±1.15E-10	3.208E-5±1.12E-5	0.051±0.017
3.1±0.8	0.410±0.07	1.615E-5±4.07E-6	5.708E-11±1.43E-11	2.46E-6±1.9E-13	70.094±7.0	1.746E-9±1.74E-10	2.302E-5±6.04E-6	0.033±0.008
3.7±1.0	0.381±0.09	1.500E-5±4.84E-6	5.302E-11±1.71E-11	2.96E-6±2.3E-13	90.038±8.0	2.243E-9±1.99E-10	1.791E-5±5.78E-6	0.024±0.007
4.2±1.1	0.378±0.07	1.489E-5±3.98E-6	5.263E-11±1.40E-11	3.44E-6±2.7E-13	109.982±10	2.740E-9±2.49E-10	1.530E-5±4.09E-6	0.019±0.005
4.8±1.3	0.374±0.17	1.473E-5±8.18E-6	5.207E-11±2.89E-11	3.92E-6±3.1E-13	129.926±12	3.236E-9±1.99E-10	1.329E-5±7.38E-6	0.016±0.008
5.5±1.4	0.379±0.18	1.492E-5±8.63E-6	5.274E-11±3.04E-11	4.40E-6±3.5E-13	149.870±14	3.733E-9±3.49E-10	1.199E-5±6.93E-6	0.014±0.008
6.0±1.6	0.408±0.17	1.609E-5±8.25E-6	5.689E-11±2.91E-11	4.80E-6±3.8E-13	166.490±16	4.140E-9±3.99E-10	1.185E-5±6.08E-6	0.014±0.007
6.6±1.7	0.401±0.15	1.578E-5±7.43E-6	5.577E-11±2.62E-11	5.28E-6±4.2E-13	186.434±17	4.644E-9±4.23E-10	1.056E-5±4.98E-6	0.012±0.005
7.2±1.9	0.409±0.18	1.613E-5±8.69E-6	5.699E-11±3.07E-11	5.76E-6±4.6E-13	206.378±19	5.141E-9±4.73E-10	9.894E-6±5.33E-6	0.011±0.006
7.8±2.0	0.456±0.10	1.798E-5±5.45E-6	6.354E-11±1.92E-11	6.24E-6±4.9E-13	226.322±21	5.637E-9±5.23E-10	1.018E-5±3.09E-6	0.011±0.003
		Equation 2.2	**Equation 3.6**	**Equation 3.8**	**Equation 2.6**	**Equation 3.9**	**Equation 3.7**	**Equation 3.5**

Table 4.3: Pt/TiO_2 particle size as determined by TEM and their corresponding specific mass activity and TOF at a reaction temperature of 170 ^oC and an O_2:CO ratio of 1:1, at a total pressure of 7.2 x 10^{-2} mbar. Parameters used to compute the activity values are also included. The equations used to compute the parameters presented in the table are shown. Silicon nitride membrane area is (1.44 ± 0.01) mm^2, silicon nitride thermal conductivity (7 ± 0.2) $Wm^{-1}K^{-1}$ and silicon nitride membrane thickness is 0.6 ± 0.02 μm. The standard deviation for the temperature change was obtained from twelve points on each low. The estimated errors in other parameters were estimated from the deference between the average value and the maximum possible value calculated using respective errors in each formula used to compute each parameter.

Pressure range	O_2-pressure (mbar)	CO-pressure (mbar)	Total pressure (mbar)	Average surface temperature change (K)
1	3.6×10^{-2}	3.6×10^{-2}	7.2×10^{-2}	0.42 ± 0.04
2	4.2×10^{-2}	4.2×10^{-2}	8.4×10^{-2}	2.99 ± 0.08
3	5.2×10^{-2}	5.2×10^{-2}	1.04×10^{-1}	3.41 ± 0.11

Table 4.4: Oxygen and Carbon monoxide gas pressure ratios, total pressure and total average mean surface temperature change across the catalyst surface from catalytic activity of Pt/TiO_2 catalyst. The reaction temperature was 170 ^oC at an exposure time of 5 minutes.

The oxidation of CO on Pt supported nanoparticle catalyst ranging between 1.3 nm and 7.8 nm particle sizes was studied at 170 ^oC. The TOF and specific mass activity increased with reduced particle size, **Figure 4.8 (a)** and **Figure 4.8 (b)**. The activity increased with increasing reactant gas pressure at the same reaction temperature. The observed TOF for a Pt particle of 1.3 nm was 0.259 s^{-1}, (specific mass activity = 6.364×10^{-5} mol_{CO} conv. $g^{-1}Pt$ mm^{-2} s^{-1}) at an O_2:CO ratio of 1:1, total pressure of 7.2×10^{-2} mbar, **Table 4.3**. The activity increased to 1.25 s^{-1}, (specific mass activity = 3.073×10^{-4} mol_{CO} conv. $g^{-1}Pt$ mm^{-2} s^{-1}), at a total pressure of 8.4×10^{-2} mbar. Further increase in reactant gas pressure up to a total pressure of 1.04×10^{-1} mbar led to further increase in activity both in TOF and specific mass activity to 1.991 s^{-1}, (specific mass activity of 4.893×10^{-4} mol_{CO} conv. $g^{-1}Pt$ mm^{-2} s^{-1}).

Figure 4.9 presents the temperature change from experiment where the catalyst surface was pre-exposed to oxygen at a reaction temperature of 170 ^oC and subsequently allowing CO gas into a reaction chamber at an O_2:CO ratio of approximately 2:1, with a total pressure of 1.5×10^{-1} mbar. The temperature change at an O_2:CO ratio of approximately 1:1, at a total pressure of 1.9×10^{-1} mbar and an O_2:CO ratio of 1:1, at a total pressure of 2.2×10^{-1} mbar is presented in appendix **$1C_1$** and **$1C_2$**, respectively. **Figure 4.10** presents the TOF and specific mass activity at an O_2:CO ratio of approximately 2:1, with a total pressure of 1.5×10^{-1} mbar, an O_2:CO ratio of approximately 1:1, with a total pressure of 1.9×10^{-1} mbar and an O_2:CO ratio of 1:1, with a total pressure of 2.2×10^{-1} mbar. **Table 4.5** presents the Pt particle sizes with their corresponding specific mass activity and TOF at a total pressure of 1.5×10^{-1} mbar. The particle sizes with their corresponding specific mass activity and TOF at a total pressure of 1.9×10^{-1} mbar and 2.2×10^{-1} mbar is presented in appendix **$1C_3$** and **$1C_4$**, respectively. **Table 4.6** presents reac-

tant gases pressure, total pressure and surface average mean temperature change across a catalyst surface.

O_2:CO ratio = 2:1, Total pressure = 1.5 x 10^{-1} mbar

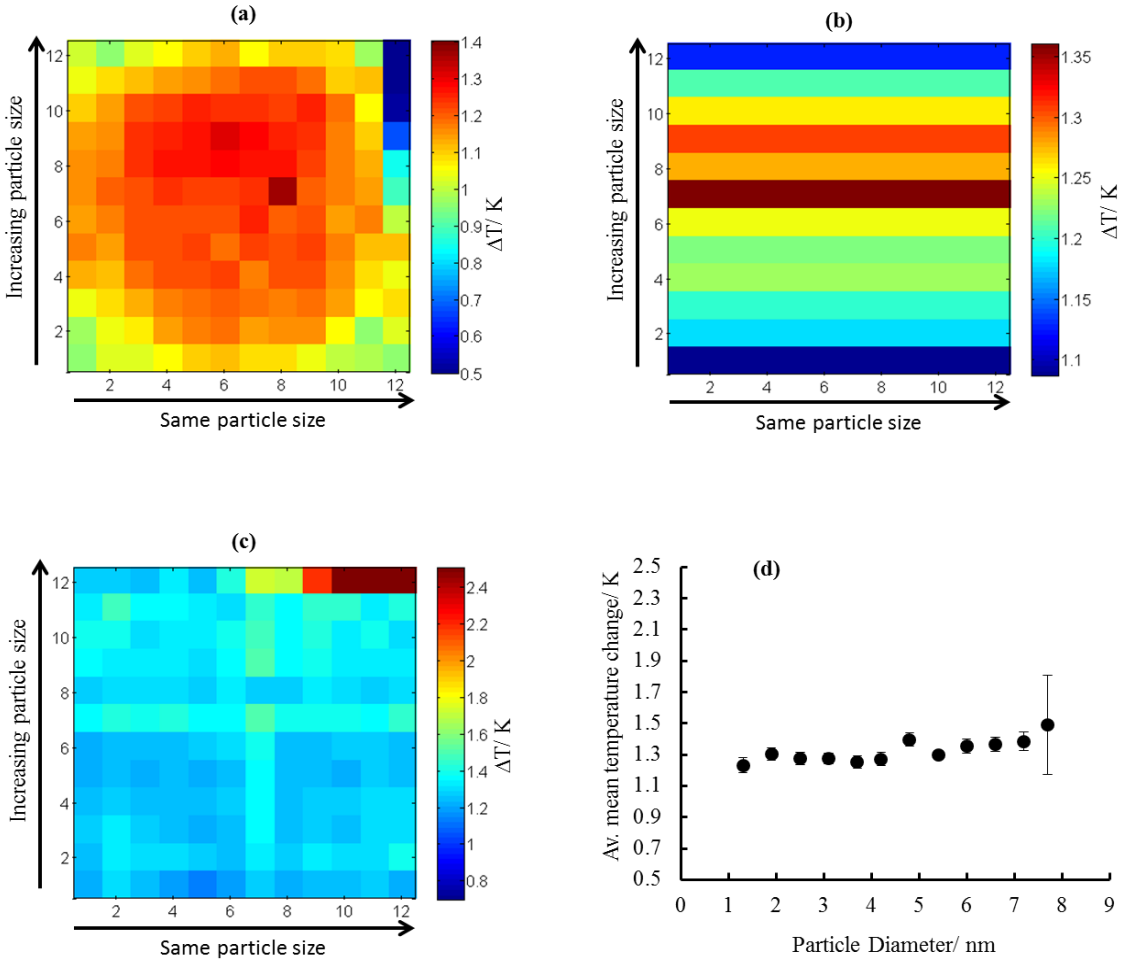

Figure 4.9: The temperature change on Pt/TiO_2 catalyst as a function of particle size at an approximately O_2:CO ratio of 2:1, total pressure of 1.5 x 10^{-1} mbar. **(a)** Presents uncompensated infrared image, **(b)** row compensated and **(c)** row and column compensated images. **(d)** Presents the average mean temperature change as a function of particle sizes for the complete compensated infrared images. The row and column numbers are shown on the x and y axes on the IR-images. The reaction temperature was 170 ^{o}C at an exposure time of 5 minutes.

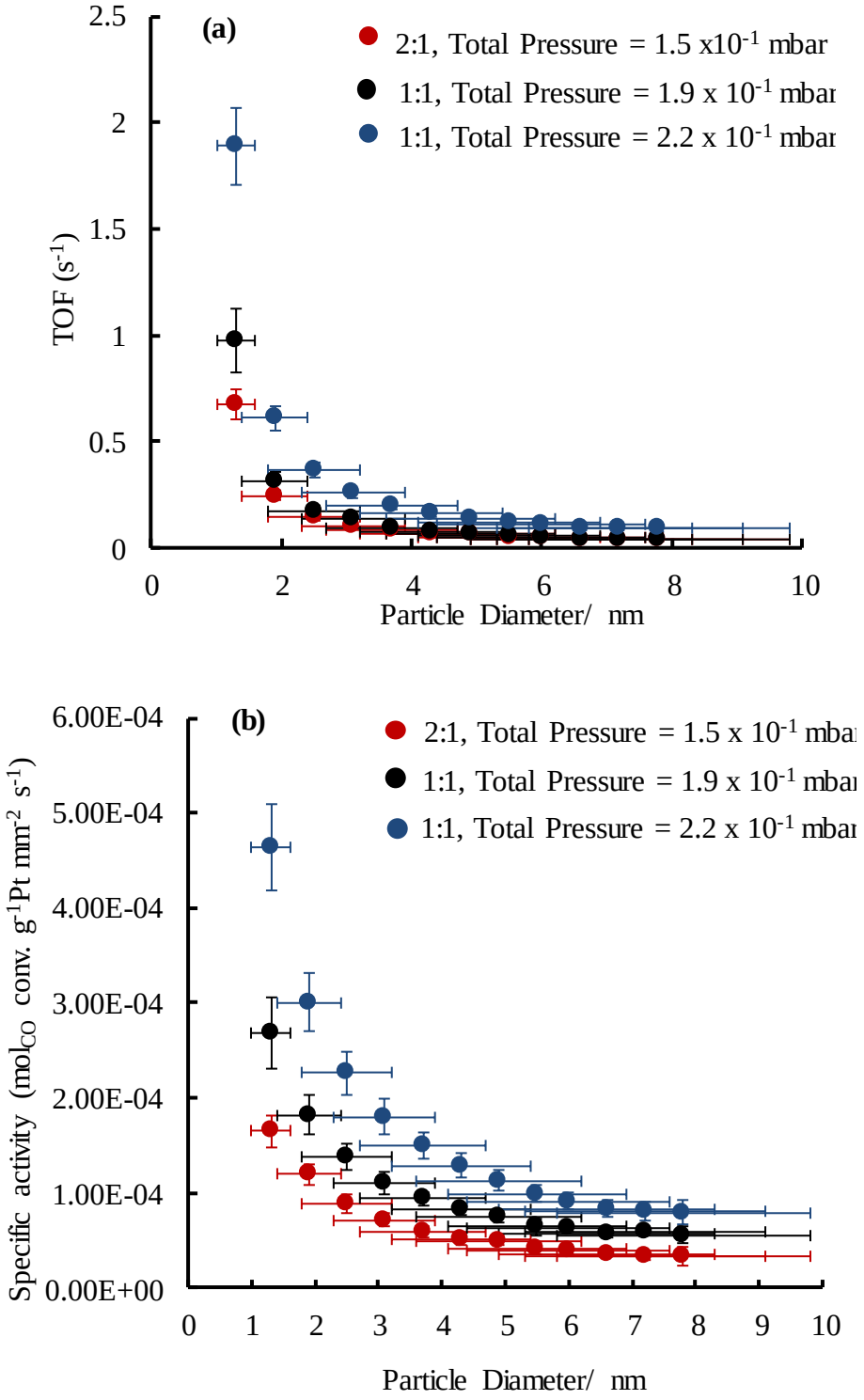

Figure 4.10: (a) TOF, **(b)** specific mass activity of Pt nanoparticle catalyst supported on titania for the CO oxidation reaction as a function of particle size (diameter/ nm) at an O_2:CO ratio of approximately 2:1, with a total pressure of 1.5 x 10^{-1} mbar, an O_2:CO ratio of approximately 1:1, at a total pressure of 1.9 x 10^{-1} mbar and an O_2:CO ratio of 1:1, with a total pressure of 2.2 x 10^{-1} mbar. The reaction temperature was 170 ^{o}C. The total pressure is also indicated in the figure legend.

P.diameter (nm)	ΔT/K	Power ($Js^{-1}mm^{-2}$)	mol_{CO} conv.($mm^{-2}s^{-1}$)	Total particle mass (g)	Total particle area (mm^2)	mol_{Pt} in the surface (mm^{-2})	Spec. mass activity (mol_{CO} conv.g^{-1}Pt mm^{-2} s^{-1})	TOF (s^{-1})
1.3±0.3	1.232±0.04	4.852E-5±5.09E-6	1.715E-10±1.80E-11	1.04E-6±8.3E-14	10.262±0.9	2.556E-10±2.24E-11	1.649E-4±1.73E-5	0.671±0.070
1.9±0.5	1.305±0.03	5.137E-5±4.89E-6	1.815E-10±1.73E-11	1.52E-6±1.2E-13	30.206±3.0	7.524E-10±7.47E-11	1.194E-4±1.14E-5	0.241±0.022
2.5±0.7	1.275±0.04	5.022E-5±5.20E-6	1.774E-10±1.84E-11	2.00E-6±1.6E-13	50.150±4.6	1.249E-9±1.15E-10	8.873E-5±9.18E-6	0.142±0.014
3.1±0.8	1.276±0.03	5.025E-5±4.79E-6	1.776E-10±1.69E-11	2.46E-6±1.9E-13	70.094±7.0	1.746E-9±1.74E-10	7.159E-5±7.46E-6	0.102±0.009
3.7±1.0	1.252±0.03	4.929E-5±4.74E-6	1.741E-10±1.67E-11	2.96E-6±2.3E-13	90.038±8.0	2.243E-9±1.99E-10	5.884E-5±5.66E-6	0.078±0.007
4.2±1.1	1.271±0.04	5.004E-5±5.21E-6	1.768E-10±1.84E-11	3.44E-6±2.7E-13	109.982±10	2.740E-9±2.49E-10	5.140E-5±5.35E-6	0.065±0.006
4.8±1.3	1.396±0.04	5.497E-5±5.55E-6	1.942E-10±1.96E-11	3.92E-6±3.1E-13	129.926±12	3.236E-9±1.99E-10	4.955E-5±5.00E-6	0.060±0.006
5.5±1.4	1.300±0.10	5.120E-5±7.80E-6	1.809E-10±2.76E-11	4.40E-6±3.5E-13	149.870±14	3.733E-9±3.49E-10	4.112E-5±6.26E-6	0.048±0.007
6.0±1.6	1.354±0.05	5.330E-5±5.87E-6	1.883E-10±2.07E-11	4.80E-6±3.8E-13	166.490±16	4.140E-9±3.99E-10	3.924E-5±4.32E-6	0.045±0.004
6.6±1.7	1.367±0.04	5.381E-5±5.48E-6	1.902E-10±1.94E-11	5.28E-6±4.2E-13	186.434±17	4.644E-9±4.23E-10	3.602E-5±3.67E-6	0.041±0.004
7.2±1.9	1.385±0.06	5.456E-5±6.34E-6	1.928E-10±2.24E-11	5.76E-6±4.6E-13	206.378±19	5.141E-9±4.73E-10	3.347E-5±3.89E-6	0.038±0.004
7.8±2.0	1.489±0.3	5.867E-5±1.67E-5	2.073E-10±5.91E-11	6.24E-6±4.9E-13	226.322±21	5.637E-9±5.23E-10	3.322E-5±9.47E-6	0.037±0.010
		Equation 2.2	**Equation 3.6**	**Equation 3.8**	**Equation 2.6**	**Equation 3.9**	**Equation 3.7**	**Equation 3.5**

Table 4.5: Pt/TiO_2 particle size as determined by TEM and their corresponding specific activity and TOF at a reaction temperature of 170 ^oC. At an O_2:CO ratio of approximately 2:1, with a total pressure of 1.5 x 10^{-1} mbar. Parameters used to compute the activity values are also included. The equations used to compute the parameters presented in the table are shown. Silicon nitride membrane area is (1.44 ± 0.01) mm^2, silicon nitride thermal conductivity (7 ± 0.2) $Wm^{-1}K^{-1}$ and silicon nitride membrane thickness is 0.6 ± 0.02 μm. The standard deviation for the temperature change was obtained from twelve points on each low. The estimated errors in other parameters were estimated from the deference between the average value and the maximum possible value calculated using errors in each formula used to compute each parameter.

Pressure range	O_2-pressure (mbar)	CO-pressure (mbar)	CO-pressure (mbar)	Average mean surface temperature change (K)
(a)	1.1×10^{-1}	4×10^{-2}	1.5×10^{-1}	1.32 ± 0.07
(b)	1.1×10^{-1}	8×10^{-2}	1.9×10^{-1}	2.08 ± 0.14
(d)	1.1×10^{-1}	1.1×10^{-1}	2.2×10^{-1}	3.26 ± 0.13

Table 4.6: Oxygen and Carbon monoxide gas pressure ratios, total reactant gas pressure and the average mean surface temperature change across the catalyst surface. The catalyst surface was pre-exposed to O_2 at a reaction temperature of 170 ^{o}C.

A linear increase in activity was observed on a pre-exposed oxygen surface by subsequently admitting the CO gas to reach a 1:1 ratio of O_2:CO mixture, at a total pressure of 2.2×10^{-1} mbar, **Figure 4.10 (a)** and **Figure 4.10 (b)**. The observed TOF was 0.671 s^{-1}, (specific mass activity = 1.649×10^{-4} mol_{CO} conv.g^{-1}Pt mm^{-2} s^{-1}) at a total pressure of 1.5×10^{-1} mbar for the smallest Pt particle size. The activity increased to 1.092 s^{-1}, (specific mass activity = 2.68×10^{-4} mol_{CO} conv.g^{-1}Pt mm^{-2} s^{-1}) at a total pressure of 1.9×10^{-1} mbar. Increasing reactant gases pressure to a total pressure of 2.2×10^{-1} mbar increased the activity to 1.889 s^{-1}, (specific mass activity = 4.64×10^{-4} mol_{CO} conv.g^{-1}Pt mm^{-2} s^{-1}).

Figure 4.11 presents the temperature change from experiment where the catalyst surface was pre-exposed to CO, at 170 ^{o}C and subsequently admitting oxygen gas into the reaction chamber at an O_2:CO ratio of approximately 1:2, with a total pressure of 1.5×10^{-1} mbar. The temperature change at an O_2:CO ratio of approximately 1:1, with a total pressure of 1.9×10^{-1} mbar and an O_2:CO ratio of 1:1, at a total pressure of 2.2×10^{-1} mbar is presented in appendix **1D$_1$** and **1D$_2$**, respectively. **Figure 4.12** presents the TOF and specific mass activity at an O_2:CO ratio of approximately 1:2, with a total pressure of 1.5×10^{-1} mbar, an O_2:CO ratio of approximately 1:1, with a total pressure of 1.9×10^{-1} mbar and an O_2:CO ratio of 1:1, with a total pressure of 2.2×10^{-1} mbar. **Table 4.7** presents the Pt particle sizes with their corresponding specific mass activity and TOF at a total pressure of 1.5×10^{-1} mbar. The particle sizes with their corresponding specific mass activity and TOF at a total pressure of 1.9×10^{-1} mbar and 2.2×10^{-1} mbar is presented in appendix **1D$_3$** and **1D$_4$**, respectively. **Table 4.8** presents reactant gas pressure, total pressure and surface average mean temperature change across a catalyst surface.

O_2:CO ratio = 1:2, Total pressure = 1.5 x 10^{-1} mbar

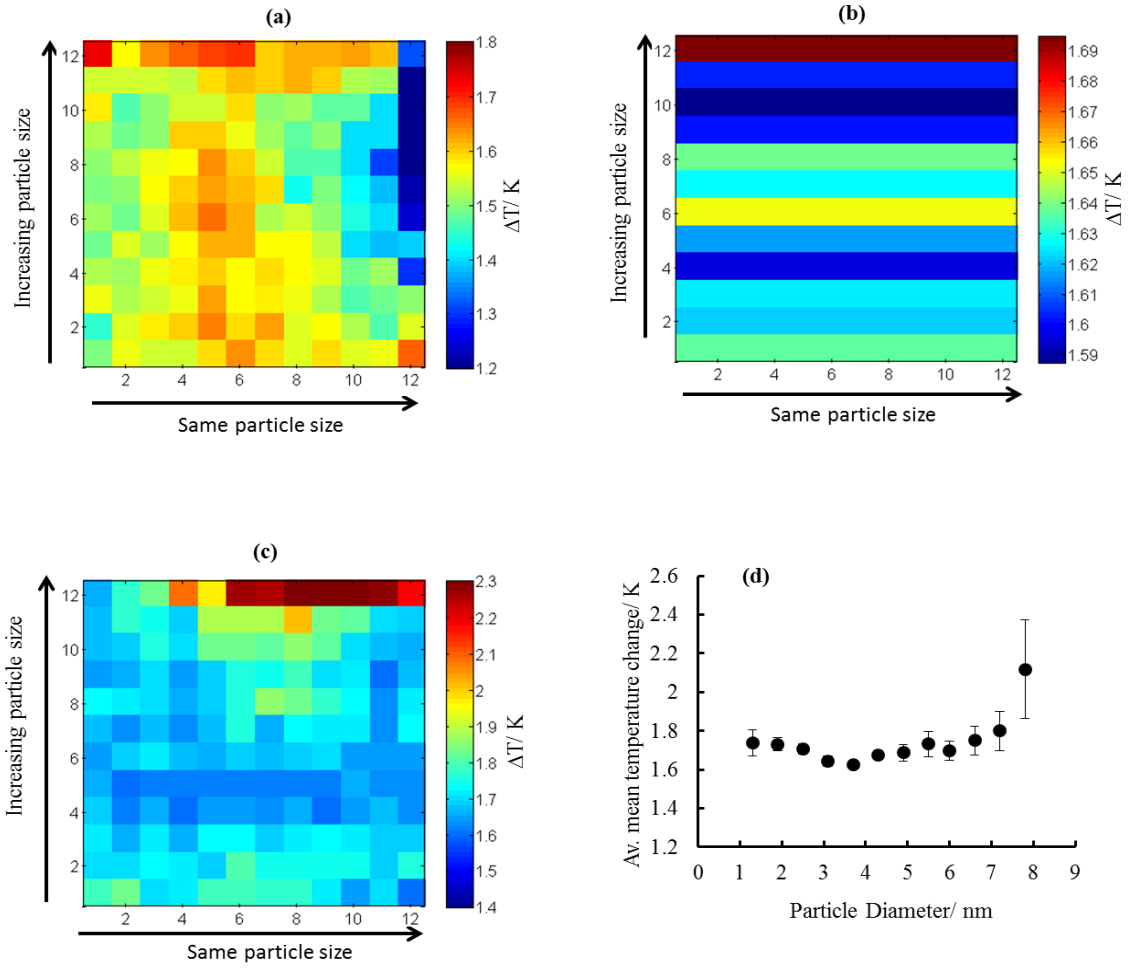

Figure 4.11: The temperature change on Pt/TiO_2 catalyst as a function of particle size at approximately O_2:CO ratio of 1:2 and 1:1, with a total pressure of 1.5 x 10^{-1} mbar. **(a)** Presents uncompensated infrared image, **(b)** row compensated and **(c)** row and column compensated images. **(d)** Presents the average mean temperature change as a function of particle sizes for the row and column compensated infrared images. The row and column numbers are shown on the x and y axes on the IR-images. The reaction temperature was 170 ^{o}C at an exposure time of 5 minutes.

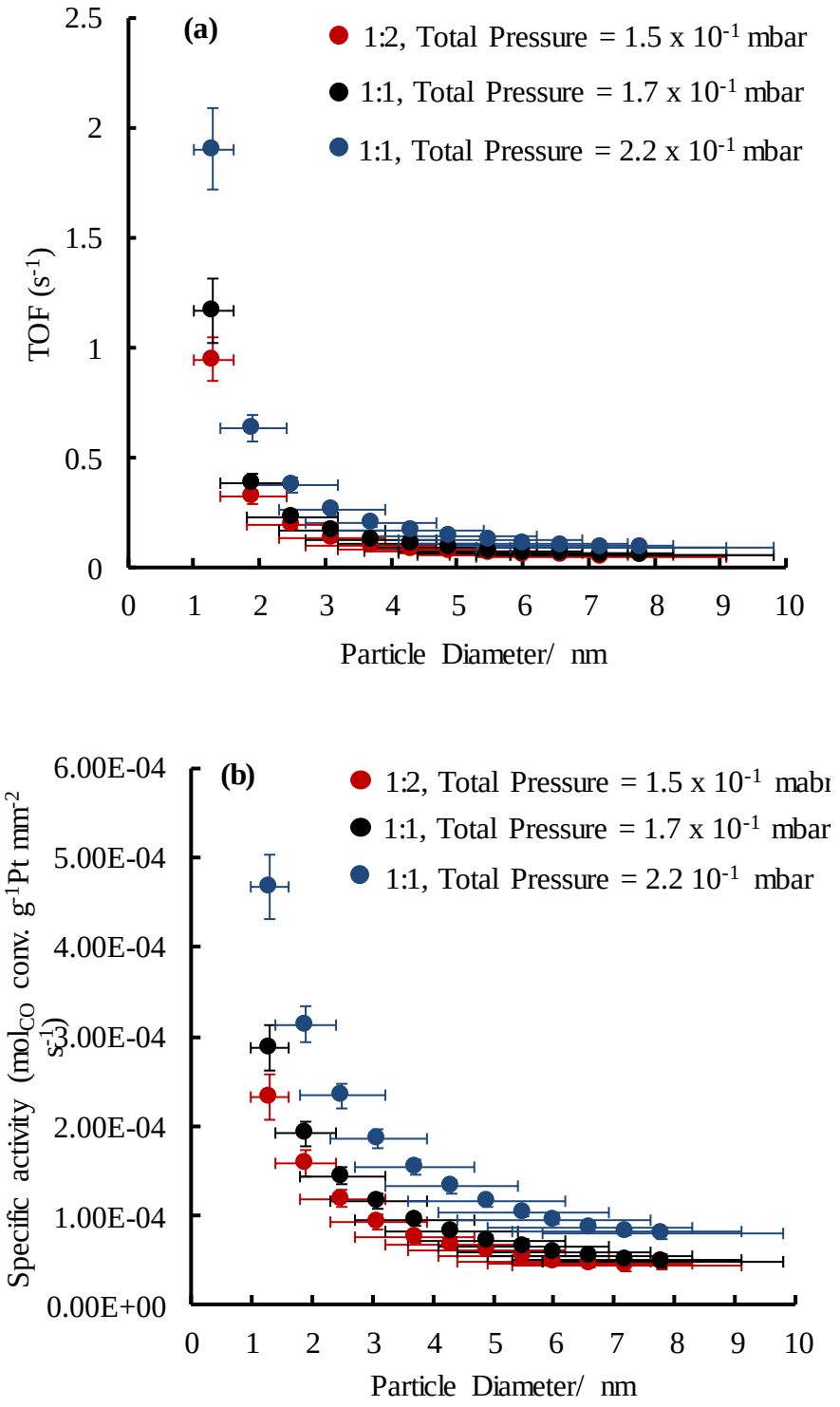

Figure 4.12: (a) TOF , **(b)** specific mass activity of Pt nanoparticle catalyst supported on titania for the CO oxidation reaction as a function of particle size (diameter/ nm) at an O_2:CO ratio of approximately 1:2, with a total pressure of 1.5 x 10^{-1} mbar, an O_2:CO ratio of approximately 1:1, at a total pressure of 1.7 x 10^{-1} mbar and an O_2:CO ratio of 1:1, with a total pressure of 2.2 x 10^{-1} mbar. The reaction temperature was 170 ^{o}C. The total pressure is also indicated in the figure legend.

P.diameter (nm)	ΔT/K	Power ($Js^{-1}mm^{-2}$)	mol_{CO} conv.($mm^{-2}s^{-1}$)	Total particle mass (g)	Total particle area (mm^2)	mol_{Pt} in the surface (mm^{-2})	Spec. mass activity (mol_{CO} conv.g^{-1}Pt mm^{-2} s^{-1})	TOF (s^{-1})
1.3±0.3	1.738±0.06	6.842E-5±7.35E-6	2.417E-10±2.60E-11	1.04E-6±8.3E-14	10.262±0.9	2.556E-10±2.24E-11	2.325E-4±2.50E-5	0.946±0.101
1.9±0.5	1.730±0.03	6.814E-5±6.03 E-6	2.407E-10±2.13E-11	1.52E-6±1.2E-13	30.206±3.0	7.524E-10±7.47E-11	1.584E-4±1.40E-5	0.320±0.028
2.5±0.7	1.704±0.02	6.711E-5±5.54 E-6	2.371E-10±1.96E-11	2.00E-6±1.6E-13	50.150±4.6	1.249E-9±1.15E-10	1.186E-4±9.79E-6	0.190±0.016
3.1±0.8	1.641±0.02	6.463E-5±5.37 E-6	2.283E-10±1.90E-11	2.46E-6±1.9E-13	70.094±7.0	1.746E-9±1.74E-10	9.209E-5±8.46E-6	0.131±0.011
3.7±1.0	1.625±0.02	6.398E-5±5.34 E-6	2.261E-10±1.89E-11	2.96E-6±2.3E-13	90.038±8.0	2.243E-9±1.99E-10	7.639E-5±6.37E-6	0.101±0.008
4.2±1.1	1.674±0.02	6.592E-5±5.47 E-6	2.329E-10±1.93E-11	3.44E-6±2.7E-13	109.982±10	2.740E-9±2.49E-10	6.772E-5±5.61E-6	0.085±0.007
4.8±1.3	1.686±0.04	6.639E-5±6.35 E-6	2.345E-10±2.24E-11	3.92E-6±3.1E-13	129.926±12	3.236E-9±1.99E-10	5.984E-5±5.72E-6	0.072±0.006
5.5±1.4	1.731±0.16	6.819E-5±1.15 E-6	2.409E-10±4.06E-11	4.40E-6±3.5E-13	149.870±14	3.733E-9±3.49E-10	5.476E-5±9.23E-6	0.065±0.011
6.0±1.6	1.696±0.05	6.678E-5±6.80 E-6	2.359E-10±2.24E-11	4.80E-6±3.8E-13	166.490±16	4.140E-9±3.99E-10	4.916E-5±5.01E-6	0.057±0.005
6.6±1.7	1.749±0.07	66.889E ±7.76 E-6	2.434E-10±2.74E-11	5.28E-6±4.2E-13	186.434±17	4.644E-9±4.23E-10	4.611E-5±5.19E-6	0.052±0.006
7.2±1.9	1.799±0.10	7.084E-5±9.19 E-6	2.503E-10±3.25E-11	5.76E-6±4.6E-13	206.378±19	5.141E-9±4.73E-10	4.346E-5±5.64E-6	0.049±0.006
7.8±2.0	2.118±0.25	8.341E-5±1.43 E-5	2.947E-10±5.04E-11	6.24E-6±4.9E-13	226.322±21	5.637E-9±5.23E-10	4.724E-5±8.08E-6	0.052±0.008
		Equation 2.2	**Equation 3.6**	**Equation 3.8**	**Equation 2.6**	**Equation 3.9**	**Equation 3.7**	**Equation 3.5**

Table 4.7: Pt/TiO_2 particle size as determined by TEM and their corresponding specific activity and TOF at a reaction temperature of 170 ^oC and an O_2:CO ratio of 1:2, at a total pressure of 1.5×10^{-1} mbar. Parameters used to compute the activity values are also included. The equations used to compute the parameters presented in the table are shown. Silicon nitride membrane area is (1.44 ± 0.01) mm^2, silicon nitride thermal conductivity (7 ± 0.2) $Wm^{-1}K^{-1}$ and silicon nitride membrane thickness is 0.6 ± 0.02 μm. The standard deviation for the temperature change was obtained from twelve points on each low. The estimated errors in other parameters were estimated from the deference between the average value and the maximum possible value calculated using errors in each formula used to compute each parameter.

Pressure range	O_2-pressure (mbar)	CO-pressure (mbar)	CO-pressure (mbar)	Average mean surface temperature change (K)
1	1.1×10^{-1}	4×10^{-2}	1.5×10^{-1}	1.74 ± 0.12
2	1.1×10^{-1}	6×10^{-2}	1.7×10^{-1}	2.07 ± 0.05
3	1.1×10^{-1}	1.1×10^{-1}	2.2×10^{-1}	3.35 ± 0.10

Table 4.8: Oxygen and Carbon monoxide gas pressure ratios, total reactant gas pressure and the average mean surface temperature change across the catalyst surface. The catalyst surface of the catalyst was pre-exposed to O_2 at a reaction temperature of 170 ^{o}C.

For a pre-adsorbed CO surface, **Figure 4.12 (a)** and **Figure 4.12 (b)**, the activity trend is similar to that of a pre-adsorbed oxygen surface. The activity increased with increasing oxygen pressure reaching a 1:1 ratio of O_2:CO, at a total pressure of 2.2×10^{-1} mbar. The TOF was 0.946 s^{-1}, (specific mass activity = 2.325×10^{-4} mol_{CO} conv.g^{-1}Pt mm^{-2} s^{-1}), at a total pressure of 1.5×10^{-1} mbar for a Pt particle size of 1.3 nm. The activity increased to 1.169 s^{-1}, (specific mass activity = 2.874×10^{-4} mol_{CO} conv.g^{-1}Pt mm^{-2} s^{-1}), at a total pressure of 1.7×10^{-1} mbar. The TOF and specific mass activity increased to 1.903 s^{-1}, (specific mass activity = 4.676×10^{-4} mol_{CO} conv.g^{-1}Pt mm^{-2} s^{-1}) at a total pressure of 2.2×10^{-1} mbar.

Further screening of Pt/TiO_2 nanoparticle catalyst was carried out at an elevated reaction temperature (240 ^{o}C) in order to investigate the effect of reaction temperature and reactant gas pressure for CO oxidation. The absolute temperature change obtained at approximately O_2:CO ratio of 1:1, with a total pressure of 6×10^{-1} mbar is presented in **Figure 4.13**. The absolute temperature change at an O_2:CO ratio of approximately 1:1, with a total pressure of 1.1 mbar and an O_2:CO ratio of approximately 1:1, at a total pressure of 2.4 mbar is presented in appendix **$1F_1$** and **$1F_2$**, respectively. **Figure 4.14** presents the TOF and specific mass activity at an O_2:CO ratio of approximately 1:1, with a total pressure of 6×10^{-1} mbar, an O_2:CO ratio of approximately 1:1, with a total pressure of 1.1 mbar and an O_2:CO ratio of 1:1, with a total pressure of 2.4 mbar. **Table 4.9** presents Pt particle sizes with their corresponding specific mass activity and TOF at a total pressure of 6×10^{-1} mbar. The particle sizes with their corresponding specific mass activity and TOF at a total pressure of 1.1 mbar and 2.4 mbar is presented in appendix **$1F_3$** and **$1F_4$**, respectively. **Table 4.10** presents the reactant gas pressure; total

reactant gas pressure and the surface average mean temperature change across the catalyst surface.

O_2:CO ratio = 1:1, Total pressure = 6 x 10^{-1} mbar

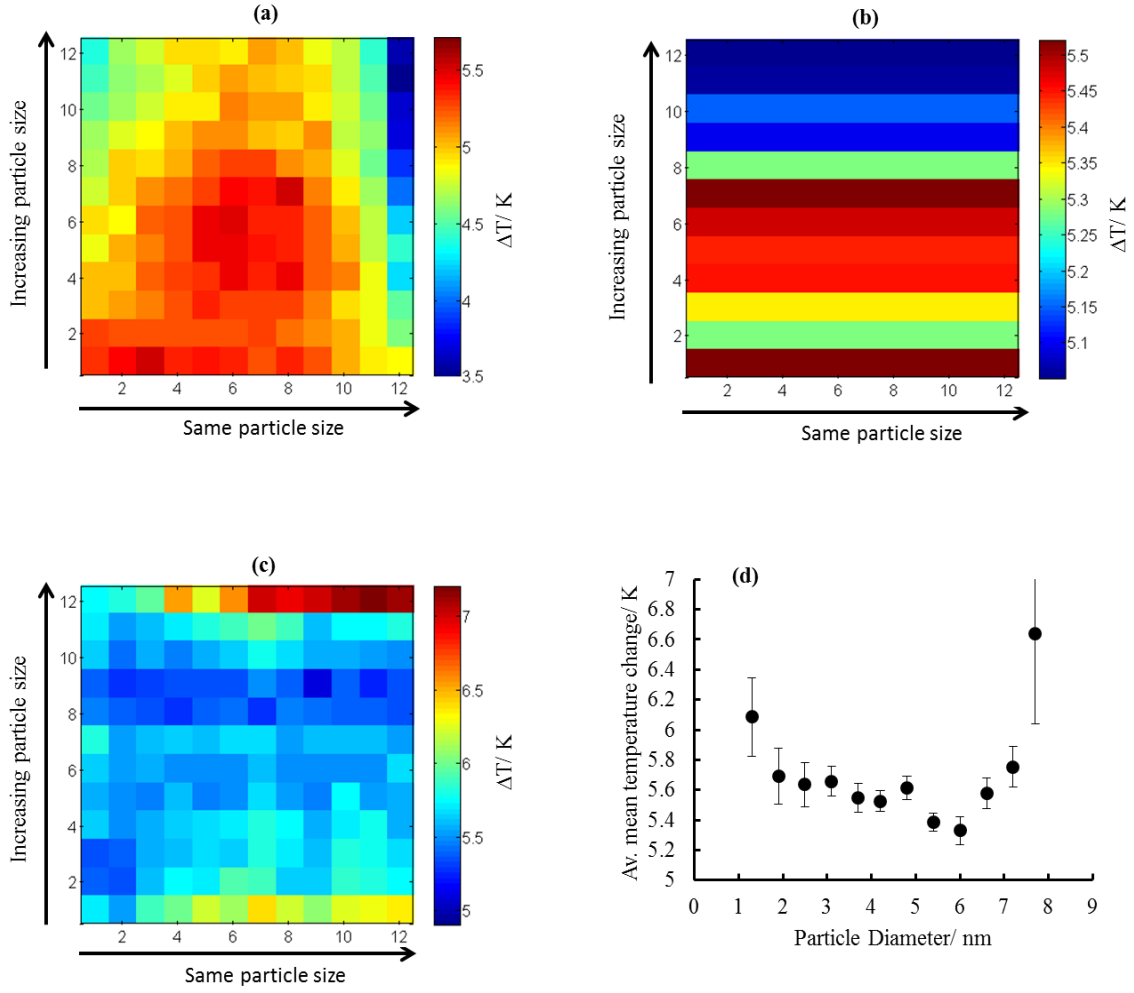

Figure 4.13: The temperature change on Pt/TiO_2 catalyst as a function of particle size at approximately O_2:CO of 1:1, with a total pressure of 6 x 10^{-1} mbar. **(a)** Presents uncompensated infrared images, **(b)** row compensated and **(c)** row and column compensated. **(d)** Presents the average mean temperature change as a function of particle sizes for the row and column compensated infrared images The row and column numbers are shown on the x and y axes on the IR-images. The reaction temperature was 240 ^{o}C at an exposure time of 5 minutes.

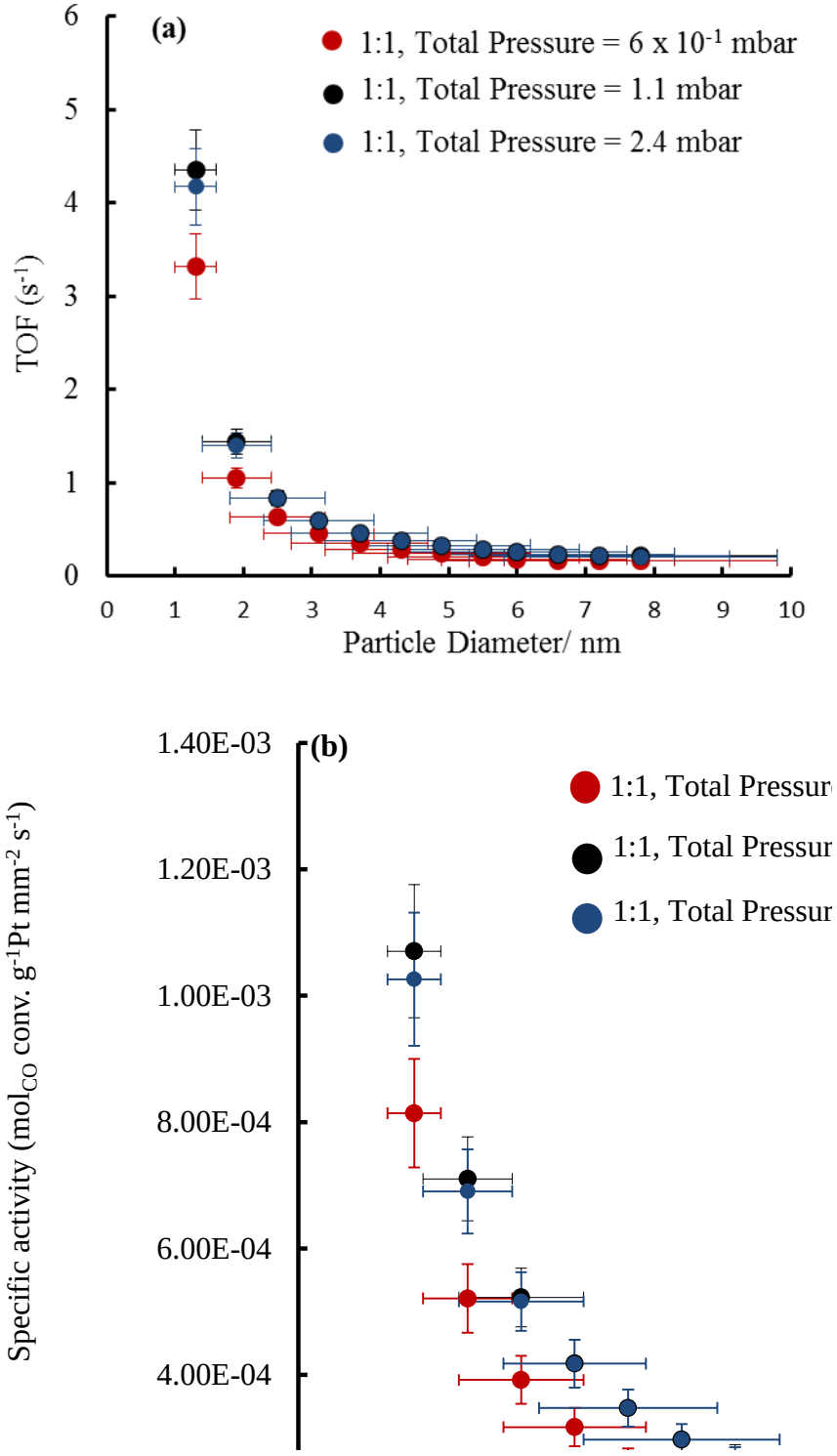

Figure 4.14: (a) TOF, **(b)** specific mass activity of Pt nanoparticle catalyst supported on titania for the CO oxidation reaction as a function of particle size (diameter/ nm) at an O_2:CO ratio of 1:1, at a total pressure of 6 x 10^{-1} mbar, an O_2:CO ratio of approximately 1:1, at a total pressure of 1.1 mbar and an O_2:CO ratio of approximately 1:1, with a total pressure of 2.4 mbar. The reaction temperature was 240 ^{o}C. The total pressure is also indicated in the figure legend.

P.diameter (nm)	ΔT/K	Power ($Js^{-1}mm^{-2}$)	mol_{CO} conv.($mm^{-2}s^{-1}$)	Total particle mass (g)	Total particle area (mm^2)	mol_{Pt} in the surface (mm^{-2})	Spec. mass activity (mol_{CO} conv.g^{-1}Pt mm^{-2} s^{-1})	TOF (s^{-1})
1.3±0.3	6.085±0.20	2.396E-4± 2.53E-5	8.467E-10±8.93E-11	1.04E-6 ±8.3E-14	10.262±0.9	2.556E-10±2.24E-11	8.141E-4±8.58E-5	3.312±0.349
1.9±0.5	5.691±0.18	2.241E-4±2.33E-5	7.919E-10±8.24E-11	1.52E-6 ±1.2E-13	30.206±3.0	7.524E-10±7.47E-11	5.210E-4 ±5.42E-5	1.052±0.109
2.5±0.7	5.635±0.14	2.219E-4±2.15E-5	7.841E-10±7.59E-11	2.00E-6 ±1.6E-13	50.150±4.6	1.249E-9±1.15E-10	3.921E-4±3.79E-5	0.628±0.061
3.1±0.8	5.657±0.09	2.227E-4±1.94E-5	7.871E-10±6.87E-11	2.46E-6 ±1.9E-13	70.094±7.0	1.746E-9±1.74E-10	3.174E-4 ±3.05E-5	0.451±0.039
3.7±1.0	5.548±0.09	2.184E-4±1.91E-5	7.720E-10±6.76E-11	2.96E-6 ±2.3E-13	90.038±8.0	2.243E-9±1.99E-10	2.608E-4± 2.28E-5	0.344±0.030
4.2±1.1	5.526±0.07	2.176E-4±1.82E-5	7.689E-10±6.44E-11	3.44E-6 ±2.7E-13	109.982±10	2.740E-9±2.49E-10	2.235E-4 ±1.87E-5	0.281±0.023
4.8±1.3	5.613±0.08	2.210E-4±1.89E-5	7.810E-10±6.68E-11	3.92E-6 ±3.1E-13	129.926±12	3.236E-9±1.99E-10	1.992E-4 ±1.70E-5	0.241±0.021
5.5±1.4	5.387±0.06	2.121E-4±1.74E-5	7.495E-10±6.16E-11	4.40E-6 ±3.5E-13	149.870±14	3.733E-9±3.49E-10	1.703E-4± 1.40E-5	0.201±0.017
6.0±1.6	5.330±0.09	2.099E-4±1.85E-5	7.415E-10±6.55E-11	4.80E-6 ±3.8E-13	166.490±16	4.140E-9±3.99E-10	1.545E-4 ±1.37E-5	0.179±0.016
6.6±1.7	5.578±0.10	2.197E-4±1.96E-5	7.762E-10±6.94E-11	5.28E-6 ±4.2E-13	186.434±17	4.644E-9±4.23E-10	1.470E-4 ±1.31E-5	0.167±0.015
7.2±1.9	5.753±0.13	2.266E-4±2.14E-5	8.005E-10±7.55E-11	5.76E-6 ±4.6E-13	206.378±19	5.141E-9±4.73E-10	1.390E-4±1.31E-5	0.156±0.015
7.8±2.0	6.638±0.60	2.614E-4±4.36E-5	9.236E-10±1.54E-10	6.24E-6 ±4.9E-13	226.322±21	5.637E-9±5.23E-10	1.480E-4±2.47E-5	0.164±0.027
		Equation 2.2	**Equation 3.6**	**Equation 3.8**	**Equation 2.6**	**Equation 3.9**	**Equation 3.7**	**Equation 3.5**

Table 4.9: Pt/TiO_2 particle size as determined by TEM and their corresponding specific mass activity and TOF at a reaction temperature of 240 ^oC and approximately O_2:CO ratio of 1:1, at a total pressure of 6 x 10^{-1} mbar. Parameters used to compute the activity values are also included. The equations used to compute the parameters presented in the table are shown. Silicon nitride membrane area is (1.44 ± 0.01) mm^2, silicon nitride thermal conductivity (7 ± 0.2) $Wm^{-1}K^{-1}$ and silicon nitride membrane thickness is 0.6 ± 0.02 μm. The standard deviation for the temperature change was obtained from twelve points on each low. The estimated errors in other parameters were estimated from the deference between the average value and the maximum possible value calculated using errors in each formula used to compute each parameter.

Pressure range	O_2-pressure (mbar)	CO-pressure (mbar)	Total pressure (mbar)	Average mean surface temperature change (K)
1	3×10^{-1}	3×10^{-1}	6×10^{-1}	5.70 ± 0.35
2	5.3×10^{-1}	5.7×10^{-1}	1.1	7.65 ± 0.35
3	1.3	1.1	2.4	7.54 ± 0.18

Table 4.10: Oxygen and Carbon monoxide gas pressure ratios, total reactant gas pressure and the average surface mean temperature change across the catalyst surface. The reaction temperature was 240 ^{o}C at an exposure time of 5 minutes.

The gas-phase oxidation of CO on Pt at an elevated reaction temperature (240 ^{o}C) and higher reactant gas pressure revealed the dependence of CO oxidation on reaction temperature and reactant gas pressure. The TOF and specific mass activity increased with increasing reactant gas pressure, **Figure 4.14 (a)** and **Figure 4.14 (b)**. The observed TOF was 3.312 s^{-1}, (specific mass activity = 8.141×10^{-4} mol_{CO} conv. g^{-1}Pt mm^{-2} s^{-1}), at an O_2:CO ratio of 1:1, with a total pressure of 6×10^{-1} mbar for a Pt particle size of 1.3 nm. The activity increased to 4.355 s^{-1}, (specific mass activity = 1.070×10^{-3} mol_{CO} conv. g^{-1}Pt mm^{-2} s^{-1}) at a total pressure of 1.1 mbar. Further increase in reactant gas pressure to a total pressure of 2.4 mbar resulted into a slight decline in activity, the TOF decreased to 4.174 s^{-1}, (specific mass activity = 1.026×10^{-3} mol_{CO} conv. g^{-1}Pt mm^{-2} s^{-1}) for the smallest particle size. Nevertheless, CO oxidation on Pt at higher reaction temperature resulted into higher activity compared to that recorded at relatively low pressure and low reaction temperatures.

4.4 Au/TiO_2 Nanoparticle Catalyst for the CO Oxidation Reaction

Figure 4.15 presents the temperature change for the CO oxidation activity on titania supported gold nanoparticles catalyst at 80 ^{o}C and an O_2:CO ratio of 1:1, with a total pressure of 1×10^{-1} mbar. Further in **Figure 4.16** is the temperature change at an O_2:CO ratio of 1:2, at a total pressure of 3×10^{-1} mbar. The temperature change at an O_2:CO ratio of 1:1, at a total pressure of 8.4×10^{-2} mbar and an O_2:CO ratio of 1:2, with a total pressure of 9×10^{-1} mbar is presented in appendix $\mathbf{2A_1}$ and $\mathbf{2A_3}$. The TOF and specific mass activity at an O_2:CO ratio of 1:1, with a total pressure of 8.4×10^{-2} mbar and 1×10^{-1} mbar and at an O_2:CO ratio of 1:2, with a total pressure of 3×10^{-1} mbar and 9×10^{-1}

mbar is presented in **Figure 4.17**. **Table 4.11** and **Table 4.12** present Au particle sizes with their corresponding specific mass activity and TOF at a total pressure of 1 x 10^{-1} mbar and 3 x 10^{-1} mbar, respectively. The particle sizes with their corresponding specific mass activity and TOF at a total pressure of 8.4 x 10^{-2} mbar and 9 x 10^{-1} mbar is presented in appendix **2A$_2$** and **2A$_4$**. **Table 4.13** presents the pressure of the reactant gas; total reactant pressure and the average mean surface temperature change across the catalyst surface.

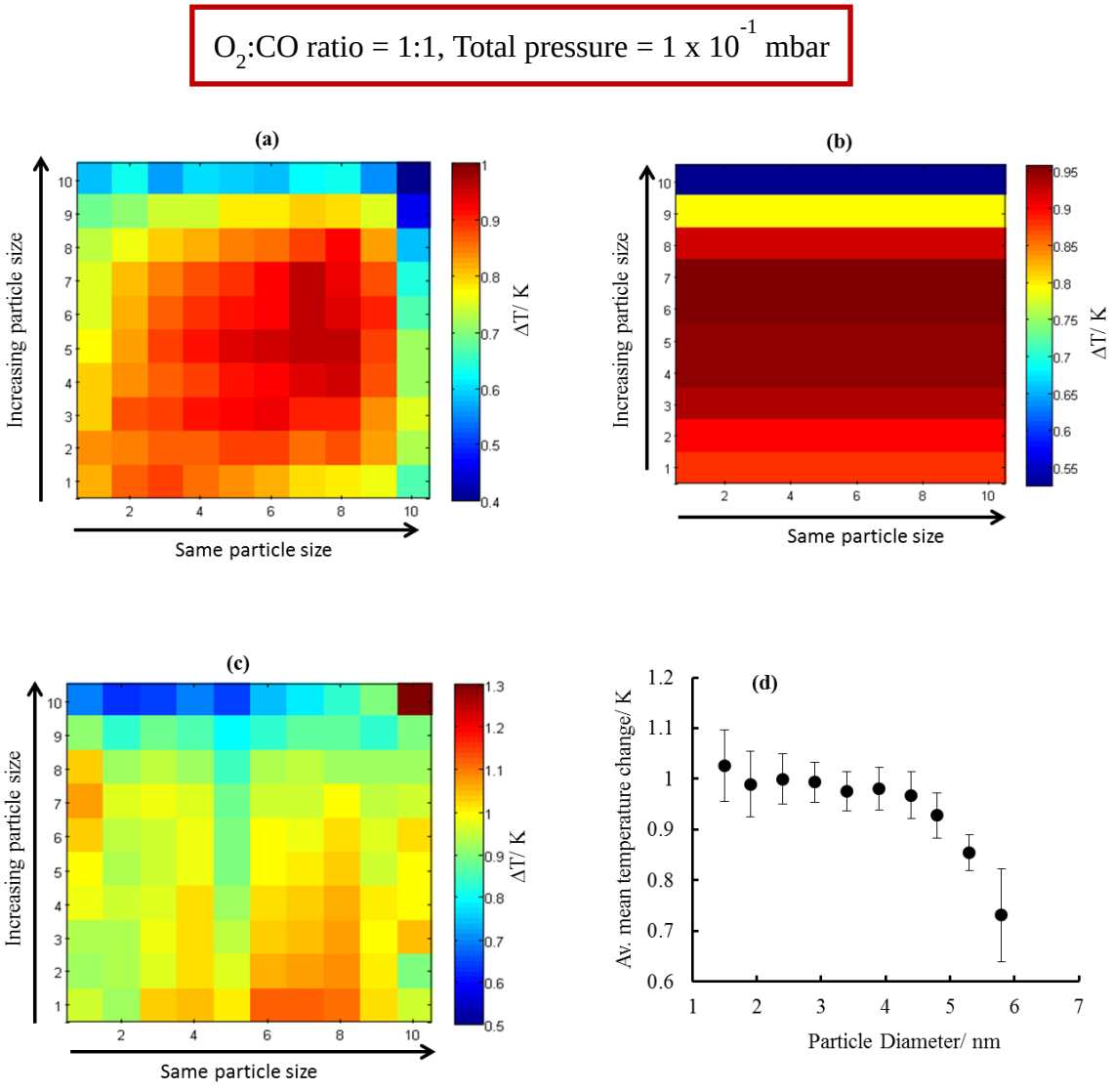

Figure 4.15: The temperature change on Au/TiO_2 catalyst as a function of particle size at an O_2:CO ratio of 1:1, at a total pressure of 1 x 10^{-1} mbar. **(a)** Presents uncompensated infrared image, **(b)** row compensated and **(c)** row and column compensated images. **(d)** Presents the average mean temperature change as a function of particle sizes for the row and column compensated infrared images. The row and column numbers are show on the x and y axes on the IR-images. The reaction temperature was 80 ^{o}C at an exposure time of 5 minutes.

O_2:CO ratio = 1:2, Total pressure = 3 x 10^{-1} mbar

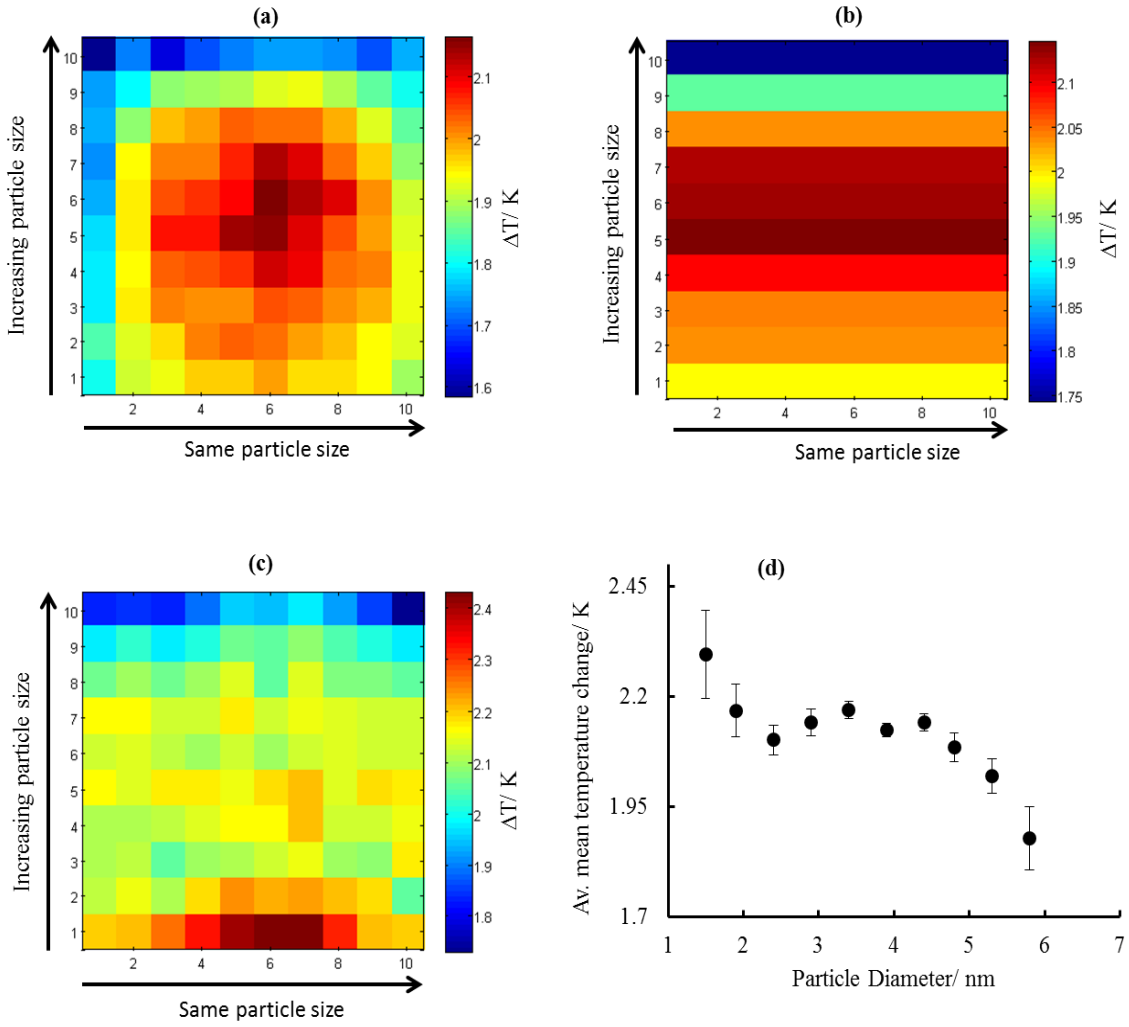

Figure 4.16: The temperature change on Au/TiO_2 catalyst as a function of particle size at an O_2:CO ratio of 1:2, at a total pressure of 3 x 10^{-1} mbar. **(a)** Presents uncompensated infrared image, **(b)** row compensated and **(c)** row and column compensated images. **(d)** Presents the average mean temperature change as a function of particle sizes for the row and column compensated infrared images. The row and column numbers are show on the x and y axes on the IR-images. The reaction temperature was 80 ^{o}C at an exposure time of 5 minutes.

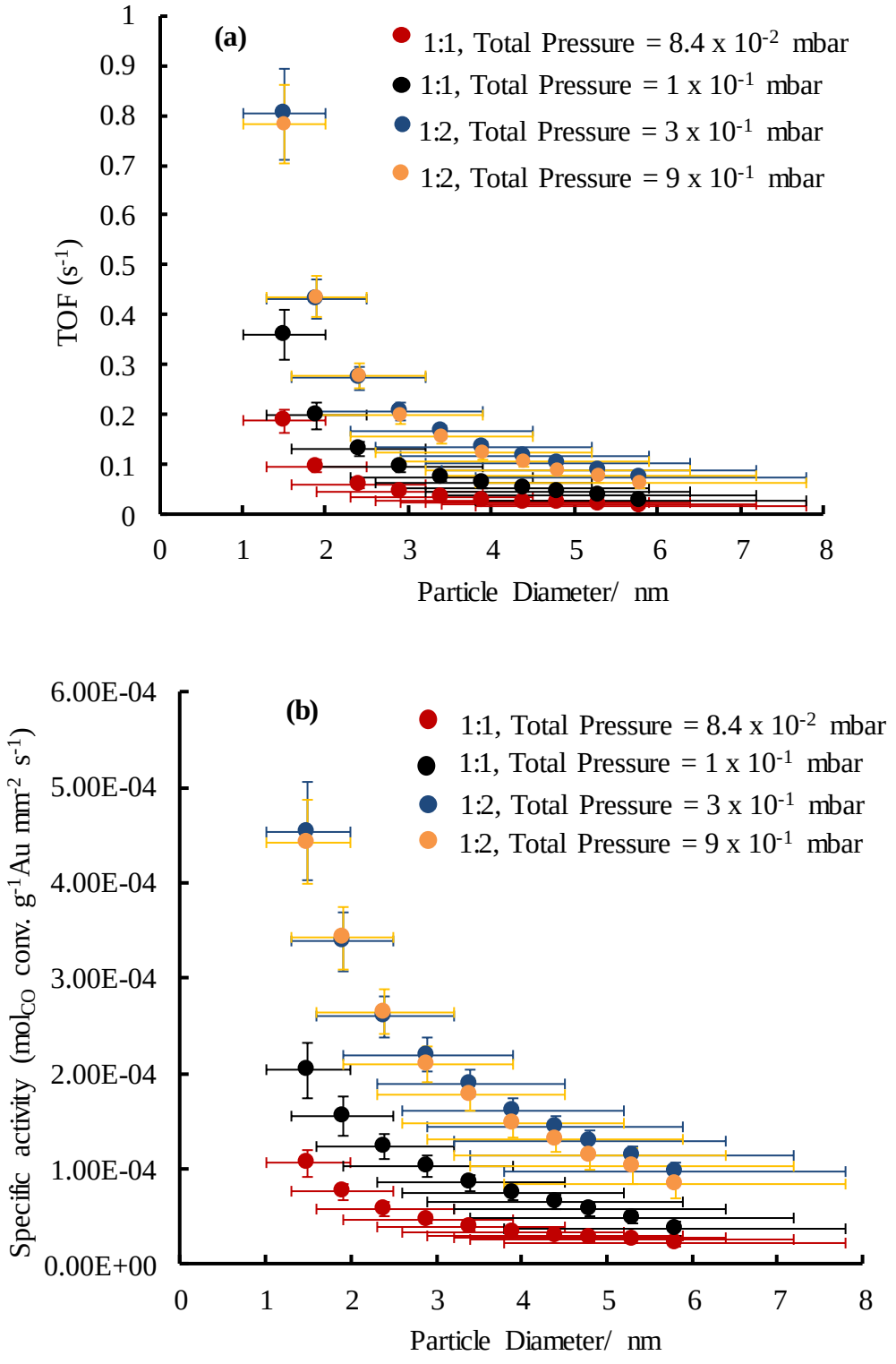

Figure 4.17: (a) TOF, **(b)** specific mass activity of Au nanoparticle catalysts supported on titania for the gas-phase CO oxidation reaction as a function of particle size (diameter/ nm) at an O_2:CO ratio of 1:1, at a total pressure of 8.4 x 10^{-2} mbar and 1 x 10^{-1} mbar and an O_2:CO ratio of 1:2, with a total pressure of 3 x 10^{-1} mbar and 9 x 10^{-1} mbar. The reaction temperature was 80 ^{o}C.

P.diameter (nm)	ΔT/K	Power ($Js^{-1}mm^{-2}$)	mol_{CO} conv.($mm^{-2}s^{-1}$)	Total particle mass (g)	Total particle area (mm^2)	mol_{Au} in the surface (mm^{-2})	Spec. mass activity (mol_{CO} conv.g^{-1}Pt mm^{-2} s^{-1})	TOF (s^{-1})
1.5±0.5	1.026±0.07	2.586E-5± 3.63E-6	9.137E-11±1.28E-11	4.50E-7±4.0E-14	10.950±0.8	2.55E-10±1.86E-11	2.03E-4±2.85E-5	0.359±0.050
1.9±0.6	0.988±0.06	2.492E-5±3.27E-6	8.806E-11±1.16E-11	5.70E-7±5.1E-14	19.206±1.5	4.47E-10±3.49E-11	1.55E-4±2.03E-5	0.197±0.026
2.5±0.8	0.999±0.04	2.517E-5± 2.77E-6	8.897E-11±9.80E-12	7.20E-7±6.4E-14	29.526±2.4	6.86E-10±5.58E-11	1.24E-4±1.36E-5	0.130±0.014
2.9±1.0	0.993±0.04	2.503E-5± 2.76E-6	8.844E-11±9.75E-12	8.70E-7±7.8E-14	39.846±3.2	9.26E-10±7.44E-11	1.02E-4±1.12E-5	0.095±0.011
3.4±1.1	0.975±0.03	2.459E-5±2.45E-6	8.689E-11±8.65E-12	1.02E-6±9.1E-14	50.166±4.1	1.17E-9±9.53E-11	8.52E-5± 8.48E-6	0.075±0.007
3.9±1.3	0.980±0.04	2.469E-5±2.74E-6	8.727E-11±9.70E-12	1.17E-6±1.0E-13	60.486±4.9	1.41E-9±1.14E-10	7.46E-5±8.29E-6	0.062±0.009
4.4±1.5	0.967±0.04	2.438E-5±2.71E-6	8.617E-11±9.56E-12	1.32E-6±1.2E-13	70.806±5.8	1.65E-9±1.35E-10	6.53E-5±7.25E-6	0.052±0.006
4.8±1.6	0.928±0.04	2.338E-5±2.66E-6	8.262E-11±9.40E-12	1.44E-6±1.3E-13	79.062±6.4	1.84E-9±1.49E-10	5.74E-5± 6.53E-6	0.045±0.005
5.3±1.9	0.854±0.03	2.154E-5±2.24E-6	7.611E-11±7.93E-12	1.59E-6±1.4E-13	89.382±7.3	2.08E-9±1.70E-10	4.79E-5±4.98E-6	0.037±0.004
5.8±2.0	0.730±0.09	1.842E-5±3.64E-6	6.508E-11±1.29E-11	1.74E-6±1.5E-13	99.702±8.1	2.32E-9±1.88E-10	3.74E-5±7.40E-6	0.028±0.005
		Equation 2.2	**Equation 3.6**	**Equation 3.8**	**Equation 2.6**	**Equation 3.9**	**Equation 3.7**	**Equation 3.5**

Table 4.11: Au/TiO_2 particle size as determined by TEM and their corresponding specific mass activity and TOF at a reaction temperature of 80 ^oC, at an O_2:CO ratio of 1:1, with a total pressure of 1 x 10^{-1} mbar. Parameters used to compute the activity values are also included. The equations used to compute the parameters presented in the table are shown. Silicon nitride membrane area is (2.25 ± 0.01) mm^2, silicon nitride thermal conductivity (7 ± 0.2) $Wm^{-1}K^{-1}$ and silicon nitride membrane thickness is 0.6 ± 0.02 μm. The standard deviation for the temperature change was obtained from ten points on each low. The estimated errors in other parameters were estimated from the deference between the average value and the maximum possible value calculated using errors in each formula used to compute each parameter.

P.diameter (nm)	ΔT/K	Power ($Js^{-1}mm^{-2}$)	mol_{CO} conv.($mm^{-2}s^{-1}$)	Total particle mass (g)	Total particle area (mm^2)	mol_{Au} in the surface (mm^{-2})	Spec. mass activity (mol_{CO} conv.$g^{-1}Pt\ mm^{-2}\ s^{-1}$)	TOF (s^{-1})
1.5±0.5	2.294±0.10	5.783E-5±6.58E-6	2.043E-10±2.32E-11	4.50E-7±4.0E-14	10.950±0.8	2.55E-10±1.86E-11	4.54E-4±5.16E-5	0.803±0.091
1.9±0.6	2.167±0.05	5.461E-5±5.03E-6	1.930E-10±1.78E-11	5.70E-7±5.1E-14	19.206±1.5	4.47E-10±3.49E-11	3.39E-4±3.12E-5	0.432±0.039
2.5±0.8	2.101±0.03	5.295E-5±4.38E-6	1.871E-10±1.55E-11	7.20E-7±6.4E-14	29.526±2.4	6.86E-10±5.58E-11	2.60E-4±2.15E-5	0.273±0.022
2.9±1.0	2.140±0.03	5.395E-5±4.43E-6	1.906E-10±1.57E-11	8.70E-7±7.8E-14	39.846±3.2	9.26E-10±7.44E-11	2.19E-4±1.80E-5	0.206±0.017
3.4±1.1	2.170±0.02	5.469E-5±4.23E-6	1.932E-10±1.49E-11	1.02E-6±9.1E-14	50.166±4.1	1.17E-9±9.53E-11	1.89E-4± 1.47E-5	0.166±0.013
3.9±1.3	2.123±0.01	5.351E-5±3.87E-6	1.891E-10±1.37E-11	1.17E-6±1.0E-13	60.486±4.9	1.41E-9±1.14E-10	1.62E-4±1.17E-5	0.134±0.009
4.4±1.5	2.141±0.02	5.396E-5±4.18E-6	1.907E-10±1.48E-11	1.32E-6±1.2E-13	70.806±5.8	1.65E-9±1.35E-10	1.44E-4±1.12E-5	0.116±0.008
4.8±1.6	2.085±0.03	5.254E-5±4.36E-6	1.857E-10±1.54E-11	1.44E-6±1.3E-13	79.062±6.4	1.84E-9±1.49E-10	1.29E-4± 1.07E-5	0.101±0.008
5.3±1.9	2.019±0.04	5.088E-5±4.51E-6	1.798E-10±1.59E-11	1.59E-6±1.4E-13	89.382±7.3	2.08E-9±1.70E-10	1.13E-4±1.00E-5	0.087±0.007
5.8±2.0	1.878±0.07	4.732E-5±5.09E-6	1.672E-10±1.80E-11	1.74E-6±1.5E-13	99.702±8.1	2.32E-9±1.88E-10	9.61E-5±1.03E-5	0.072±0.007
		Equation 2.2	**Equation 3.6**	**Equation 3.8**	**Equation 2.6**	**Equation 3.9**	**Equation 3.7**	**Equation 3.5**

Table 4.12: Au/TiO_2 particle size as determined by TEM and their corresponding specific mass activity and TOF at a reaction temperature of 80 ^oC, at an O_2:CO ratio of 1:2, with a total pressure of 3×10^{-1} mbar. Parameters used to compute the activity values are also included. The equations used to compute the parameters presented in the table are shown. Silicon nitride membrane area is (2.25 ± 0.01) mm^2, silicon nitride thermal conductivity (7 ± 0.2) $Wm^{-1}K^{-1}$ and silicon nitride membrane thickness is 0.6 ± 0.02 μm. The standard deviation for the temperature change was obtained from ten points on each low. The estimated errors in other parameters were estimated from the deference between the average value and the maximum possible value calculated using errors in each formula used to compute each parameter.

Pressure range	O_2-pressure (mbar)	CO-pressure (mbar)	Total pressure (mbar)	Average surface temperature change (K)
1	4.2×10^{-2}	4.2×10^{-2}	8.4×10^{-2}	0.46 ± 0.03
2	5×10^{-2}	5×10^{-2}	1×10^{-1}	0.94 ± 0.08
3	1×10^{-1}	2×10^{-1}	3×10^{-1}	2.11 ± 0.11
4	3×10^{-1}	6×10^{-1}	9×10^{-1}	1.99 ± 0.18

Table 4.13: Oxygen and Carbon monoxide pressure ratios, total reactant gas pressure and average mean temperature change across the catalyst surface. The reaction temperature was 80 ^{o}C at an exposure time of 5 minutes.

The oxidation of CO on titania supported Au nanoparticles ranging between 1.5 nm to 5.8 nm was studied at various CO and O_2 pressures at 80 ^{o}C, **Figure 4.15** and **Figure 4.16**. The TOF and specific mass activity show that CO oxidation on Au particles is dependent on particle size. The TOF and specific mass activity of Au particles increases dramatically with decreasing particle size, whereby the smallest particles size displays the highest activity, **Figure 4.17**. The TOF of Au particles for CO oxidation reaction increased from 0.016 s^{-1}, (specific mass activity = 2.110×10^{-5} mol_{CO} conv. g^{-1}Au mm^{-2} s^{-1}) for a Au particle size of 5.8 nm to 0.186 s^{-1}, (specific mass activity = 1.050×10^{-4} mol_{CO} conv. g^{-1}Au mm^{-2} s^{-1}) for a Au particle size of 1.5 nm, at an O_2:CO ratio of 1:1, with a total pressure of 8.4×10^{-2} mbar. A similar activity trend of reactivity increasing with decreasing Au particle size can be observed shown in **Table 4.11** and **Table 4.12**, respectively. However, increasing reactant gas pressure at the same reaction temperature increased the activity of Au nanoparticle catalyst. The activity increased from 0.186 s^{-1}, (specific mass activity = 1.050×10^{-4} mol_{CO} conv. g^{-1}Au mm^{-2} s^{-1}) for a Au particle size of 1.5 nm, at a total pressure of 8.4×10^{-2} mbar to 0.359 s^{-1}, (specific mass activity =2.03×10^{-4} mol_{CO} conv. g^{-1}Au mm^{-2} s^{-1}), at a total pressure of 1×10^{-1} mbar. Increasing the reactant gas pressure to a total pressure of 3×10^{-1} mbar increased the activity to 0.803 s^{-1}, (specific mass activity = 4.54×10^{-4} mol_{CO} conv. g^{-1}Au mm^{-2} s^{-1}). Further increase of reactant gas pressure to a total pressure of 9 $x10^{-1}$ mbar did not increase the activity, suggesting the catalyst surface was saturated with reactants.

Screening of Au/TiO_2 nanoparticle catalyst for CO oxidation was undertaken at an elevated reaction temperature (170 ^oC) in order to investigate the effect of reaction temperature on CO oxidation reaction at different reactant gas pressure. The results for the reaction conducted at this temperature at an O_2:CO ratio of 1:1, with a total pressure of 6 x 10^{-2} mbar and an O_2:CO ratio of 1:2, at a total pressure of 1.5 mbar are presented in **Figure 4.18** and **Figure 4.19**, respectively. The temperature change at an O_2:CO ratio of 1:2, with a total pressure of 9 x 10^{-2} mbar and 9 x 10^{-1} mbar is presented in appendix **$2B_1$** and **$2B_3$**. The TOF and specific mass activity of Au particles at an O_2:CO ratio of 1:1, total pressure of 6 x 10^{-2} mbar and an O_2:CO ratio of 1:2, with a total pressure of 9 x 10^{-2} mbar, 9 x 10^{-1} mbar and 1.5 mbar is presented in **Figure 4.20**. **Table 4.14** and **Table 4.15** present Au particle sizes with their corresponding specific mass activity and TOF at a total pressure of 6 x 10^{-2} mbar and 1.5 mbar, respectively. The particle sizes with their corresponding specific mass activity and TOF at a total pressure of 9 x 10^{-2} mbar and 9 x 10^{-1} mbar is presented in appendix **$2B_2$** and **$2B_4$**. **Table 4.16** presents the pressure of reactant gas, total reactant gas pressure and the average mean surface temperature change across the catalyst surface from the CO oxidation reaction.

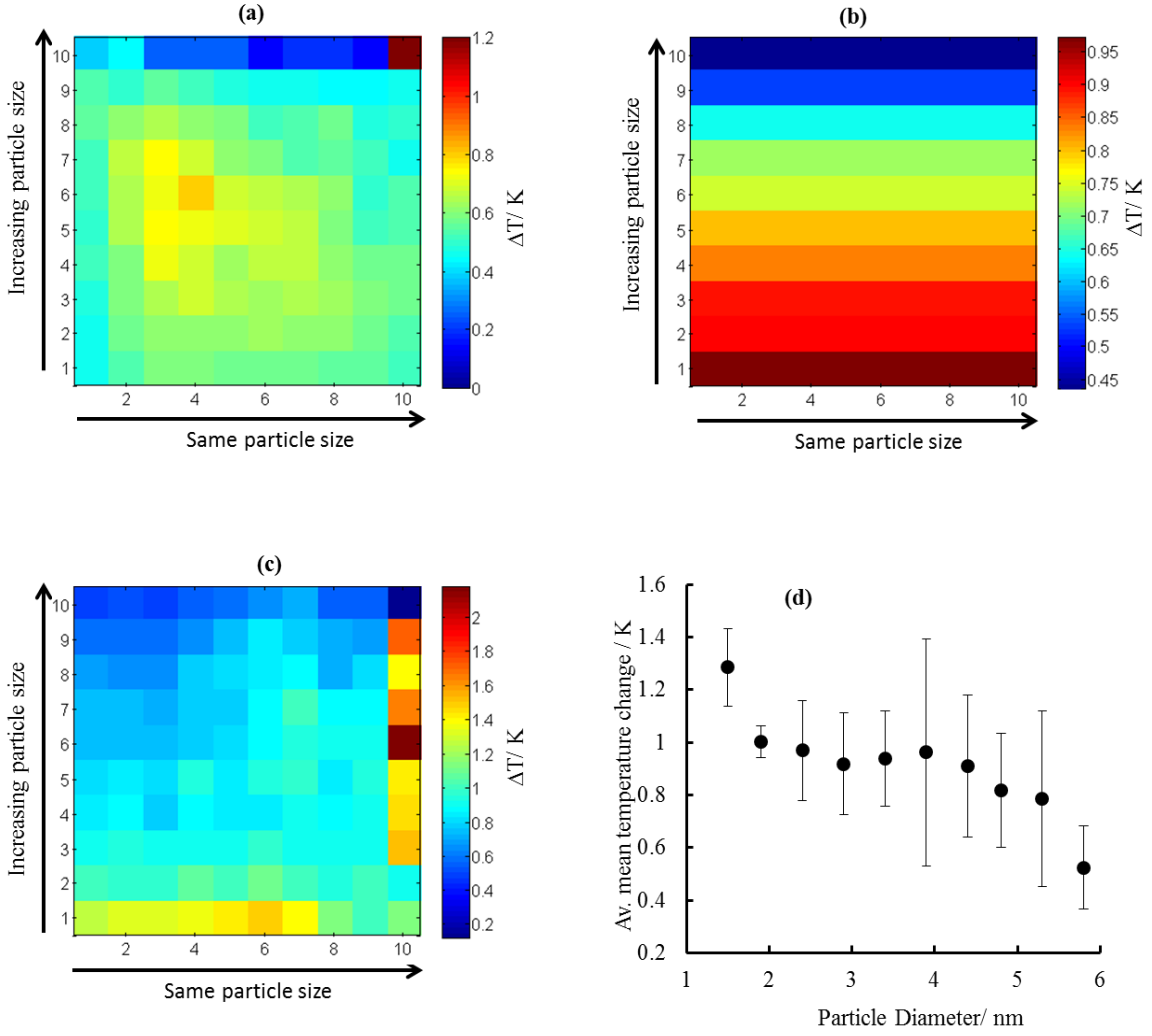

Figure 4.18: The temperature change on Au/TiO_2 catalyst as a function of particle size at an O_2:CO ratio of 1:1, at a total pressure of 6 x 10^{-2} mbar. **(a)** Presents uncompensated infrared image, **(b)** row compensated and **(c)** completely compensated. **(d)** Presents the average mean temperature change as a function of particle sizes for the complete compensated infrared images. The row and column numbers are show on the x and y axes on the IR-images. The reaction temperature was 170 ^{o}C at an exposure time of 5 minutes.

O_2: CO ratio = 1:2, Total pressure = 1.5 mbar

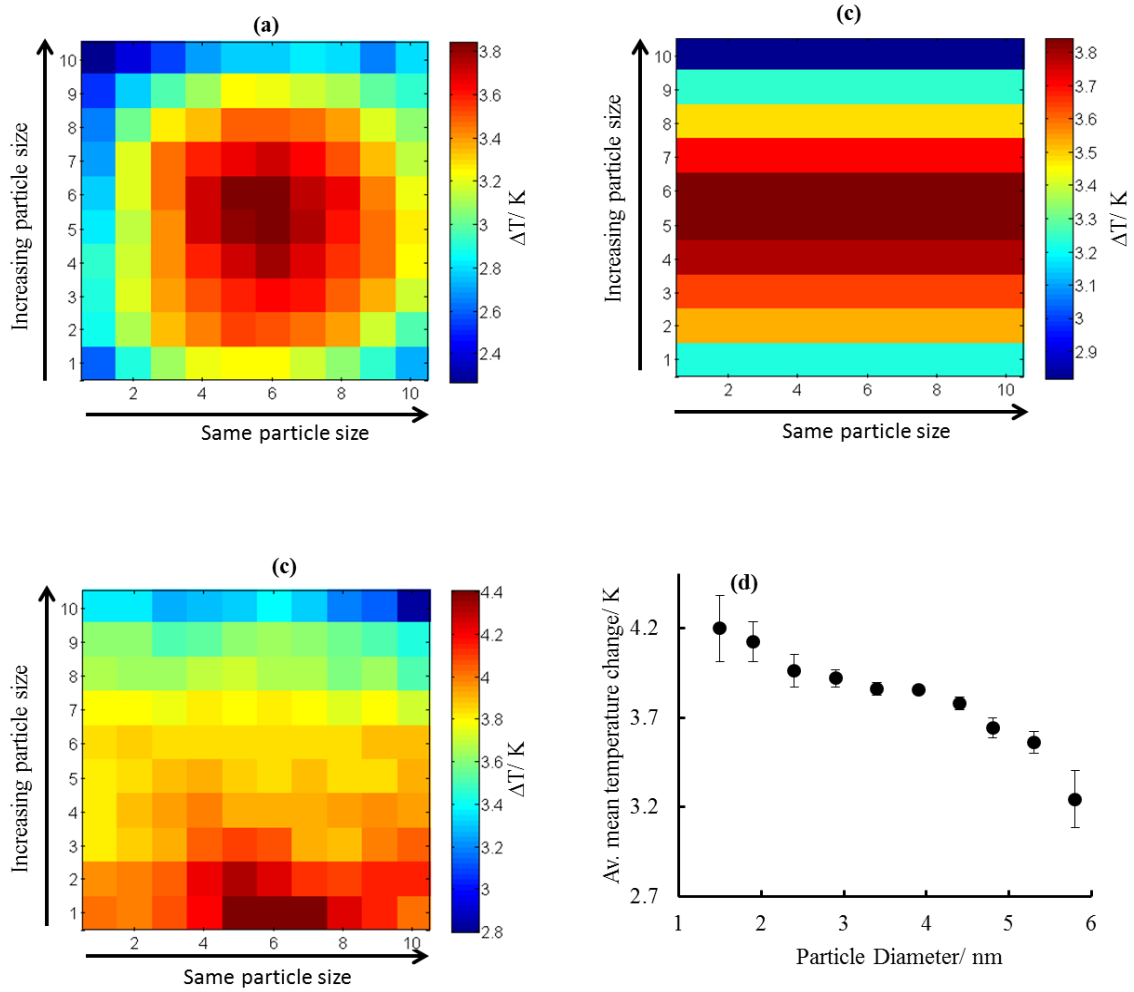

Figure 4.19: The temperature change on Au/TiO_2 catalyst as a function of particle size at an O_2:CO ratio of 1:2, with a total pressure of 1.5 mbar. **(a)** Presents uncompensated infrared image, **(b)** row compensated and **(c)** completely compensated. **(d)** Presents the average mean temperature change as a function of particle sizes for the complete compensated infrared images. The row and column numbers are show on the x and y axes on the IR-images. The reaction temperature was 170 ^{o}C at an exposure time of 5 minutes.

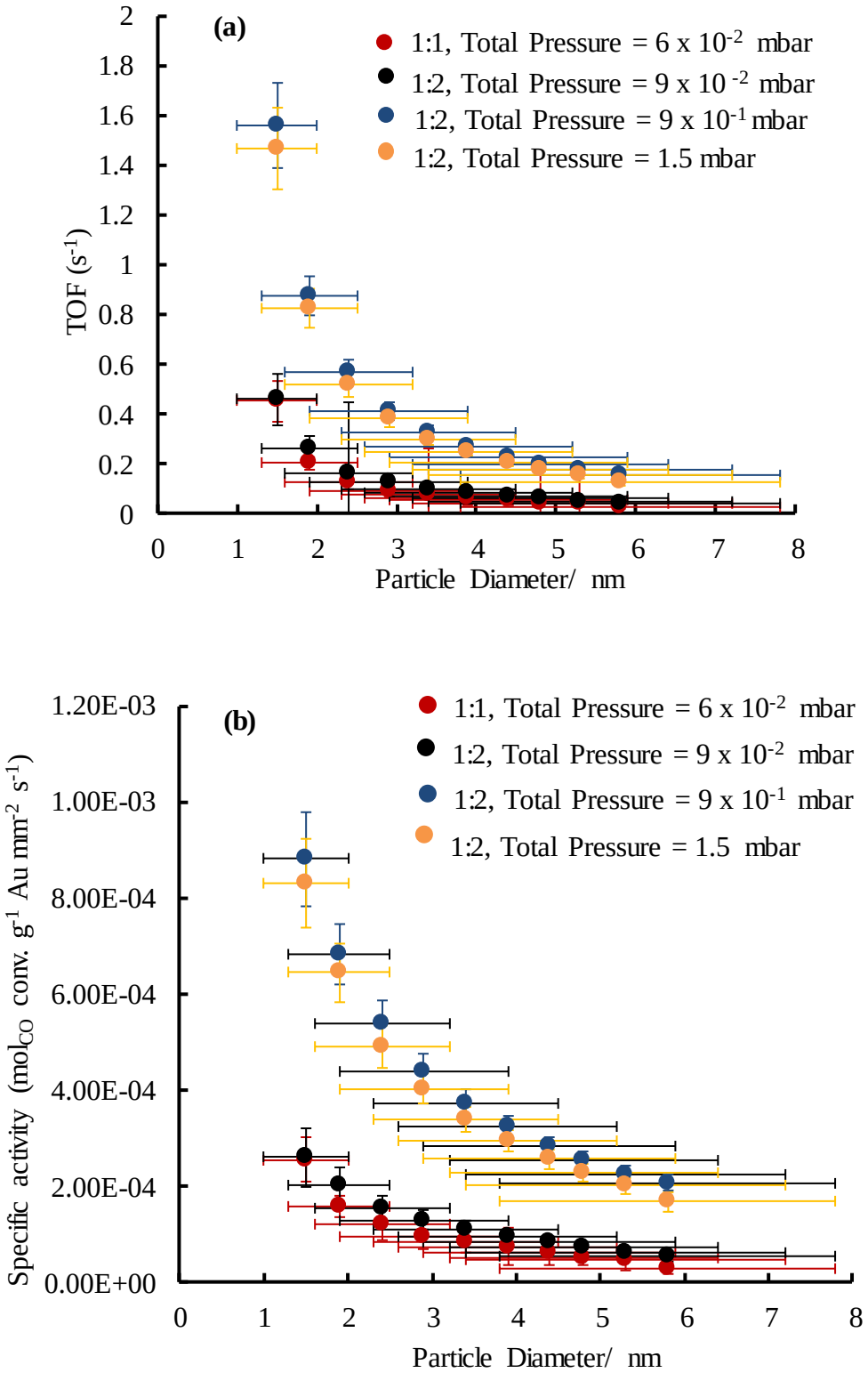

Figure 4.20: (a) TOF, **(b)** specific mass activity of Au nanoparticle catalysts supported on titania for the CO oxidation reaction as a function of particle size (diameter/ nm) at an O_2:CO ratio of 1:1, with a total pressure of 6 x 10^{-2} mbar and an O_2:CO ratio of 1:2, with a total pressure of 9 x 10^{-2} mbar, 9 x 10^{-1} mbar and 1.5 mbar. The reaction temperature was 170 ^{o}C.

P.diameter (nm)	ΔT/K	Power ($Js^{-1}mm^{-2}$)	mol_{CO} conv.($mm^{-2}s^{-1}$)	Total particle mass (g)	Total particle area (mm^2)	mol_{Au} in the surface (mm^{-2})	Spec. mass activity (mol_{CO} conv.g^{-1}Pt mm^{-2} s^{-1})	TOF (s^{-1})
1.5±0.5	1.284±0.14	3.236E-5±5.95E-6	1.144E-10±2.10E-11	4.50E-7±4.0E-14	10.950±0.8	2.55E-10±1.86E-11	2.54E-4±4.67E-5	0.449±0.083
1.9±0.6	1.002±0.06	2.526E-5±3.31E-6	8.927E-11±1.17E-11	5.70E-7±5.1E-14	19.206±1.5	4.47E-10±3.49E-11	1.57E-4±2.05E-5	0.200±0.026
2.5±0.8	0.969±0.19	2.443E-5±6.75E-6	8.633E-11±2.38E-11	7.20E-7±6.4E-14	29.526±2.4	6.86E-10±5.58E-11	1.20E-4±3.31E-5	0.126±0.034
2.9±1.0	0.918±0.19	2.314E-5±6.67E-6	8.176E-11±2.36E-11	8.70E-7±7.8E-14	39.846±3.2	9.26E-10±7.44E-11	9.40E-5±2.71E-5	0.088±0.025
3.4±1.1	0.938±0.18	2.365E-5±6.42E-6	8.358E-11±2.27E-11	1.02E-6±9.1E-14	50.166±4.1	1.17E-9±9.53E-11	8.19E-5± 2.23E-5	0.072±0.019
3.9±1.3	0.962±0.40	2.424E-5±1.24E-6	8.566E-11±4.38E-11	1.17E-6±1.0E-13	60.486±4.9	1.41E-9±1.14E-10	7.32E-5±3.75E-5	0.061±0.031
4.4±1.5	0.908±0.30	2.290E-5±9.60E-6	8.092E-11±3.39E-11	1.32E-6±1.2E-13	70.806±5.8	1.65E-9±1.35E-10	6.13E-5±2.57E-5	0.049±0.021
4.8±1.6	0.816 0.20	2.057E-5±6.76E-6	7.271E-11±2.39E-11	1.44E-6±1.3E-13	79.062±6.4	1.84E-9±1.49E-10	5.05E-5± 1.66E-5	0.040±0.013
5.3±1.9	0.785±0.30	1.978E-5±9.41E-6	6.990E-11±3.32E-11	1.59E-6±1.4E-13	89.382±7.3	2.08E-9±1.70E-10	4.40E-5±2.09E-5	0.034±0.016
5.8±2.0	0.523±0.15	1.319E-5±4.91E-6	4.661E-11±1.74E-11	1.74E-6±1.5E-13	99.702±8.1	2.32E-9±1.88E-10	2.68E-5±9.98E-6	0.020±0.007
		Equation 2.2	**Equation 3.6**	**Equation 3.8**	**Equation 2.6**	**Equation 3.9**	**Equation 3.7**	**Equation 3.5**

Table 4.14: Au/TiO_2 particle size as determined by TEM and their corresponding specific mass activity and TOF at a reaction temperature of 170 ^oC at an O_2:CO ratio of 1:1, with a total pressure of 6 x 10^{-2} mbar. Parameters used to compute the activity values are also included. The equations used to compute the parameters presented in the table are shown. Silicon nitride membrane area is (2.25 ± 0.01) mm^2, silicon nitride thermal conductivity (7 ± 0.2) $Wm^{-1}K^{-1}$ and silicon nitride membrane thickness is 0.6 ± 0.02 μm. The standard deviation for the temperature change was obtained from ten points on each low. The estimated errors in other parameters were estimated from the deference between the average value and the maximum possible value calculated using errors in each formula used to compute each parameter.

P.diameter (nm)	ΔT/K	Power ($Js^{-1}mm^{-2}$)	mol_{CO} conv.($mm^{-2}s^{-1}$)	Total particle mass (g)	Total particle area (mm^2)	mol_{Au} in the surface (mm^{-2})	Spec. mass activity (mol_{CO} conv.g^{-1}Pt mm^{-2} s^{-1})	TOF (s^{-1})
1.5±0.5	4.197±0.18	1.058E-4±1.20E-5	3.738E-10±4.23E-11	4.50E-7±4.0E-14	10.950±0.8	2.55E-10±1.86E-11	8.31E-4±9.41E-5	1.468±0.166
1.9±0.6	4.122±0.11	1.039E-4±9.98E-6	3.670E-10±3.53E-11	5.70E-7±5.1E-14	19.206±1.5	4.47E-10±3.49E-11	6.44E-4±6.19E-5	0.822±0.079
2.5 0.8	3.962±0.09	9.984E-5±9.19E-6	3.528E-10±3.24E-11	7.20E-7±6.4E-14	29.526±2.4	6.86E-10±5.58E-11	4.90E-4±4.50E-5	0.514±0.047
2.9±1.0	3.919±0.04	9.876E-5±7.74E-6	3.490E-10±2.74E-11	8.70E-7±7.8E-14	39.846±3.2	9.26E-10±7.44E-11	4.01E-4±3.14E-5	0.377±0.029
3.4±1.1	3.861±0.03	9.731E-5±7.37E-6	3.439E-10±2.60E-11	1.02E-6±9.1E-14	50.166±4.1	1.17E-9±9.53E-11	3.37E-4± 2.55E-5	0.295±0.022
3.9±1.3	3.854±0.02	9.712E-5±7.10E-6	3.432E-10±2.51E-11	1.17E-6±1.0E-13	60.486±4.9	1.41E-9±1.14E-10	2.93E-4±2.15E-5	0.244±0.017
4.4±1.5	3.778±0.03	9.521E-5±7.24E-6	3.364E-10±2.56E-11	1.32E-6±1.2E-13	70.806±5.8	1.65E-9±1.35E-10	2.55E-4±1.94E-5	0.204±0.016
4.8±1.6	3.641±0.05	9.176E-5±7.54E-6	3.243E-10±2.66E-11	1.44E-6±1.3E-13	79.062±6.4	1.84E-9±1.49E-10	2.25E-4± 1.85E-5	0.176±0.014
5.3±1.9	3.563±0.06	8.979E-5±7.68E-6	3.173E-10±2.71E-11	1.59E-6±1.4E-13	89.382±7.3	2.08E-9±1.70E-10	2.00E-4±1.71E-5	0.153±0.013
5.8±2.0	3.244±0.16	8.176E-5±9.82E-6	2.889E-10±3.47E-11	1.74E-6±1.5E-13	99.702±8.1	2.32E-9±1.88E-10	1.66E-4±1.99E-5	0.125±0.015
		Equation 2.2	**Equation 3.6**	**Equation 3.8**	**Equation 2.6**	**Equation 3.9**	**Equation 3.7**	**Equation 3.5**

Table 4.15: Au/TiO_2 particle size as determined by TEM and their corresponding specific mass activity and TOF at a reaction temperature of 170 ^oC, and O_2:CO ratio of 1:2, at a total pressure of 1.5 mbar. Parameters used to compute the activity values are also included. The equations used to compute the parameters presented in the table are shown. Silicon nitride membrane area is (2.25 ± 0.01) mm^2, silicon nitride thermal conductivity (7 ± 0.2) $Wm^{-1}K^{-1}$ and silicon nitride membrane thickness is 0.6 ± 0.02 μm. The standard deviation for the temperature change was obtained from ten points on each low. The estimated errors in other parameters were estimated from the deference between the average value and the maximum possible value calculated using errors in each formula used to compute each parameter.

Pressure range	O_2-pressure (mbar)	CO-pressure (mbar)	Total pressure (mbar)	Average mean surface temperature change (K)
1	3×10^{-2}	3×10^{-2}	6×10^{-2}	0.91 ± 0.19
2	3×10^{-2}	6×10^{-2}	9×10^{-2}	1.20 ± 0.09
3	3×10^{-1}	6×10^{-1}	9×10^{-1}	4.22 ± 0.15
4	5×10^{-1}	1	1.5	3.81 ± 0.27

Table 4.16: Oxygen and Carbon monoxide gas pressure ratios, total reactant gas pressure and the average mean temperature change across the catalyst surface. The reaction temperature was 170 ^{o}C at an exposure time of 5 minutes.

The oxidation of CO on a titania supported Au particle catalyst at an elevated reaction temperature (170 ^{o}C) revealed that Au activity towards CO oxidation increases with increasing reaction temperature as shown in **Figure 4.20**. At 170 ^{o}C, a dramatic increase in Au activity was observed by increasing reactant gas pressure. The observed TOF was 0.449 s^{-1}, (specific mass activity = 2.54×10^{-4} mol_{CO} conv. g^{-1}Au mm^{-2} s^{-1}) for a Au particle size of 1.5 nm, at an O_2: CO ratio of 1:1, at a total pressure of 6×10^{-2} mbar, **Table 4.14**. The activity increased to 0.457 s^{-1}, (specific mass activity = 2.59×10^{-4} mol_{CO} conv. g^{-1}Au mm^{-2} s^{-1}) at an O_2:CO ratio of 1:2, with a total pressure of 9×10^{-2} mbar. Increasing the reactant gas pressure to an O_2:CO ratio of 1:2, total pressure of 9×10^{-1} mbar, increased the activity to 1.558 s^{-1}, (specific mass activity = 8.81×10^{-4} mol_{CO} conv. g^{-1}Au mm^{-2} s^{-1}) as demonstrated through the activity results presented in **Figure 4.20**. Further increase in reactant gases pressure to O_2:CO ratio of 1:2, total pressure of 1.5 mbar observed no further increase in activity, **Table 4.15**.

Generally, from the activity results of titania supported Au nanoparticle catalyst for the CO oxidation reaction at low reaction temperature presented, it is observed that Au particle size plays a greater role in activity. Additionally, the increase in reaction temperature and reactants gases pressure increases CO conversion on Au particles with the smallest particles displaying the highest activity.

5 Discussion

5.1 Platinum Nanoparticles Catalyst

The oxidation of CO on Pt supported nanoparticle catalyst ranging between 1.3 nm and 7.8 nm sizes were investigated at relatively low reaction temperatures. The TOF and specific mass activity results clearly show that the CO oxidation reaction on Pt/TiO_2 is particle size dependent as shown in **Section 4.3**. The TOF and specific mass activity increases as the Pt particle size decreases. The smallest Pt particle size displayed the highest activity for the CO oxidation compared to the largest particle size. For example, at 80 ^oC and a $CO:O_2$ ratio of 1:1 (**Figure 4.6**), the TOF increased from 0.01 s^{-1}, (specific mass activity = 9.312 x 10^{-6} mol_{CO} conv. $g^{-1}Pt$ mm^{-2} s^{-1}) for a Pt particle size of 7.8 nm, to 0.171 s^{-1}, (specific mass activity = 4.210 x 10^{-5} mol_{CO} conv. $g^{-1}Pt$ mm^{-2} s^{-1}) for a Pt particle size of 1.3 nm, an increase in activity by a factor of 17. This observation is inconsistent with the previous reports that either the activity for CO oxidation on Pt particles smaller than 5 nm supported on titania decreases with decreasing Pt particle size[62, 74, 118] or there was no strong dependence on particle size.[118] However, the explanation for why this is so was not addressed in these studies.[118] Rashkeev *et al.*[118] in their theoretical study, suggested that the nanoscale features resulted in the observed behaviour. They concluded that, bonding of CO or O_2 on Pt does not weakens the Pt-Pt bonds, this retards the activity as Pt would not benefit from perimeter sites compared to Au nanoparticles.[118] In the same study, they ruled out the effect on activity due to physical charge transfer. However, quite recently, Li and co-workers[81] have demonstrated that the activity of titania supported Pt particles in the range between 1.1 nm and 10 nm for the CO oxidation reaction at various reaction temperatures increases with decreasing particle sizes, consistent with the dependence in activity obtained in this work. In their study, the activity of Pt/SiO_2 catalyst was studied alongside Pt/TiO_2 and found to be less active and oxidized CO at a temperature approximately 200 ^oC higher compared to Pt/TiO_2, confirming the participation of titania in the reaction. This observation suggests that the activity of Pt for CO oxidation depends on the nature of a support among other factors. Similar observation on the influence of support type on the activity of Pt nanoparticles for the CO oxidation reaction was reported by Liu *et al.*[109] in their study of CO oxidation on Pt supported on a range of supports. Their findings show that the type of

support changes the reactivity of supported Pt towards CO oxidation. In the study carried out by Alexeev *et al.*[80] for CO oxidation on Pt supported on TiO_2 and Al_2O_3, they found the most active catalysts for CO oxidation were the TiO_2 supported catalysts when reduced in H_2 at 400 ^oC. **Figure 5.1** compares the reactivity results obtained in this work and that reported in the literature by Li *et al.*[81] and Bamwenda *et al.*[62] for the CO oxidation reaction on titania supported Pt nanoparticles, although the pressure conditions used were not reported in these papers. Note that the results of Li *et al.*[81] show an increase of a factor of ca. seven times on decreasing particle size from 10 nm to 1 nm. Since the incipient wet methods of the high area catalyst preparation used in the latter study is likely to produce broader particle distributions than produced here in the model systems, the factor of 7 (compared to a factor of 17 observed for similar particle size ranges in this study) are also understandable.

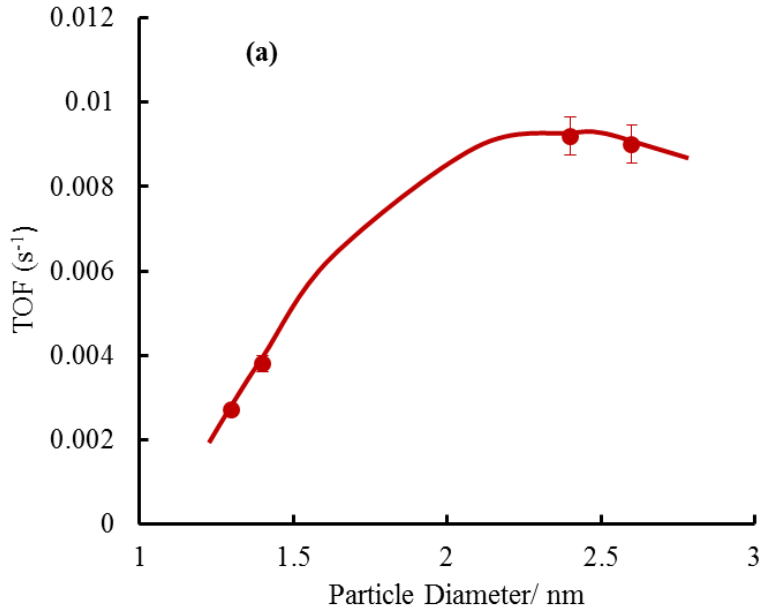

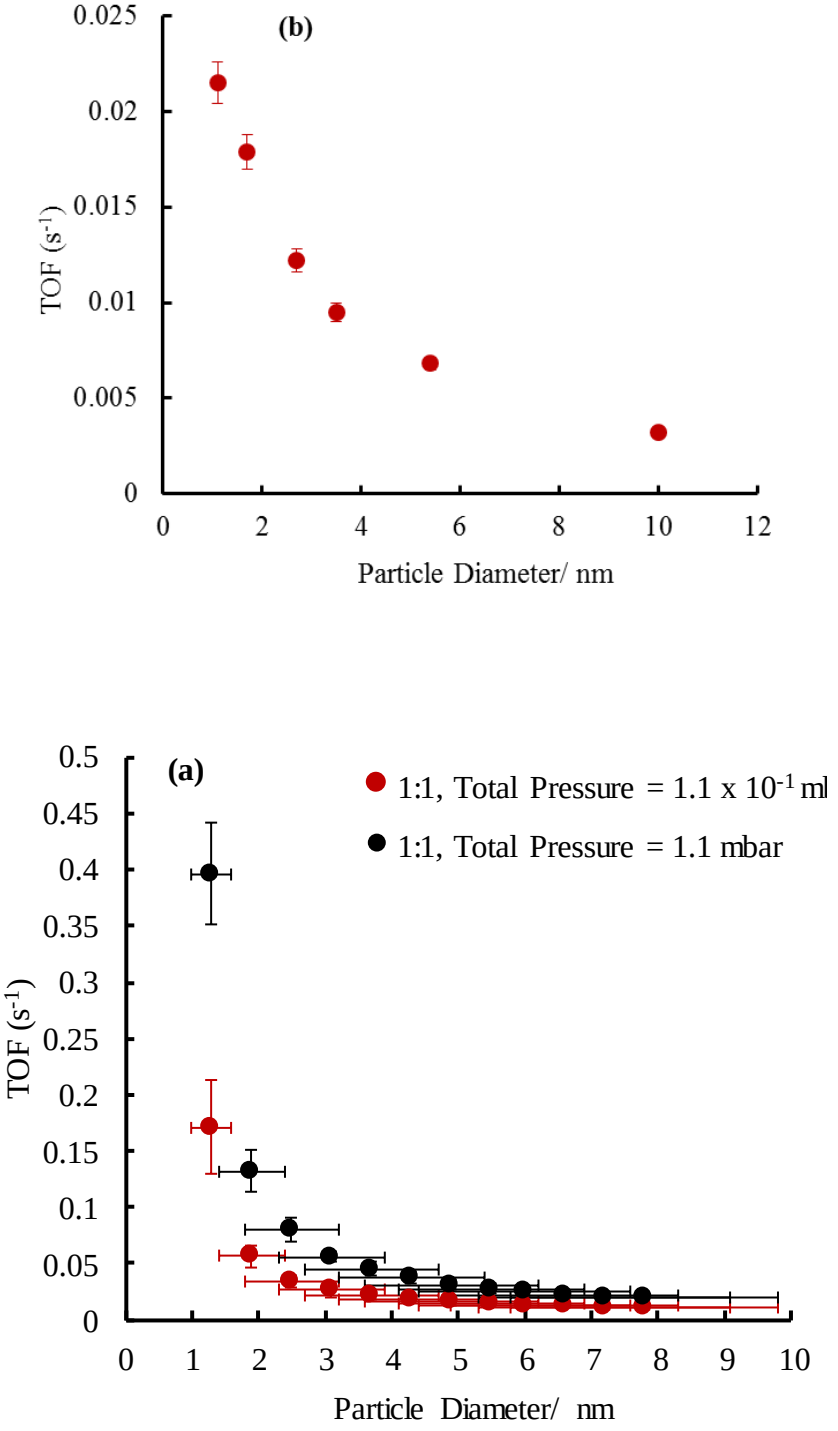

Figure 5.1: The TOF of Pt nanoparticle catalyst supported on titania for the CO oxidation reaction as a function of particle size (diameter/ nm). **(a)** Activity results from Bamwenda *et al.*[62] at a reaction temperature of 300 K. **(b)** Activity results reported by Li *et al*[81] at a reaction temperature of 40 ^{o}C and **(c)** activity results obtained in this work at a reaction temperature of 80 ^{o}C.

Kageyama *et al.*[108] in their study of the CO oxidation reaction on titania supported Pt nanoparticles between 2 nm to 5 nm in the temperature range between 60 ^{o}C to 140 ^{o}C observed the highest CO conversion for the Pt nanoparticles of 2 nm size at 60 ^{o}C. Theoretical study conducted by Dobrin[119] on the CO oxidation reaction on Pt particles containing 55-atom cluster (1.1 nm) and 147-atoms cluster (1.6 nm) suggested that Pt particles of around 2 nm size would be the most efficient in CO oxidation compared to particles of 1.1 nm size or less. This observation suggests that there exists an optimum Pt cluster size to achieve the maximum activity towards CO oxidation. The study suggests that larger clusters such as 147-atom cluster contain high coordinated CO adsorption sites on the Pt (111) and Pt (100) faces which are supplemented by the presence of adjacent low-coordinated oxygen adsorption sites on the edges of the cluster. This observation is supported by experimental findings for CO oxidation reaction on Pt clusters, that activity for CO oxidation on Pt increases with increasing Pt cluster size.[13, 104, 180] Although these studies report the findings on smaller Pt particles than that investigated in this study, they serve to illustrate the strong particle size dependence for CO oxidation of Pt particles.

The activity of Pt nanoparticles for CO oxidation increased with the increase in reactant gas pressure at a particular reaction temperature. **Figure 5.2** illustrates the increase in TOF as a function of total pressure at a reaction temperature of 170 ^{o}C.

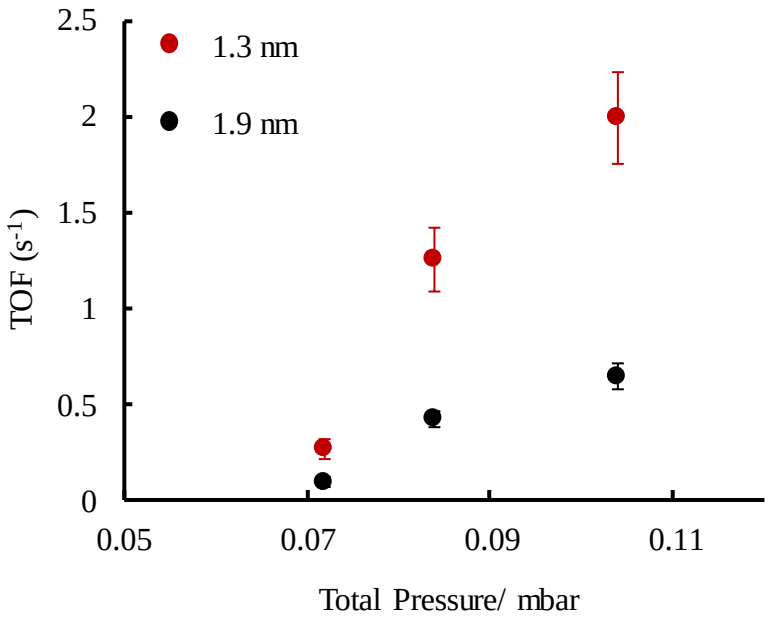

Figure 5.2: The TOF of Pt nanoparticle catalyst supported on titania for the CO oxidation reaction as a function of total pressure (mbar) at an O_2:CO ratio of 1:1, with a total pressure of 7.2 x 10^{-2} mbar, 8.4 x 10^{-2} mbar and 1.04 x 10^{-1} mbar for the Pt particle sizes of 1.3 n and 1.9 nm. The reaction temperature was 170 ^{o}C. The plot identification is also indicated in the figure legend.

From the figure above, a linear relationship is observed between the TOF and total pressure. This confirms the dependence of Pt nanoparticles reactivity toward CO oxidation on reactant gas pressure at a particular reaction temperature. This observation is in good agreement with the previous reports addressing the dependences of the partial pressures of O_2 and CO on the reaction rate for CO oxidation.[81] Similar observation was reported by Berlowitz *et al.*[95] in their activity study of CO oxidation on Pt (100) single crystal as a function of temperature and CO:O_2 partial pressure over the temperature range of 425 K to 725 K and pressure range 0.1 Torr to 600 Torr. However, it is important to note here that Berlowitz *et al.*[95] in their study of CO oxidation they used higher reactant gas pressure as compared to that used in this work as shown in **Figure 5.2** that illustrates the increase in reaction rate as a function of total pressure.

The experiments with pre-exposed O_2-and CO-rich regimes and subsequently admitting a complimentary reactant gas, revealed a linear relationship reaching a 1:1 ratio of O_2:CO mixture, total pressure of 2.2 x 10^{-1} mbar, at 170 ^{o}C. **Figure 5.3** presents the TOF as a function of reactant gas total pressure for a pre-exposed O_2 and CO Pt surface,

respectively, for a Pt particle size of 1.3 nm. Within experimental errors the rates and dependences are the same, indicating that a common steady state of reaction has been reached in both experimental conditions.

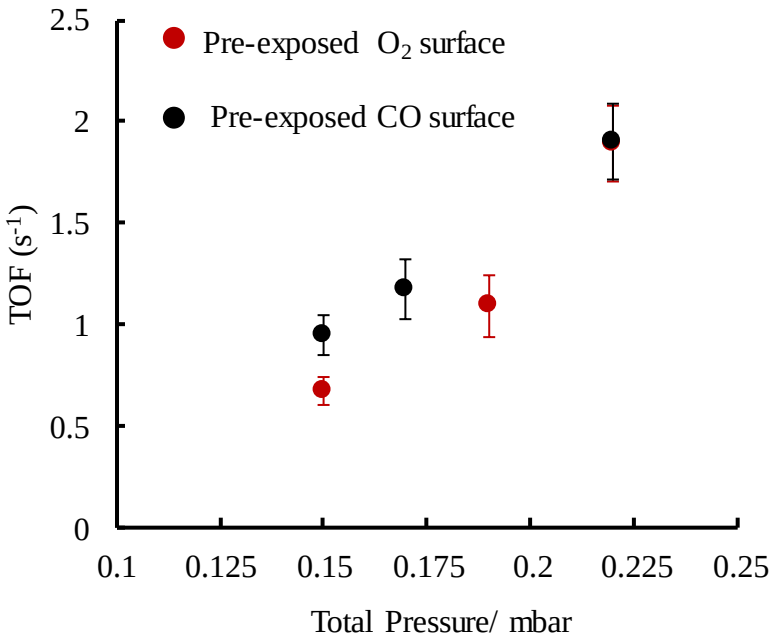

Figure 5.3: The TOF of Pt nanoparticle catalyst supported on titania for the CO oxidation reaction as a function of total pressure at an O_2:CO ratio of approximately 2:1 and 1:2, with a total pressure of 1.5 x 10^{-1} mbar, an O_2:CO ratio of approximately 1:1, at a total pressure of 1.9 x 10^{-1} mbar and 1.7 x 10^{-1} mbar, and an O_2:CO ratio of 1:1, with a total pressure of 2.2 x 10^{-1} mbar for a Pt particle size of 1.3 nm. The reaction temperature was 170 ^{o}C. The plot identification is also indicated in the figure legend.

For a surface pre-adsorbed with O_2, the TOF increased with increasing CO pressure up to an O_2:CO ratio of 1:1, total pressure of 2.2 x 10^{-1} mbar, **Figure 5.3**. A similar trend in activity was observed for a pre-adsorbed CO surface, reaching an O_2:CO ratio of 1:1, total pressure of 2.2 x 10^{-1} mbar, consistent with reported findings in the literature.[81] Johanek *et al.*[181] reported such findings in their study to assess the dependence of the reaction rate of CO oxidation on either an O_2 or CO pre-adsorbed surface, a study of the CO oxidation reaction on Pd nanoparticle catalyst. Similar observations were reported by Berlowitz *et al.*[95] in their study of CO oxidation on Pt (100) single crystal catalyst.

The activity of Pt at elevated reaction temperatures (240 ^{o}C) and relatively higher reactant gas pressure revealed the dependence of CO oxidation on temperature and reactant gas pressure. The highest reaction temperature resulted into the highest activity compared to that recorded at relatively low temperatures and pressures. A typical activity trend illustrating the activity increase with increasing reaction temperature for CO oxidation on titania supported Pt nanoparticles is shown in **Figure 5.4**.

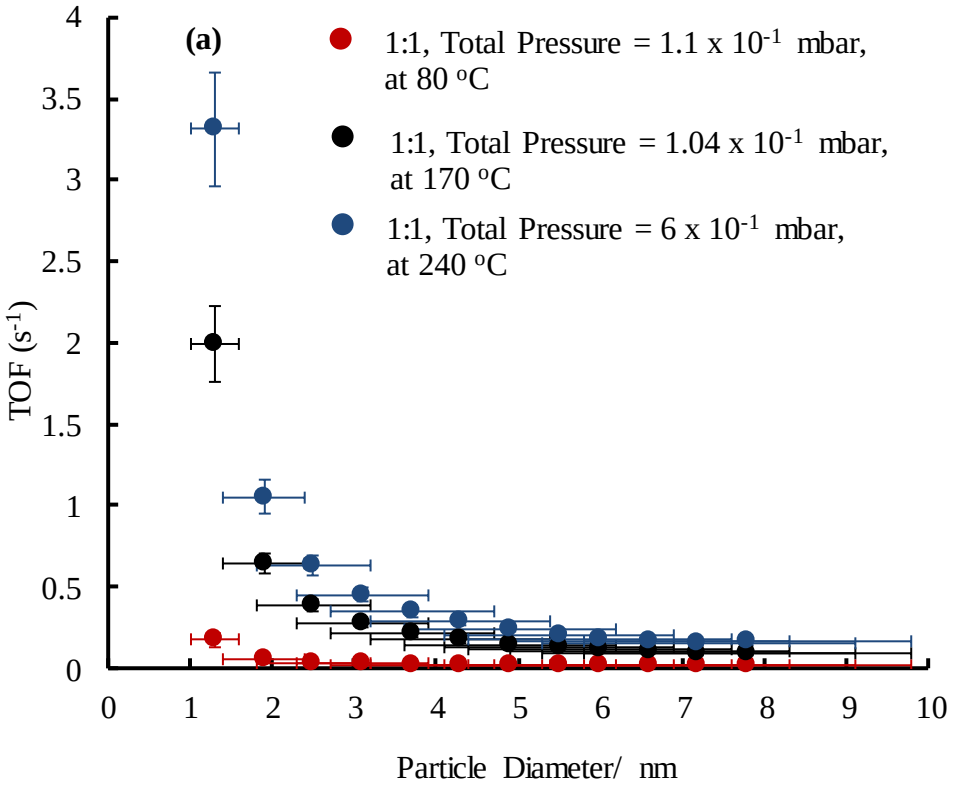

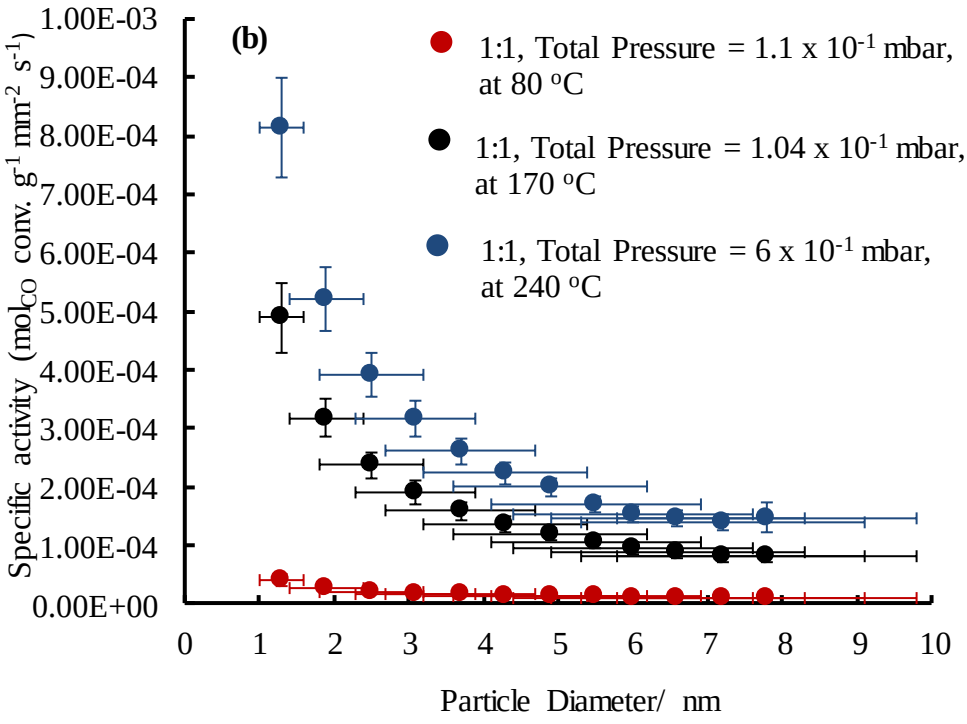

Figure 5.4: (a) TOF , **(b)** specific mass activity of Pt nanoparticle catalyst supported on titania for the CO oxidation reaction as a function of particle size (diameter/ nm) at an O_2:CO ratio of 1:1, with a total pressure of 1.1 x 10^{-1} mbar, 1.04 x 10^{-1} mbar and 6 x 10^{-1} mbar illustrating the activity increase with increasing reaction temperature. The reaction temperatures and total pressure are also indicated in the figure legend.

The maximum TOF of 4.355 s^{-1}, (specific mass activity = 1.070 x 10^{-3} mol_{CO} conv. g^{-1}Pt mm^{-2} s^{-1}) was achieved at an O_2:CO ratio of 1:1, total pressure of 1.1 mbar, **Figure 4.14**. Further increase of the reactant gas pressure to an O_2:CO ratio of 1:1, total pressure of 2.4 mbar led to a slight decrease in activity to 4.174 s^{-1}, (specific mass activity = 1.026 x 10^{-3} mol_{CO} conv. g^{-1}Pt mm^{-2} s^{-1}) as demonstrated in **Figure 4.14**. The decline in activity can be associated with the CO poisoning of the Pt catalyst surface inhibiting O_2 adsorption and dissociation on the catalyst surface, a crucial process for the reaction to take place, hence retarding Pt catalyst activity. Earlier research by Goodman *et al.*[52] reported a similar observation for CO oxidation on a Pt catalyst. In their findings, an extremely active surface of Pt was observed at high reactant gas pressure and high reaction temperature. It was addressed that, at low reaction temperatures, the CO inhibited regime is involved, where the reaction is inhibited by adsorbed CO which hinders the adsorption and dissociation of O_2, resulting in the low catalytic activity of the Pt catalyst.[49, 52, 110]

Figure 5.5 presents the activity dependence of CO oxidation on Pt nanoparticles catalyst for Pt particle sizes of 1.3 nm, 3.1 nm and 5.5 nm at 80 ^{o}C, 170 ^{o}C and 240 ^{o}C.

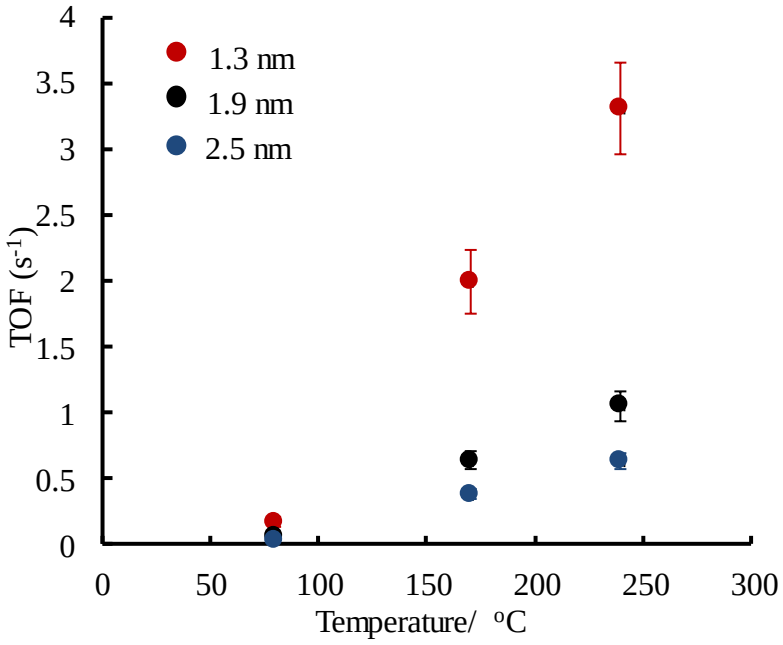

Figure 5.5: The TOF of Pt nanoparticle catalyst supported on titania for the CO oxidation reaction as a function of reaction temperature (^{o}C), at an O_2:CO ratio of 1:1, with a total pressure of 1.1 x 10^{-1} mbar, 1.04 x 10^{-1} mbar and 6 x 10^{-1} mbar illustrating the activity increase with increasing reaction temperature for Pt particle sizes of 1.3 nm, 1.9 nm and 2.5 nm. Plot identification is also indicated in the figure legend.

Figure 5.6 presents the Arrhenius-type plot of logarithmic reaction rate as a function of the reciprocal temperature (K^{-1}) for CO oxidation on titania supported Pt nanoparticles catalyst.

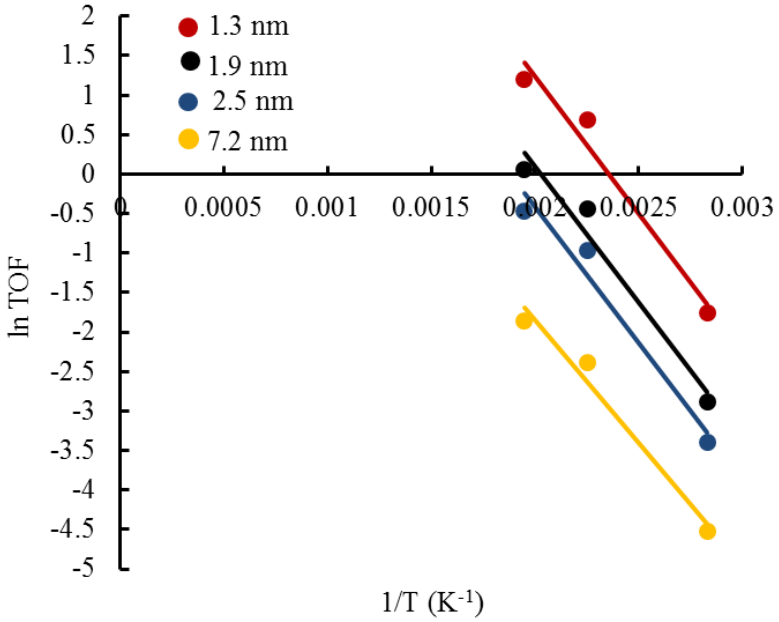

Figure 5.6: Logarithm of reaction rate (TOF) of CO oxidation over titania supported Pt nanoparticles catalyst as a function of the reciprocal temperature (K^{-1}) at an O_2:CO ratio of 1:1, with a total pressure of 1.1 x 10^{-1} mbar, 1.04 x 10^{-1} mbar and 6 x 10^{-1} mbar illustrating the activity increase with increasing reaction temperature for Pt particle sizes of 1.3 nm, 1.9 nm, 2.5 nm and 7.2 nm. Plot identification is indicated in the figure legend.

From Arrhenius-type plot above, the activation energy for the CO oxidation reaction on titania supported Pt nanoparticles catalysts was computed. The activation energy was 28 ± 2 kJ mol^{-1}, and the error was calculated from the difference between the maximum activation energy obtained with TOFs plus errors in TOFs and the minimum activation energy with no errors in TOFs. From Figure 5.6, it can be observed that the slope of Arrhenius-type plot is steep, which means the activation energy is higher. The practical implication of such behaviour is that the reaction rate for CO oxidation on titania supported Pt nanoparticle catalyst appears to be very sensitive to the reaction temperature.[8] Increasing reaction temperature for such a reaction would significantly increase the rate of a reaction, which has indeed, has been observed in this study. Bamwenda *et al.*[62] reported activation energy ranging between 49 kJ mol^{-1} to 60 $kJmol^{-1}$ for titania supported Pt nanoparticles catalyst at 300 K, the pressure conditions were not reported in this paper. Liu *et al.*[49] reported the activation energy of 33 kJ mol^{-1} at a temperature range between 20 ^{o}C to 105 ^{o}C and atmospheric pressure for CO oxidation on Pt nanoparticles supported on FeO_x. Goodman *et al.*[95] observed the activation energy ranging between

22 kJ mol^{-1} -33 kJ mol^{-1} in their study of CO oxidation on Pt (100) single crystal over temperature range of 425-725 K and pressure range between 0.1-600 Torr.

5.2 Gold Nanoparticles Catalyst

The oxidation of CO on titania supported Au nanoparticles was investigated on Au particles ranging in size between 1.5 nm to 5.8 nm at various CO and O_2 pressures and relatively low reaction temperatures. Generally, based on the activity data obtained and presented in **Section 4.4**, Au particle size governs the activity for the CO oxidation reaction. The general activity trend shows increased activity with decreasing particle size, consistent with most published results in the literature.[57, 74, 76, 115, 182] For example, at 80 ^oC and a CO:O_2 ratio of 1:1, with a total pressure of 8.4 x 10^{-2} mbar (**Figure 4.17**), the TOF increased from 0.016 s^{-1}, (specific mass activity = 2.11 x 10^{-5} mol_{CO} conv. g^{-1}Au mm^{-2} s^{-1}) for an Au particle size of 5.8 nm, to 0.186 s^{-1}, (specific mass activity = 1.05 x 10^{-4} mol_{CO} conv. g^{-1}Au mm^{-2} s^{-1}) for Au particle size of 1.5 nm, an increase in activity by a factor of 19. However, previous reports on titania supported Au nanoparticles activity for the CO oxidation reaction by Bamwenda *et al.*[62] and Goodman *et al.*[22] show a maximum activity for particles of approximately 3 nm in size. In their study, they addressed the effect of quantum size effect (electron confinement) for particle size less than 3 nm, however quantum size effect start to dominate in clusters with equivalent sizes less than 1 nm.[115] Since the reactivity of active metal particle depends on its surface properties, the catalytic properties vary accordingly as particle size changes because of monotonic change in particle morphology, such as the density of steps and kinks. However, for small clusters, these parameters fail and valence electrons are highly confined, hence quantum effect dominates.[13] For the Au particle sizes investigated in this study at various reaction temperatures and pressure, no decline in activity with decreasing particle size was observed. This is due to the fact that for the metal particles falling within the range of particle sizes studied, the number of under-coordinated adsorption sites for CO and O_2 are enormous which play a greater role in the CO oxidation reaction, therefore the decline in activity should be an exception. **Figure 5.7** presents the particle size dependence of CO oxidation on titania supported Au nanoparticles catalyst reported by Bamwenda *et al.*[62] (although they did not report the pressure condition used) and that obtained in this work.

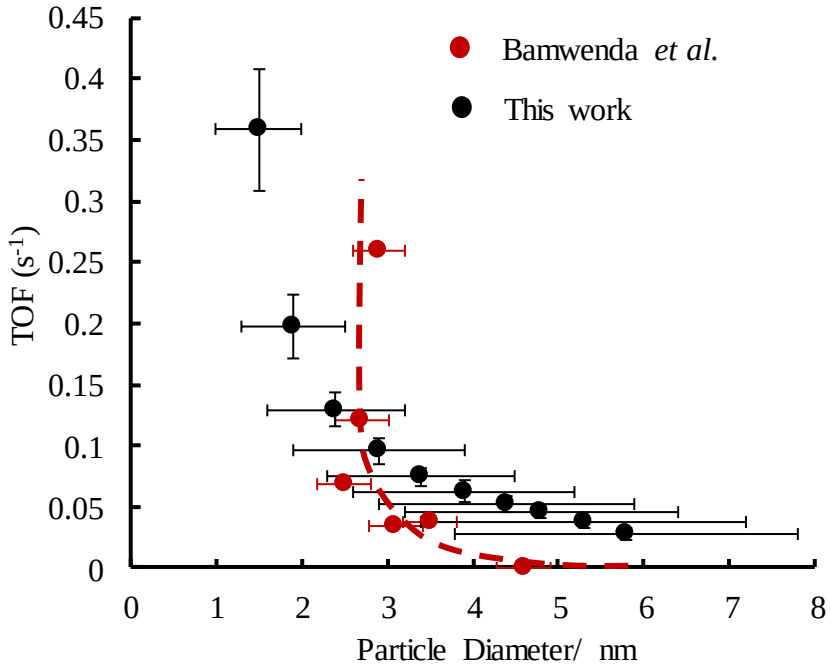

Figure 5.7: The TOF of Au nanoparticle catalyst supported on titania for the CO oxidation reaction as a function of particle size (diameter/ nm). Red plot presents activity results from Bamwenda *et al.*[62] with extrapolation shown by a blue dashed line, at a reaction temperature of 300 K and black plot presents activity results obtained in this work at an $CO:O_2$ ratio of 1:1, with a total pressure of 1 x 10^{-1} mbar and reaction temperature of 80 ^{o}C.

When the activity trend obtained in this work is compared with that reported by Bamwenda *et al.*[62], extrapolation of their data shows no maximum, meaning that the trend would be the same.

Haruta *et al.*[62] reported a Au/TiO_2 maximum TOF of 0.26 s^{-1} at 300 K for a Au particle size of 2.9 nm. Goodman *et al.*[22] on the other hand reported a Au/TiO_2 maximum TOF of approximately 2 s^{-1} for a Au particle size of 3 nm at 350 K, with a total pressure of 40 Torr. Herranz *et al.*[57] reported a Au/TiO_2 specific mass activity increase with decreasing Au particle size, no observed optimum activity of Au with decreasing particle size, consistent with activity trend obtained in this work. Overbury *et al.*[183] have recently investigated the Au particle size dependences for CO oxidation at 289 K, and report no evidence of optimum activity for smaller Au particle sizes, consistent with results obtained in this work. In these studies, the low-coordinated adsorption sites highly present in particles within this particle range in addition to the influence of support were addressed to play a key role in the increased activity. **Figure 5.8** presents the activity for CO oxida-

tion on titania supported Au nanoparticles as a function of particle size reported in the literature and that obtained in this work.

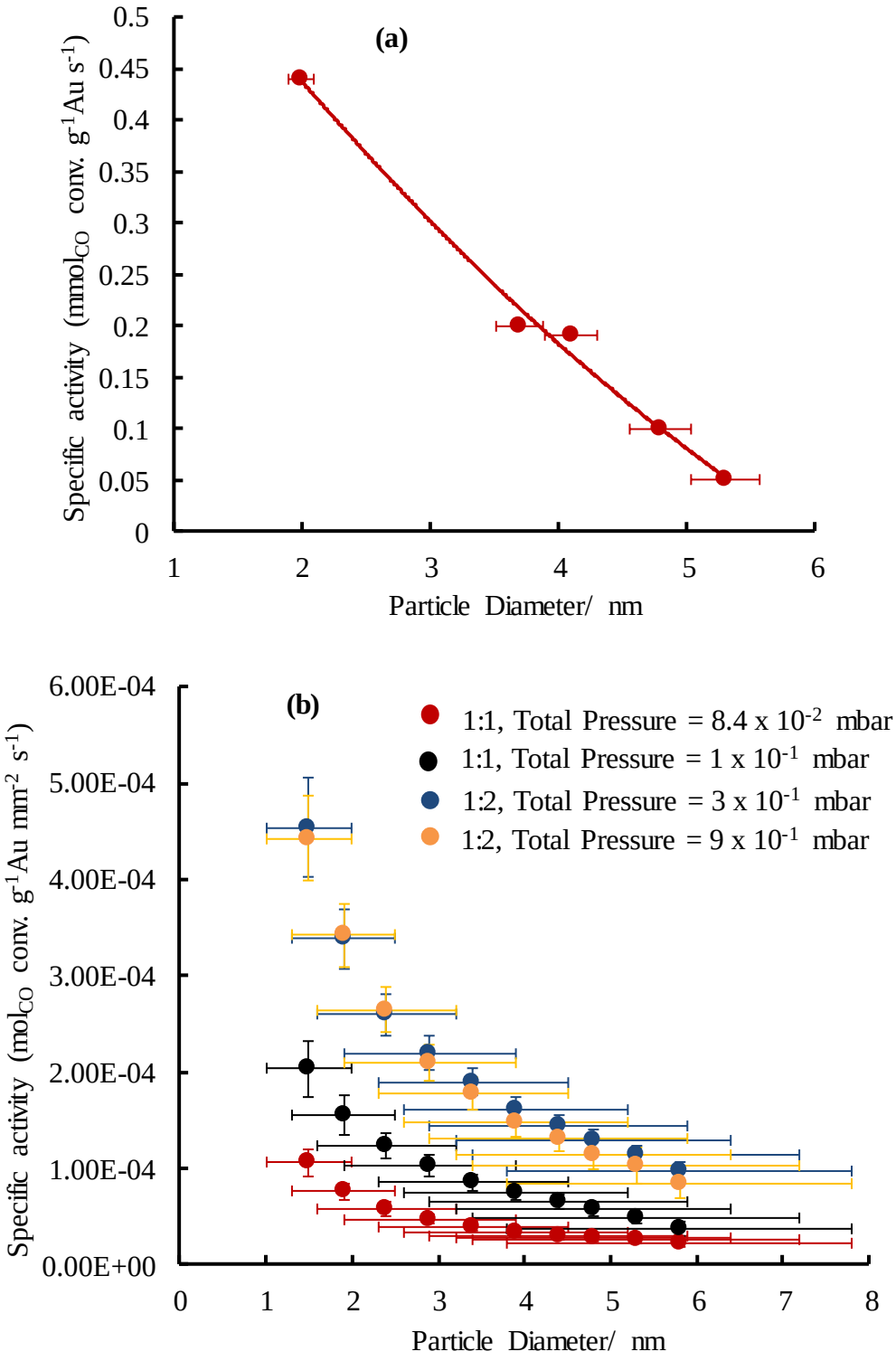

Figure 5.8: The activity of Au nanoparticle catalyst supported on titania for the CO oxidation reaction as a function of particle size (diameter/ nm). **(a)** Specific mass activity results from Herranz *et al.*[57] at a reaction temperature of 70 °C. **(c)** Specific mass activity results obtained in this work at a reaction temperature of 80 °C.

The activity results achieved in this work are therefore consistent with most data published on titania supported Au nanoparticle catalyst for the CO oxidation reaction.

The oxidation of CO on a Au/TiO_2 catalyst at 170 ^oC, revealed that Au activity increases with increasing reaction temperature and reactant gas pressure. For example, at 80 ^oC the activity increased from 0.783 s^{-1}, (specific mass activity = 4.43 x 10^{-4} mol_{CO} conv. $g^{-1}Au$ mm^{-2} s^{-1}) for a Au particle size of 1.5 nm (**Figure 4.17**) at an O_2:CO ratio of 1:2, total pressure 9 x 10^{-1} mbar to 1.558 s^{-1}, (specific mass activity = 8.81 x 10^{-4} mol_{CO} conv. $g^{-1}Au$ mm^{-2} s^{-1}) at an O_2:CO ratio of 1:2, total pressure of 9 x 10^{-1} mbar at 170 ^oC (**Figure 4.20**), the increase in activity by a factor of 2, in good agreement with published findings by Herranz *et al*..[57] In their study, the activity of Au/SiO_2 catalyst was studied alongside with Au/TiO_2 catalyst at various reaction temperatures, it was found that Au/SiO_2 is less active compared to Au/TiO_2 with increasing reaction temperature. The highest activity displayed by titania supported Au nanoparticles with increasing temperature was explained in terms of support effect.[57] The typical results illustrating the increase in the Au activity with increasing reaction temperature obtained in this work can be seen in **Figure 5.9**.

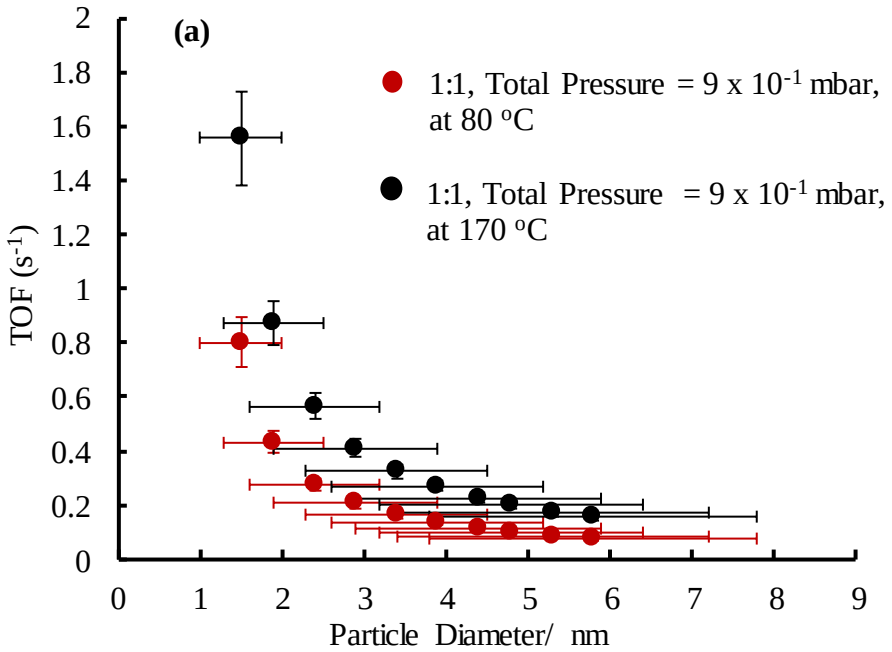

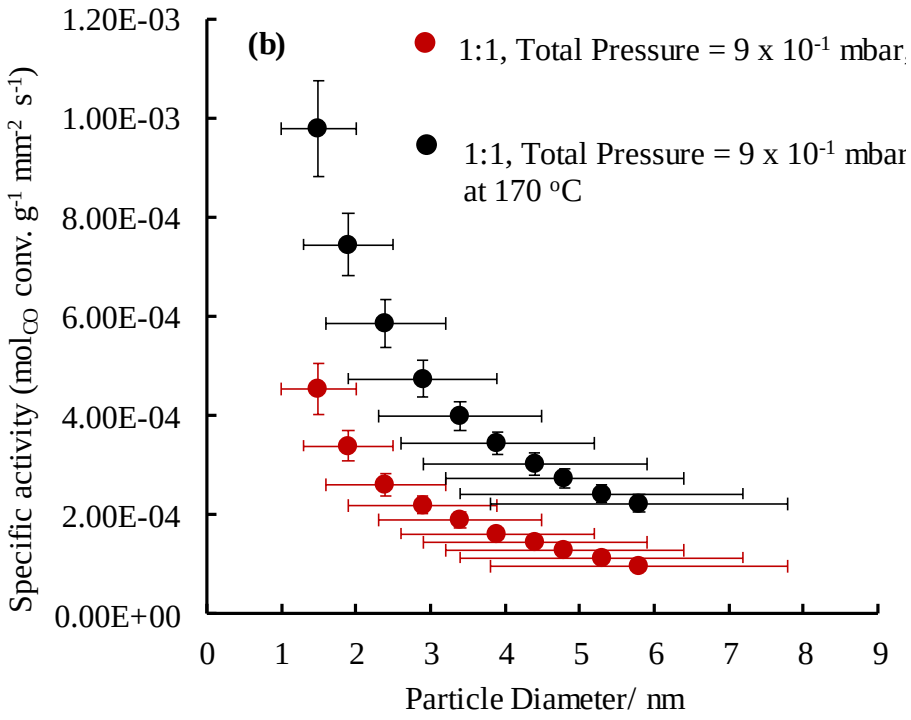

Figure 5.9: (a) TOF, **(b)** specific mass activity of Au nanoparticle catalyst supported on titania for the CO oxidation reaction as a function of particle size (diameter/ nm) at an O_2:CO ratio of 1:1, with a total pressure of 9 x 10^{-1} mbar illustrating the activity increase with increasing reaction temperature. The reaction temperatures and total pressures are also indicated in the figure legend.

Herranz *et al.*[57] reported an increase in specific mass activity of titania supported Au nanoparticles of 2.2 x 10^{-5} mol. CO conv. g^{-1}Au s^{-1} at 70 ^{o}C to 1 x 10^{-4} mol_{CO} conv. g^{-1}Au s^{-1} at 190 ^{o}C for a Au particle size of 2 nm. Lin *et al.*[184] reported an increase in specific mass activity of titania supported Au with increasing reaction temperature of 7 x 10^{-9} mol_{CO} conv. g^{-1}Au s^{-1} at 40 ^{o}C to 2.4 x 10^{-8} mol_{CO} conv. g^{-1}Au s^{-1} at 160 ^{o}C. **Figure 5.10** presents the TOF of titania supported Au nanoparticles as a function of temperature for the Au particle size of 1.9 nm, 24 nm and 2.9 nm.

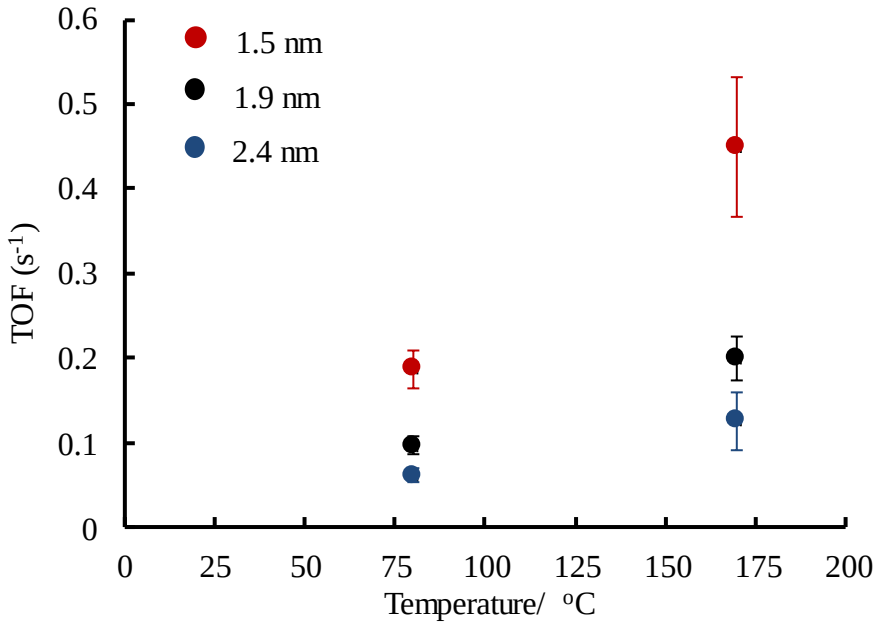

Figure 5.10: The TOF of Pt nanoparticle catalyst supported on titania for the CO oxidation reaction as a function of reaction temperature (^{o}C), at an O_2:CO ratio of 1:1, with a total pressure of 8.4 x 10^{-2} mbar and 6 x 10^{-2} mbar illustrating the activity increase with increasing reaction temperature for Au particle sizes of 1.5 nm, 1.9 nm and 2.4 nm. Plot identification is also indicated in the figure legend.

Figure 5.11 presents the Arrhenius-type plot of logarithmic reaction rate as a function of the reciprocal temperature (K^{-1}) for CO oxidation on titania supported Au nanoparticles catalyst.

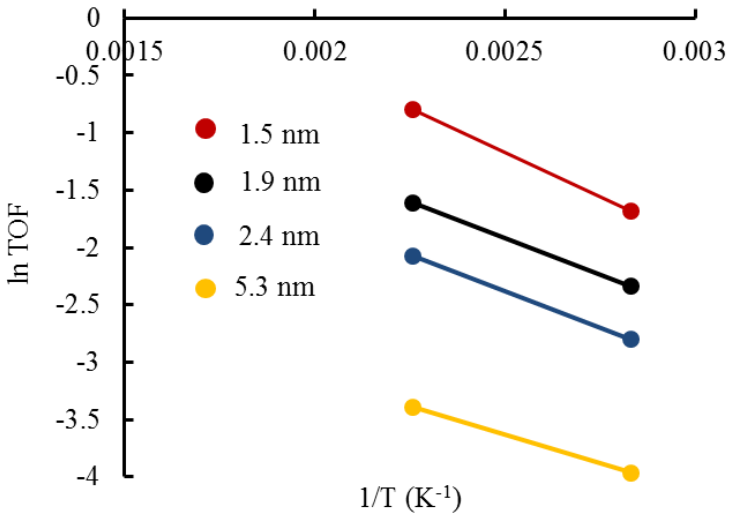

Figure 5.11: Logarithm of reaction rate (TOF) of CO oxidation over titania supported Au nanoparticles catalyst as a function of the reciprocal temperature (K^{-1}) at an O_2:CO ratio of 1:1, with a total pressure of 8.4 x 10^{-2} mbar and 6 x 10^{-2} mbar illustrating the activity increase with increasing reaction temperature for Au particle sizes of 1.5 nm, 1.9 nm, 2.4 nm and 5.3 nm. Plot identification is indicated in the figure legend.

From Arrhenius-type plot above, the activation energy for the CO oxidation reaction on titania supported Au nanoparticles catalysts was computed. The activation energy was 13 ± 3 kJ mol^{-1}, and the error was calculated from the difference between the maximum activation energy obtained with TOFs plus errors in TOFs and the minimum activation energy with no errors in TOFs. From **Figure 5.11**, it can be observed that the slope of the Arrhenius-type plot is not steep, hence less activation energy. This means in practical terms, the reaction rate for CO oxidation on titania supported Au nanoparticle varies only slightly with increasing reaction temperature,[8] which has indeed, been observed in this study. The CO oxidation follows Langmuir-Hinshelwood as suggested below:

$CO\ (g) \rightarrow CO_{(ad)}\ (gold)$ fast

$O_2\ (g) \rightarrow 2O_{(ad)}\ (titania)$ fast

$O_{(a)}\ (titania) \rightarrow O_{(a)}\ (gold)$ fast

$O_{(a)}\ (gold) + CO_{(ad)}\ (gold) \rightarrow CO_{2(ad)}\ (gold)$ rate determining step

$CO_{2(ad)}\ (gold) \rightarrow CO_2\ (g)$ fast

In L-H model, and keeping CO pressure constant, increasing oxygen pressures causes the catalyst to be saturated with many oxygen molecules, and vice versa. No detailed kinetic measurements were made in this work in order to establish the pressure dependence of this reaction in either the CO or O_2 adsorption regimes. Increasing the pressure of both O_2 and CO systematically resulted in a saturation of the rate of reaction, consistent with the suggestion that the reaction take place through a L-H reaction mechanisms as discussed above.

Bamwenda *et al.*[62] reported activation energy ranging between 18 kJ mol^{-1} to 57 $kJmol^{-1}$ for titania supported Au nanoparticles catalyst at 300 K, no pressure condition was reported in this paper. Schubert *et al.*[76] reported the activation energy of 21 kJ mol^{-1} for CO oxidation on titania supported Au nanoparticles catalyst at an O_2:CO ratio of 1:1, with a total pressure of 2 kPa and reaction temperature of 80 ^oC. Kozlov *et al.*[185] reported the activation energy of 13 kJ mol^{-1} for CO oxidation on titania supported Au nanoparticles at 313 K, no pressure condition was reported in this paper.

Further increase of reactant gas pressure at the same reaction temperature of 80 ^oC or 170 ^oC did not increase the activity of Au/TiO_2, instead the constant activity was maintained and even slightly declined. **Figure 5.12** illustrates the increase in TOF as a function of total pressure at a reaction temperature of 80 ^oC.

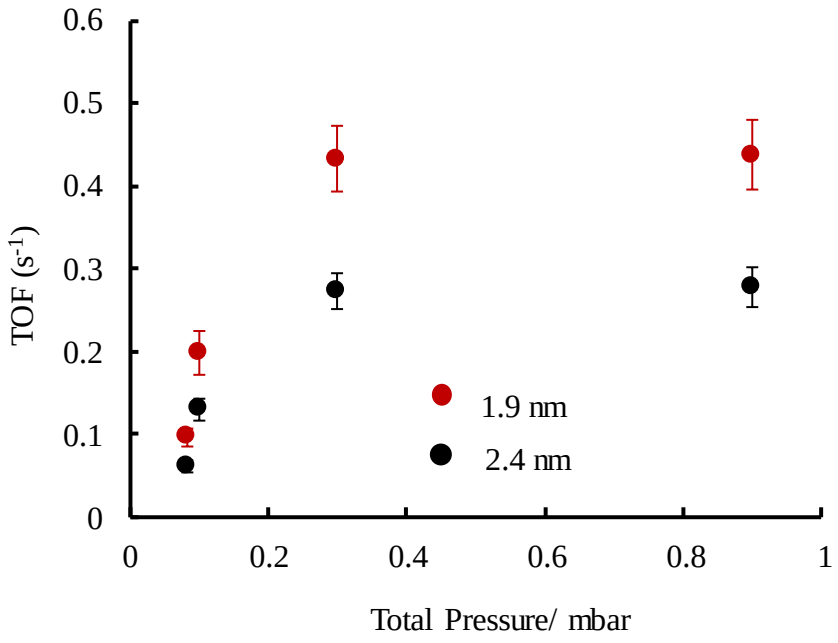

Figure 5.12: The TOF of Au nanoparticle catalyst supported on titania for the CO oxidation reaction as a function of total pressure (mbar) at an O_2:CO ratio of 1:1, with a total pressure of 8.4 x 10^{-2} mbar, 1 x 10^{-1} mbar and O_2:CO ratio of 1:2, with a total pressure of 3 x 10^{-1} mbar and 9 x 10^{-1} mbar for the Au particle sizes of 1.9 nm and 2.4 nm. The reaction temperature was 80 ^{o}C. The plot identification is also indicated in the figure legend.

Nevertheless, at a particular reaction temperature, increasing the reactant gas pressure increased the activity for the CO oxidation reaction.

5.3 Comparison of Titania Supported Pt and Au Catalysts

Having presented and discussed the activity results obtained from activity of both Pt/TiO_2 and Au/TiO_2 catalysts for the CO oxidation reaction at relatively low reaction temperatures, it is worthwhile comparing these results for two catalyst systems studied in this work.

This work has addressed the heterogeneously catalysed CO oxidation by O_2 on supported Pt and Au nanoparticle catalysts at relatively low reaction temperatures and pressure. This reaction is envisaged to play a key role in CO removal from the environment as well as in PEMFCs, where CO oxidation has to take place at low temperatures. Pt is commonly considered as the most active heterogeneous catalyst for the conversion of

CO as addressed previously, however, it is an expensive precious metal which means it is unfavourable for application in commercial systems. Additionally, the fact that Pt catalyst gets poisoned by CO during catalytic processes at low reaction temperature, demand for improvement of Pt based catalysts systems. Catalysis by Au on the other hand has been recently exploited, and its activity for low temperature CO oxidation is enormously reported. Therefore, application of Au nanoparticles catalyst in such a reaction is highly promising, hence its use in commercial systems would be feasible pending to further research. The results presented in this thesis reveal the use of a HT-PVD technique for synthesis of a wide range of supported Pt and Au nanoparticles catalysts and the robustness of a newly developed high throughput heterogeneous catalyst screening methodology to study the catalytic properties of titania supported Pt and Au nanoparticles of various sizes for CO oxidation at low reaction temperatures. The initial time during this research was spent in developing a high throughput heterogeneous catalyst screening chip. A high throughput IR-thermography was selected as the best technique for direct measurement of heat produced on the catalyst library as a result of CO oxidation. The catalytic results obtained for both Pt/TiO_2 and Au/TiO_2 catalysts can be used to assess the suitability of their application where low temperature oxidation is desired and therefore assess the commercialization feasibility of the systems where these catalysts systems receive scientific interest.

Comparison of the activity results obtained in this work on both Pt/TiO_2 and Au/TiO_2 nanoparticle catalysts were presented and discussed, and set into the context of previous work. Based on the activity results obtained in this work, it is without doubt that the TOF and specific mass activity of Au/TiO_2 recorded at 80 ^oC is higher by a factor of 2 compared to that of Pt/TiO_2. The highest activities of Au/TiO_2 recorded in this study were 0.803 s^{-1}, (specific mass activity = 4.54 x 10^{-4} mol_{CO} conv. $g^{-1}Au$ mm^{-2} s^{-1}) at 80 ^oC and 1.558 s^{-1}, (specific mass activity = 8.81 x 10^{-4} mol_{CO} conv. $g^{-1}Au$ mm^{-2} s^{-1}) at 170 ^oC for an Au particle size of 1.5 nm, respectively. The highest activities of Pt/TiO_2 catalyst recorded were 0.396 s^{-1}, (specific mass activity of 9.743 x 10^{-5} mol_{CO} conv. $g^{-1}Pt$ mm^{-2} s^{-1}) at 80 ^oC, 1.991 s^{-1}, (specific mass activity = 4.893 x 10^{-4} mol_{CO} conv. $g^{-1}Pt$ mm^{-2} s^{-1}) at 170 ^oC and 4.355 s^{-1}, (specific mass activity of 1.070 x 10^{-3} mol_{CO} conv. $g^{-1}Pt$ mm^{-2} s^{-1}) at 240 ^oC, for a Pt particle size of 1.3 nm. It is crucial to insist here based on the activity results presented in this work that, despite the fact that CO oxidation on

both Au and Pt catalysts is particle size dependent, Au shows the strongest particle size dependence towards CO oxidation as illustrated in **Figure 5.13**.

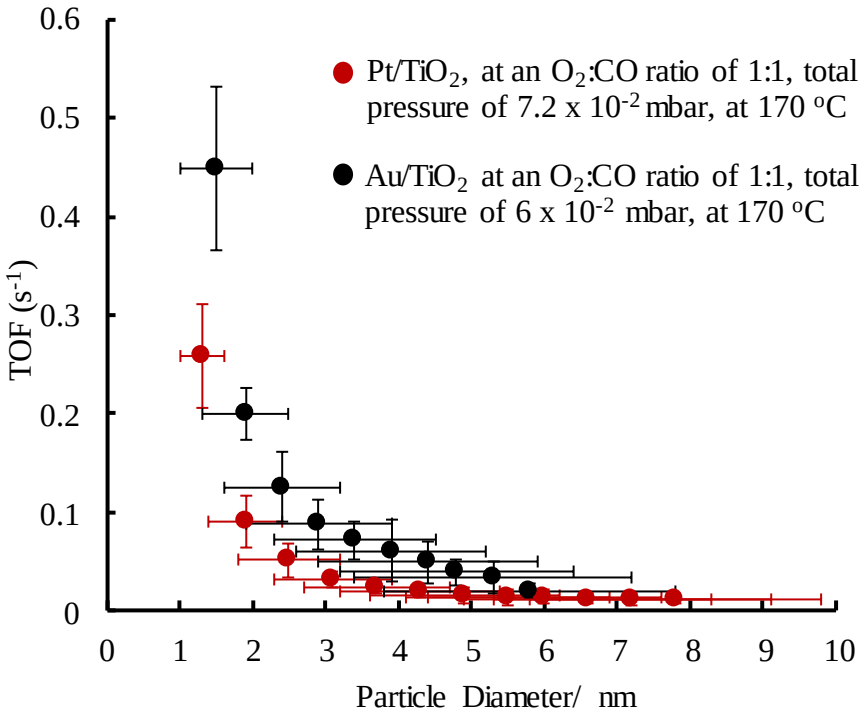

Figure 5.13: The TOF of Au and Pt nanoparticle catalysts supported on titania for the CO oxidation reaction as a function of particle size (diameter/ nm) illustrating the particle size dependence for both catalysts. The reaction conditions are shown in the figure legend.

However, for Pt/TiO_2 and Au/TiO_2 catalysts, the effect of reaction temperature on CO oxidation activity revealed that both catalysts exhibited increased activity as the reaction temperature was increased, in agreement with previous reports.[57, 184] Investigation of the effect of reactant gas pressure on the other hand, has shown that at a particular reaction temperature, increasing the reactant gas pressure increases the activity for Au/TiO_2 catalyst to a point where further increase in pressure does not change the activity. In case of Pt/TiO_2 catalyst, increasing reactant gas pressure at a particular reaction temperature equally resulted in an increase in the activity with a consequent decline in activity at high pressures and temperature. The decline in activity is perhaps due to CO poisoning of Pt catalyst. Importantly still, this study has shown that the CO oxidation reaction is particle size dependent on both titania supported Au and Pt nanoparticle catalysts, in agreement to most of published findings in the literature. However, activity results in

this work reveal that titania supported Au nanoparticles catalyst displays strongest particle size dependence for the CO oxidation reaction.

6 Conclusions and Further Work

A high throughput approach[32] for study of catalytic properties of supported nanoparticles for CO oxidation at relatively low reaction temperatures has been successfully developed and demonstrated. The approach was coupled with a new high throughput heterogeneous catalyst screening chip developed in this work to screen heterogeneous catalysis reactions on model catalysts. The setup required the application of an IR-thermography technique to simultaneously study the activity of nanoparticle catalyst for low temperature CO oxidation. We have unambiguously demonstrated that the activities of both supported Pt and Au for CO oxidation can be measured. The thermography has been achieved by measuring the temperature of the membranes by using carbon, producing a constant emissivity. The titania is thin and effectively transparent and we assume the effect of the relatively low density of particles is not significant with respect to emissivity. It remains unclear whether the method would work on continuous thin films of metal catalysts where the emissivity may vary with composition.

A wide range of Pt and Au particles has been synthesised on amorphous titania support across the catalyst screening chip. Characterization by TEM shows that during particle nucleation, a mean particle size of 1.3 nm was observed for Pt. When the coverage is increased, the nuclei increased to achieve a maximum particle density of 4.6×10^{12} cm^{-2}. However, for Au initial particle nucleation, a mean particle size of 1.5 nm was observed. Increasing coverage increased the number of nuclei achieving a maximum particle density of 3.89×10^{12} cm^{-2}. For both Pt and Au particles, particle sizes increased at higher coverage resulting in a dramatic decrease in particle density. The smallest Pt particles exhibit a binding energy shift in the (4f) core level of 0.9 eV to higher binding energy from bulk platinum, and the shift is 0.5 eV as the particles grow to a mean size of 6.6 nm. In the case of Au, the smallest Au particles exhibit a binding energy shift in the (4f) core level of 0.42 eV to higher binding energy from bulk gold, and the shift is 0.2 eV below bulk Au as the particles grow to a mean size of 5.8 nm. XPS studies on both Pt and Au nanoparticle catalysts before and after catalytic reaction show no significant change in their binding energy as compared to that of fresh catalysts, confirming that the catalysts were still intact after being subjected to the reaction conditions used in this work. Significant change in particle size due to sintering/agglomeration for a structure sensitive reaction such as CO oxidation on Au and Pt supported nanoparticles would

significantly reduce their catalytic activity. From the activation energy data, Pt/TiO_2 shows high sensitivity on reaction temperature as compared to Au/TiO_2.

Combined with a new catalyst screening chip, the approach[32] provides a suitable way to study particle size effect for the low temperature CO oxidation. Further, increased reaction temperature was observed to increase the activity for both Pt and Au catalysts. It is observed that at a particular reaction temperature, increasing the reactant gas pressure increases the activity for both Pt and Au, although, at higher pressure and temperature, further increase in pressure results into a slight decline in activity for titania supported Pt catalyst. Generally, results from this work demonstrate that, Au/TiO_2 catalyst displays superior activity at low reaction temperature compared to its Pt/TiO_2 counterpart. Both Au and Pt nanoparticles catalysts supported on titania show particle size dependent toward CO oxidation with a monotonic increase in activity with decreasing particle size. However, from the XPS measurements on both titania supported Pt and Au nanoparticles catalysts before and after reaction, we find no correlation between electronic properties of supported nanoparticles and their activities toward CO oxidation.

The observations presented here for titania supported Pt and Au catalysts agree well with reports in the literature for low temperature CO oxidation. However, the initial experiments presented in this thesis are highly promising in the search of a better and more efficient catalyst for low temperature CO oxidation. Nevertheless, for further work, the newly developed heterogeneous catalyst screening technique developed during the course of this work can be optimized, particular by incorporating into it a controlled localised heating element for each membrane window to improve the temperature gradient across the chip. Further work is also needed to deepen our understanding of these catalyst systems despite the fact that the results provide the breakthrough into the discovery of a suitable catalyst and a high throughput screening method for the low temperature CO oxidation reaction. Although the reaction trends with particle sizes have been established in this study for both catalyst systems, there still a need to understand the mechanisms that lead to such behaviour for supported nanoparticles. Since the support and nature of the support on which these particles are supported are addressed to have a significant effect on their reactivity, more research is needed to scrutinise this parameter of the catalyst system and establish a common understanding. Pt and Au nanoparticles supported on supports such as carbon, silica and alumina would be studied

alongside Pt and Au on TiO_2, Fe_2O_3 and NiO in order to establish fully their influences on the reactivity's of these catalysts. In the interest of the robustness of the new screening methodology used in this work, thin films catalyst systems would be important to be investigated. However, for further study, improvement of the screening reactor is required in order to study products distribution from different particle sizes that show higher activity for CO oxidation. Additionally, the study would involve the investigation of the impact of water vapour on the reactivity of supported Au nanoparticles which has been reported to have a dramatic effect in activity.[186, 187]

Appendix 1

O_2:CO ratio = 1:1, Total pressure = 1.1 mbar

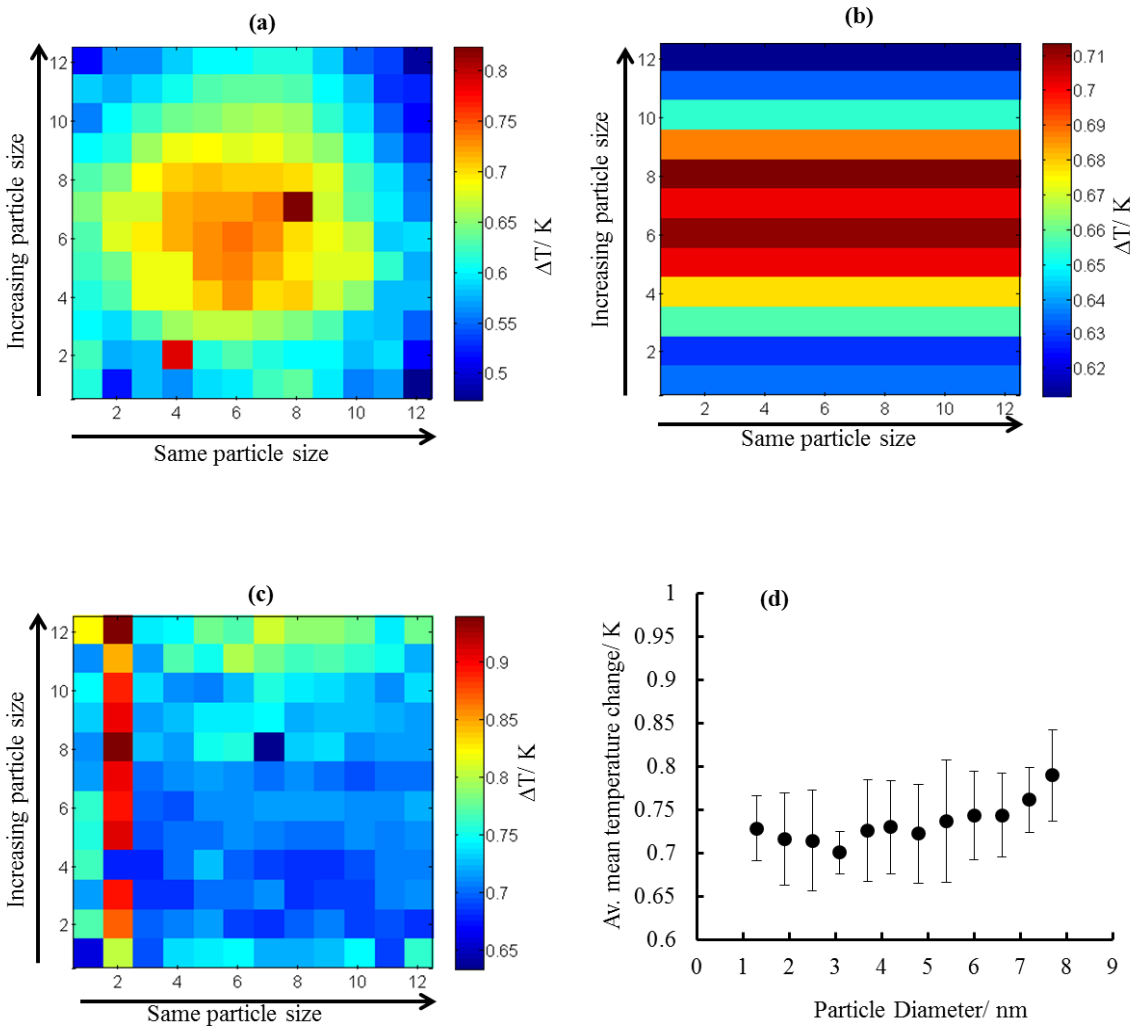

1A$_1$: The temperature change on Pt/TiO_2 catalyst as a function of particle size at approximately O_2:CO of 1:1, total pressure 1.1 mbar. **(a)** Presents uncompensated infrared image, **(b)** row compensated and **(c)** row and column compensated image. **(d)** Presents the average mean temperature change as a function of particle sizes for the row and column compensated infrared images. The row and column numbers are shown on the x and y axes on the IR-images. The reaction temperature was 80 ^{o}C at an exposure time of 5 minutes.

P.diameter (nm)	ΔT/K	Power ($Js^{-1}mm^{-2}$)	mol_{CO} conv.($mm^{-2}s^{-1}$)	Total particle mass (g)	Total particle area (mm^2)	mol_{Pt} in the surface (mm^{-2})	Spec. mass activity (mol_{CO} conv.g^{-1}Pt mm^{-2} s^{-1})	TOF (s^{-1})
1.3±0.3	0.728±0.03	2.867E-5±3.269E-6	1.013E-10±1.55E-11	1.04E-6 ±8.3E-14	10.262±0.9	2.556E-10±2.24E-11	9.743E-5±1.11E-5	0.396±0.045
1.9±0.5	0.716±0.05	2.818E-5±4.094E-6	9.760E-11±1.44E-11	1.52E-6 ±1.2E-13	30.206±3.0	7.524E-10±7.47E-11	6.553E-5±9.51E-6	0.320±0.019
2.5±0.7	0.714±0.05	2.811E-5±4.078E-6	9.336E-11±1.44E-11	2.00E-6 ±1.6E-13	50.150±4.6	1.249E-9±1.15E-10	4.968E-5±7.20E-6	0.080±0.011
3.1±0.8	0.701±0.02	2.758E-5±2.801E-6	9.747E-11±9.89E-12	2.46E-6 ±1.9E-13	70.094±7.0	1.746E-9±1.74E-10	3.930E-5±4.34E-6	0.056±0.005
3.7±1.0	0.726±0.05	2.858E-5±4.113E-6	1.010E-10±1.45E-11	2.96E-6 ±2.3E-13	90.038±8.0	2.243E-9±1.99E-10	3.413E-5±4.91E-6	0.045±0.006
4.2±1.1	0.729±0.05	2.873E-5±4.094E-6	1.015E-10±1.44E-11	3.44E-6 ±2.7E-13	109.982±10	2.740E-9±2.49E-10	2.952E-5±4.20E-6	0.037±0.005
4.8±1.3	0.722±0.05	2.843E-5±4.103E-6	1.004E-10±1.45E-11	3.92E-6 ±3.1E-13	129.926±12	3.236E-9±1.99E-10	2.563E-5±3.69E-6	0.031±0.004
5.5±1.4	0.736±0.07	2.899E-5±4.969E-6	1.025E-10±1.75E-11	4.40E-6 ±3.5E-13	149.870±14	3.733E-9±3.49E-10	2.329E-5±3.99E-6	0.027±0.004
6.0±1.6	0.743±0.05	2.926E-5±4.150E-6	1.034E-10±1.46E-11	4.80E-6 ±3.8E-13	166.490±16	4.140E-9±3.99E-10	2.155E-5±3.05E-6	0.025±0.003
6.6±1.7	0.743±0.04	2.926E-5±3.729E-6	1.034E-10±1.31E-11	5.28E-6 ±4.2E-13	186.434±17	4.644E-9±4.23E-10	1.959E-5±2.49E-6	0.022±0.002
7.2±1.9	0.761±0.03	2.998E-5±3.347E-6	1.059E-10±1.18E-11	5.76E-6 ±4.6E-13	206.378±19	5.141E-9±4.73E-10	1.840E-5±2.05E-6	0.021±0.002
7.8±2.0	0.789±0.05	3.108E-5±4.274E-6	1.098E-10±1.51E-11	6.24E-6 ±4.9E-13	226.322±21	5.637E-9±5.23E-10	1.760E-5±2.42E-6	0.019±0.002
		Equation 2.2	**Equation 3.6**	**Equation 3.8**	**Equation 2.6**	**Equation 3.9**	**Equation 3.7**	**Equation 3.5**

1A2:Pt/TiO_2 particle size and their corresponding specific mass activity and TOF at a reaction temperature of 80 ^oC and approximately O_2:CO ratio of 1:1, at a total pressure of 1.1 mbar. Parameters used to compute the activity values are also included. The equations used to compute the parameters presented in the table are shown. Silicon nitride membrane area is (1.44 ± 0.01) mm^2, silicon nitride thermal conductivity (7 ± 0.2) $Wm^{-1}K^{-1}$ and silicon nitride membrane thickness is 0.6 ± 0.02 μm. The standard deviation for the temperature change was obtained from twelve points on each low. The estimated errors in other parameters were estimated from the deference between the average value and the maximum possible value calculated using errors in each formula used to compute each parameter.

O_2:CO ratio = 1:1, Total pressure = 8.4 x 10^{-2} mbar

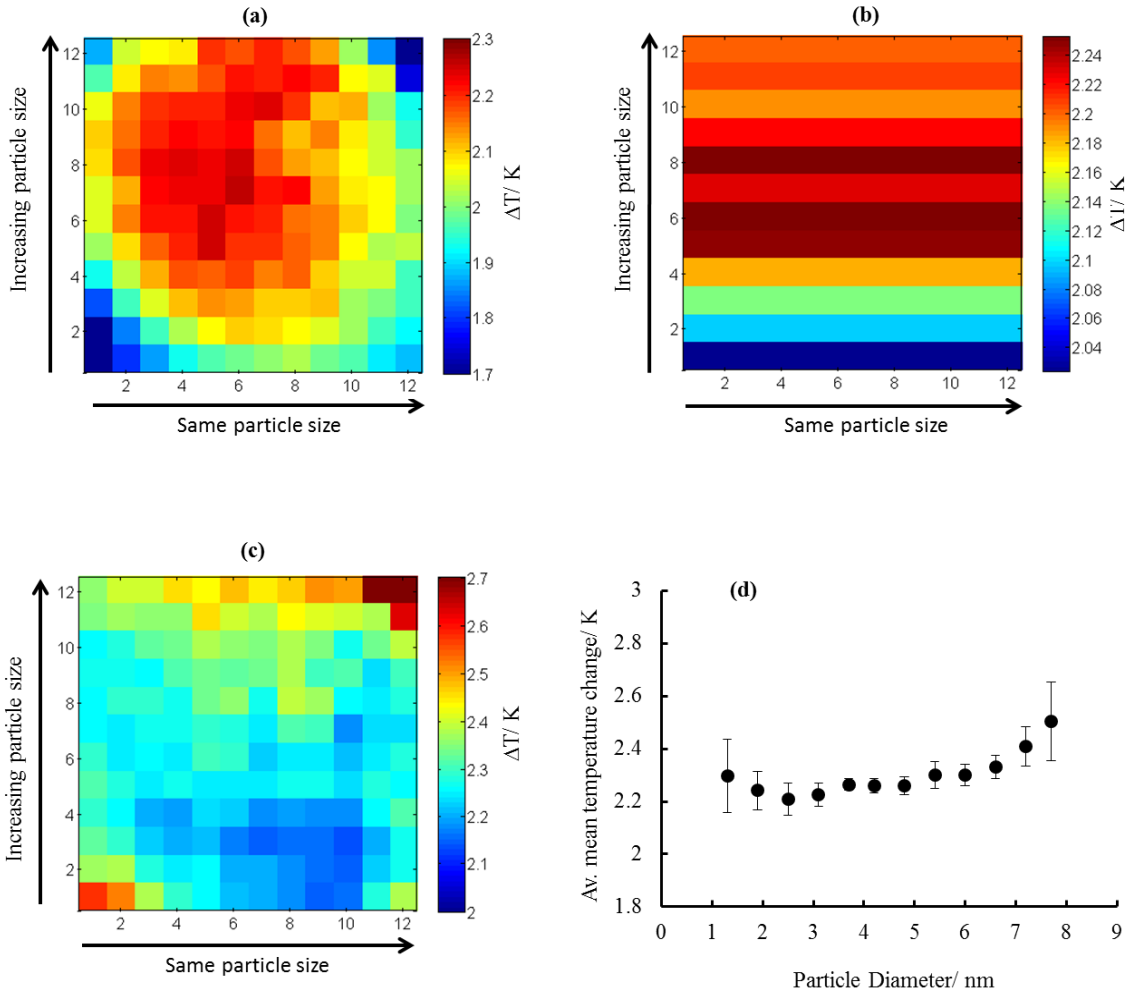

1B$_1$: The temperature change on Pt/TiO_2 catalyst as a function of particle size at approximately O_2:CO ratio of 1:1, total pressure of 8.4 x 10^{-2} mbar **(a)** Presents uncompensated infrared image, **(b)** row compensated and **(c)** row and column compensated images. **(d)** Presents the average mean temperature change as a function of particle sizes for the row and column compensated infrared images with column and row numbers indicated on the x and y axes. The reaction temperature was 170 ^{o}C at an exposure time of 5 minutes.

O_2:CO ratio = 1:1, Total pressure = 1.04 x 10^{-1} mbar

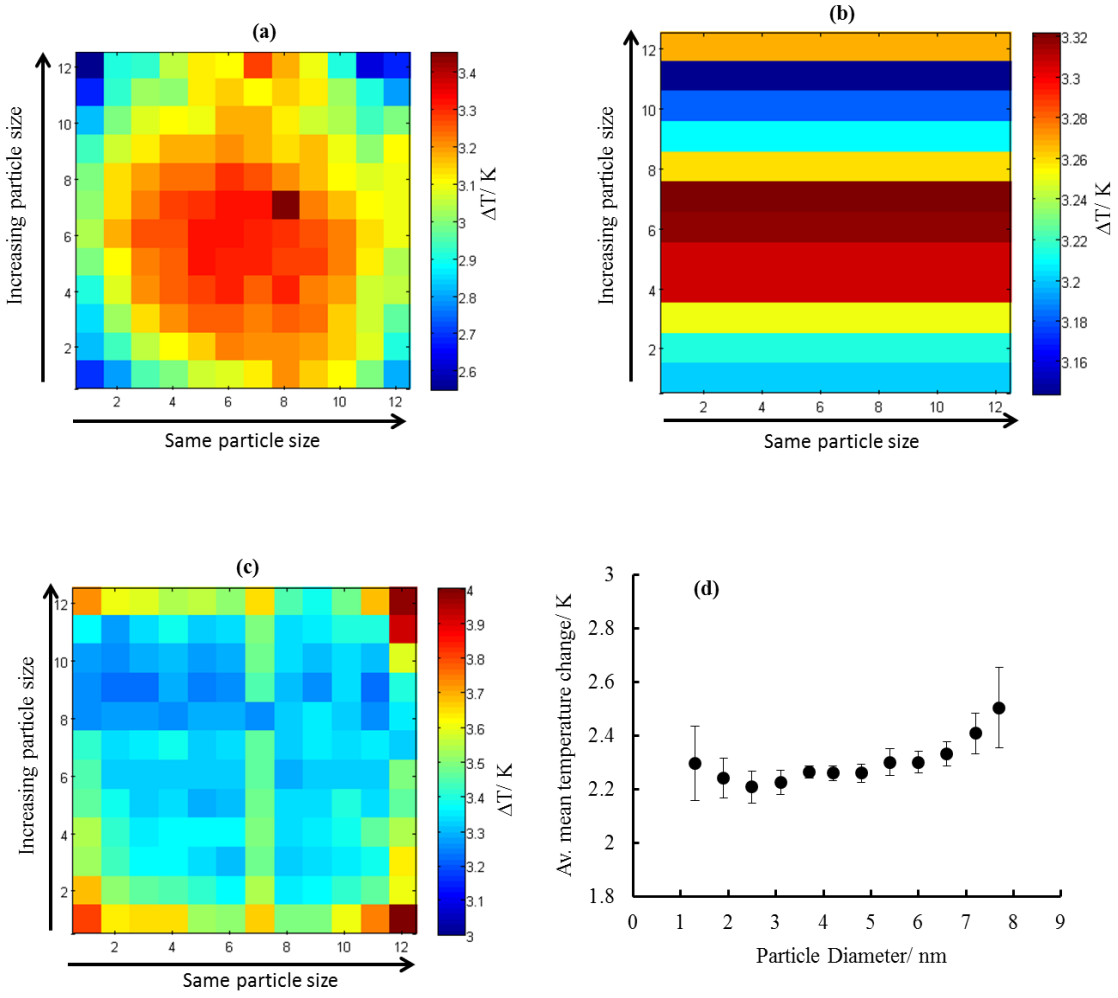

1B$_2$: The temperature change on Pt/TiO_2 catalyst as a function of particle size at approximately O_2:CO ratio of 1:1, total pressure of 1.04 x 10^{-1} mbar. **(a)** Presents uncompensated infrared image, **(b)** row compensated and **(c)** row and column compensated images. **(d)** Presents the average mean temperature change as a function of particle sizes for the row and column compensated infrared images with column and row numbers indicated on the x and y axes. The reaction temperature was 170 ^{o}C at an exposure time of 5 minutes.

P.diameter (nm)	ΔT/K	Power ($Js^{-1}mm^{-2}$)	mol_{CO} conv.($mm^{-2}s^{-1}$)	Total particle mass (g)	Total particle area (mm^2)	mol_{Pt} in the surface (mm^{-2})	Spec. mass activity (mol_{CO} conv.$g^{-1}Pt\ mm^{-2}\ s^{-1}$)	TOF (s^{-1})
1.3±0.3	2.296±0.13	9.044E-5±1.18E-5	3.195E-10±4.17E-11	1.04E-6±8.3E-14	10.262±0.9	2.556E-10±2.24E-11	3.073E-4±4.01E-5	1.250±0.163
1.9±0.5	2.241±0.07	8.826E-5±9.13E-6	3.118E-10±3.23E-11	1.52E-6±1.2E-13	30.206±3.0	7.524E-10±7.47E-11	2.052E-4±2.12E-5	0.414±0.042
2.5±0.7	2.208±0.60	8.694E-5±3.14E-6	3.072E-10±1.11E-10	2.00E-6±1.6E-13	50.150±4.6	1.249E-9±1.15E-10	1.536E-4±5.55E-5	0.246±0.088
3.1±0.8	2.225±0.04	8.762E-5±7.83E-6	3.096E-10±2.77E-11	2.46E-6±1.9E-13	70.094±7.0	1.746E-9±1.74E-10	1.249E-4±1.23E-5	0.177±0.015
3.7±1.0	2.264±0.02	8.914E-5±7.11E-6	3.149E-10±2.51E-11	2.96E-6±2.3E-13	90.038±8.0	2.243E-9±1.99E-10	1.064E-4±8.49E-6	0.140±0.011
4.2±1.1	2.259±0.03	8.897E-5±7.50E-6	3.143E-10±2.65E-11	3.44E-6±2.7E-13	109.982±10	2.740E-9±2.49E-10	9.139E-5±7.70E-6	0.115±0.009
4.8±1.3	2.259±0.03	8.896E-5±7.50E-6	3.143E-10±2.65E-11	3.92E-6±3.1E-13	129.926±12	3.236E-9±1.99E-10	8.019E-5±6.76E-6	0.097±0.008
5.5±1.4	2.299±0.05	9.055E-5±8.44E-6	3.199E-10±2.98E-11	4.40E-6±3.5E-13	149.870±14	3.733E-9±3.49E-10	7.273E-5±6.77E-6	0.086±0.007
6.0±1.6	2.300±0.04	9.057E-5±8.05E-6	3.200E-10±2.84E-11	4.80E-6±3.8E-13	166.490±16	4.140E-9±3.99E-10	6.667E-5±5.92E-6	0.077±0.006
6.6±1.7	2.331±0.04	9.180E-5±8.12E-6	3.243E-10±2.87E-11	5.28E-6±4.2E-13	186.434±17	4.644E-9±4.23E-10	6.144E-5±5.43E-6	0.069±0.006
7.2±1.9	2.408±0.07	9.482E-5±9.61E-6	3.350E-10±3.40E-11	5.76E-6±4.6E-13	206.378±19	5.141E-9±4.73E-10	5.817E-5±5.90E-6	0.065±0.006
7.8±2.0	2.503±0.15	9.856E-5±1.32E-6	3.482E-10±4.68E-11	6.24E-6±4.9E-13	226.322±21	5.637E-9±5.23E-10	5.582E-5±7.50E-6	0.062±0.008
		Equation 2.2	**Equation 3.6**	**Equation 3.8**	**Equation 2.6**	**Equation 3.9**	**Equation 3.7**	**Equation 3.5**

$1B_3$: Pt/TiO_2 particle size as determined by TEM and their corresponding specific mass activity and TOF at a reaction temperature of 170 ^oC. At an O_2:CO ratio of 1:1, total pressure of 8.4 x 10^{-2} mbar. Parameters used to compute the activity values are also included. The equations used to compute the parameters presented in the table are shown. Silicon nitride membrane area is (1.44 ± 0.01) mm^2, silicon nitride thermal conductivity (7 ± 0.2) $Wm^{-1}K^{-1}$ and silicon nitride membrane thickness is 0.6 ± 0.02 μm. The standard deviation for the temperature change was obtained from twelve points on each low. The estimated errors in other parameters were estimated from the deference between the average value and the maximum possible value calculated using errors in each formula used to compute each parameter.

P.diameter (nm)	ΔT/K	Power ($Js^{-1}mm^{-2}$)	mol_{CO} conv.($mm^{-2}s^{-1}$)	Total particle mass (g)	Total particle area (mm^2)	mol_{Pt} in the surface (mm^{-2})	Spec. mass activity (mol_{CO} conv.$g^{-1}Pt\ mm^{-2}\ s^{-1}$)	TOF (s^{-1})
1.3±0.3	3.657±0.17	1.439E-4±1.73E-5	5.088E-10±6.11E-11	1.04E-6±8.3E-14	10.262±0.9	2.556E-10±2.24E-11	4.893E-4±5.87E-5	1.991±0.238
1.9±0.5	3.469±0.10	1.366E-4±1.38E-5	4.827E-10±4.88E-11	1.52E-6±1.2E-13	30.206±3.0	7.524E-10±7.47E-11	3.176E-4±3.21E-5	0.642±0.064
2.5±0.7	3.402±0.09	1.339E-4±1.32E-5	4.734E-10±4.65E-11	2.00E-6±1.6E-13	50.150±4.6	1.249E-9±1.15E-10	2.367E-4±2.33E-5	0.379±0.037
3.1±0.8	3.412±0.08	1.344E-4±1.28E-5	4.748E-10±4.52E-11	2.46E-6±1.9E-13	70.094±7.0	1.746E-9±1.74E-10	1.915E-4±1.99E-5	0.272±0.025
3.7±1.0	3.368±0.06	1.326E-4±1.18E-5	4.687E-10±4.18E-11	2.96E-6±2.3E-13	90.038±8.0	2.243E-9±1.99E-10	1.583E-4±1.41E-5	0.209±0.018
4.2±1.1	3.355±0.07	1.321E-4±1.22E-5	4.668E-10±4.32E-11	3.44E-6±2.7E-13	109.982±10	2.740E-9±2.49E-10	1.357E-4±1.26E-5	0.170±0.015
4.8±1.3	3.356±0.04	1.321E-4±1.10E-5	4.669E-10±3.88E-11	3.92E-6±3.1E-13	129.926±12	3.236E-9±1.99E-10	1.191E-4±9.89E-6	0.144±0.011
5.5±1.4	3.290±0.03	1.295E-4±1.04E-5	4.577E-10±3.66E-11	4.40E-6±3.5E-13	149.870±14	3.733E-9±3.49E-10	1.040E-4±8.33E-6	0.123±0.009
6.0±1.6	3.291±0.07	1.296E-4±1.20E-5	4.580E-10±4.25E-11	4.80E-6±3.8E-13	166.490±16	4.140E-9±3.99E-10	9.542E-5±8.85E-6	0.110±0.010
6.6±1.7	3.334±0.09	1.313E-4±1.30E-5	4.639E-10±4.60E-11	5.28E-6±4.2E-13	186.434±17	4.644E-9±4.23E-10	8.786E-5±8.70E-6	0.10±0.009
7.2±1.9	3.410±0.16	1.343E-4±1.62E-5	4.744E-10±5.71E-11	5.76E-6±4.6E-13	206.378±19	5.141E-9±4.73E-10	8.238E-5±9.92E-6	0.092±0.011
7.8±2.0	3.595±0.16	1.415E-4±1.67E-5	5.001E-10±5.90E-11	6.24E-6±4.9E-13	226.322±21	5.637E-9±5.23E-10	8.015E-5±9.46E-6	0.089±0.010
		Equation 2.2	**Equation 3.6**	**Equation 3.8**	**Equation 2.6**	**Equation 3.9**	**Equation 3.7**	**Equation 3.5**

$1B_4$: Pt/TiO_2 particle size as determined by TEM and their corresponding specific mass activity and TOF at a reaction temperature of 170 ^oC at an O_2:CO ratio of 1:1, total pressure of 1.04 x 10^{-1} mbar. Parameters used to compute the activity values are also included. The equations used to compute the parameters presented in the table are shown. Silicon nitride membrane area is (1.44 ± 0.01) mm^2, silicon nitride thermal conductivity (7 ± 0.2) $Wk^{-1}K^{-1}$ and silicon nitride membrane thickness is 0.6 ± 0.02 μm. The standard deviation for the temperature change was obtained from twelve points on each low. The estimated errors in other parameters were estimated from the deference between the average value and the maximum possible value calculated using errors in each formula used to compute each parameter.

O_2:CO ratio = 1:1, Total pressure = 1.9 x 10^{-1} mbar

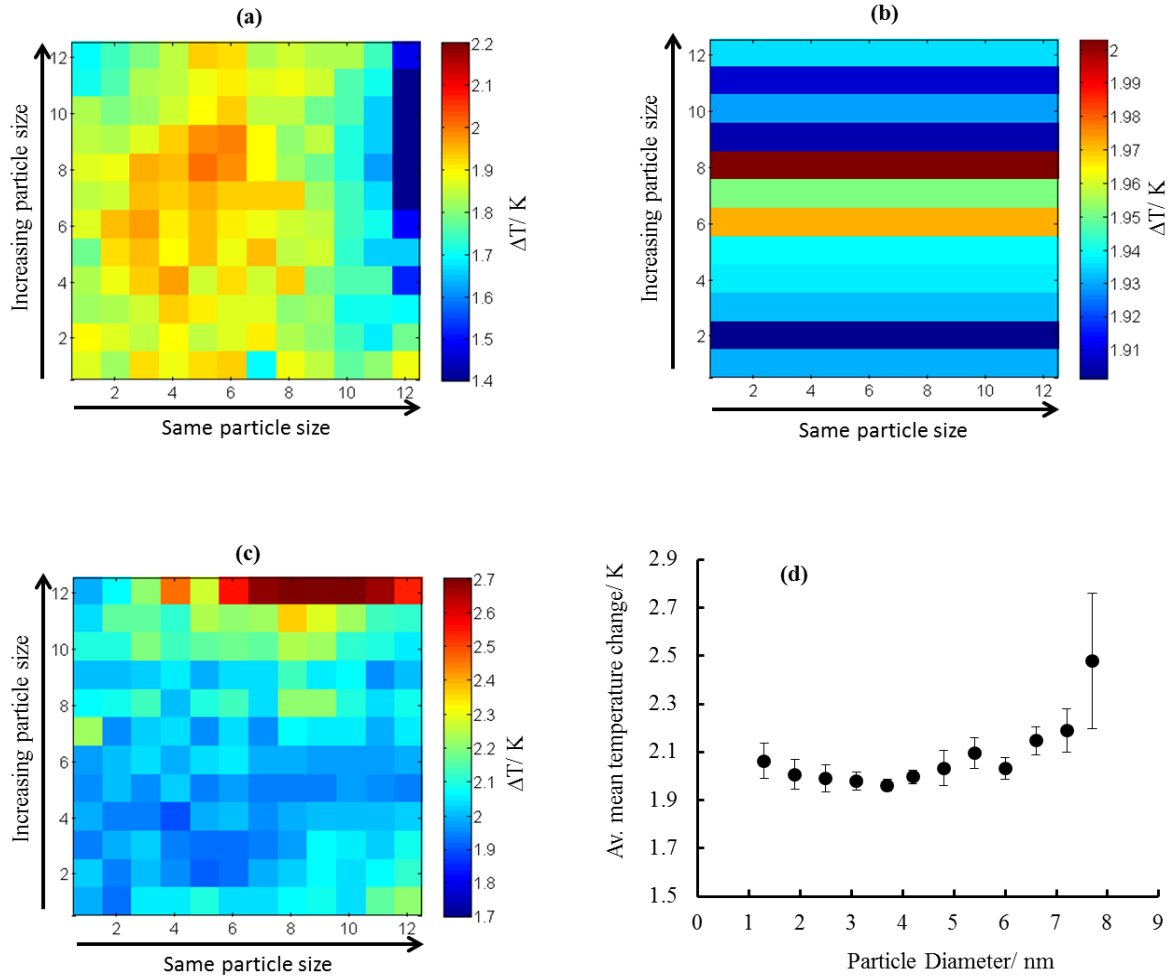

1C$_1$: The temperature change on Pt/TiO_2 catalyst as a function of particle size at approximately O_2:CO ratio of 1:1, total pressure of 1.9 x 10^{-1} mbar. **(a)** Presents uncompensated infrared image, **(b)** row compensated and **(c)** row and column compensated images. **(d)** Presents the average mean temperature change as a function of particle sizes for the complete compensated infrared images. The row and column numbers are shown on the x and y axes on the IR-images. The reaction temperature was 170 ^{o}C at an exposure time of 5 minutes.

O_2:CO ratio = 1:1, Total pressure = 2.2 x 10^{-1} mbar

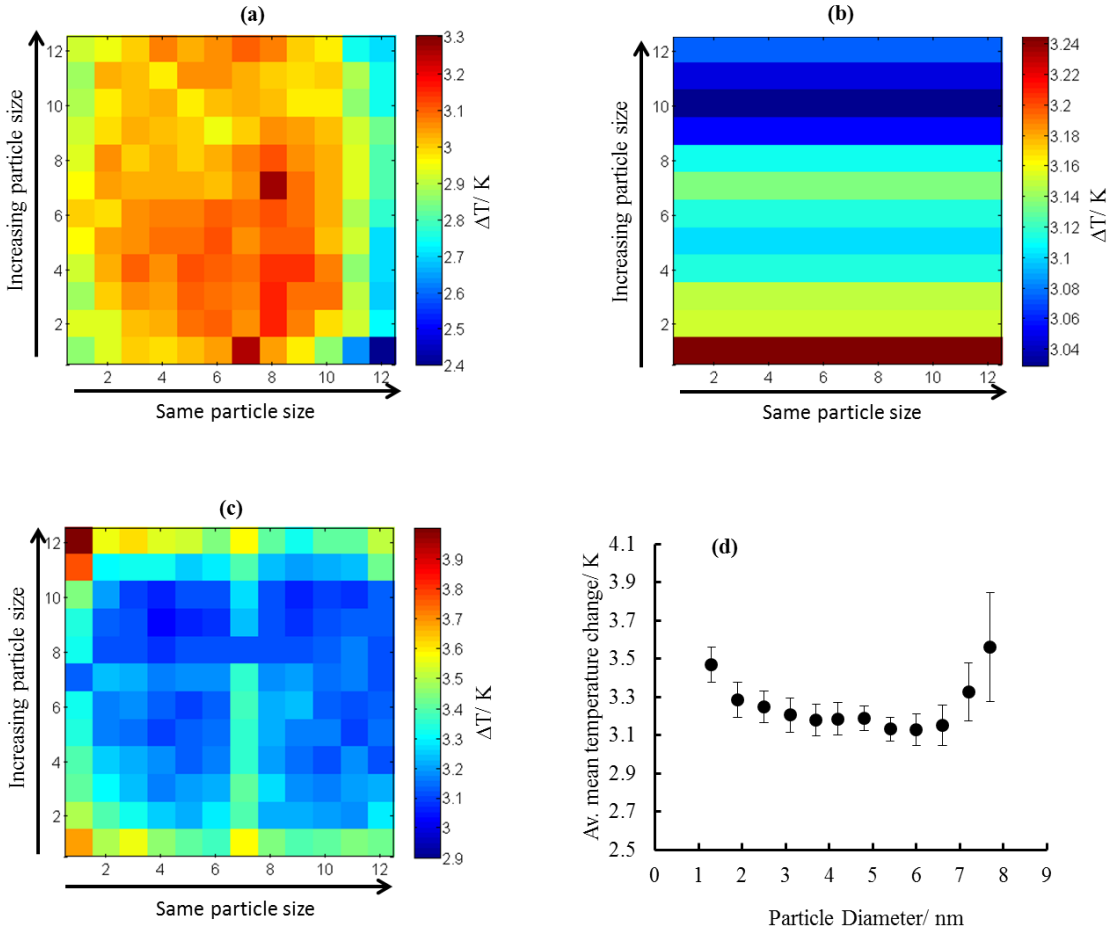

1C$_2$: The temperature change on Pt/TiO_2 catalyst as a function of particle size at an O_2:CO ratio of 1:1, total pressure of 2.2 x 10^{-1} mbar. **(a)** Presents uncompensated infrared image, **(b)** row compensated and **(c)** row and column compensated images. **(d)** Presents the average mean temperature change as a function of particle sizes for the complete compensated infrared images. The row and column numbers are shown on the x and y axes on the IR-images. The reaction temperature was 170 ^{o}C at an exposure time of 5 minutes.

P.diameter (nm)	ΔT/K	Power ($Js^{-1}mm^{-2}$)	mol_{CO} conv.($mm^{-2}s^{-1}$)	Total particle mass (g)	Total particle area (mm^2)	mol_{Pt} in the surface (mm^{-2})	Spec. mass activity (mol_{CO} conv.g^{-1}Pt mm^{-2} s^{-1})	TOF (s^{-1})
1.3±0.3	2.063±0.07	7.896E-5±1.09E-5	2.79E-10±3.86E-11	1.04E-6±8.3E-14	10.262±0.9	2.556E-10±2.24E-11	2.68E-4±3.71E-5	1.092±0.151
1.9±0.5	2.005±0.06	7.835E-5±8.68E-6	2.77E-10±3.01E-11	1.52E-6±1.2E-13	30.206±3.0	7.524E-10±7.47E-11	1.82E-4±2.02E-5	0.368±0.041
2.5±0.7	1.989±0.05	7.792E-5±8.01E-6	2.75E-10±2.83E-11	2.00E-6±1.6E-13	50.150±4.6	1.249E-9±1.15E-10	1.38E-4±1.42E-5	0.220±0.023
3.1±0.8	1.979±0.04	7.725E-5±7.84E-6	2.73E-10±2.77E-11	2.46E-6±1.9E-13	70.094±7.0	1.746E-9±1.74E-10	1.10E-4±1.22E-5	0.156±0.016
3.7±1.0	1.962±0.03	7.863E-5±5.31E-6	2.78E-10±1.88E-11	2.96E-6±2.3E-13	90.038±8.0	2.243E-9±1.99E-10	9.39E-5±6.34E-6	0.124±0.008
4.2±1.1	1.997±0.03	8.006E-5±5.37E-6	2.83E-10±1.90E-11	3.44E-6±2.7E-13	109.982±10	2.740E-9±2.49E-10	8.22E-5±5.51E-6	0.103±0.006
4.8±1.3	2.033±0.07	8.253E-5±6.10E-6	2.92E-10±2.16E-11	3.92E-6±3.1E-13	129.926±12	3.236E-9±1.99E-10	7.44E-5±5.50E-6	0.090±0.006
5.5±1.4	2.095±0.06	7.999E-5±1.08E-6	2.83E-10±3.83E-11	4.40E-6±3.5E-13	149.870±14	3.733E-9±3.49E-10	6.42E-5±8.69E-6	0.076±0.010
6.0±1.6	2.034±0.05	8.452E-5±3.30E-6	2.99E-10±1.17E-11	4.80E-6±3.8E-13	166.490±16	4.140E-9±3.99E-10	6.22E-5±2.43E-6	0.072±0.002
6.6±1.7	2.146±0.06	8.619E-5±6.77E-6	3.05E-10±2.39E-11	5.28E-6±4.2E-13	186.434±17	4.644E-9±4.23E-10	5.77E-5±4.53E-6	0.066±0.005
7.2±1.9	2.189±0.08	9.756E-5±1.90E-6	3.45E-10±6.88E-12	5.76E-6±4.6E-13	206.378±19	5.141E-9±4.73E-10	5.99E-5±1.19E-6	0.067±0.001
7.8±2.0	2.477±0.2	9.757E-5±1.52E-5	3.45E-10±5.39E-11	6.24E-6±4.9E-13	226.322±21	5.637E-9±5.23E-10	5.53E-5±8.63E-6	0.061±0.009
		Equation 2.2	**Equation 3.6**	**Equation 3.8**	**Equation 2.6**	**Equation 3.9**	**Equation 3.7**	**Equation 3.5**

$1C_3$: Pt/TiO_2 particle size as determined by TEM and their corresponding specific activity and TOF at a reaction temperature of 170 ^oC. At an O_2:CO ratio of approximately 1:1, with a total pressure of 1.9×10^{-1} mbar. Parameters used to compute the activity values are also included. The equations used to compute the parameters presented in the table are shown. Silicon nitride membrane area is (1.44 ± 0.01) mm^2, silicon nitride thermal conductivity (7 ± 0.2) $Wm^{-1}K^{-1}$ and silicon nitride membrane thickness is 0.6 ± 0.02 μm. The standard deviation for the temperature change was obtained from twelve points on each low. The estimated errors in other parameters were estimated from the deference between the average value and the maximum possible value calculated using errors in each formula used to compute each parameter.

P.diameter (nm)	ΔT/K	Power ($Js^{-1}mm^{-2}$)	mol_{CO} conv.($mm^{-2}s^{-1}$)	Total particle mass (g)	Total particle area (mm^2)	mol_{Pt} in the surface (mm^{-2})	Spec. mass activity (mol_{CO} conv.$g^{-1}Pt\ mm^{-2}\ s^{-1}$)	TOF (s^{-1})
1.3±0.3	3.470±0.09	1.366E-4±1.34E-5	4.828E-10±4.73E-11	1.04E-6±8.3E-14	10.262±0.9	2.556E-10±2.24E-11	4.64E-4±4.55E-5	1.889±0.185
1.9±0.5	3.287±0.09	1.294E-4±1.29E-5	4.573E-10±4.56E-11	1.52E-6±1.2E-13	30.206±3.0	7.524E-10±7.47E-11	3.01E-4±3.00E-5	0.608±0.061
2.5±0.7	3.247±0.08	1.278E-4±1.24E-5	4.517E-10±4.37E-11	2.00E-6±1.6E-13	50.150±4.6	1.249E-9±1.15E-10	2.26E-4±2.19E-5	0.362±0.034
3.1±0.8	3.205±0.08	1.262E-4±1.22E-5	4.460E-10±4.32E-11	2.46E-6±1.9E-13	70.094±7.0	1.746E-9±1.74E-10	1.80E-4±1.90E-5	0.255±0.025
3.7±1.0	3.180±0.08	1.252E-4±1.22E-5	4.425E-10±4.30E-11	2.96E-6±2.3E-13	90.038±8.0	2.243E-9±1.99E-10	1.49E-4±1.45E-5	0.197±0.019
4.2 ±1.1	3.186±0.08	1.255E-4±1.22E-5	4.433E-10±4.30E-11	3.44E-6±2.7E-13	109.982±10	2.740E-9±2.49E-10	1.29E-4±1.25E-5	0.162±0.015
4.8±1.3	3.188±0.06	1.255E-4±1.23E-5	4.436E-10±4.01E-11	3.92E-6±3.1E-13	129.926±12	3.236E-9±1.99E-10	1.13E-4±1.02E-5	0.137±0.012
5.5±1.4	3.133±0.06	1.234E-4±1.12E-5	4.359E-10±3.96E-11	4.40E-6±3.5E-13	149.870±14	3.733E-9±3.49E-10	9.91E-5±9.00E-6	0.117±0.011
6.0±1.6	3.130±0.08	1.233E-4±1.20E-5	4.355E-10±4.25E-11	4.80E-6±3.8E-13	166.490±16	4.140E-9±3.99E-10	9.07E-5±8.85E-6	0.105±0.010
6.6±1.7	3.150±0.10	1.241E-4±1.29E-5	4.384E-10±4.56E-11	5.28E-6±4.2E-13	186.434±17	4.644E-9±4.23E-10	8.30E-5±8.63E-6	0.094±0.009
7.2±1.9	3.328±0.15	1.310E-4±1.55E-5	4.630E-10±5.49E-11	5.76E-6±4.6E-13	206.378±19	5.141E-9±4.73E-10	8.04E-5±9.53E-6	0.090±0.011
7.8±2.0	3.561±0.3	1.402E-4±2.25E-5	4.955E-10±7.95E-11	6.24E-6±4.9E-13	226.322±21	5.637E-9±5.23E-10	7.94E-5±1.27E-5	0.088±0.014
		Equation 2.2	**Equation 3.6**	**Equation 3.8**	**Equation 2.6**	**Equation 3.9**	**Equation 3.7**	**Equation 3.5**

$1C_4$: Pt/TiO_2 particle size as determined by TEM and their corresponding specific activity and TOF at a reaction temperature of 170 ^oC, at approximately O_2:CO ratio of 1:1, with a total pressure of 2.2 x 10^{-1} mbar. Parameters used to compute the activity values are also included. The equations used to compute the parameters presented in the table are shown. Silicon nitride membrane area is (1.44 ± 0.01) mm^2, silicon nitride thermal conductivity (7 ± 0.2) $Wm^{-1}K^{-1}$ and silicon nitride membrane thickness is 0.6 ± 0.02 μm. The standard deviation for the temperature change was obtained from twelve points on each low. The estimated errors in other parameters were estimated from the deference between the average value and the maximum possible value calculated using errors in each formula used to compute each parameter.

O_2:CO ratio = 1:2, Total pressure = 1.7 x 10^{-1} mbar

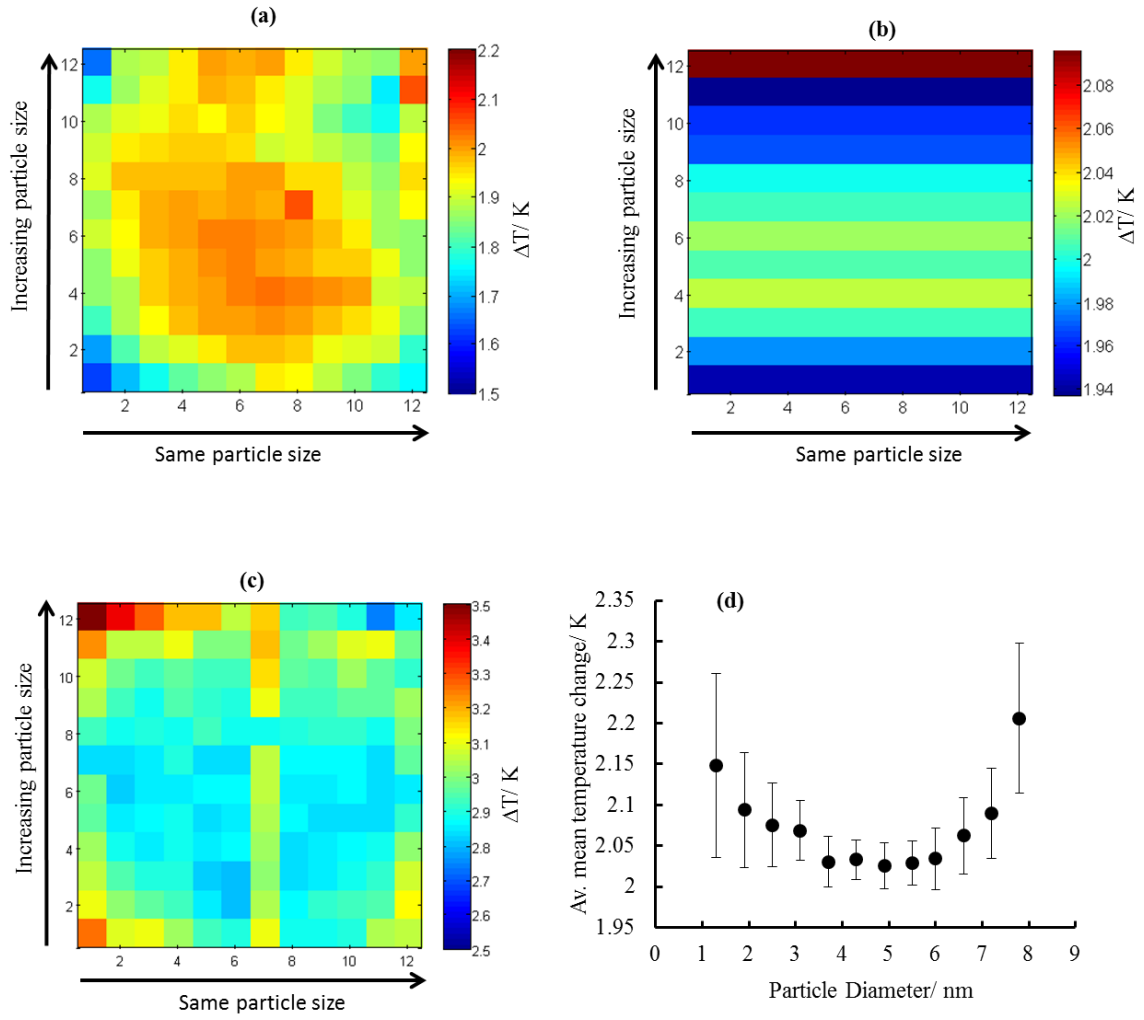

1D$_1$: The temperature change on Pt/TiO_2 catalyst as a function of particle size at approximately O_2:CO ratio of approximately 1:1, with a total pressure of 1.7 x 10^{-1} mbar. **(a)** Presents uncompensated infrared image, **(b)** row compensated and **(c)** row and column compensated images. **(d)** Presents the average mean temperature change as a function of particle sizes for the row and column compensated infrared images. The row and column numbers are shown on the x and y axes on the IR-images. The reaction temperature was 170 ^{o}C at an exposure time of 5 minutes.

O_2:CO ratio = 1:1, Total pressure = 2.2 x 10^{-1} mbar

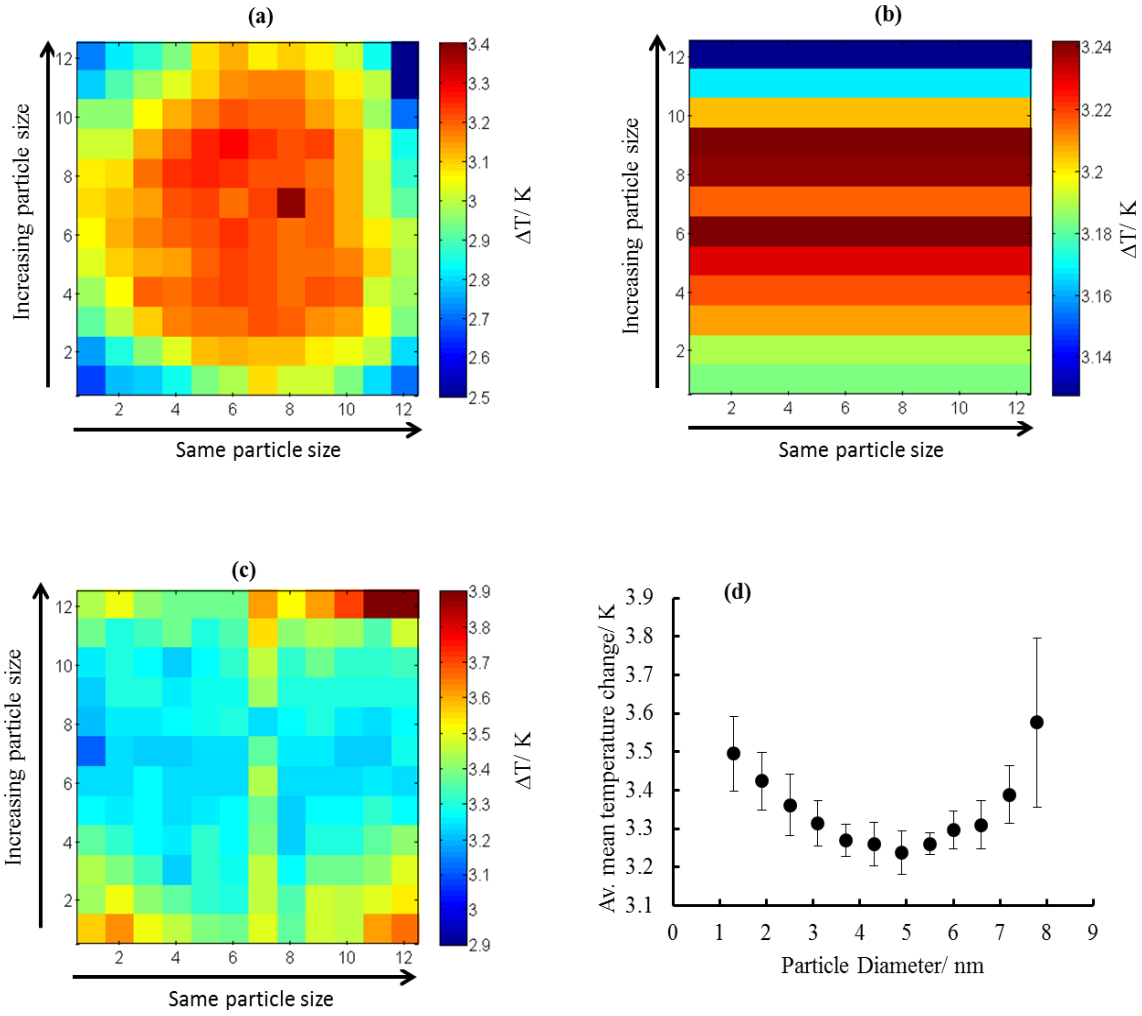

1D$_2$: The temperature change on Pt/TiO_2 catalyst as a function of particle size at approximately O_2:CO ratio of 1:1, with a total pressure of 2.2 x 10^{-1} mbar. **(a)** Presents uncompensated infrared image, **(b)** row compensated and **(c)** row and column compensated images. **(d)** Presents the average mean temperature change as a function of particle sizes for the row and column compensated infrared images. The row and column numbers are shown on the x and y axes on the IR-images. The reaction temperature was 170 ^{o}C at an exposure time of 5 minutes.

P.diameter (nm)	ΔT/K	Power ($Js^{-1}mm^{-2}$)	mol_{CO} conv.($mm^{-2}s^{-1}$)	Total particle mass (g)	Total particle area (mm^2)	mol_{Pt} in the surface (mm^{-2})	Spec. mass activity (mol_{CO} conv.$g^{-1}Pt\ mm^{-2}\ s^{-1}$)	TOF (s^{-1})
1.3±0.3	2.148±0.11	8.459E-5±1.06 E-5	2.989E-10±3.73E-11	1.04E-6±8.3E-14	10.262± 0.9	2.556E-10±2.24E-11	2.874E-4±3.59E-5	1.169±0.146
1.9±0.5	2.093±0.07	8.243E-5±8.72E-6	2.912E-10±3.08E-11	1.52E-6±1.2E-13	30.206±3.0	7.524E-10±7.47E-11	1.916E-4±2.03E-5	0.387±0.041
2.5±0.7	2.075±0.05	8.172E-5±7.83E-6	2.887E-10±2.77E-11	2.00E-6±1.6E-13	50.150±4.6	1.249E-9±1.15E-10	1.444E-4±1.38E-5	0.231±0.022
3.1±0.8	2.069±0.03	8.146E-5±7.00E-6	2.878E-10±2.47E-11	2.46E-6±1.9E-13	70.094±7.0	1.746E-9±1.74E-10	1.161E-4±1.10E-5	0.165±0.014
3.7±1.0	2.030±0.03	7.995E-5±6.87E-6	2.825E-10±2.43E-11	2.96E-6±2.3E-13	90.038±8.0	2.243E-9±1.99E-10	9.544E-5±8.20E-6	0.126±0.011
4.2±1.1	2.033±0.02	8.005E-5±6.47E-6	2.829E-10±2.29E-11	3.44E-6±2.7E-13	109.982±10	2.740E-9±2.49E-10	8.222E-5±6.65E-6	0.103±0.008
4.8±1.3	2.026±0.03	7.977E-5±6.88E-6	2.817E-10±2.43E-11	3.92E-6±3.1E-13	129.926±12	3.236E-9±1.99E-10	7.190E-5±6.20E-6	0.087±0.007
5.5±1.4	2.029±0.02	7.989E-5±6.45E-6	2.823E-10±2.28E-11	4.40E-6±3.5E-13	149.870±14	3.733E-9±3.49E-10	6.416E-5±5.18E-6	0.076±0.006
6.0±1.6	2.034±0.03	8.009E-5±6.88E-6	2.830E-10±2.43E-11	4.80E-6±3.8E-13	166.490±16	4.140E-9±3.99E-10	5.897E-5±5.07E-6	0.068±0.005
6.6±1.7	2.062±0.04	8.119E-5±7.38E-6	2.869E-10±2.61E-11	5.28E-6±4.2E-13	186.434±17	4.644E-9±4.23E-10	5.434E-5±4.94E-6	0.062±0.005
7.2±1.9	2.089±0.05	8.228E-5±7.86E-6	2.907E-10±2.78E-11	5.76E-6±4.6E-13	206.378±19	5.141E-9±4.73E-10	5.048E-5±4.82E-6	0.057±0.005
7.8±2.0	2.206±0.09	8.686E-5±9.90E-6	3.069E-10±3.50E-11	6.24E-6±4.9E-13	226.322± 21	5.637E-9±5.23E-10	4.919E-5±5.60E-6	0.054±0.006
		Equation 2.2	**Equation 3.6**	**Equation 3.8**	**Equation 2.6**	**Equation 3.9**	**Equation 3.7**	**Equation 3.5**

$1D_3$: Pt/TiO_2 particle size as determined by TEM and their corresponding specific activity and TOF at a reaction temperature of 170 ^oC and approximately O_2:CO ratio of 1:2, at a total pressure of 1.7×10^{-1} mbar. Parameters used to compute the activity values are also included. The equations used to compute the parameters presented in the table are shown Silicon nitride membrane area is (1.44 ± 0.01) mm^2, silicon nitride thermal conductivity (7 ± 0.2) $Wm^{-1}K^{-1}$ and silicon nitride membrane thickness is 0.6 ± 0.02 μm. The standard deviation for the temperature change was obtained from twelve points on each low. The estimated errors in other parameters were estimated from the deference between the average value and the maximum possible value calculated using errors in each formula used to compute each parameter.

P.diameter (nm)	ΔT/K	Power ($Js^{-1}mm^{-2}$)	mol_{CO} conv.($mm^{-2}s^{-1}$)	Total particle mass (g)	Total particle area (mm^2)	mol_{Pt} in the surface (mm^{-2})	Spec. mass activity (mol_{CO} conv.$g^{-1}Pt\ mm^{-2}\ s^{-1}$)	TOF (s^{-1})
1.3±0.3	3.495±0.09	1.376E-4±1.06E-5	4.863E-10±3.73E-11	1.04E-6±8.3E-14	10.262±0.9	2.556E-10±2.24E-11	4.676E-4±3.59E-5	1.903±0.185
1.9±0.5	3.424±0.07	1.348E-4±8.72E-6	4.764E-10±3.08E-11	1.52E-6±1.2E-13	30.206±3.0	7.524E-10±7.47E-11	3.135E-4±2.02E-5	0.633±0.059
2.5±0.7	3.362±0.08	1.324E-4±7.83E-6	4.678E-10±2.77E-11	2.00E-6±1.6E-13	50.150±4.6	1.249E-9±1.15E-10	2.339E-4±1.38E-5	0.374±0.035
3.1±0.8	3.314±0.06	1.305E-4±7.00E-6	4.612E-10±2.47E-11	2.46E-6±1.9E-13	70.094±7.0	1.746E-9±1.74E-10	1.860E-4±1.10E-5	0.264±0.024
3.7±1.0	3.270±0.04	1.287E-4±6.87E-6	4.549E-10±2.43E-11	2.96E-6±2.3E-13	90.038±8.0	2.243E-9±1.99E-10	1.537E-4±8.20E-6	0.203±0.017
4.2±1.1	3.260±0.05	1.284E-4±6.47E-6	4.536E-10±2.29E-11	3.44E-6±2.7E-13	109.982±10	2.740E-9±2.49E-10	1.319E-4±6.65E-6	0.166±0.014
4.8±1.3	3.238±0.05	1.275E-4±6.88E-6	4.504E-10±2.43E-11	3.92E-6±3.1E-13	129.926±12	3.236E-9±1.99E-10	1.149E-4±6.20E-6	0.139±0.012
5.5±1.4	3.261±0.03	1.284E-4±6.45E-6	4.537E-10±2.28E-11	4.40E-6±3.5E-13	149.870±14	3.733E-9±3.49E-10	1.031E-4±5.18E-6	0.122±0.009
6.0±1.6	3.296±0.05	1.298E-4±6.88E-6	4.586E-10±2.43E-11	4.80E-6±3.8E-13	166.490±16	4.140E-9±3.99E-10	9.554E-5±5.07E-6	0.111±0.009
6.6±1.7	3.310±0.06	1.304E-4±7.38E-6	4.606E-10±2.61E-11	5.28E-6±4.2E-13	186.434±17	4.644E-9±4.23E-10	8.724E-5±4.94E-6	0.099±0.008
7.2±1.9	3.389±0.07	1.334E-4±7.86E-6	4.715E-10±2.78E-11	5.76E-6±4.6E-13	206.378±19	5.141E-9±4.73E-10	8.186E-5±4.82E-6	0.092±0.008
7.8±2.0	3.576±0.22	1.408E-4±9.90E-6	4.976E-10±3.50E-11	6.24E-6±4.9E-13	226.322±21	5.637E-9±5.23E-10	7.974E-5±5.60E-6	0.088±0.012
		Equation 2.2	**Equation 3.6**	**Equation 3.8**	**Equation 2.6**	**Equation 3.9**	**Equation 3.7**	**Equation 3.5**

$1D_4$: Pt/TiO_2 particle size as determined by TEM and their corresponding specific activity and TOF at a reaction temperature of 170 °C at an O_2:CO ratio of 1:1, with a total pressure of 2.2×10^{-1} mbar. Parameters used to compute the activity values are also included. The equations used to compute the parameters presented in the table are shown. Silicon nitride membrane area is (1.44 ± 0.01) mm^2, silicon nitride thermal conductivity (7 ± 0.2) $Wm^{-1}K^{-1}$ and silicon nitride membrane thickness is 0.6 ± 0.02 μm. The standard deviation for the temperature change was obtained from twelve points on each low. The estimated errors in other parameters were estimated from the deference between the average value and the maximum possible value calculated using errors in each formula used to compute each parameter.

O_2:CO ratio = 1:1, Total pressure = 1.1 mbar

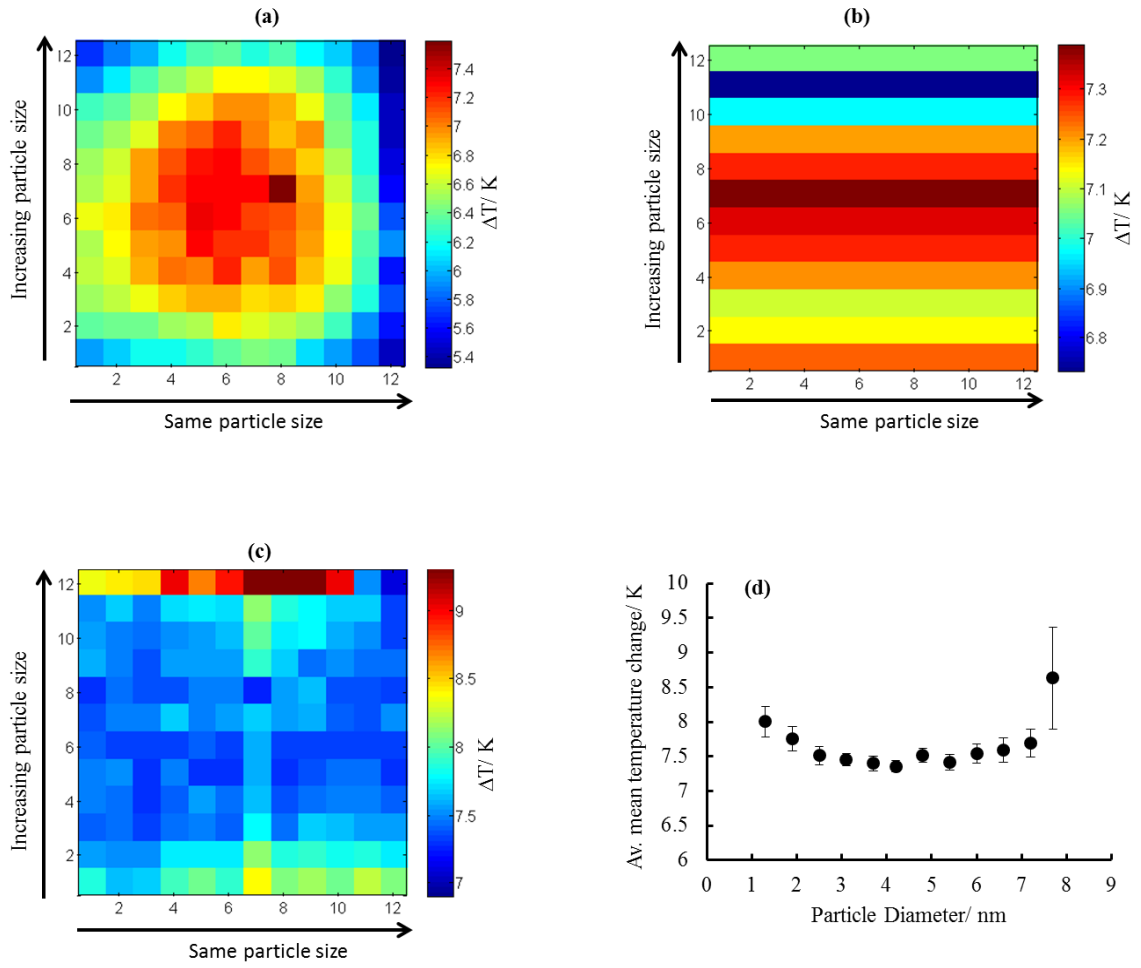

1F$_1$: The temperature change on Pt/TiO_2 catalyst as a function of particle size at approximately O_2:CO of 1:1, with a total pressure of 1.1 mbar. **(a)** Presents uncompensated infrared images, **(b)** row compensated and **(c)** row and column compensated. **(d)** presents the average mean temperature change as a function of particle sizes for the row and column compensated infrared images The row and column numbers are shown on the x and y axes on the IR-images. The reaction temperature was 240 ^{o}C at an exposure time of 5 minutes.

O_2:CO ratio = 1:1, Total pressure = 2.4 mbar

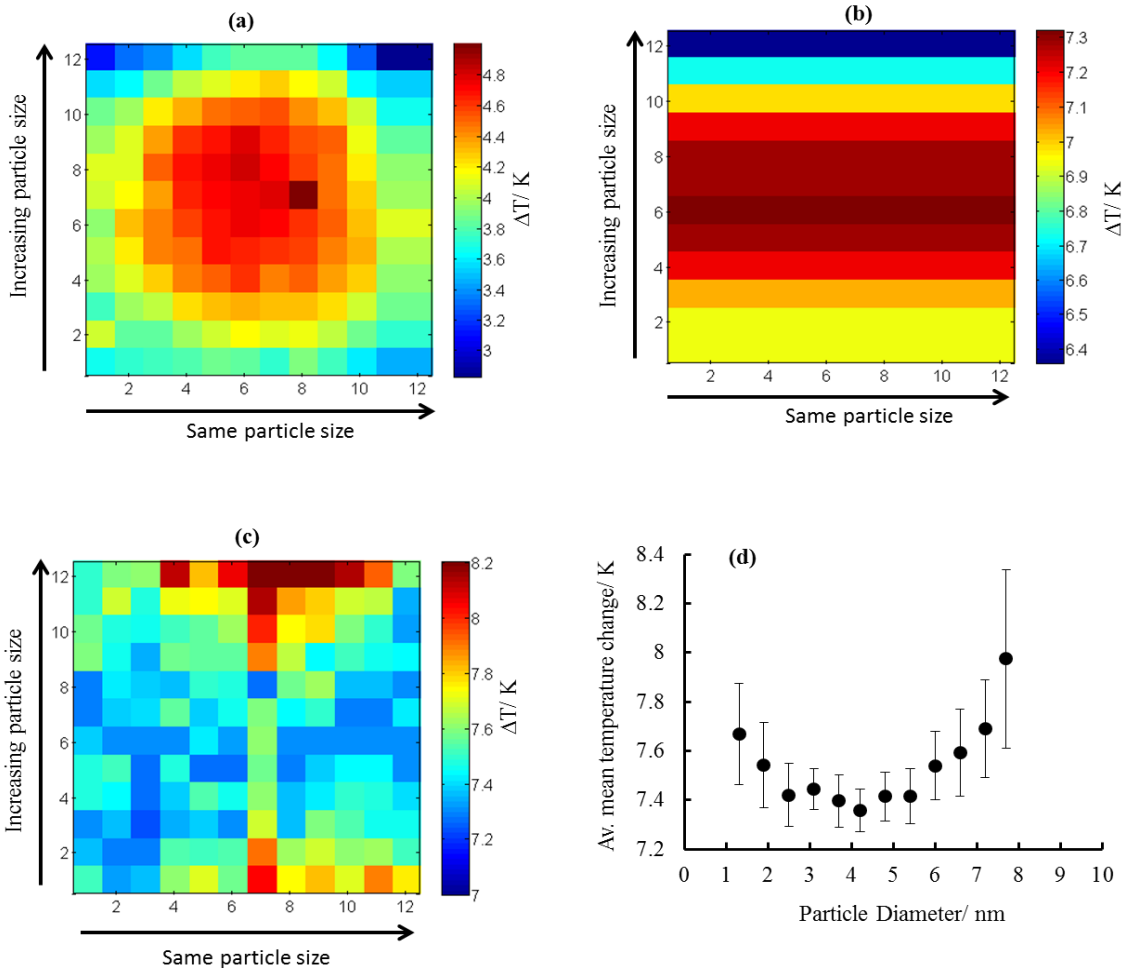

1F$_2$: The temperature change on Pt/TiO_2 catalyst as a function of particle size at approximately O_2:CO of 1:1, with a total pressure of 2.4 mbar. **(a)** Presents uncompensated infrared images, **(b)** row compensated and **(c)** row and column compensated. **(d)** presents the average mean temperature change as a function of particle sizes for the row and column compensated infrared images The row and column numbers are shown on the x and y axes on the IR-images. The reaction temperature was 240 ^{o}C at an exposure time of 5 minutes.

P.diameter (nm)	ΔT/K	Power ($Js^{-1}mm^{-2}$)	mol_{CO} conv.($mm^{-2}s^{-1}$)	Total particle mass (g)	Total particle area (mm^2)	mol_{Pt} in the surface (mm^{-2})	Spec. mass activity (mol_{CO} conv.$g^{-1}Pt\ mm^{-2}\ s^{-1}$)	TOF (s^{-1})
1.3±0.3	8.001±0.21	3.150E-4± 3.10E-5	1.113E-9±1.10E-10	1.04E-6 ±8.3E-14	10.262±0.9	2.556E-10±2.24E-11	1.070E-3±1.05E-4	4.355±0.428
1.9±0.5	7.758±0.17	3.055E-4±2.86E-5	1.079E-9±1.01E-10	1.52E-6 ±1.2E-13	30.206±3.0	7.524E-10±7.47E-11	7.102E-4±6.65E-5	1.435±0.134
2.5±0.7	7.510±0.13	2.957E-4±2.62E-5	1.044E-9±9.27E-11	2.00E-6 ±1.6E-13	50.150±4.6	1.249E-9±1.15E-10	5.225E-4±4.64E-5	0.837±0.074
3.1±0.8	7.452±0.08	2.934E-4±2.40E-5	1.037E-9±8.48E-11	2.46E-6 ±1.9E-13	70.094±7.0	1.746E-9±1.74E-10	4.181E-4±3.79E-5	0.594±0.048
3.7±1.0	7.396±0.10	2.912E-4±2.47E-5	1.029E-9±8.72E-11	2.96E-6 ±2.3E-13	90.038±8.0	2.243E-9±1.99E-10	3.477E-4±2.95E-5	0.459±0.039
4.2±1.1	7.357±0.08	2.896E-4±2.37E-5	1.024E-9±8.38E-11	3.44E-6 ±2.7E-13	109.982±10	2.740E-9±2.49E-10	2.976E-4±2.44E-5	0.374±0.031
4.8±1.3	7.517±0.10	2.959E-4±2.50E-5	1.046E-9±8.84E-11	3.92E-6 ±3.1E-13	129.926±12	3.236E-9±1.99E-10	2.668E-4±2.26E-5	0.323±0.027
5.5±1.4	7.414±0.11	2.919E-4±2.51E-5	1.032E-9±8.89E-11	4.40E-6 ±3.5E-13	149.870±14	3.733E-9±3.49E-10	2.344E-4±2.02E-5	0.276±0.023
6.0±1.6	7.538±0.14	2.968E-4±2.67E-5	1.049E-9±9.44E-11	4.80E-6 ±3.8E-13	166.490±16	4.140E-9±3.99E-10	2.185E-4±1.97E-5	0.253±0.022
6.6±1.7	7.594±0.18	2.990E-4±2.86E-5	1.057E-9±1.01E-10	5.28E-6 ±4.2E-13	186.434±17	4.644E-9±4.23E-10	2.001E-4±1.91E-5	0.228±0.021
7.2±1.9	7.690±0.19	3.028E-4±2.93E-5	1.070E-9±1.03E-10	5.76E-6 ±4.6E-13	206.378±19	5.141E-9±4.73E-10	1.858E-4±1.80E-5	0.208±0.020
7.8±2.0	8.633±0.73	3.399E-4±5.46E-5	1.201E-9±1.93E-10	6.24E-6 ±4.9E-13	226.322±21	5.637E-9±5.23E-10	1.925E-4±3.09E-5	0.213±0.034
		Equation 2.2	**Equation 3.6**	**Equation 3.8**	**Equation 2.6**	**Equation 3.9**	**Equation 3.7**	**Equation 3.5**

$1F_3$: Pt/TiO_2 particle size as determined by TEM and their corresponding specific activity and TOF results at a reaction temperature of 240 ^oC, at approximately O_2:CO ratio of 1:1, with a total pressure of 1.1 mbar. Parameters used to compute the activity values are also included. The equations used to compute the parameters presented in the table are shown. Silicon nitride membrane area is (1.44 ± 0.01) mm^2, silicon nitride thermal conductivity (7 ± 0.2) $Wm^{-1}K^{-1}$ and silicon nitride membrane thickness is 0.6 ± 0.02 μm. The standard deviation for the temperature change was obtained from twelve points on each low. The estimated errors in other parameters were estimated from the deference between the average value and the maximum possible value calculated using errors in each formula used to compute each parameter.

P.diameter (nm)	ΔT/K	Power ($Js^{-1}mm^{-2}$)	mol_{CO} conv.($mm^{-2}s^{-1}$)	Total particle mass (g)	Total particle area (mm^2)	mol_{Pt} in the surface (mm^{-2})	Spec. mass activity (mol_{CO} conv.$g^{-1}Pt\ mm^{-2}\ s^{-1}$)	TOF (s^{-1})
1.3±0.3	7.669±0.20	3.019E-4± 3.10E-5	1.066E-9±1.10E-10	1.04E-6 ±8.3E-14	10.262±0.9	2.556E-10±2.24E-11	1.026E-3±1.05E-4	4.174±0.410
1.9±0.5	7.541±0.17	2.969E-4±2.86E-5	1.049E-9±1.01E-10	1.52E-6 ±1.2E-13	30.206±3.0	7.524E-10±7.47E-11	6.903E-4±6.65E-5	1.394±0.131
2.5±0.7	7.421±0.13	2.922E-4±2.62E-5	1.032E-9±9.27E-11	2.00E-6 ±1.6E-13	50.150±4.6	1.249E-9±1.15E-10	5.162E-4±4.63E-5	0.827±0.074
3.1±0.8	7.445±0.08	2.931E-4±2.40E-5	1.036E-9±8.48E-11	2.46E-6 ±1.9E-13	70.094±7.0	1.746E-9±1.74E-10	4.177E-4±3.78E-5	0.593±0.048
3.7±1.0	7.396±0.10	2.912E-4±2.47E-5	1.029E-9±8.72E-11	2.96E-6 ±2.3E-13	90.038±8.0	2.243E-9±1.99E-10	3.477E-4±2.94E-5	0.459±0.038
4.2±1.1	7.357±0.08	2.897E-4±2.37E-5	1.024E-9±8.38E-11	3.44E-6 ±2.7E-13	109.982±10	2.740E-9±2.49E-10	2.976E-4±2.43E-5	0.374±0.031
4.8±1.3	7.415±0.09	2.919E-4±2.50E-5	1.032E-9±8.84E-11	3.92E-6 ±3.1E-13	129.926±12	3.236E-9±1.99E-10	2.632E-4±2.25E-5	0.319±0.026
5.5±1.4	7.414±0.11	2.919E-4±2.51E-5	1.032E-9±8.89E-11	4.40E-6 ±3.5E-13	149.870±14	3.733E-9±3.49E-10	2.344E-4±2.01E-5	0.276±0.024
6.0±1.6	7.539±0.14	2.968E-4±2.67E-5	1.049E-9±9.44E-11	4.80E-6 ±3.8E-13	166.490±16	4.140E-9±3.99E-10	2.185E-4±1.96E-5	0.253±0.022
6.6±1.7	7.594±0.17	2.990E-4±2.86E-5	1.057E-9±1.01E-10	5.28E-6 ±4.2E-13	186.434±17	4.644E-9±4.23E-10	2.001E-4±1.91E-5	0.228±0.021
7.2±1.9	7.689±0.19	3.028E-4±2.93E-5	1.069E-9±1.03E-10	5.76E-6 ±4.6E-13	206.378±19	5.141E-9±4.73E-10	1.857E-4±1.79E-5	0.208±0.020
7.8±2.0	7.974±0.36	3.139E-4±5.46E-5	1.109E-9±1.93E-10	6.24E-6 ±4.9E-13	226.322±21	5.637E-9±5.23E-10	1.778E-4±3.09E-5	0.197±0.023
		Equation 2.2	**Equation 3.6**	**Equation 3.8**	**Equation 2.6**	**Equation 3.9**	**Equation 3.7**	**Equation 3.5**

$1F_4$: Pt/TiO_2 particle size as determined by TEM and their corresponding specific activity and TOF at a reaction temperature of 240 ^oC and approximately O_2:CO ratio of 1:1, at a total pressure of 2.4 mbar. Parameters used to compute the activity values are also included. The equations used to compute the parameters presented in the table are shown. Silicon nitride membrane area is (1.44 ± 0.01) mm^2, silicon nitride thermal conductivity (7 ± 0.2) $Wm^{-1}K^{-1}$ and silicon nitride membrane thickness is 0.6 ± 0.02 μm. The standard deviation for the temperature change was obtained from twelve points on each low. The estimated errors in other parameters were estimated from the deference between the average value and the maximum possible value calculated using errors in each formula used to compute each parameter.

Appendix 2

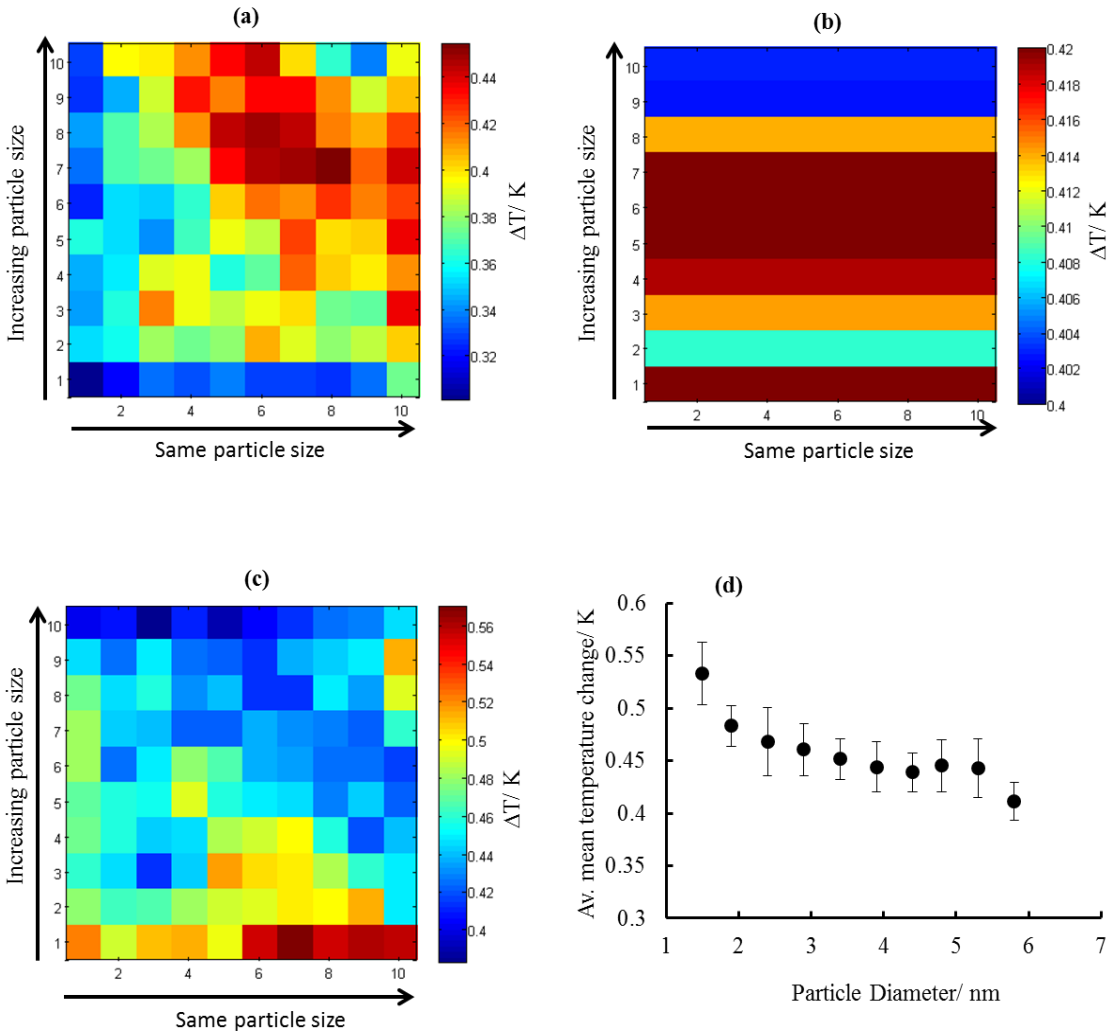

2A$_1$: The temperature change on Au/TiO_2 catalyst as a function of particle size at an O_2:CO ratio of 1:1, at a total pressure of 8.4 x 10^{-2} mbar. **(a)** Presents uncompensated infrared image, **(b)** row compensated and **(c)** row and column compensated images. **(d)** Presents the average mean temperature change as a function of particle sizes for the row and column compensated infrared images. The row and column numbers are show on the x and y axes on the IR-images. The reaction temperature was 80 ^{o}C at an exposure time of 5 minutes.

P.diameter (nm)	ΔT/K	Power ($Js^{-1}mm^{-2}$)	mol_{CO} conv.($mm^{-2}s^{-1}$)	Total particle mass (g)	Total particle area (mm^2)	mol_{Au} in the surface (mm^{-2})	Spec. mass activity (mol_{CO} conv.g^{-1}Pt mm^{-2} s^{-1})	TOF (s^{-1})
1.5±0.5	0.532±0.03	1.343E-5±1.69E-6	4.75E-11±5.97E-12	4.50E-7±4.0E-14	10.950±0.8	2.55E-10±1.86E-11	1.05E-4±1.33E-5	0.186±0.023
1.9±0.6	0.483±0.02	1.217E-5±1.36E-6	4.30E-11±4.80E-12	5.70E-7±5.1E-14	19.206±1.5	4.47E-10±3.49E-11	7.55E-5±8.82E-6	0.096±0.011
2.5±0.8	0.468±0.03	1.179E-5±1.60E-6	4.17E-11±5.65E-12	7.20E-7±6.4E-14	29.526±2.4	6.86E-10±5.58E-11	5.79E-5±7.85E-6	0.061±0.008
2.9±1.0	0.461±0.02	1.160E-5±1.33E-6	4.10E-11±4.71E-12	8.70E-7±7.8E-14	39.846±3.2	9.26E-10±7.44E-11	4.71E-5±5.42E-6	0.044±0.005
3.4±1.1	0.452±0.02	1.138E-5±1.31E-6	4.02E-11±4.64E-12	1.02E-6±9.1E-14	50.166±4.1	1.17E-9±9.53E-11	3.94E-5±4.55E-6	0.034±0.004
3.9±1.3	0.444±0.02	1.118E-5±1.30E-6	3.95E-11±4.58E-12	1.17E-6±1.0E-13	60.486±4.9	1.41E-9±1.14E-10	3.38E-5±3.91E-6	0.028±0.003
4.4±1.5	0.439±0.02	1.106E-5±1.29E-6	3.91E-11±4.54E-12	1.32E-6±1.2E-13	70.806±5.8	1.65E-9±1.35E-10	2.96E-5±3.44E-6	0.024±0.002
4.8±1.6	0.445±0.02	1.121E-5±1.29E-6	3.96E-11±4.56E-12	1.44E-6±1.3E-13	79.062±6.4	1.84E-9±1.49E-10	2.75E-5±3.17E-6	0.022±0.002
5.3±1.9	0.443±0.03	1.116E-5±1.56E-6	3.94E-11±5.53E-12	1.59E-6±1.4E-13	89.382±7.3	2.08E-9±1.70E-10	2.48E-5±3.48E-6	0.019±0.003
5.8±2.0	0.412±0.02	1.037E-5±1.25E-6	3.66E-11±4.42E-12	1.74E-6±1.5E-13	99.702±8.1	2.32E-9±1.88E-10	2.11E-5±2.54E-6	0.016±0.002
		Equation 2.2	**Equation 3.6**	**Equation 3.8**	**Equation 2.6**	**Equation 3.9**	**Equation 3.7**	**Equation 3.5**

$2A_2$: Au/TiO_2 particle size as determined by TEM and their corresponding specific activity and TOF at a reaction temperature of 80 ^oC and an O_2:CO ratio of 1:1, at a total pressure of 8.4 x 10^{-2} mbar. Parameters used to compute the activity values are also included. The equations used to compute the parameters presented in the table are shown. Silicon nitride membrane area is (2.25 ± 0.01) mm^2, silicon nitride thermal conductivity (7 ± 0.5) $Wm^{-1}K^{-1}$ and silicon nitride membrane thickness is 0.6 ± 0.02 μm. The standard deviation for the temperature change was obtained from twelve points on each low. The estimated errors in other parameters were estimated from the deference between the average value and the maximum possible value calculated using errors in each formula used to compute each parameter.

O_2:CO ratio = 1:2, Total pressure = 9 x 10^{-1} mbar

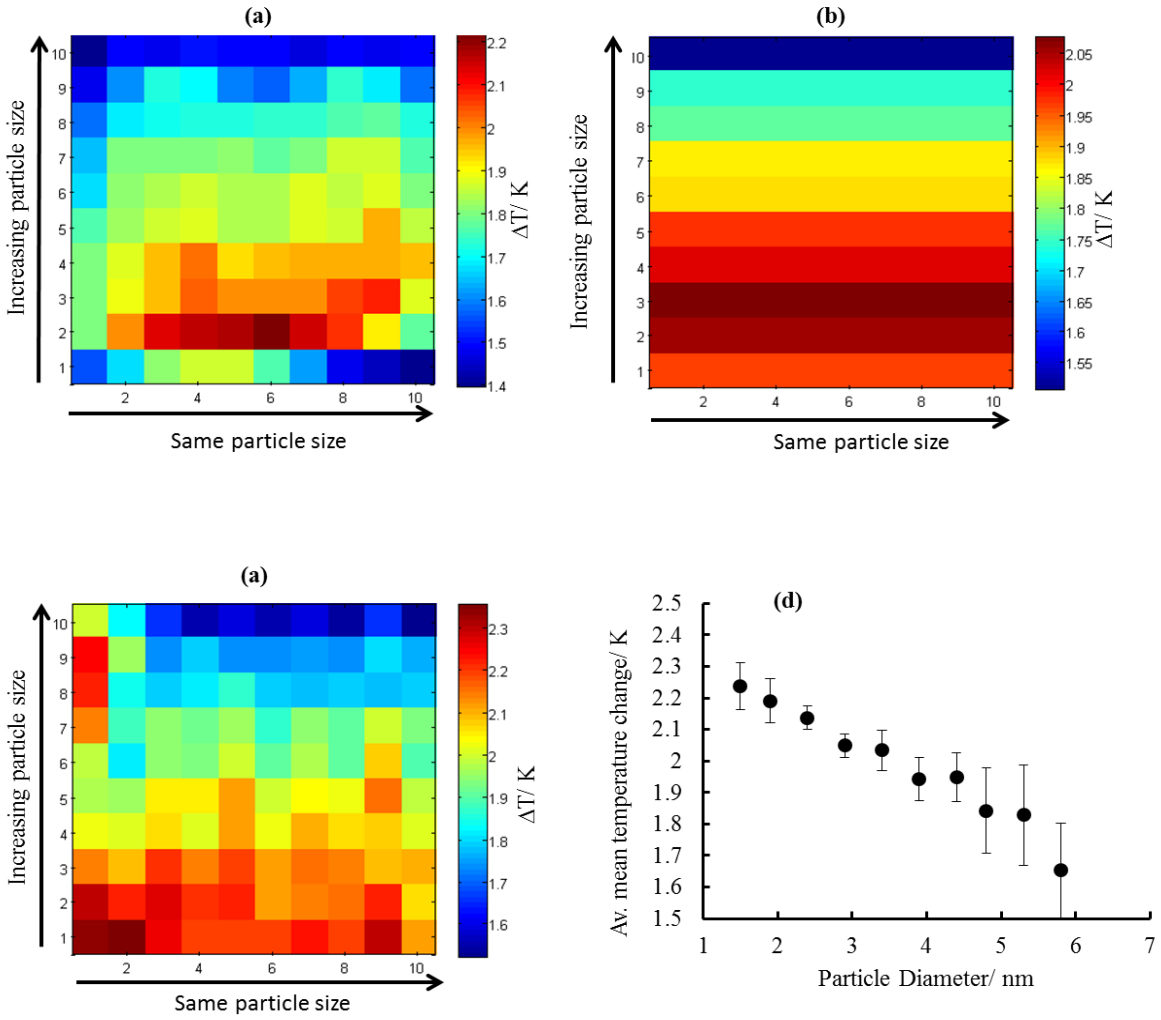

2A$_3$: The temperature change on Au/TiO_2 catalyst as a function of particle size at an O_2:CO ratio of 1:2, with a total pressure 9 x 10^{-1} mbar. **(a)** Presents uncompensated infrared image, **(b)** row compensated and **(c)** row and column compensated images. **(d)** Presents the average mean temperature change as a function of particle sizes for the row and column compensated infrared images. The row and column numbers are show on the x and y axes on the IR-images. The reaction temperature was 80 ^{o}C at an exposure time of 5 minutes.

P.diameter (nm)	ΔT/K	Power ($Js^{-1}mm^{-2}$)	mol_{CO} conv.($mm^{-2}s^{-1}$)	Total particle mass (g)	Total particle area (mm^2)	mol_{Au} in the surface (mm^{-2})	Spec. mass activity (mol_{CO} conv.g^{-1}Pt mm^{-2} s^{-1})	TOF (s^{-1})
1.5±0.5	2.237±0.07	5.638E-5±5.69E-6	1.99E-10±2.01E-11	4.50E-7±4.0E-14	10.950±0.8	2.55E-10±1.86E-11	4.43E-4±4.47E-5	0.783±0.079
1.9±0.6	2.190±0.06	5.519E-5±5.34E-6	1.95E-10±1.89E-11	5.70E-7±5.1E-14	19.206±1.5	4.47E-10±3.49E-11	3.42E-4±3.31E-5	0.437±0.042
2.5±0.8	2.137±0.04	5.385E-5± 4.71E-6	1.90E-10±1.67E-11	7.20E-7±6.4E-14	29.526±2.4	6.86E-10±5.58E-11	2.64E-4±2.31E-5	0.277±0.024
2.9±1.0	2.048±0.04	5.162E-5±4.55E-6	1.82E-10±1.61E-11	8.70E-7±7.8E-14	39.846±3.2	9.26E-10±7.44E-11	2.10E-4±1.85E-5	0.197±0.017
3.4±1.1	2.033±0.06	5.124E-5±5.07E-6	1.81E-10±1.79E-11	1.02E-6±9.1E-14	50.166±4.1	1.17E-9±9.53E-11	1.78E-4± 1.76E-5	0.155±0.015
3.9±1.3	1.942±0.07	4.896E-5±5.17E-6	1.73E-10±1.83E-11	1.17E-6±1.0E-13	60.486±4.9	1.41E-9±1.14E-10	1.48E-4±1.56E-5	0.123±0.013
4.4±1.5	1.947±0.08	4.908E-5±5.45E-6	1.73E-10±1.92E-11	1.32E-6±1.2E-13	70.806±5.8	1.65E-9±1.35E-10	1.31E-4±1.46E-5	0.105±0.012
4.8±1.6	1.84±0.10	4.641E-5±5.80E-6	1.64E-10±2.05E-11	1.44E-6±1.3E-13	79.062±6.4	1.84E-9±1.49E-10	1.14E-4± 1.42E-5	0.089±0.011
5.3±1.9	1.828±0.20	4.606E-5±8.50E-6	1.63E-10±3.00E-11	1.59E-6±1.4E-13	89.382±7.3	2.08E-9±1.70E-10	1.02E-4±1.89E-5	0.078±0.014
5.8±2.0	1.652±0.20	4.164E-5±8.19E-6	1.47E-10±2.89E-11	1.74E-6±1.5E-13	99.702±8.1	2.32E-9±1.88E-10	8.46E-5±166E-5	0.063±0.012
		Equation 2.2	**Equation 3.6**	**Equation 3.8**	**Equation 2.6**	**Equation 3.9**	**Equation 3.7**	**Equation 3.5**

$2A_4$: Au/TiO_2 particle size as determined by TEM and their corresponding specific activity and TOF at a reaction temperature of 80 ^oC and an O_2:CO ratio of 1:1, at a total pressure of 9 x 10^{-1} mbar. Parameters used to compute the activity values are also included. The equations used to compute the parameters presented in the table are shown. Silicon nitride membrane area is (2.25 ± 0.01) mm^2, silicon nitride thermal conductivity (7 ± 0.5) $Wm^{-1}K^{-1}$ and silicon nitride membrane thickness is 0.6 ± 0.02 μm. The standard deviation for the temperature change was obtained from ten points on each low. The estimated errors in other parameters were estimated from the deference between the average value and the maximum possible value calculated using errors in each formula used to compute each parameter.

O_2:CO ratio = 1:2, Total pressure = 9 x 10^{-2} mbar

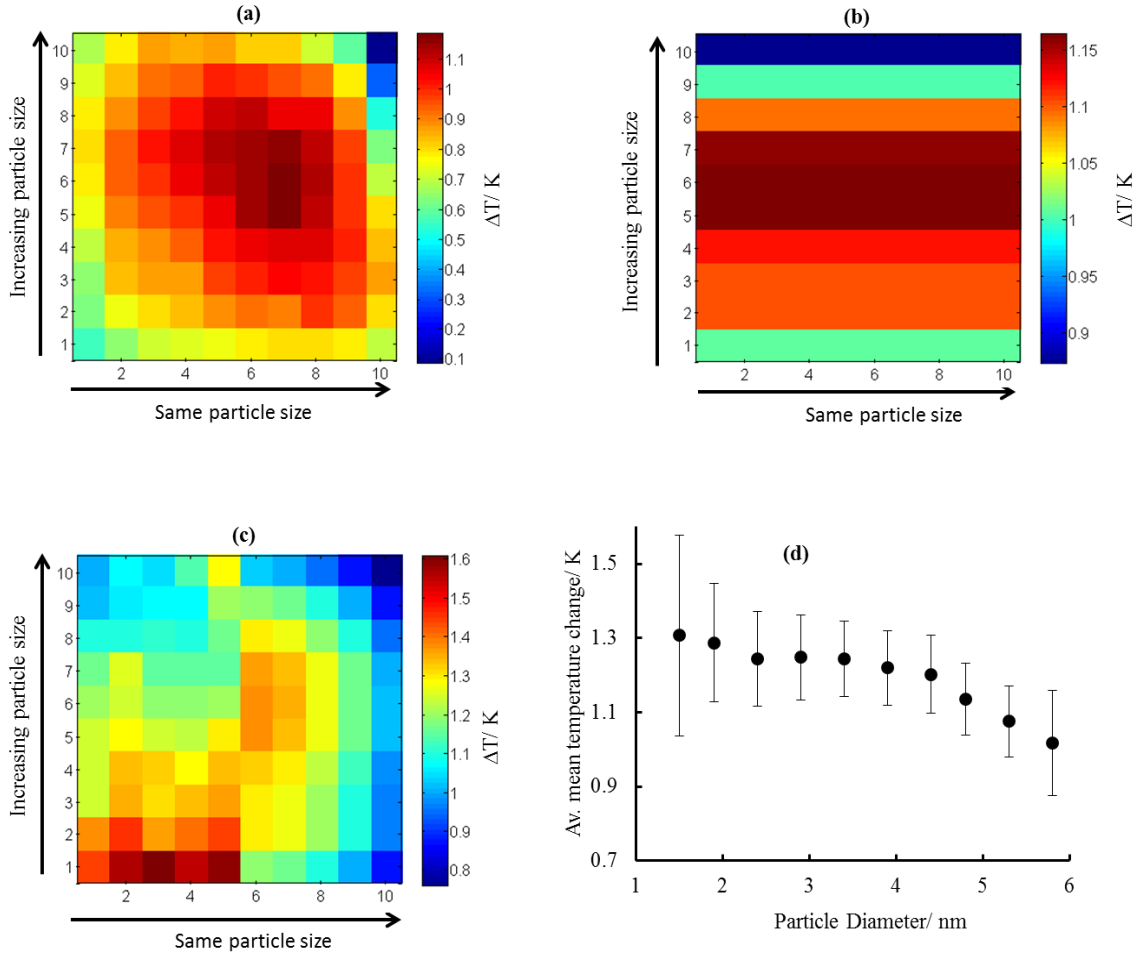

2B$_1$: The temperature change on Au/TiO_2 catalyst as a function of particle size at an O_2:CO ratio of 1:2, total pressure of 9 x 10^{-2} mbar. **(a)** Presents uncompensated infrared image, **(b)** row compensated and **(c)** completely compensated. **(d)** Presents the average mean temperature change as a function of particle sizes for the complete compensated infrared images. The row and column numbers are show on the x and y axes on the IR-images. The reaction temperature was 170 ^{o}C at an exposure time of 5 minutes.

P.diameter (nm)	ΔT/K	Power ($Js^{-1}mm^{-2}$)	mol_{CO} conv.($mm^{-2}s^{-1}$)	Total particle mass (g)	Total particle area (mm^2)	mol_{Au} in the surface (mm^{-2})	Spec. mass activity (mol_{CO} conv.g^{-1}Pt mm^{-2} s^{-1})	TOF (s^{-1})
1.5±0.5	1.307±0.20	3.293E-5± 7.61E-6	1.16E-10±2.69E-11	4.50E-7±4.0E-14	10.950±0.8	2.55E-10±1.86E-11	2.59E-4±5.98E-5	0.457±0.105
1.9±0.6	1.287±0.15	3.243E-5±6.22E-6	1.15E-10±2.20E-11	5.70E-7±5.1E-14	19.206±1.5	4.47E-10±3.49E-11	2.01E-4±3.86E-5	0.257±0.049
2.5±0.8	1.244±0.12	3.134E-5±5.35E-6	1.11E-10±1.89E-11	7.20E-7±6.4E-14	29.526±2.4	6.86E-10±5.58E-11	1.54E-4±2.63E-5	0.161±0.028
2.9±1.0	1.248±0.11	3.145E-5±5.09E-6	1.11E-10±1.80E-11	8.70E-7±7.8E-14	39.846±3.2	9.26E-10±7.44E-11	1.28E-4±2.07E-5	0.120±0.019
3.4±1.1	1.244±0.10	3.135E-5±4.81E-6	1.11E-10±1.70E-11	1.02E-6±9.1E-14	50.166±4.1	1.17E-9±9.53E-11	1.09E-4± 1.67E-5	0.095±0.015
3.9±1.3	1.219±0.10	3.073E-5±4.76E-6	1.09E-10±1.68E-11	1.17E-6±1.0E-13	60.486±4.9	1.41E-9±1.14E-10	9.28E-5±1.44E-5	0.077±0.012
4.4±1.5	1.202±0.10	3.030E-5±4.73E-6	1.07E-10±1.67E-11	1.32E-6±1.2E-13	70.806±5.8	1.65E-9±1.35E-10	8.11E-5±1.27E-5	0.065±0.010
4.8±1.6	1.135±0.09	2.861E-5±4.34E-6	1.01E-10±1.54E-11	1.44E-6±1.3E-13	79.062±6.4	1.84E-9±1.49E-10	7.02E-5± 1.07E-5	0.055±0.008
5.3±1.9	1.075±0.09	2.709E-5±4.24E-6	9.58E-11±1.50E-11	1.59E-6±1.4E-13	89.382±7.3	2.08E-9±1.70E-10	6.02E-5±9.43E-5	0.046±0.007
5.8±2.0	1.017±0.14	2.563E-5±5.50E-6	9.06E-11±1.94E-11	1.74E-6±1.5E-13	99.702±8.1	2.32E-9±1.88E-10	5.20E-5±1.12E-5	0.039±0.008
		Equation 2.2	**Equation 3.6**	**Equation 3.8**	**Equation 2.6**	**Equation 3.9**	**Equation 3.7**	**Equation 3.5**

$2B_2$: Au/TiO_2 particle size as determined by TEM and their corresponding specific mass activity and TOF at a reaction temperature of 170 ^oC at an O_2:CO ratio of 1:2, at a total pressure of 9 x 10^{-2} mbar. Parameters used to compute the activity values are also included. The equations used to compute the parameters presented in the table are shown. Silicon nitride membrane area is (2.25 ± 0.01) mm^2, silicon nitride thermal conductivity (7 ± 0.2) $Wm^{-1}K^{-1}$ and silicon nitride membrane thickness is 0.6 ± 0.02 μm. The standard deviation for the temperature change was obtained from ten points on each low. The estimated errors in other parameters were estimated from the deference between the average value and the maximum possible value calculated using errors in each formula used to compute each parameter.

O_2:CO ratio = 1:2, Total pressure = 9 x 10^{-1} mbar

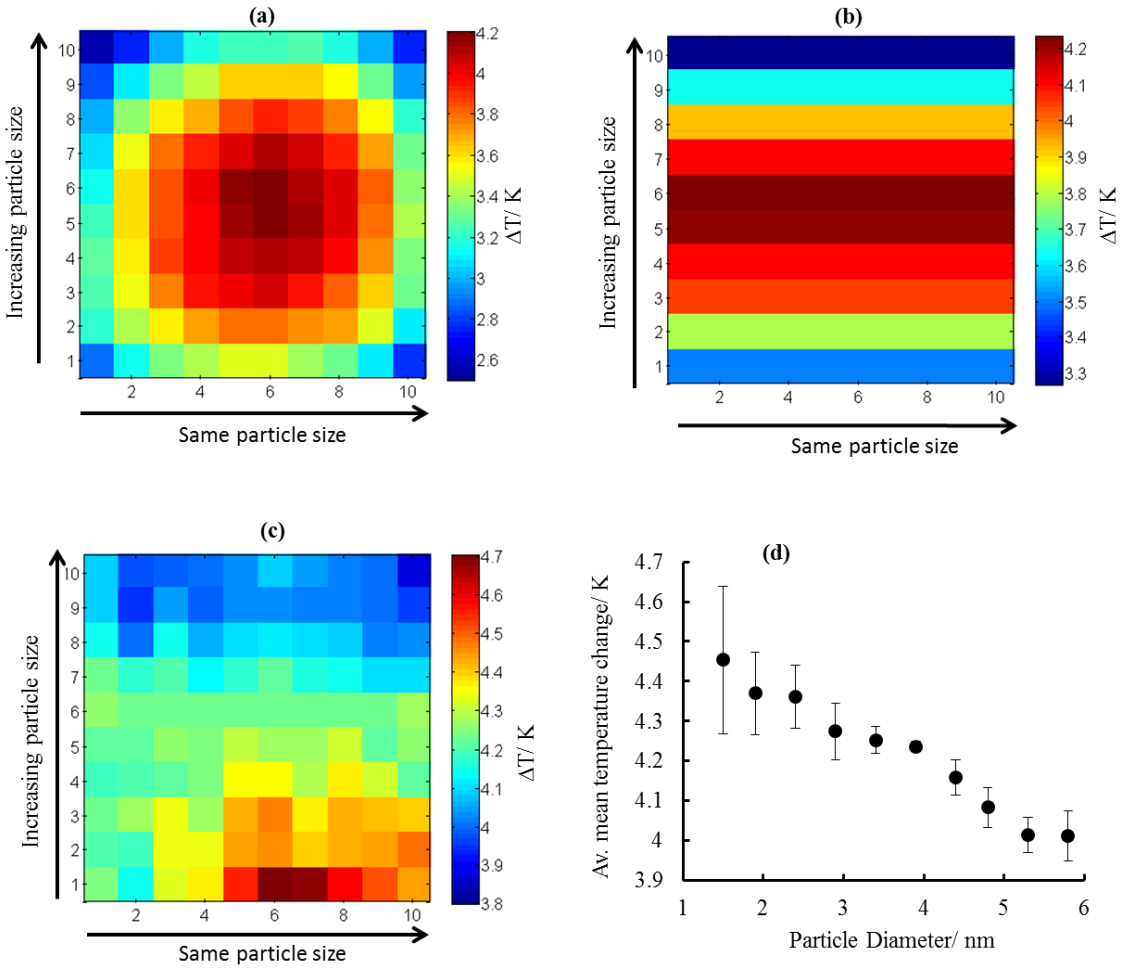

2B$_3$: The temperature change on Au/TiO_2 catalyst as a function of particle size at an O_2:CO ratio of 1:2, with a total pressure of 9 x 10^{-1} mbar. **(a)** Presents uncompensated infrared image, **(b)** row compensated and **(c)** completely compensated. **(d)** Presents the average mean temperature change as a function of particle sizes for the complete compensated infrared images. The row and column numbers are show on the x and y axes on the IR-images. The reaction temperature was 170 ^{o}C at an exposure time of 5 minutes.

P.diameter (nm)	ΔT/K	Power ($Js^{-1}mm^{-2}$)	mol_{CO} conv.($mm^{-2}s^{-1}$)	Total particle mass (g)	Total particle area (mm^2)	mol_{Au} in the surface (mm^{-2})	Spec. mass activity (mol_{CO} conv.g^{-1}Pt mm^{-2} s^{-1})	TOF (s^{-1})
1.5±0.5	4.454±0.18	1.122E-4±1.24E-5	3.966E-10±4.39E-11	4.50E-7±4.0E-14	10.950±0.8	2.55E-10±1.86E-11	8.81E-4±9.76E-5	1.558±0.172
1.9±0.6	4.369±0.10	1.101E-4±1.01E-5	3.891E-10±3.57E-11	5.70E-7±5.1E-14	19.206±1.5	4.47E-10±3.49E-11	6.63E-4±6.27E-5	0.871±0.080
2.5±0.8	4.360±0.08	1.098E-4± 9.57E-6	3.883E-10±3.38E-11	7.20E-7±6.4E-14	29.526±2.4	6.86E-10±5.58E-11	5.39E-4±4.70E-5	0.566±0.049
2.9±1.0	4.274±0.07	1.077E-4± 9.16E-6	3.806E-10±3.24E-11	8.70E-7±7.8E-14	39.846±3.2	9.26E-10±7.44E-11	4.37E-4±3.72E-5	0.411±0.035
3.4±1.1	4.253±0.03	1.071E-4±8.05E-6	3.787E-10±2.85E-11	1.02E-6±9.1E-14	50.166±4.1	1.17E-9±9.53E-11	3.71E-4± 2.79E-5	0.325±0.024
3.9±1.3	4.236±0.01	1.067E-4±7.48E-6	3.772E-10±2.64E-11	1.17E-6±1.0E-13	60.486±4.9	1.41E-9±1.14E-10	3.22E-4±2.26E-5	0.268±0.019
4.4±1.5	4.159±0.04	1.048E-4±8.15E-6	3.704E-10±2.88E-11	1.32E-6±1.2E-13	70.806±5.8	1.65E-9±1.35E-10	2.81E-4±2.18E-5	0.225±0.017
4.8±1.6	4.083±0.05	1.029E-4±8.29E-6	3.636E-10±2.93E-11	1.44E-6±1.3E-13	79.062±6.4	1.84E-9±1.49E-10	2.53E-4± 2.03E-5	0.198±0.015
5.3±1.9	4.014±0.04	1.011E-4±7.92E-6	3.574E-10±2.80E-11	1.59E-6±1.4E-13	89.382±7.3	2.08E-9±1.70E-10	2.25E-4±1.76E-5	0.172±0.013
5.8±2.0	4.012±0.06	1.011E-4±8.44E-6	3.573E-10±2.98E-11	1.74E-6±1.5E-13	99.702±8.1	2.32E-9±1.88E-10	2.05E-4±1.71E-5	0.154±0.013
		Equation 2.2	**Equation 3.6**	**Equation 3.8**	**Equation 2.6**	**Equation 3.9**	**Equation 3.7**	**Equation 3.5**

$2B_4$: Au/TiO_2 particle size as determined by TEM and their corresponding specific mass activity and TOF at a reaction temperature of 170 ^oC, and O_2:CO ratio of 1:2, total pressure of 9 x 10^{-1} mbar. Parameters used to compute the activity values are also included. The equations used to compute the parameters presented in the table are shown. Silicon nitride membrane area is (2.25 ± 0.01) mm^2, silicon nitride thermal conductivity (7 ± 0.2) $Wm^{-1}K^{-1}$ and silicon nitride membrane thickness is 0.6 ± 0.02 μm. The standard deviation for the temperature change was obtained from ten points on each low. The estimated errors in other parameters were estimated from the deference between the average value and the maximum possible value calculated using errors in each formula used to compute each parameter.

Appendix 3

- From the data in **Table 4.1** for the smallest (1.3 nm) Pt particle size, with the temperature change of 0.314 K, the power is computed using equation 2.2:

$$P\left[Js^{-1}mm^{-2}\right]=\frac{13.5\times 0.6(\mu m)\times 0.314(K)\times 7\left(Wm^{-1}K^{-1}\right)\times 10^{-6}}{1.44\left(mm^{2}\right)} \quad =1.239 \text{ x}10^{-5} \text{ Js}^{-1} \text{ mm}^{-2}$$

- The number of mole of CO converted per mm^2 per second is obtained through equation 3.6:

$$n_{CO}conv.\left[mm^{-2}s^{-1}\right]=\frac{1.239\times 10^{-5}\left[Js^{-1}mm^{-2}\right]}{283\times 10^{3}\left[J\right]} \quad = 4.378 \text{ x } 10^{-11} \text{ mol}_{CO} \text{ mm}^{-2} \text{ s}^{-1}$$

- The number of mole of Pt in the surface is calculated from equation 3.9, given the atom density of 1.5 x 10^{13} mm^{-2} and total Pt area of 10.262:

$$Moles_{Au/Pt}\left[mm^{-2}\right]=\frac{10.262_{Pt/Au}\times 1.5\times 10^{13}\left(mm^{-2}\right)}{6.022\times 10^{23}} \quad = 2.556 \text{ x } 10^{-10}\text{mol}_{Pt} \text{ mm}^{-2}$$

- Specific mass activity is therefore computed by using equation 3.7, given the particle mass of 1.04 x 10^{-6} g.

$$Spec.activity\left[mol_{CO}conv.g^{-1}{}_{Au/Pt}mm^{-2}s^{-1}\right]=\frac{4.378\times 10^{-11}\left[molmm^{-2}s^{-1}\right]}{1.04\times 10^{-6}\left[g\right]} \quad =$$

$4.21\text{x}10^{-5}$ mol_{CO} conv.g^{-1}Pt mm^{-2} s^{-1}

- The TOF is given by equation 3.5:

$$TOF\left[s^{-1}\right]=\frac{4.378\times 10^{-11}\left[mm^{-2}s^{-1}\right]}{2.556\times 10^{-10}\left[mm^{2}\right]} \quad = 0.171 \text{ s}^{-1}$$

Similar approach applies for activity computation for particle sizes.

7 References

1. Scheidtmann, J.; Weiss, P. A.; Maier, W. F., *Appl. Catal. A-Gen.* **2001,** *222* (1-2), 79-89.
2. Armor, J. N., *Catal. Today* **2011,** *163* (1), 3-9.
3. Jandeleit, B.; Schaefer, D. J.; Powers, T. S.; Turner, H. W.; Weinberg, W. H., *Angew.Chem.-Int.Edit* **1999,** *38* (17), 2494-2532.
4. Lindstrom, B.; Pettersson, L. J., *Cattech* **2003,** *7* (4), 130-138.
5. Wisniak, J., *The History of Catalysis. From the Beginning to Nobel Prizes*. Universidad Nacional Autónoma de México: 2010; Vol. 1.
6. Ertl, G.; Freund, H.-J., *Phys. Today* **1999**, 32-38.
7. Tsapatsaris, N. High-Throughput Structure/Function Screening of Materials and Catalysts under Process Conditions using Synchrotron Radiation. University of Manchester 2008.
8. P.W.Atkins, *The Elements of Physical Chemistry*. Oxford University Press: Oxford New York, 1996; p 499.
9. Senkan, S., *Angew. Chem.-Int. Edit.* **2001,** *40* (2), 312-329.
10. Somorjai, G. A.; Rioux, R. M., *Catal. Today* **2005,** *100* (3-4), 201-215.
11. Boudart, M., *Chem. Rev.* **1995,** *95* (3), 661-666.
12. Tsirlin, T.; Zhu, J.; Grunes, J.; Somorjai, G. A., *Top. Catal.* **2002,** *19* (2), 165-170.
13. Heiz, U.; Sanchez, A.; Abbet, S.; Schneider, W. D., *Chem. Phys.* **2000,** *262* (1), 189-200.
14. Hammer, B.; Nielsen, O. H.; Norskov, J. K., *Catalysis Letters* **1997,** *46* (1-2), 31-35.
15. Zhang, L.; Persaud, R.; Madey, T. E., *Phys. Rev. B* **1997,** *56* (16), 10549-10557.
16. Lopez, N.; Norskov, J. K.; Janssens, T. V. W.; Carlsson, A.; Puig-Molina, A.; Clausen, B. S.; Grunwaldt, J. D., *J. Catal.* **2004,** *225* (1), 86-94.
17. Hvolbaek, B.; Janssens, T. V. W.; Clausen, B. S.; Falsig, H.; Christensen, C. H.; Norskov, J. K., *Nano Today* **2007,** *2* (4), 14-18.
18. Haruta, M., *Catal. Today* **1997,** *36* (1), 153-166.
19. Remediakis, I. N.; Lopez, N.; Norskov, J. K., *Appl. Catal. A-Gen.* **2005,** *291* (1-2), 13-20.
20. Chen, M. S.; Goodman, D. W., *Accounts Chem. Res.* **2006,** *39* (10), 739-746.

21. Guerin, S.; Hayden, B. E.; Lee, C. E.; Mormiche, C.; Russell, A. E., *J. Phys. Chem. B* **2006,** *110* (29), 14355-14362.
22. Valden, M.; Lai, X.; Goodman, D. W., *Science* **1998,** *281* (5383), 1647-1650.
23. Tauster, S. J.; Fung, S. C.; Garten, R. L., *J. Am. Chem. Soc.* **1978,** *100* (1), 170-175.
24. Tauster, S. J., *Accounts Chem. Res.* **1987,** *20* (11), 389-394.
25. Pesty, F.; Steinriick, H.-P.; Madey, T. E., *Surf. Sci. Rep.* **1995,** *339*, 83-95.
26. Diebold, U., *Surf. Sci. Rep.* **2003,** *48* (5-8), 53-229.
27. Domenech-Ferrer, R.; Rodriguez-Viejo, J.; Garcia, G., *Catal. Today* **2011,** *159* (1), 144-149.
28. Turner, H. W.; Volpe, A. F.; Weinberg, W. H., *Surf. Sci.* **2009,** *603* (10-12), 1763-1769.
29. Hagemeyer, A.; Strasser, P.; Anthony F. Volpe, J., *High-Throughput Screening in Chemical Catalysis*. WILEY-VCH Verlag GmbH & Co. KGaA,: Weinheim, 2004.
30. Michalak, W. D.; Miller, J. B.; Yolcu, C.; Gellman, A. J., *Thin Solid Films* **2012,** *522* (0), 473-479.
31. Hanak, J. J., *J. Mater. Sci.* **1970,** *5* (11), 964-971.
32. Guerin, S.; Hayden, B. E., *J. Comb. Chem.* **2006,** *8* (1), 66-73.
33. Al-Odail, F. A.; Anastasopoulos, A.; Hayden, B. E., *Phys. Chem. Chem. Phys.* **2010,** *12* (37), 11398-11406.
34. Guerin, S.; Hayden, B. E.; Pletcher, D.; Rendall, M. E.; Suchsland, J. P.; Williams, L. J., *J. Comb. Chem.* **2006,** *8* (5), 791-798.
35. Penney, D. G., *Carbon monoxide poisoning*. Taylor & Francis Group: New York, 2008.
36. Braubach, M.; Algoet, A.; Beaton, M.; Lauriou, S.; Heroux, M. E.; Krzyzanowski, M., *Indoor Air* **2013,** *23* (2), 115-125.
37. Tseng, C. H.; Yang, T. C. K.; Wu, H. E.; Chiang, H. C., *J. Hazard. Mater.* **2009,** *166* (2-3), 686-694.
38. Bull, S., Carbon monoxide General Information. 2009.
39. Uysal, C.; Celik, S.; Altuntas, A. D.; Kandemir, E.; Kaya, M.; Karapirli, M.; Sezer, S.; Akyol, O., *Inhal. Toxicol.* **2013,** *25* (2), 102-106.
40. Raub, J. A.; Mathieu-Nolf, M.; Hampson, N. B.; Thom, S. R., *Toxicology* **2000,** *145* (1), 1-14.

41. WHO *Carbon Monoxide*; Denmark, 2000.
42. Kramer, M.; Duisberg, M.; Stowe, K.; Maier, W. F., *J. Catal.* **2007,** *251* (2), 410-422.
43. Wang, Y.; Chen, K. S.; Mishler, J.; Cho, S. C.; Adroher, X. C., *Appl. Energy* **2011,** *88* (4), 981-1007.
44. Kim, G.; Jhi, S. H., *Acs Nano* **2011,** *5* (2), 805-810.
45. Cameron, D.; Holliday, R.; Thompson, D., *J. Power Sources* **2003,** *118* (1-2), 298-303.
46. Hayden, B. E.; Rendall, M. E.; South, O., *J. Am. Chem. Soc.* **2003,** *125* (25), 7738-7742.
47. Saalfrank, J. W.; Maier, W. F., *C. R. Chim.* **2004,** *7* (5), 483-494.
48. Cypes, S.; Hagemeyer, A.; Hogan, Z.; Lesik, A.; Streukens, G.; Volpe, A. F.; Weinberg, W. H.; Yaccato, K., *Comb. Chem. High Throughput Screen* **2007,** *10* (1), 25-35.
49. Liu, L. Q.; Zhou, F.; Wang, L. G.; Qi, X. J.; Shi, F.; Deng, Y. Q., *J. Catal.* **2010,** *274* (1), 1-10.
50. Shaikhutdinov, S. K.; Meyer, R.; Naschitzki, M.; Baumer, M.; Freund, H. J., *Catal. Lett.* **2003,** *86* (4), 211-219.
51. Haruta, M.; Koboyashi, T.; Sano, H.; Yamada, N., *Chem. Lett.* **1987**, 405-408.
52. McClure, S. M.; Goodman, D. W., *Chem. Phys. Lett.* **2009,** *469* (1-3), 1-13.
53. Kolasinski, K. W., *Surface Science: Foundation of Catalysis and Nanoscience*. John Wiley & Sons, LTD: Queen Mary, University of London 2002.
54. M.McCash, E., *Surface Chemistry*. Oxford University Press: New York, 2001.
55. Bowker, M., *The Basis and Application of Heterogeneous Catalysis*. Oxford University Press Inc., : New York, 1998.
56. Comotti, M.; Li, W.-C.; Spliethoff, B.; Schuth, F., *J. Amer. Chem. Soc.* **2006,** *128*, 917-924.
57. Herranz, T.; Deng, X. Y.; Cabot, A.; Alivisatos, P.; Liu, Z.; Soler-Illia, G.; Salmeron, M., *Catal. Today* **2009,** *143* (1-2), 158-166.
58. Goodman, D. W., *J. Catal.* **2003,** *216* (1-2), 213-222.
59. Hayden, B. E.; Pletcher, D.; Suchsland, J. P.; Williams, L. J., *Phys. Chem. Chem. Phys.* **2009,** *11* (10), 1564-1570.

60. Hayden, B. E.; Pletcher, D.; Rendall, M. E.; Suchsland, J. P., *J. Phys. Chem. C* **2007,** *111* (45), 17044-17051.
61. Hayden, B. E., *Accounts Chem. Res.* **2013,** *46* (8), 1858-1866.
62. Bamwenda, G. R.; Tsubota, S.; Nakamura, T.; Haruta, M., *Catal. Lett.* **1997,** *44* (1-2), 83-87.
63. Haruta, M., *Catal. Surv. Jpn.* **1997,** *1*, 61 – 73.
64. Haruta, M., *J. New Mat.Electrochem. Syst.* **2004,** *7* (3), 163-172.
65. Franceschetti, A.; Pennycook, S. J.; Pantelides, S. T., *Chem. Phys. Lett.* **2003,** *374* (5-6), 471-475.
66. Meier, D. C.; Goodman, D. W., *J. Am. Chem. Soc.* **2004,** *126* (6), 1892-1899.
67. Chen, M. S.; Goodman, D. W., *Catal. Today* **2006,** *111* (1-2), 22-33.
68. Kim, S. H.; Jung, C. H.; Sahu, N.; Park, D.; Yun, J. Y.; Ha, H.; Park, J. Y., *Appl. Catal. A-Gen* **2013,** *454*, 53-58.
69. Allian, A. D.; Takanabe, K.; Fujdala, K. L.; Hao, X. H.; Truex, T. J.; Cai, J.; Buda, C.; Neurock, M.; Iglesia, E., *J. Am. Chem. Soc.* **2012,** *134* (1), 743-743.
70. Miller, J. T.; Kropf, A. J.; Zha, Y.; Regalbuto, J. R.; Delannoy, L.; Louis, C.; Bus, E.; van Bokhoven, J. A., *J. Catal.* **2006,** *240* (2), 222-234.
71. Haruta, M., *Gold Bull.* **2004,** *37* (1-2), 27-36.
72. Somorjai, G. A. In *Catalysis and Surface Science* European conference on surface science, Cambridge, England, Lawrence Berkeley National Laboratory: Cambridge, England, 1979; pp 1-56.
73. Comotti, M.; Weidenthaler, C.; Li, W. C.; Schuth, F., *Top. Catal.* **2007,** *44* (1-2), 275-284.
74. Haruta, M., *The Chemical Record* **2003,** *3*, 75-87.
75. Overbury, S. H.; Ortiz-Soto, L.; Zhu, H. G.; Lee, B.; Amiridis, M. D.; Dai, S., *Catal. Lett.* **2004,** *95* (3-4), 99-106.
76. Schubert, M. M.; Hackenberg, S.; van Veen, A. C.; Muhler, M.; Plzak, V.; Behm, R. J., *J. Catal.* **2001,** *197* (1), 113-122.
77. Comotti, M.; Li, W. C.; Spliethoff, B.; Schuth, F., *J. Am. Chem. Soc.* **2006,** *128* (3), 917-924.
78. Hayden, B. E.; Pletcher, D.; Suchsland, J. P., *Angew. Chem.-Int. Edit.* **2007,** *46* (19), 3530-3532.
79. Chen, M. S.; Goodman, D. W., *Top. Catal.* **2007,** *44* (1-2), 41-47.

80. Alexeev, O. S.; Chin, S. Y.; Engelhard, M. H.; Ortiz-Soto, L.; Amiridis, M. D., *J. Phys. Chem. B* **2005,** *109* (49), 23430-23443.
81. Li, N.; Chen, Q. Y.; Luo, L. F.; Huang, W. X.; Luo, M. F.; Hu, G. S.; Lu, J. Q., *Appl. Catal. B-Environ.* **2013,** *142*, 523-532.
82. Arrii, S.; Morfin, F.; Renouprez, A. J.; Rousset, J. L., *J. Am. Chem. Soc.* **2004,** *126* (4), 1199-1205.
83. Parker, S. C.; Grant, A. W.; Bondzie, V. A.; Campbell, C. T., *Surf. Sci.* **1999,** *441* (1), 10-20.
84. Yang, Z. X.; Wu, R. Q.; Goodman, D. W., *Phys. Rev. B* **2000,** *61* (20), 14066-14071.
85. Diebold, U.; Li, S. C.; Schmid, M., Oxide Surface Science. In *Annual Review of Physical Chemistry, Vol 61*, Leone, S. R.; Cremer, P. S.; Groves, J. T.; Johnson, M. A.; Richmond, G., Eds. Annual Reviews: Palo Alto, 2010; Vol. 61, pp 129-148.
86. Henry, C. R., *Prog. Surf. Sci.* **2005,** *80* (3-4), 92-116.
87. Baumer, M.; Freund, H. J., *Prog. Surf. Sci.* **1999,** *61* (7-8), 127-198.
88. Wahlstro¨m, E.; Lopez., N.; Schaub, R.; Thostrup, P.; Rønnau, A.; Africh, C.; Lægsgaard, E.; Nørskov, J. K.; Besenbacher, F.,*Amer.Phys. Soc.***2003**, 026101-4.
89. Jiang, Z. Q.; Zhang, W. H.; Jin, L.; Yang, X.; Xu, F. Q.; Zhu, J. F.; Huang, W. X., *J. Phys. Chem. C* **2007,** *111* (33), 12434-12439.
90. Lai, X.; St Clair, T. P.; Valden, M.; Goodman, D. W., *Prog. Surf. Sci.* **1998,** *59* (1-4), 25-52.
91. Cosandey, F.; Madey, T. E., *Surf. Rev. Lett.* **2001,** *8* (1-2), 73-93.
92. Suchslands, J.-P. Particle Size and Substrate Effects in Electrocatalysis. University of Southampton, 2007.
93. Nix, R. M. An Introduction to Surface Chemistry. (accessed 03/11/2014).
94. Fielicke, A.; Gruene, P.; Meijer, G.; Rayner, D. M., *Surf. Sci.* **2009,** *603* (10-12), 1427-1433.
95. Berlowitz, P. J.; Peden, C. H. F.; Goodman, D. W., *J. Phys. Chem.* **1998,** *92*, 5213-5221.
96. Xu, J.; Henriksen, P.; Yates, J. T.,*J.Chem.Phys.* **1992,** *97* (7), 5250-5252.
97. Santra, A. K.; Goodman, D. W., *Electrochim. Acta* **2002,** *47* (22-23), 3595-3609.
98. Morikawa, Y.; Mortensen, J. J.; Hammer, B.; Norskov, J. K., *Surf. Sci.* **1997,** *386* (1-3), 67-72.

99. Kolasinski:, K. W., *Surface Science:Foundation of Catalysis and Nanoscience*. John Wiley & Sons, LTD: Queen Mary, University of London, UK, 2002.
100. Blyholder, G.,*J.Phys.Chem.* **1964,** *68* (10), 2772-2777.
101. Aizawa, H.; Tsuneyuki, S., *Surf. Sci.* **1998,** *399* (2-3), L364-L370.
102. Sung, S. S.; Hoffmann, R., *J. Am. Chem. Soc.* **1985,** *107* (3), 578-584.
103. Xu, J.; Yates, J. T.,*J.Chem.Phys.* **1993,** *99* (1), 725-732.
104. Watanabe, Y.; Wu, X. Y.; Hirata, H.; Isomura, N., *Catal. Sci. Technol.* **2011,** *1* (8), 1490-1495.
105. Dakkaa, A.; Lafaitb, J.; Abd-Lefdila, M.; Sellab, C., *The Moroccan Statistical Physical Society* **1999**, 153-156.
106. Nowotny, M. K.; Bak, T.; Nowotny, J., *J. Phys. Chem. B* **2006,** *110* (33), 16270-16282.
107. Remediakis, I. N.; Lopez, N.; Nørskov, J. K., *Angew. Chem. Int. Ed.* **2005,** *44*, 1824 –1826.
108. Kageyama, S.; Sugano, Y.; Hamaguchi, Y.; Kugai, J.; Ohkubo, Y.; Seino, S.; Nakagawa, T.; Ichikawa, S.; Yamamoto, T. A., *Mater. Res. Bull.* **2013,** *48* (4), 1347-1351.
109. Li, S. Y.; Liu, G.; Lian, H. L.; Jia, M. J.; Zhao, G. M.; Jiang, D. Z.; Zhang, W. X., *Catal. Commun.* **2008,** *9* (6), 1045-1049.
110. Gao, F.; Wang, Y.; Cai, Y.; Goodman, D. W., *J. Phys. Chem.* **2009,** *113*, 174-181.
111. Risse, T.; Shaikhutdinov, S.; Nilius, N.; Sterrer, M.; Freund, H. J., *Accounts Chem. Res.* **2008,** *41* (8), 949-956.
112. Arenz, M.; Landman, U.; Heiz, U., *Chemphyschem* **2006,** *7* (9), 1871-1879.
113. Chen, M.; Goodman, D. W., *Chem. Soc. Rev.* **2008,** *37* (9), 1860-1870.
114. Kung, H. H.; Kung, M. C.; Costello, C. K., *J. Catal.* **2003,** *216* (1-2), 425-432.
115. Lopez, N.; Janssens, T. V. W.; Clausen, B. S.; Xu, Y.; Mavrikakis, M.; Bligaard, T.; Norskov, J. K., *J. Catal.* **2004,** *223* (1), 232-235.
116. Molina, L. M.; Lesarri, A.; Alonso, J. A., *Chem. Phys. Lett.* **2009,** *468* (4-6), 201-204.
117. Somorjai, G. A., *Introduction to Surface Chemistry and Catalysis*. John Wiley & Sons, Inc.: New York, 1994.
118. Rashkeev, S. N.; Lupini, A. R.; Overbury, S. H.; Pennycook, S. J.; Pantelides, S. T., *Phys. Rev. B* **2007,** *76* (3).
119. Dobrin, S., *Phys. Chem. Chem. Phys.* **2012,** *14* (35), 12122-12129.

120. Slavinskaya, E. M.; Gulyaev, R. V.; Stonkus, O. A.; Zadesenets, A. V.; Plyusnin, P. E.; Shubin, Y. V.; Korenev, S. V.; Ivanova, A. S.; Zaikovskii, V. I.; Danilova, I. G.; Boronin, A. I., *Kinet. Catal.* **2011,** *52* (2), 282-295.
121. Santos, V. P.; Carabineiro, S. A. C.; Tavares, P. B.; Pereira, M. F. R.; Orfao, J. J. M.; Figueiredo, J. L., *Appl. Catal. B-Environ.* **2010,** *99* (1-2), 198-205.
122. Newsam, J. M.; Schuth, F., *Biotechn.Bioeng.***1999,** *61* (4), 203-216.
123. Merrifield, R. B., *J. Am. Chem. Soc.* **1963,** *85* (14), 2149-2154.
124. Moates, F. C.; Somani, M.; Annamalai, J.; Richardson, J. T.; Luss, D.; Willson, R. C., *Ind. Eng. Chem. Res.* **1996,** *35* (12), 4801-4803.
125. Cong, P. J.; Doolen, R. D.; Fan, Q.; Giaquinta, D. M.; Guan, S. H.; McFarland, E. W.; Poojary, D. M.; Self, K.; Turner, H. W.; Weinberg, W. H., *Angew. Chem.-Int. Edit.* **1999,** *38* (4), 484-488.
126. Hahndorf, I.; Buyevskaya, O.; Langpape, M.; Grubert, G.; Kolf, S.; Guillon, E.; Baerns, M., *Chem. Eng. J.* **2002,** *89* (1-3), 119-125.
127. Senkan, S. M.; Ozturk, S., *Angew. Chem.-Int. Edit.* **1999,** *38* (6), 791-795.
128. Guerin, S.; Hayden, B. E.; Smith, D. C. A., *J.Comb.Chem* **2008,** *10* (1), 37-43.
129. Guerin, S.; Hayden, B. E.; Pletcher, D.; Rendall, M. E.; Suchsland, J. P., *J.Comb.Chem.* **2006,** *8* (5), 679-686.
130. Guerin, S.; Hayden, B. E.; Lee, C. E.; Mormiche, C.; Owen, J. R.; Russell, A. E.; Theobald, B.; Thompsett, D., *J.Comb.Chem.* **2004,** *6* (1), 149-158.
131. Aljohani, T. A.; Hayden, B. E.; Anastasopoulos, A., *Electrochim. Acta* **2012,** *76*, 389– 393.
132. Hayden, B. E.; Pletcher, D.; Suchsland, J.-P., *Angew. Chem. Int. Ed.* **2007,** *46*, 1-4.
133. Holzwarth, A.; Maier, W. F., *Platinum Met. Rev.* **2000,** *44*, 16-21.
134. Fleutot, B.; Miller, J. B.; Gellman, A. J., *J. Vac. Sci. Technol. A* **2012,** *30* (6), 061511-061511-10.
135. Holzwarth, A.; Schmidt, P. W.; Maier, W. E., *Angew. Chem.-Int. Edit.* **1998,** *37* (19), 2644-2647.
136. Biniwale, R. B.; Yamashiro, H.; Ichikawa, M., *Catal. Lett.* **2005,** *102* (1-2), 23-31.
137. Digilov, R.; Nekhamkina, O.; Sheintuch, M., *Aiche J.* **2004,** *50* (1), 163-172.
138. Loskyll, J.; Stoewe, K.; Maier, W. F., *ACS Comb. Sci.* **2012,** *14* (5), 295-303.
139. Domènech-Ferrer, R.; Rodríguez-Viejo, J.; Garcia, G., *Catal. Today* **2011,** *159*, 144–149.

140. Biniwalea, R. B.; Yamashirob, H.; Ichikawac, M., *Catal. Lett.* **2005,** *102*, 23-31.
141. Krämer, M.; Duisberg, M.; Stöwea, K.; Maier, W. F., *J. Catal.* **2007,** *251*, 410–422.
142. A.Potyrailo, R.; Amis, E. J., *High Throughput Analysis*. Kluwer Academic/Plenum Publishers: New York, 2003; Vol. 1.
143. Guerin, S.; Hayden, B. E.; Smith, D. C. A., *J. Comb. Chem.* **2008,** *10* (1), 37-43.
144. Kondratyuk, P.; Gumuslu, G.; Shukla, S.; Miller, J. B.; Morreale, B. D.; Gellman, A. J., *J. Catal.* **2013,** *300* (0), 55-62.
145. Guerin, S.; Hayden, B. E.; Lee, C. E.; Mormiche, C.; Owen, J. R.; Russell, A. E.; Theobald, B.; Thompsett, D., *J. Comb. Chem.* **2004,** *6* (1), 149-158.
146. Hayden, B. E.; Pletcher, D.; Suchsland, J. P.; Williams, L. J., *Phys. Chem. Chem. Phys.* **2009,** *11* (40), 9141-9148.
147. Woo, S. I.; Kim, K. W.; Cho, H. Y.; Oh, K. S.; Jeon, M. K.; Tarte, N. H.; Kim, T. S.; Mahmood, A., *QSAR Comb. Sci.* **2005,** *24* (1), 138-154.
148. O'Brien, C. P.; Miller, J. B.; Morreale, B. D.; Gellman, A. J., *The Journal of Physical Chemistry C* **2012,** *116* (33), 17657-17667.
149. Wang, H.; Liu, Z. M.; Shen, J. H.; Liu, H. C., *Catal. Commun.* **2004,** *5* (1), 55-58.
150. Claus, P.; Honicke, D.; Zech, T., *Catal. Today* **2001,** *67* (4), 319-339.
151. Hosneara; Hasnat; Bhuyan, A. H., *Daffodil Inter.Univer. J. Sci.Techn.***2012,** *7*, 50-58.
152. Gardeniers, J. G. E.; Tilmans, H. A. C.; Visser, C. C. G., *J. Vac. Sci. Technol. A-Vac. Surf. Films* **1996,** *14* (5), 2879-2892.
153. Ni, H.; Lee, H. J.; Ramirez, A. G., *Sensor. Actuat. A-Phys.* **2005,** *119* (2), 553-558.
154. Fedder, G. K. In *MEMS Fabrication* ITC International test conference USA: 2003; pp 691-698.
155. Madou, M., *Fundamentals of Microfabrication*. CRC Press LLC: Washington, D.C, 1997.
156. Beirong, Z.; Chen, Z.; Quan, W.; Yifeng, C.; Wei, X., *Adv. Mater. Sci. Eng.* **2013**, 835942 (4 pp.)-835942 (4 pp.).
157. Temple-Boyer, P.; Rossi, C.; Saint-Etienne, E.; Scheid, E., *J. Vac. Sci. Technol. A-Vac. Surf. Films* **1998,** *16* (4), 2003-2007.
158. Ekkels, P.; Tjerkstra, R. W.; Krijnen, G. J. M.; Berenschot, J. W.; Brugger, J.; Elwenspoek, M. C., *Microelectron. Eng.* **2003,** *67-8*, 422-429.

159. Jianqiang, H.; Yan, L.; Senlin, L.; Qing, L., *J. Semicond.* **2014,** *35*.
160. Minhee, Y., *J. Korean Phys. Soc.* **2000,** *37* (5), 605-610.
161. Sikora, A.; Ftouni, H.; Richard, J.; Hebert, C.; Eon, D.; Omnes, F.; Bourgeois, O., *Rev. Sci. Instrum.* **2012,** *83* (5).
162. Jain, A.; Goodson, K. E., *J. Heat Transfer* **2008,** *130* (10).
163. Coquil, T.; Reitz, C.; Brezesinski, T.; Nemanick, E. J.; Tolbert, S. H.; Pilon, L., *J. Phys. Chem. C* **2010,** *114* (29), 12451-12458.
164. Shahil, K. M. F.; Balandin, A. A., *Solid State Commun.* **2012,** *152* (15), 1331-1340.
165. Price, G., *Thermodynamics of Chemical Processes*. Oxford University Press New York, 1998.
166. Hannah, L. M. V. The High Through-put Synthesis & Screening of Electrocatalysts for the Reduction of Nitrate in Groundwater and Waste Streams. University of Southampton, 2012.
167. Aljohani, T. A.; Hayden, B. E.; Anastasopoulos, A., *Electrochim. Acta* **2012,** *76*, 389-393.
168. Aljohani, T. A. M. High Throughput Synthesis and Corrosion Studies on Alloys. University of Southampton, 2013.
169. Beal, M. S.; Hayden, B. E.; Le Gall, T.; Lee, C. E.; Lu, X. J.; Mirsaneh, M.; Mormiche, C.; Pasero, D.; Smith, D. C. A.; Weld, A.; Yada, C.; Yokoishi, S., *ACS Comb. Sci.* **2011,** *13* (4), 375-381.
170. Attard, G.; Barnes, C., *Surfaces*. Oxford University Press Inc.: New York, 1998.
171. Hasan, M. M.; Haseeb, A. S. M. A.; Saidur, R.; Masjuki, H. H., *Inter. J.Chem.Biol. Eng.* **2008,** *1*, 92-96.
172. Lee, W. G.; Woo, S. I.; Kim, J. C.; Choi, S. H.; b, K. H. O., *Thin Solid Films* **1994,** *237*, 105-111.
173. Carp, O.; Huisman, C. L.; Reller, A., *Prog. Solid State Chem.* **2004,** *32* (1-2), 33-177.
174. Gao, Y. F.; Masuda, Y.; Peng, Z. F.; Yonezawa, T.; Koumoto, K., *J. Mater. Chem.* **2003,** *13* (3), 608-613.
175. Guerin, S.; Hayden, B. E.; Pletcher, D.; Rendall, M. E.; Suchsland, J. P., *J. Comb. Chem.* **2006,** *8* (5), 679-686.
176. Wu, C.; Marshall, M. S. J.; Castell, M. R., *J. Phys. Chem. C* **2011,** *115* (17), 8643-8652.

177. McClure, S. M.; Lundwall, M.; Zhou, Z.; Yang, F.; Goodman, D. W., *Catal. Lett.* **2009,** *133* (3-4), 298-306.
178. Liu, C.; Li, G.; Kauffman, D. R.; Pang, G.; Jin, R., *J. Colloid Interface Sci.* **2014,** *423*, 123-128.
179. Meyer, R.; Lemire, C.; Shaikhutdinov, S. K.; Freund, H., *Gold Bull.* **2004,** *37* (1-2), 72.
180. Heiz, U.; Sanchez, A.; Abbet, S.; Schneider, W. D., *J. Am. Chem. Soc.* **1999,** *121* (13), 3214-3217.
181. Johanek, V.; Laurin, M.; Grant, A. W.; Kasemo, B.; Henry, C. R.; Libuda, J., *Science* **2004,** *304* (5677), 1639-1644.
182. Carabineiro, S. A. C.; Bogdanchikova, N.; Avalos-Borja, M.; Pestryakov, A.; Tavares, P. B.; Figueiredo, J. L., *Nano Res.* **2011,** *4* (2), 180-193.
183. Overbury, S. H.; Schwartz, V.; Mullim, D. R.; Yan, W. F.; Dai, S., *J. Catal.* **2006,** *241* (1), 56-65.
184. Lin, S. D.; Bollinger, M.; Vannice, M. A., *Catal. Lett.* **1993,** *17* (3-4), 245-262.
185. Kozlov, A. I.; Kozlova, A. P.; Liu, H. C.; Iwasawa, Y., *Applied Catalysis a-General* **1999,** *182* (1), 9-28.
186. Gao, F.; Wood, T. E.; Goodman, D. W., *Cataly. Lett.* **2010,** *134* (1-2), 9-12.
187. Liu, L. M.; McAllister, B.; Ye, H. Q.; Hu, P., *J. Am. Chem. Soc.* **2006,** *128* (12), 4017-4022.